

CANADA • INLAND WATERS DIRECTORATE
SCIENTIFIC SERIES

#134 (C2)

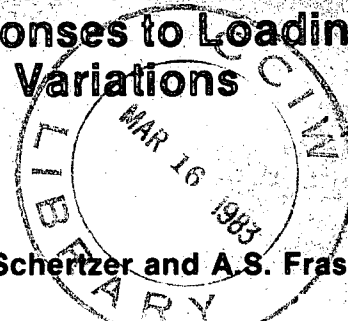


Environnement
Canada

Environnement
Canada

Simulation of Lake Erie Water
Quality Responses to Loading
and Weather Variations

D.C.L. Lam, W.M. Schertzer and A.S. Fraser



SCIENTIFIC SERIES NO. 134

NATIONAL WATER RESEARCH INSTITUTE
INLAND WATERS DIRECTORATE
CANADA CENTRE FOR INLAND WATERS
BURLINGTON, ONTARIO, 1983

Canada

SIMULATION OF LAKE ERIE WATER QUALITY RESPONSES TO LOADING AND WEATHER VARIATIONS • LAM, SCHERTZER AND FRASER

GB
707
C335
no. 134
c.2



Environment
Canada

Environnement
Canada

Simulation of Lake Erie Water Quality Responses to Loading and Weather Variations

D.C.L. Lam, W.M. Schertzer and A.S. Fraser

SCIENTIFIC SERIES NO. 134

**NATIONAL WATER RESEARCH INSTITUTE
INLAND WATERS DIRECTORATE
CANADA CENTRE FOR INLAND WATERS
BURLINGTON, ONTARIO, 1983**

Canada

© Minister of Supply and Services Canada 1983

Cat. No. En 36-502/134E

ISBN 0-662-12443-X

Contents

	Page
ABSTRACT	xv
RESUME	xvii
ACKNOWLEDGMENTS	xix
SUMMARY	S-1
1. LAKE ERIE BASINS	1-1
1.1 Introduction	1-1
1.2 Physical characteristics	1-6
2. LAKE ERIE LOADING	2-1
2.1 Sources of loading data	2-1
2.1.1 Tributaries	2-2
2.1.2 Municipal and industrial loads	2-2
2.1.3 Atmospheric loads	2-3
2.2 Connecting channels	2-4
2.2.1 Detroit River	2-4
2.2.2 Niagara River	2-6
2.2.3 Estimation method	2-7
2.3 Loading estimates	2-8
2.3.1 Total phosphorus	2-8
2.3.2 Soluble reactive phosphorus	2-13
2.3.3 Nitrogen	2-15
2.3.4 Chloride	2-17
3. LAKE CHEMISTRY	3-1
3.1 Introduction	3-1
3.2 Two-dimensional interpolated data	3-4
3.2.1 Temperature	3-4
3.2.2 Total phosphorus	3-6
3.2.3 Soluble reactive phosphorus	3-7
3.2.4 Dissolved oxygen	3-9
3.2.5 Chlorophyll <u>a</u>	3-10
3.2.6 Nitrate plus nitrite	3-12
3.2.7 Ammonia	3-13
3.2.8 Chloride	3-13
3.3 Diagnostic mass balances	3-15
3.3.1 Sensitivity of the lake concentration data	3-17
3.3.2 Diagnostic results using total phosphorus data	3-19
3.3.3 Diagnostic results from soluble reactive phosphorus data	3-22
3.3.4 Sedimentation coefficient	3-26

	Page
4. PHYSICAL DATA BASE	4-1
4.1 Introduction	4-1
4.2 Physical Data	4-2
4.2.1 Water temperature	4-4
4.2.2 Air temperature and vapour pressure gradients	4-7
4.2.3 Wind speed	4-11
4.2.4 Comparison of meteorological data and buoy values	4-12
4.2.5 Lake inflow and outflow	4-13
4.2.6 Water level	4-15
4.2.7 Mean vertical extinction coefficient	4-16
4.2.8 Light and primary production	4-19
4.2.9 Heat content	4-20
5. HEAT AND MASS BALANCE MODELS	5-1
5.1 Introduction	5-1
5.2 Heat balance model	5-1
5.2.1 Lake-wide heat balance analysis	5-2
5.2.2 Radiation components	5-7
5.2.3 Evaporation	5-7
5.2.4 Lake-wide surface heat flux	5-11
5.3 Scaling and Interpolation Technique (SIT) for optimizing the lake-wide heat balance	5-13
5.4 Basin heat balance and exchange rates	5-17
5.4.1 Approximation of basin heat storage	5-17
5.4.2 Heat exchanged at the air-water interface	5-19
5.4.3 Basin net horizontal exchange	5-21
5.5 Diagnostic mass balance models	5-26
5.6 Three-box model	5-27
5.7 Six-box model	5-30
5.7.1 Hydraulic flow	5-34
5.7.2 Interbasin transport	5-35
5.7.3 Effective vertical velocity parameter W_1 : entrainment, hydraulic flows, interbasin trans- ports, and water levels	5-38
5.7.4 Turbulent diffusion	5-41
5.8 Nine-box model	5-44
6. PROGNOSTIC MASS BALANCE MODELS	6-1
6.1 Introduction	6-1
6.2 Six-box three-variable model	6-3
6.2.1 Model structure	6-5
6.2.2 Calibration	6-8
6.2.3 Long-term simulation: 1967 to 1978	6-11
6.2.4 Dissolved oxygen: verification, 1967 to 1977	6-18
6.2.5 Soluble reactive phosphorus: verification, 1967 to 1977	6-20
6.2.6 Total phosphorus: verification, 1967 to 1977	6-22

	Page
6.3 Nine-box three-variable model	6-25
6.3.1 Model structure	6-26
6.3.2 Calibration	6-31
6.3.3 Dissolved oxygen: verification, 1967 to 1977	6-34
6.3.4 Soluble reactive phosphorus: verification, 1967 to 1977	6-40
6.3.5 Total phosphorus: verification, 1967 to 1977	6-44
7. ONE-DIMENSIONAL THERMOCLINE MODEL	7-1
7.1 Introduction	7-1
7.2 Physical processes and model structure	7-2
7.3 Model calibration	7-8
7.4 Verification: temperature, 1967 to 1978	7-14
7.4.1 Verification: thermocline positions, 1978	7-16
7.4.2 Verification: averaged temperatures for box models, 1967 to 1978	7-28
7.5 Feedback of heat flux and thermocline models	7-34
8. SYNTHESIS MODELS OF FINER SPATIAL RESOLUTIONS	8-1
8.1 Introduction	8-1
8.2 One-dimensional (z) dissolved oxygen model	8-3
8.3 Two-dimensional (x-z) temperature and flow model	8-7
8.4 Two-dimensional (x-y) model	8-13
8.5 Three-dimensional (x-y-z) models	8-18
9. MODEL APPLICATION: ESTIMATED LAKE RESPONSES TO METEOROLOGICAL AND LOADING EFFECTS	9-1
9.1 Potentials and pitfalls	9-1
9.2 Error analysis	9-3
9.3 Sensitivity analysis	9-11
9.4 Estimated water quality response to phosphorus loading reduction	9-17
9.5 Estimated water quality response to water level changes	9-22
9.6 Further research needs for Lake Erie water quality modelling	9-24
REFERENCES	R-1
BIBLIOGRAPHY	B-1
APPENDIX. Interpolation scheme for Lake Erie water quality data	A-1

Tables

	Page
Table 1.1a. Physical characteristics of Lake Erie	1-7
Table 1.1b. Physical characteristics of Lake Erie basins . . .	1-7
Table 3.1. Lake Erie horizontal gradients	3-2
Table 3.2. Primary CCIW cruises used in lake chemistry analysis	3-3
Table 3.3. Total phosphorus box model reduction	3-18
Table 3.4. Dissolved oxygen box model reduction	3-18
Table 3.5. Spring values for sedimentation coefficient (σ) and settling velocity (σ')	3-28
Table 4.1. Comparison of monthly lake/land humidity ratios .	4-10
Table 5.1. Heat balance relationships	5-4
Table 5.2. Meteorological and radiation factors	5-5
Table 5.3. Comparison of Lake Erie radiation flux computations	5-5
Table 6.1a. Equations of six-box three-variable model	6-7
Table 6.1b. Constants and formulas of six-box three-variable model	6-7
Table 6.2a. Equations of nine-box three-variable model	6-29
Table 6.2b. Constants and formulas of nine-box three-variable model	6-30
Table 7.1. Constants used in one-dimensional thermocline model	7-12
Table 7.2. Accuracy (σ = standard error) of surface water temperature (T_s in $^{\circ}\text{C}$) calculations by coupled heat flux - thermocline model approach	7-35
Table 9.1. Median relative errors in % of the variables in the six-box model based on computed and observed results for 1967 to 1978	9-6
Table 9.2. Median relative errors in % of the variables in the nine-box model based on computed and observed results for 1967 to 1978	9-9

Illustrations

	Page
Figure 1.1. Lake Erie Basin in relation to the Great Lakes . .	1-5
Figure 1.2. Profile of the Great Lakes	1-5
Figure 1.3. Lake Erie bathymetry	1-7
Figure 1.4. Lake Erie hypsometric curves	1-8
Figure 2.1. Detroit River concentrations	2-5
Figure 2.2. Lower Detroit River Bar-Lee section	2-5
Figure 2.3. Total phosphorus loading to Lake Erie	2-9
Figure 2.4. Source distribution of total phosphorus loading to Lake Erie	2-9
Figure 2.5. Total phosphorus loads to Lake Erie basins	2-12
Figure 2.6. Soluble reactive phosphorus loads to Lake Erie basins	2-14
Figure 2.7. Chemical loadings to Lake Erie	2-16
Figure 3.1. Two-dimensional representation of observed data for temperature and total phosphorus for the August-September period	3-5
Figure 3.2. Two-dimensional representation of observed data for soluble reactive phosphorus and dissolved oxygen for the August-September period	3-8
Figure 3.3. Two-dimensional representation of observed data for chlorophyll <u>a</u> and nitrate plus nitrite for the August-September period	3-11
Figure 3.4. Two-dimensional representation of observed data for ammonia and chloride for the August-September period	3-14
Figure 3.5. Schematic of Lake Erie dynamic mass balance model .	3-16
Figure 3.6. Rate correlation during growth phase in the Central Basin derived from the three-box representation of observed data	3-16

Illustrations (Cont.)

	Page
Figure 3.7. Net sedimentation rate of total phosphorus derived from diagnostic mass balances	3-20
Figure 3.8. Phosphorus uptake and regeneration rate derived from diagnostic mass balances	3-24
Figure 3.9. Sedimentation coefficient for the Central Basin (1967 to 1978)	3-27
Figure 4.1. Location of meteorological stations, water level recording stations and meteorological buoy	4-3
Figure 4.2. Basin surface water temperature and vertically integrated water temperature averages computed from CCIW surveys in the period 1967 to 1978	4-5
Figure 4.3. Polynomial fit to Lake Erie Basin (a) water surface temperature and (b) vertically integrated water temperature for the period 1967 to 1978	4-5
Figure 4.4. Comparison of long-term means of computed over-lake meteorological components for Lake Erie	4-8
Figure 4.5. Comparison of long-term monthly mean over-lake wind speed for Lake Erie basins and lake-wide case	4-8
Figure 4.6. Comparison of computed Central Basin monthly mean meteorological data with means of observed mid-lake values for 1977	4-14
Figure 4.7. Detroit River and Niagara River inflow and outflow volumes and estimation of average river water temperatures for 1967 to 1978	4-14
Figure 4.8. Lake Erie water level approximation	4-18
Figure 4.9. Lake Erie mean vertical extinction coefficient based on CCIW surveys in the period 1967 to 1978	4-18
Figure 4.10. Light factor computed for Lake Erie basins for the (1) epilimnion; (2) mesolimnion; (3) hypolimnion layers for 1967	4-18
Figure 4.11. Lake Erie basin heat content based on CCIW water temperature surveys in the period 1967 to 1978	4-21

Illustrations (Cont.)

	Page
Figure 4.12. Lake Erie lake-wide heat content from CCIW water temperature surveys from 1967 to 1978, and comparison of mean values derived from this study with those of Derecki (1975) for the period 1952 to 1968	4-21
Figure 4.13. Ten-day means of lake-wide wind speed, solar radiation and basin-wide averages of mean vertical extinction coefficient for Lake Erie in the period April through November for 1967 to 1978	4-22
Figure 5.1. Monthly means of Lake Erie radiation components computed for 1967 to 1978	5-3
Figure 5.2. Comparison of long-term monthly mean lake-wide evaporation estimates for Lake Erie	5-6
Figure 5.3. Comparison of 1967 and 1968 monthly mean evaporation from the mass transfer approach in the present study with values of evaporation computed by water balance and mass transfer	5-6
Figure 5.4. Average monthly evaporation for Lake Erie basins for the period 1967 to 1978 for the months April through November	5-8
Figure 5.5. Lake Erie long-term monthly mean surface heat flux components and computed surface heat flux for the lake-wide case	5-10
Figure 5.6. Examples of Lake Erie computed lake-wide heat content as the summation of computed lake-wide surface heat flux beginning at an initial value usually in April	5-12
Figure 5.7. Computed Lake Erie lake-wide heat content modified through Scaling and Interpolation Technique and estimation of basin heat content as a proportion of the computed lake-wide heat content	5-15
Figure 5.8. Average difference between lake-wide surface heat flux computations determined through modification by Scaling and Interpolation Technique and with no modification for the period 1967 to 1978	5-16
Figure 5.9. Comparison of computed Central Basin evaporative heat flux and sensible heat flux with Buoy 11A values for 1977	5-16

Illustrations (Cont.)

	Page
Figure 5.10. Schematic of components considered in the evaluation of the net heat exchanged between Lake Erie basins using a Heat Balance approach	5-18
Figure 5.11. Ratio of basin to lake-wide heat content for Lake Erie based on polynomial fit through observations in the period 1967 to 1978	5-18
Figure 5.12. Comparison of long-term monthly mean surface heat flux modified through Scaling and Interpolation Technique with unmodified calculations for Lake Erie basins	5-20
Figure 5.13. An example of the computed summertime net quantity of heat and net velocities exchanged across Lake Erie basins determined through Heat Balance approach for 1969	5-20
Figure 5.14. Basin boundaries and major components incorporated in the three-box mass balance model of Lake Erie	5-24
Figure 5.15. Computed net exchange rates between the West-Central and Central-East basins based on the hydraulic flows	5-24
Figure 5.16. Basin boundaries and major components incorporated in the six-box mass balance model of Lake Erie	5-32
Figure 5.17. Schematic of the major processes parameterized in the six-box mass balance model of Lake Erie	5-32
Figure 5.18. Mesolimnion and hypolimnion flow at the Pennsylvania Ridge computed as 48-hour averages for the period June through September 1978	5-37
Figure 5.19. Time-series computed (five-day mean) plot of (a) the thermocline position; (b) the transport velocities U_{11} and U_{12} between the West and Central basins; and (c) the transport velocities U_{21} and U_{22} between the Central and East basins for Lake Erie, 1978	5-37
Figure 5.20. Basin boundaries and major components incorporated in the nine-box mass balance model of Lake Erie	5-43
Figure 5.21. Schematic of the major processes parameterized in the nine-box mass balance model of Lake Erie	5-43

Illustrations (Cont.)

	Page
Figure 5.22. Relationship between two-day averaged east component winds from Long Point and two-day average hypolimnion flow at the Pennsylvania Ridge in the period June to September, 1978	5-49
Figure 5.23. Relationship between 48-hour averages of (a) computed mesolimnion velocities to hypolimnion velocities and (b) computed mesolimnion flow to hypolimnion flow, at the Pennsylvania Ridge during the period June to September in 1978	5-49
Figure 6.1. Model structure of the six-box three-variable model in a typical water column	6-6
Figure 6.2. Calibration of the six-box model using 1978 data	6-9
Figure 6.3. Computed positions of the thermocline and the upper and lower mesolimnion boundaries of the Central Basin for 1967 to 1978	6-12
Figure 6.4. Verification of the six-box model for Lake Erie basins for dissolved oxygen, 1967 to 1978	6-14
Figure 6.5. Verification of the six-box model for Lake Erie basins for soluble reactive phosphorus, 1967 to 1978	6-16
Figure 6.6. Verification of the six-box model for Lake Erie basins for total phosphorus, 1967 to 1978	6-23
Figure 6.7. Model structure of the nine-box three-variable model in a typical water column	6-28
Figure 6.8. Calibration of the nine-box model using 1978 data	6-32
Figure 6.9. Verification of the nine-box model for Lake Erie basins for dissolved oxygen, 1967 to 1978	6-35
Figure 6.10. Verification of the nine-box model for Lake Erie basins for soluble reactive phosphorus, 1967 to 1978	6-41
Figure 6.11. Verification of the nine-box model for Lake Erie basins for total phosphorus, 1967 to 1978	6-45
Figure 7.1. Hourly averaged temperature profiles	7-5
Figure 7.2. Two-dimensional (x-z) contours generated by interpolation (Program TWIST) of ship cruise temperature data (September 13-19, 1978)	7-5

Illustrations (Cont.)

	Page
Figure 7.3. One-dimensional volume-weighted averaged temperature profiles obtained from results of Figure 7.2 for calibrating the one-dimensional thermocline model	7-5
Figure 7.4. Computed and observed temperature, and computed eddy diffusivity for the Central Basin, 1970	7-15
Figure 7.5. Computed and observed thermocline positions for the Central Basin, 1970	7-15
Figure 7.6. Computed and observed temperature for the Central Basin of Lake Erie	7-17
Figure 7.7. Computed and observed temperature for the East Basin of Lake Erie	7-20
Figure 7.8. Sampling network near the Pennsylvania Ridge, Lake Erie, 1978	7-26
Figure 7.9. Computed mean depth for the Central Basin and observed minimum and maximum positions for the Pennsylvania Ridge of (a) the upper mesolimnion boundary, (b) the thermocline, and (c) the lower mesolimnion boundary	7-26
Figure 7.10. Computed positions of the thermocline, and the upper and lower mesolimnion boundaries of the Central Basin for 1967 to 1978	7-27
Figure 7.11. Computed and observed upper and lower layer temperatures for Lake Erie basins	7-29
Figure 7.12. Computed and observed epilimnion, mesolimnion and hypolimnion temperatures for Lake Erie basins	7-31
Figure 7.13. Feedback scheme for coupling the heat flux model and the thermocline model	7-35
Figure 8.1. One-dimensional (z) vertical profiles of dissolved oxygen for the Central Basin, 1970	8-5
Figure 8.2. Comparison of computed and observed dissolved oxygen concentrations at 1 m above the sediment for the Central Basin, 1970	8-5
Figure 8.3. Finite-element mesh of the Lake Erie x-z model	8-10
Figure 8.4. Computed and observed currents for September 30, 1978	8-10

Illustrations (Cont.)

	Page
Figure 8.5a. Observed temperature in the x-z plane for Lake Erie (September 30, 1978)	8-12
Figure 8.5b. Computed temperature in the x-z plane for Lake Erie (September 30, 1978)	8-12
Figure 8.6. Schematic of the wind-wave sediment resuspension model	8-14
Figure 8.7. Computed mean wave bottom orbital velocities for November 1970	8-16
Figure 8.8. Computed amounts of (a) resuspended total phosphorus and (b) settled total phosphorus for the period October 21 to November 28, 1970	8-16
Figure 8.9. Computed and observed currents for July 16 to August 16, 1970 for epilimnion and hypolimnion layers	8-19
Figure 8.10. Computed and observed chloride distributions for epilimnion and hypolimnion, July 28 to August 2, 1970	8-21
Figure 8.11. Interrelationships of models of varying spatial complexity	8-24
Figure 9.1. Relative errors vs. sample percentile for (a) total phosphorus and soluble reactive phosphorus, and (b) dissolved oxygen and temperature, as computed for the six-box model	9-4
Figure 9.2. Relative errors vs. sample percentile for (a) total phosphorus and soluble reactive phosphorus, and (b) dissolved oxygen and temperature, as computed for the nine-box model	9-8
Figure 9.3. Simulated results of total phosphorus concentration in the Central Basin hypolimnion using meteorological data of (i) the actual observations 1967-78, (ii) 1970 and (iii) 1972	9-12
Figure 9.4. Simulated results of dissolved oxygen concentration in the Central Basin hypolimnion using meteorological data of (i) the actual observations 1967-78, (ii) 1970 and (iii) 1972	9-14

Illustrations (Cont.)

	Page
Figure 9.5. Simulated results of total phosphorus concentration in the Central Basin hypolimnion using (i) the actual observations of total phosphorus loading and water levels, 1967 to 1978; (ii) a hypothetical 30% loading increase of (i); (iii) a hypothetical increase of 0.5 m in the water levels of (i)	9-16
Figure 9.6. Estimated equilibrium summer epilimnetic total phosphorus concentration based on the nine-box model in response to lake-wide loading for (1) a twelve-year simulation; (2) a "shallow hypolimnion" type of thermal structure and (3) an "entrainment reversal" type of thermal structure	9-19
Figure 9.7. Estimated Central Basin hypolimnetic dissolved oxygen concentration (a) for summer averaged values and (b) for overturn values, based on the nine-box model in response to lake-wide loading for (1) a twelve-year simulation; (2) a "shallow hypolimnion" type of thermal structure and (3) an "entrainment reversal" type of thermal structure	9-21
Figure 9.8. Estimated Central Basin hypolimnetic dissolved oxygen concentration (a) for summer averaged values and (b) for overturn values, based on the nine-box model in response to water level changes, with respect to the 1955 IGLD for (1) a twelve-year simulation; (2) a "shallow hypolimnion" type of thermal structure; and (3) an "entrainment reversal" type of thermal structure	9-25
Figure 9.9. Proposed plan for the future water quality modeling research for Lake Erie	9-29

Abstract

This report presents simulation results and observational data relating to the water quality conditions of Lake Erie for the twelve-year period from 1967 to 1978. In an attempt to explain the large seasonal variations manifested in the observations, detailed weather records were used to reconstruct, through computer simulation, the thermal stratification regimes in the lake. By allowing the thermal layer thicknesses to change dynamically, the mass balance models can now simulate accurately weather-dominant phenomena in the lake. Specifically, regular seasonal patterns in dissolved oxygen in the epilimnion and irregular patterns of anoxic chemical regeneration of soluble reactive phosphorus were both found to be in accordance with well-defined prevailing weather conditions.

Similarly, modelling of interbasin transport, vertical entrainment and wind-wave resuspension has led to improvement in the long-term simulation of total phosphorus concentrations. Indeed, from the twelve-year simulations and observations, it is concluded that lake total phosphorus concentration has decreased, primarily in response to the phosphorus removal program. However, even with the inclusion of detailed meteorological influences, the simulation of dissolved oxygen response to the phosphorus removal program remains, at best, a rough guess; better long-term loading and sediment chemistry data are required to find more definitive answers. In the meantime, preliminary estimates of these water quality responses are provided for averaged weather conditions, and to underscore their limitations, probable responses to favourable and adverse weather are also presented.

Résumé

La présent rapport fait état de résultats de simulation et de données d'observation concernant les conditions de la qualité de l'eau du lac Erié pour la période de douze ans écoulée de 1967 à 1978. Pour tenter d'expliquer les variations saisonnières importantes constatées dans les observations, des renseignements détaillés sur le climat ont été utilisés pour reconstruire, grâce à la simulation par ordinateur, les régimes de stratification thermique du lac. En permettant à l'épaisseur des couches thermiques de varier de façon dynamique, les modèles de bilan massique ont pu servir à étudier les phénomènes déterminés par le climat survenant dans le lac. De façon plus précise, on a constaté que les caractéristiques saisonnières régulières de l'oxygène dissous dans l'épilimnion et que les caractéristiques irrégulières de la régénération chimique anoxique du phosphore réactif soluble étaient toutes deux liées à des conditions climatiques dominantes bien définies.

De même, l'utilisation du modèle pour le transport interbassin, l'entraînement vertical et la resuspension due à l'action des vents et des vagues a amélioré la simulation à long terme des concentrations de phosphore total. En effet, à partir de ces douze ans de simulation et d'observation, on conclut que la concentration de phosphore total dans le lac a diminué, principalement en réponse au programme d'élimination du phosphore. Toutefois, même avec l'inclusion de données détaillées concernant les influences météorologiques, la simulation de la réponse de l'oxygène dissous au programme d'élimination du phosphore demeure, au mieux, une hypothèse de premier ordre. Pour obtenir des réponses plus sûres, il faudra compter sur des meilleures données concernant la charge à long terme et les caractéristiques chimiques à long terme des sédiments. Dans l'intervalle, des estimations provisoires de ces réponses de la qualité de l'eau sont fournies pour des conditions climatiques moyennes. Et, pour souligner leurs limites, des réponses probables à des conditions climatiques favorables et défavorables sont également présentées.

Acknowledgments

This report is a sequel to the Inland Waters Directorate Scientific Series No. 111 (Simons et al., 1979) on the assessment of simulation capability of water quality models for the lower Great Lakes. The study forms part of the Environmental Simulation Program at the National Water Research Institute. The authors are particularly grateful to T.J. Simons, who provided general guidance to the Environmental Simulation Program, and in particular, for his critical review of the present study. Special acknowledgments are due to R.A. Vollenweider for scientific advice and to both C.R. Murthy and R.A. Vollenweider for their encouragement and continued interest throughout the study.

The authors are indebted to F.M. Boyce, N.M. Burns, J.O. Nriagu, F. Chiocchio, M. Charlton and F. Rosa for their helpful discussions on scientific aspects of Lake Erie processes, and to the many agencies and individuals who generously provided their data and private communications. In addition, we wish to thank G.K. Rodgers, F.C. Elder and J. Barica for their continuing support of the project.

Special thanks are due to J. Hodson for her efficient computer programming, to C. Minnie for her adeptness in typing the manuscript, to W. Finn and his staff for the production of some of the figures contained herein and to D. Whyte and J. Arda for their editorial comments.

Summary

This report presents and interprets the observed environmental data and simulation modelling results pertaining to the water quality of Lake Erie for the twelve-year period from 1967 to 1978. During this period, the phosphorus removal program was introduced and reinforced while the weather exhibited extreme environmental conditions affecting the hypolimnetic oxygen depletion in the Central Basin. By applying new systems modelling methodologies, both the man-made effect of nutrient reduction and the natural influence of meteorological and limnological processes on the lake water quality have been simulated and verified with the observed data. The confidence level achieved in the simulation results has enabled the construction of new response curves of lake water quality to changes in total phosphorus loading and water levels, which are, for the first time to our knowledge, accompanied by enveloping curves representing possible responses to favourable and unfavourable weather conditions.

Main Findings

The following are the major findings of the report:

1. Over the twelve-year period, the lake total phosphorus concentration showed a general reduction trend, particularly in the Western Basin. There were irregularities in the downward trend of the lake phosphorus concentrations, as a result of occasional loading pulses, wind-wave resuspension, and anoxic chemical regeneration.
2. The effect of the phosphorus removal program on the dissolved oxygen concentration in the Central Basin hypolimnion was masked by large seasonal variations in the concentration. Weather

factors, which included wind, solar radiation, heat fluxes, air temperature and water vapour pressure, controlled the thermal layer thicknesses, water temperature, interbasin transport, vertical entrainment and turbulent diffusion, which in turn dominated the seasonal variations of the lake temperature and dissolved oxygen concentration.

3. There are three main meteorologically induced thermal responses of the lake identified in the twelve-year period, namely the "normal", the "shallow-hypolimnion" and the "entrainment reversal" types. At the present rate of phosphorus loading reduction, anoxia will always occur in the Central Basin in response to the shallow-hypolimnion type as in the case of 1977, and will not likely occur with the entrainment reversal type as shown in 1972. These two response types approximate the upper and lower bounds of meteorological influences.
4. Only when these seasonal meteorological changes were accurately accounted for could the long-term effect of phosphorus loading reduction on the hypolimnetic oxygen depletion in the Central Basin be estimated. Even then, limitations of available loading and sediment chemistry data prevent accurate calculation of this effect. An initial estimate is for a reduction of about $0.1 \text{ g O}_2/\text{m}^2/\text{day}$ in the sediment oxygen demand in response to an assumed linear decline of phosphorus loading from 25 000 MT (metric tons) to 15 000 MT per year over the twelve-year period.
5. Anoxia may be averted by the careful regulation of the lake water level under normal meteorological conditions. However, the possibilities of significant shoreline property damage and ecological effects resulting from adverse weather events may preclude this solution.

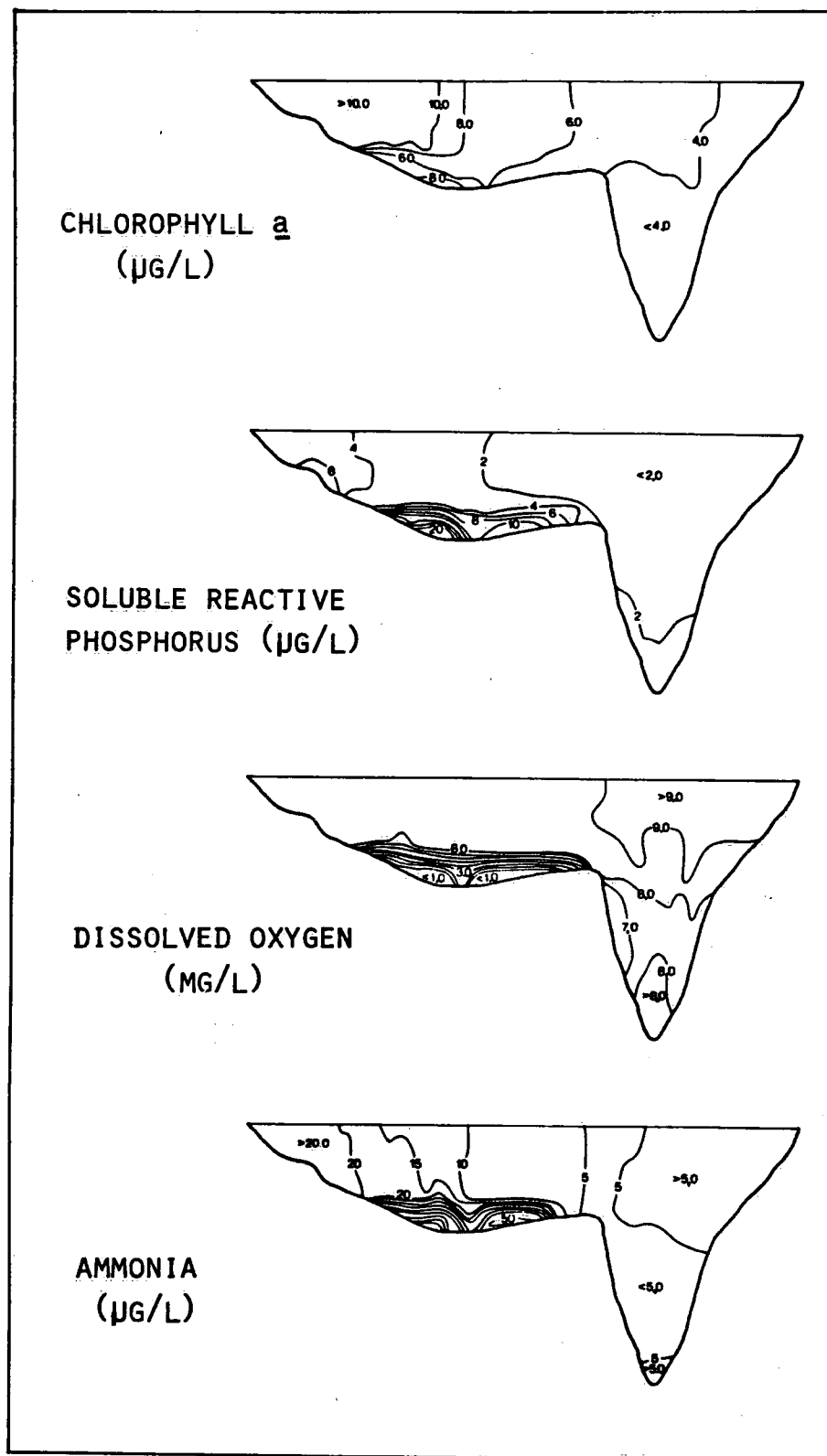


Figure S.1. Two-dimensional (longitudinal and vertical) representation of observed cruise data (September 13-19, 1978).

Table S.1. Diagnostic Results of Spring Values of the Settling Velocity of Particulate Phosphorus

Year	Settling velocity (m/day)
1967	0.23
1968	0.18
1969	0.39
1970	0.19
1971	0.18
1972	0.14
1973	0.09
1974	0.23
1975	0.16
1976	0.19
1977	0.23
1978	0.21
MEAN	0.20

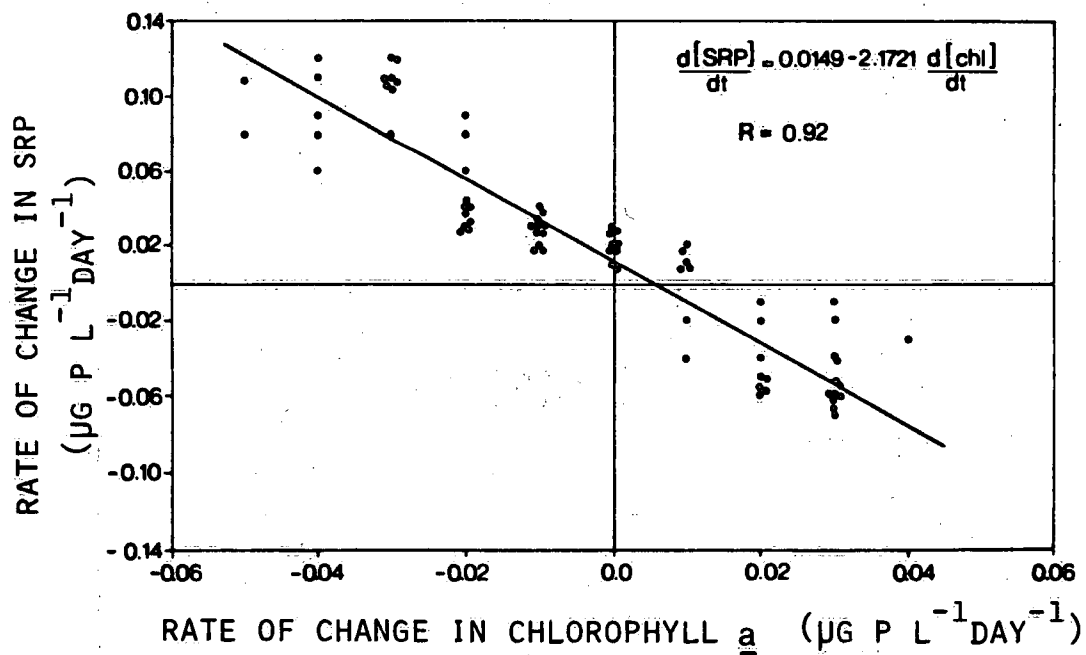


Figure S.2. Rate correlation during growth phase.

Mass and Heat Budgets

The observed nutrient loading data have been interpolated into monthly estimates for the three basins for application to budget computations. A new interpolation scheme, TWIST, was designed to interpolate the lake concentration data, according to the observed three-dimensional thermal structure (see Appendix). The three-dimensional interpolated data were then collapsed into a two-dimensional representation showing the vertical and longitudinal variations (e.g. Fig. S.1). Further reduction in the dimensionality of the interpolated data is possible to meet the requirement of, for example, a three-basin three-layer model. By assuming knowledge of loading and lake concentrations in the three basins, an estimate can be made by mass balance methods of the particulate phosphorus sedimentation rate (Table S.1) and the uptake rate of soluble reactive phosphorus for chlorophyll a production (Fig. S.2). Similarly, heat exchanges between the lake and the atmosphere can be calculated by heat balance methods. From observed heat contents of the lake and estimated incoming heat fluxes, an improved version of the total heat flux into the lake can be derived (Fig. S.3). Detailed records of meteorological data over the twelve-year period were used to provide comprehensive coverage of the day-to-day weather events affecting both the mass and heat balances in the lake (Fig. S.4).

This diagnostic screening of observed data (Chapters 2, 3, 4 and 5) is an important step in providing useful empirical results and in facilitating the calibration and verification of the prognostic models (Chapter 6).

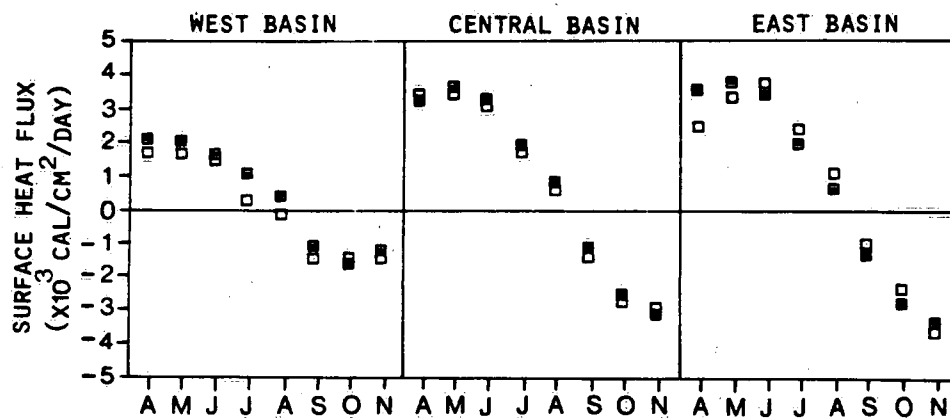


Figure S.3. Comparison of long-term average heat flux estimates (□) modified by heat content data vs. unmodified estimates (■).

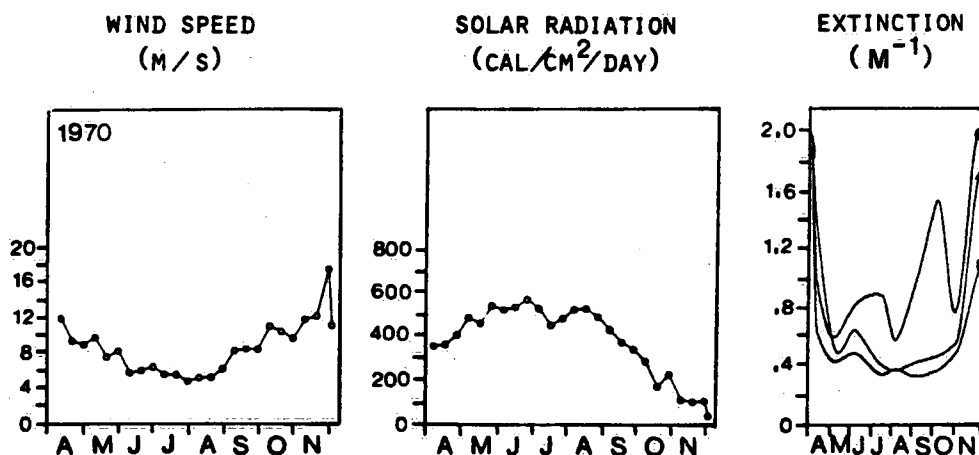


Figure S.4. Examples of meteorological input data for 1970 (● West Basin; ▲ Central Basin; ■ East Basin).

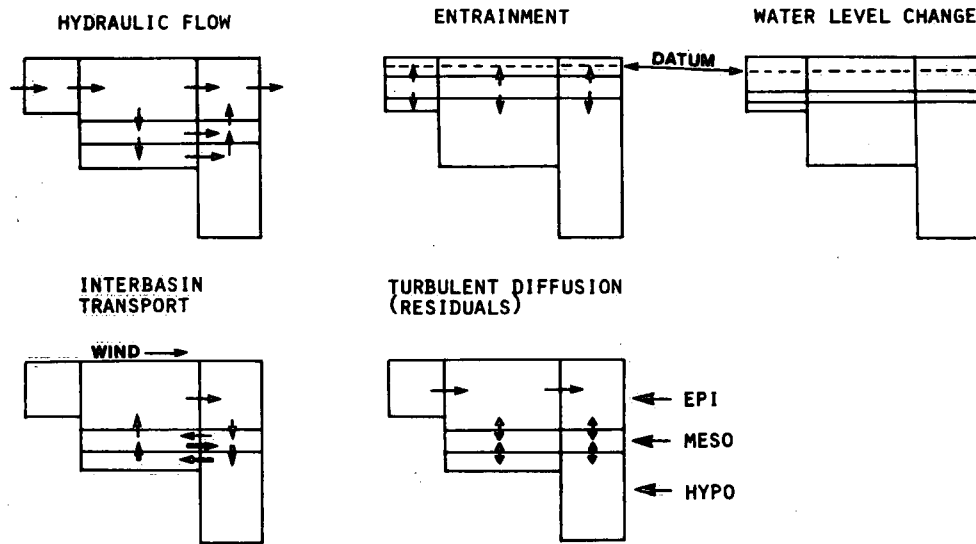


Figure S.5. Physical components of the nine-box three-variable water quality model for Lake Erie.

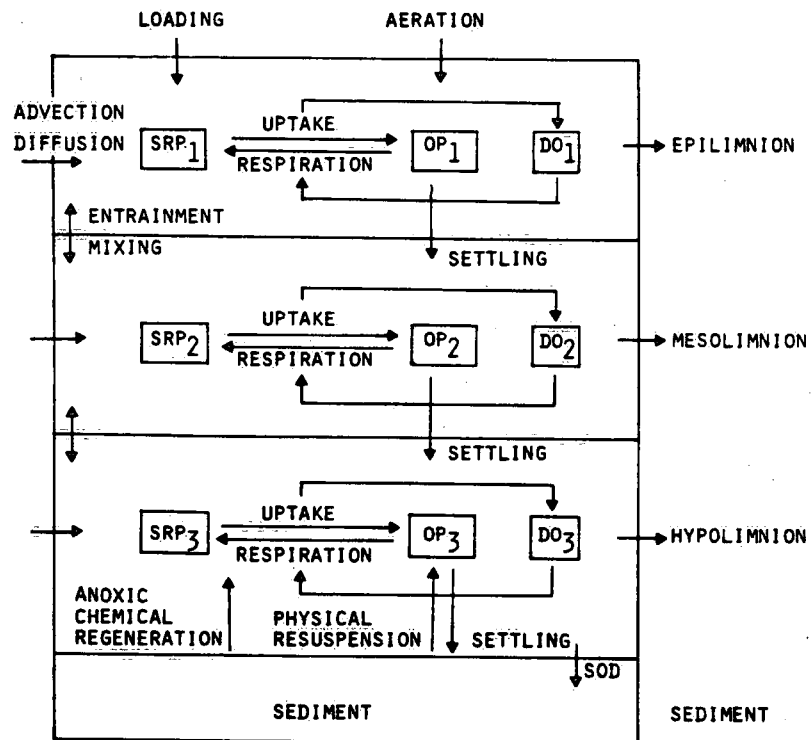


Figure S.6. Biochemical components of the nine-box three-variable water quality model for Lake Erie.

Modelling Framework

Figure S.5 shows the framework of the three-basin three-layer model, i.e., a nine-box model. The novel feature of this design is that it allows for dynamic changes in the thermal layers in the model. The spatial positions of the epilimnion, mesolimnion and hypolimnion are determined on a daily basis by a one-dimensional thermocline model. Thus, the nine-box model allows for processes of water level, hydraulic flow, entrainment, eddy diffusion and interbasin transports. These physical processes apply to all variables in the biochemical submodel.

Figure S.6 shows the components in the biochemical submodel, which consists of soluble reactive phosphorus (SRP), organic phosphorus (OP) and dissolved oxygen (DO). The loading data, the meteorological data, and the computed water temperature and thermal layer positions are all inputs to this model. The 1978 data were used for calibration, and the data for 1967 through 1977, for verification.

Model Results

A detailed display of the model results is given in Chapters 5, 6, 7 and 8, which also encompass the concept of developing water quality models of intermediate complexity. Briefly, models of the type shown in Figure S.5 are found to depend on models of different spatial resolutions to compensate for the spatial details lost in the definition of the framework. For example, an important link to the nine-box model is the one-dimensional thermocline model. Figures S.7a and b illustrate computed vertical temperature profiles and thermocline positions, respectively, for the Central Basin for 1970. Similar computations for the period 1967 to 1978 revealed three basic classifications for the thermal structure which are related to weather (Fig. S.8). In the "shallow hypolimnion" type, the

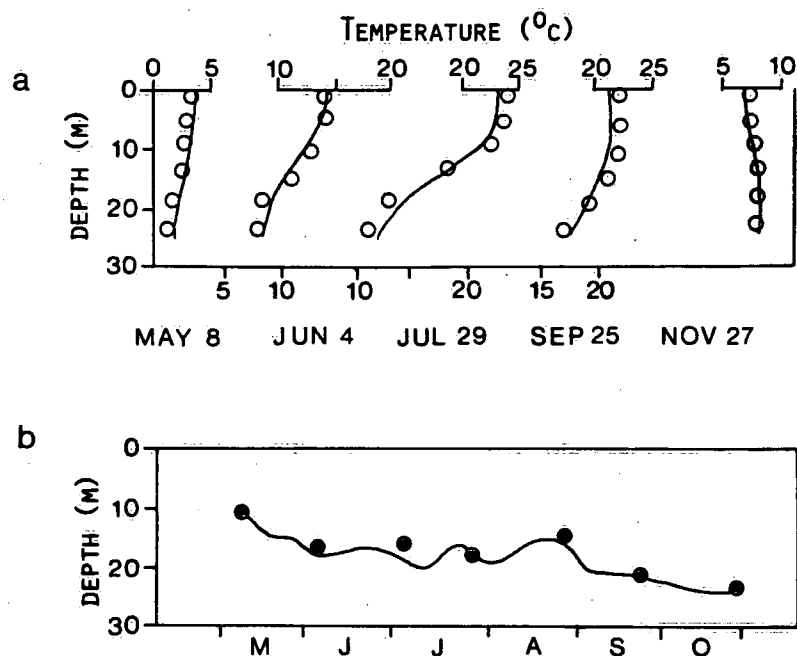


Figure S.7. Computed (line) and observed (dot) results of (a) vertical temperature profiles and (b) thermocline positions of the Central Basin in 1970.

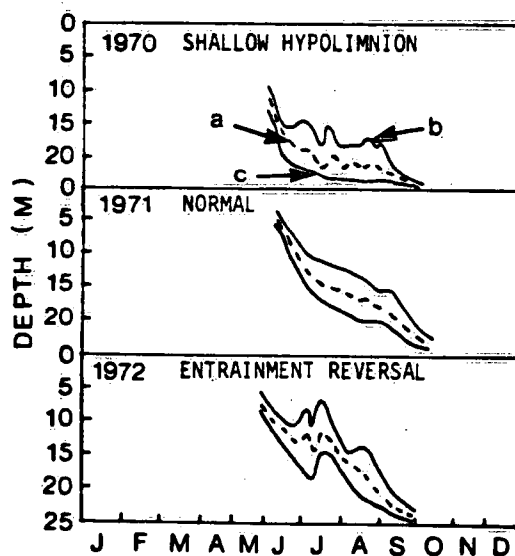


Figure S.8. Examples of identified weather-induced thermocline positions based on thermocline model results: a - thermocline position; b - top of the mesolimnion; c - bottom of the mesolimnion.

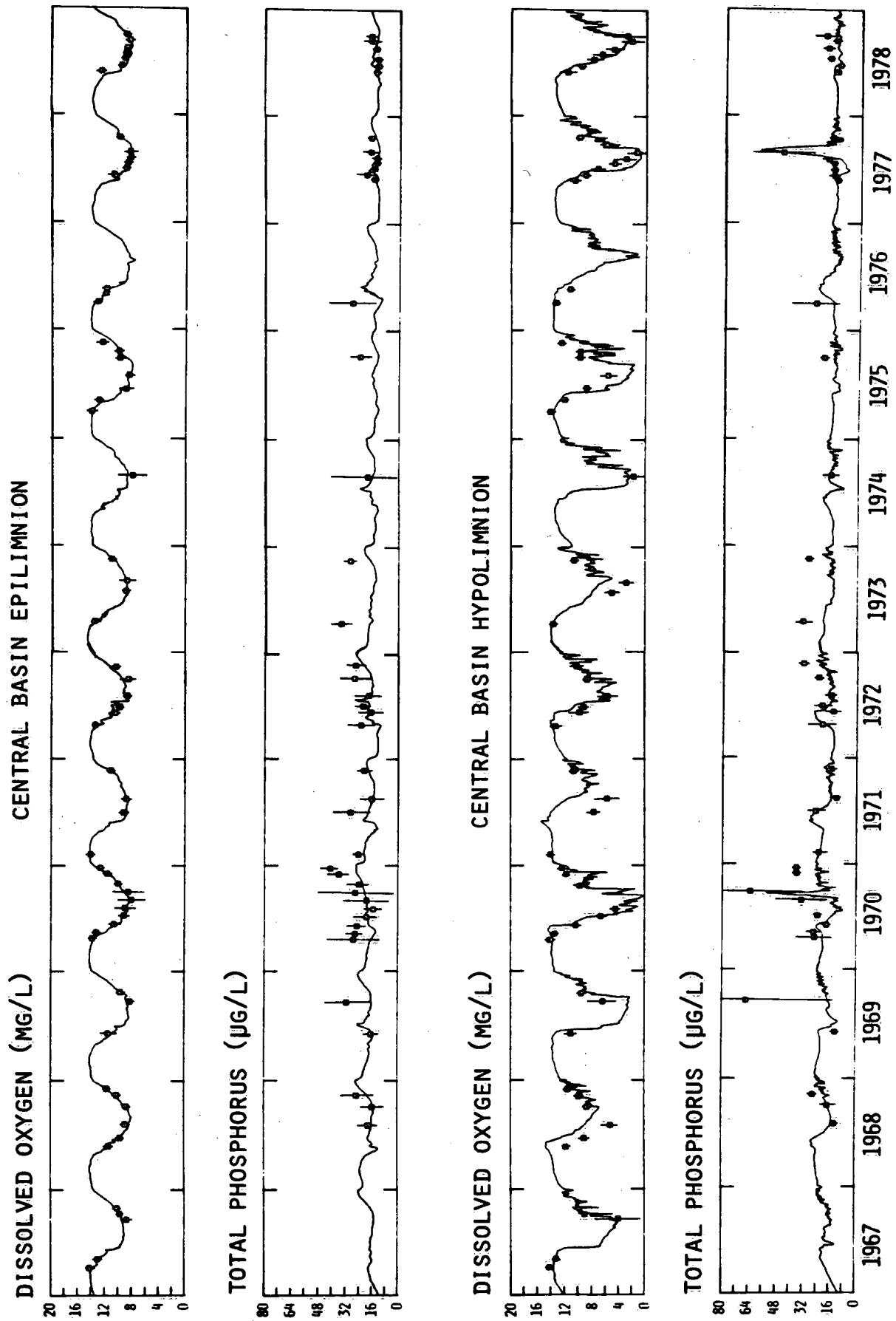


Figure S.9. Computer (—) and observed (---) concentrations of total phosphorus ($\mu\text{g/L}$) and dissolved oxygen (mg/L) for Central Basin epilimnion and hypolimnion, 1967 to 1978.

sediment oxygen demand was able to deplete the oxygen substantially in the Central Basin hypolimnion in spite of the biological production and physical sources. This then led to the biochemical regeneration of soluble reactive phosphorus, ammonia and even hydrogen sulphide from the sediment. In the "entrainment reversal" type, the formation of the thermocline was disrupted by storm events and a large supply of oxygen due to wind mixing and upward entrainment prevented the onset of anoxia. The effect of the "normal" meteorological type is intermediate between those of the other two types. Similarly, models of higher dimensions were used to ascertain the empirical formulae for such physical processes as interbasin transports, wind-wave resuspension, and upwelling and downwelling episodes.

Figure S.9 shows the computed and observed concentrations of total phosphorus and dissolved oxygen for the epilimnion and hypolimnion for the Central Basin during the period 1967 through 1978. The dissolved oxygen concentration in the epilimnion remained saturated most of the time and was therefore a strong function of water temperature, which exhibited regular seasonal patterns. By contrast, the total phosphorus concentration in the epilimnion at springtime has gone down from 25 $\mu\text{g/L}$ to about 17 $\mu\text{g/L}$, mainly as a result of loading reductions. On the other hand, the dissolved oxygen in the hypolimnion underwent seasonal cycles, but the extent of anoxia was influenced by the weather-induced thermal structure types. The total phosphorus concentration in the hypolimnion was strongly marked by the anoxic regeneration events. In these computations, the sediment oxygen demand was fixed at a rate of $0.15 \text{ g O}_2/\text{m}^2 \text{ day}$ (cf. Eq. 9.2 in Chapter 9).

Application

The computed results of Figure S.9 show remarkable agreement with the observed data, particularly for the dissolved oxygen at the

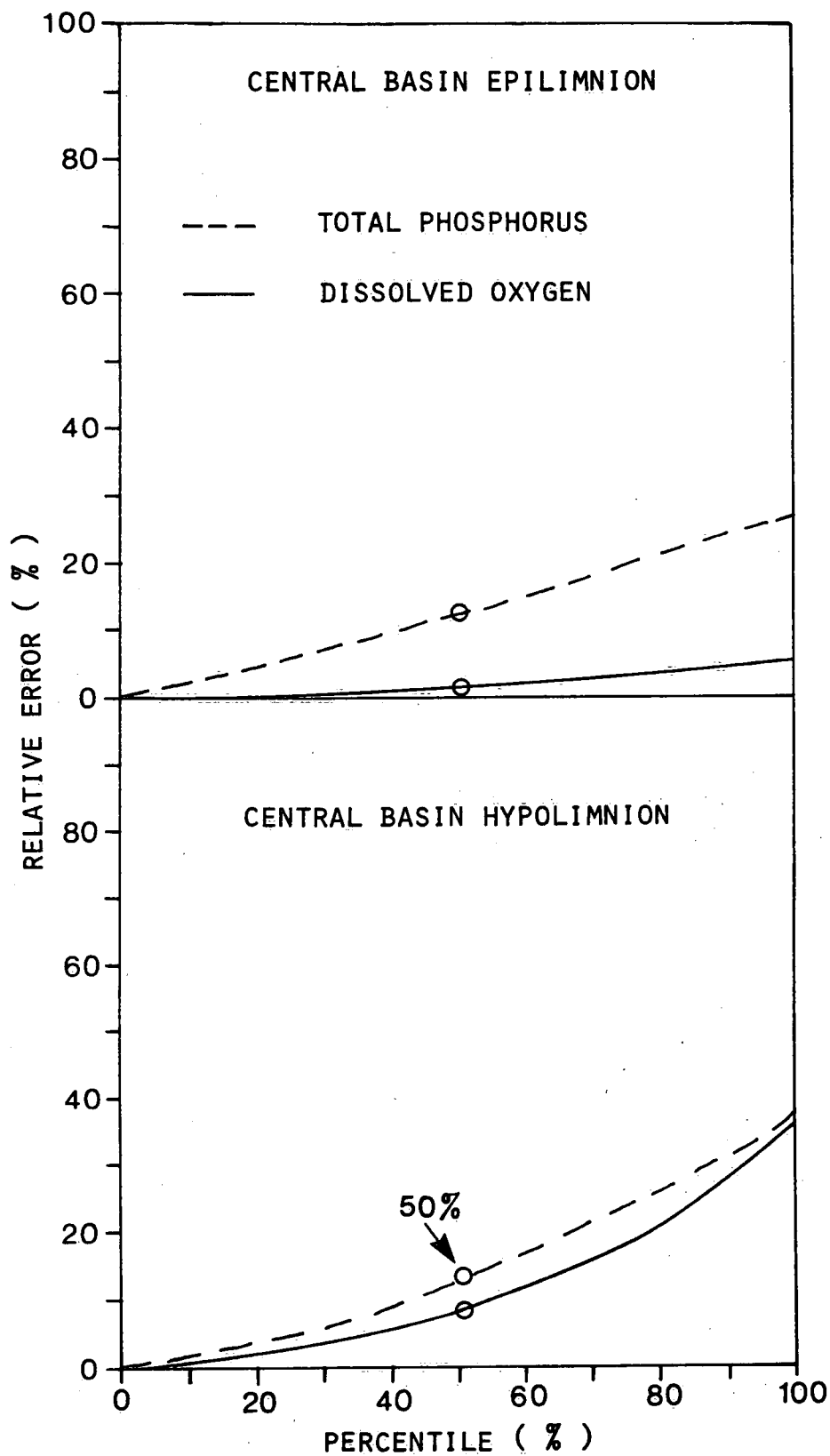


Figure S.10. Relative errors vs. percentile frequency of observed data (cf. Fig. S.9).

epilimnion. A detailed examination of the relative errors for these variables is shown in Figure S.10. For example, the median relative errors of the epilimnetic dissolved oxygen and total phosphorus and their hypolimnetic counterparts are 1.3%, 11.7%, 7.9% and 12.2%, respectively. However, in spite of this partial success, the application of the nine-box model for deriving long-term equilibrium concentrations of total phosphorus in response to loading changes must proceed with caution.

Because of the prominent effects of meteorology displayed in the verification results, a new approach to define these equilibrium concentrations is proposed. Briefly, if one would let the total phosphorus loading be a given constant, then the equilibrium lake concentration could be reached after five or six years of simulation, provided that the same annual meteorological pattern is used for each year. However, if the weather pattern is allowed to change from year to year, a longer simulation time is needed. An example is to use the twelve years (i.e. 1967 to 1978) of meteorological data as a climatic cycle, and with the loading fixed at a constant rate, to use the results at the twelfth year (i.e. 1978) to represent the "weathered" equilibrium concentrations. Furthermore, the results at the fourth year (i.e. 1970) will be influenced by the "shallow hypolimnion" thermal structure, whereas those at the sixth year (1972) will be influenced by the "entrainment reversal" thermal structure. These latter two equilibrium concentrations provide the upper and lower bounds of the weather influences. By computing different equilibrium concentrations for different loading rates, response curves of lake concentration to loading can be obtained.

Figure S.11 shows equilibrium concentration curves for (a) the epilimnetic total phosphorus concentration of the Western Basin in response to total phosphorus loading, (b) the hypolimnetic dissolved oxygen concentration of the Central Basin just before fall overturn,

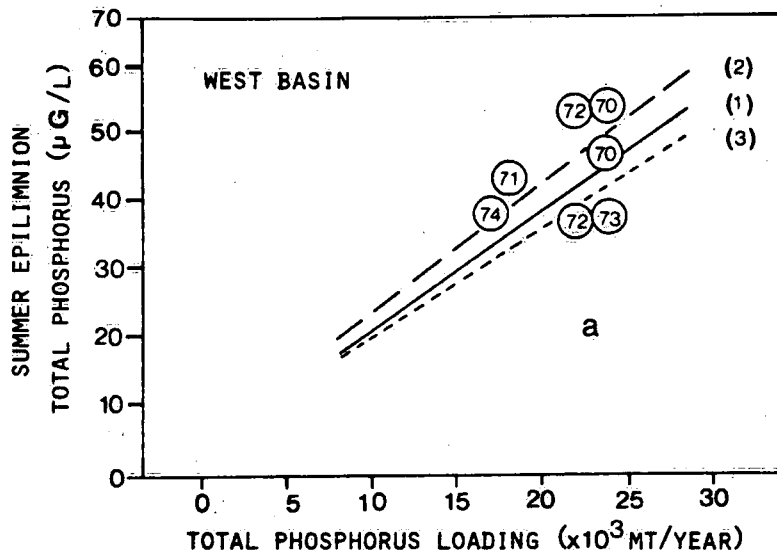
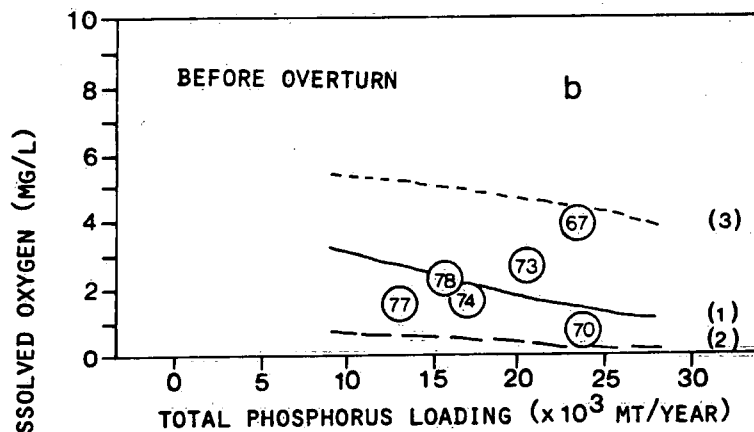
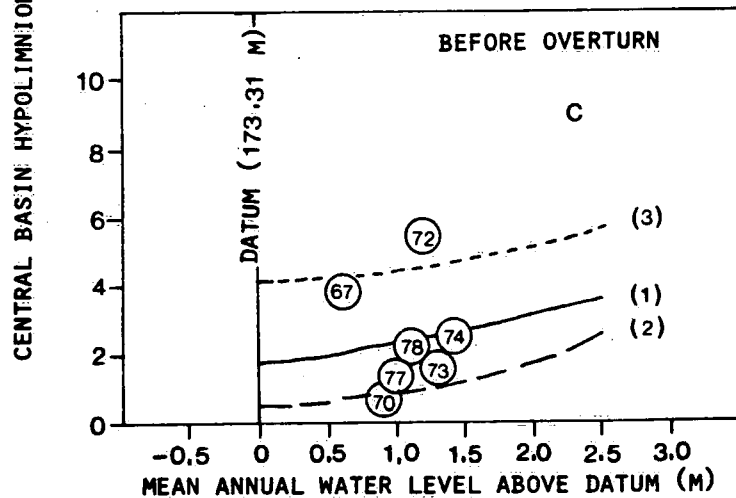


Figure S.11. Equilibrium curves of:



(a) Summer averaged West Basin epilimnetic total phosphorus conc. vs. lake-wide loading, (b) Central Basin hypo. dissolved oxygen conc. just before overturn vs. phosphorus loading, and (c) same as (b) but vs. water level.



Curves (1), (2) and (3) denote mean, shallow hypolimnion and reversal entrainment thermal structure types; circles with numbers denote observed (nonequilibrium) results.

in response to total phosphorus loading, and (c) the same dissolved oxygen concentration in response to water level changes. To demonstrate the usefulness of these curves, the observed values from ship cruise observations are also plotted in the figure. Note that the observed values are dynamic values and that they do not reflect equilibrium conditions. They should also be treated as approximate values because of the inaccuracies in the loading estimates and in the timing of the fall turnover dates. Nevertheless, the spread of the observed data conforms well to the envelope of the computed equilibrium curves, and their trend is in agreement with the mean curves, particularly for the Western Basin (Fig. S.11a). Similar curves are given in Chapter 9.

Recommendations

1. The response curves provided in Chapter 9 offer a preliminary estimation of the lake water quality response to the combined effects of man-made phosphorus loading reduction and natural weather forcing; similar curves for nearshore zones are required for more detailed analysis.
2. The nine-box model should be applied beyond the twelve-year period with particular emphasis to update the long-term effect of nutrient loading reduction on the sediment oxygen demand. This requires continued usage of lake surveillance data and necessitates improved methods of estimating nutrient loadings.
3. Research on climatic influences on water quality should be strengthened; new results from nutrient dynamics and sediment chemistry should be incorporated into the model formulation; and toxicant effects on primary production should be included in the model if such effects are found to be significant.

4. Research on the development of models of intermediate complexity should be directed towards a more efficient modelling framework; the computer programs should be made interactive to facilitate the incorporation of these recommendations efficiently, and for management applications.

Lake Erie Basins

1.1 Introduction

In recent years, industrial and municipal discharges have had deleterious effects on Lake Erie water quality. On the basis of the trophic status defined with reference to phosphorus loading and hydraulic retention time (Vollenweider et al., 1980), Lake Erie can be considered mesotrophic to eutrophic. Regulations have been instituted which restrict the input loading of such nutrients as phosphorus. However, Lake Erie physiography and the influence of weather systems over the basins are also important considerations in regard to Lake Erie's recovery from eutrophy.

The physiography of Lake Erie is unique among the Great Lakes in the sense that the lake is the shallowest and can be distinctly divided into three basins. The Western Basin, with a maximum depth of 10 m and being the smallest in area of the three basins, receives more than half of the total load of phosphorus of the entire lake. This basin is still considered as eutrophic by many researchers. The Central Basin, which is the largest in area, has a maximum depth of 25 m. Such a physiography is prone to the formation of a rather broad but shallow hypolimnion in the summer. Often, the hypolimnion becomes anoxic as a result of strong sediment oxygen demand. The Eastern Basin, being the deepest basin with a maximum depth of 65 m, is also stratified, but the waters remain oxic and eutrophication is less acute.

On the other hand, being the southernmost of the Great Lakes, Lake Erie is affected by warmer weather in the summer and

strong westerly winds in the winter. These weather systems cause non-homogeneity in the distribution of water quality variables. In particular, during the stratified period, there are distinctly different distributions of water temperature, dissolved oxygen, soluble reactive phosphorus and phytoplankton in the vertical water column. The hydraulic flow and wind-driven circulation influence the transport and spreading of the pollutants from the loading sources to offshore areas and, in general, create a longitudinal concentration gradient from the Western Basin to the Eastern Basin. These weather effects render the observational data difficult to analyse unless an appropriate data zoning method, accounting for the spatial heterogeneity, is devised.

The importance of the data zoning method becomes apparent when ship cruise data are used to derive the oxygen depletion rates for the Central Basin. Dobson and Gilbertson (1971) defined the hypolimnetic waters as water which is no more than 3°C higher than the minimum temperatures observed within a particular cruise survey. This definition made possible the inclusion of the thermocline waters at the eastern end of the basin but not the warmer hypolimnetic waters at the western end. Charlton (1980) used temperature traces where available to define the hypolimnion, but had to use a temperature-thickness regression relationship when these traces were not available. Rosa and Burns (1981), however, found that there was no such relationship. Instead, they advocated a representative area approach in which a mesolimnion exchange model was used with corrections for interbasin transports and vertical diffusion. The drawback of this method is that it requires close cruise intervals and the mass balances among the three basins as a system are disregarded, since the corrections are applied only to the Central Basin hypolimnion. Instead of using these diagnostic methods, Di Toro and Connolly (1980) used a mass balance model to predict oxygen concentrations for various segments of Lake Erie. The partition of the vertical layers in this

model was fixed throughout the stratified cycle. While this constant layer-thickness prognostic approach is applicable to deep lakes such as Lake Ontario (Simons and Lam, 1980), its application to Lake Erie is questionable. Indeed, Di Toro and Connolly (1980) had to change the epilimnion thickness from 17 m for the calibration year (1970) to 13 m for the verification year (1975) in order to fit the data. For shallow lakes where the displacement of the thermocline is comparable to the hypolimnetic thickness itself, it is known (Ivey and Boyce, 1982) that diffusion alone is not sufficient to explain the entrainment processes. Therefore, the constant layer-thickness model has the tendency to diffuse more oxygen from the epilimnion to the hypolimnion than the entrainment models would, particularly when the thermocline is actually below the prescribed position.

Nevertheless, it is clear that the analysis of Lake Erie data should not consist merely of a statistical exercise, but must involve calculations (Vollenweider and Janus, 1981) with sound knowledge of limnology. Of course, one extreme form of calculation is to divide the lake into hundreds of cells and to utilize the fully three-dimensional description of the thermocline surface in the analysis. An example is the three-dimensional model of Lam and Simons (1976). However, such a detailed approach would quickly be faced with a large number of unknown coefficients (Simons *et al.*, 1979) and is not as economical as models with less spatial complexity. The problem, therefore, is the choice of the proper complexity, preferably intermediate complexity, for the model.

Thus, a new modelling approach emerges as follows. The centre of many controversies (e.g. Charlton, 1980; Rosa and Burns, 1981) surrounding water quality studies in Lake Erie lies with the definition of the hypolimnion. If the water temperature data were densely sampled in space and time, this definition would have been easy. However, the lake data are not always collected so densely. On

the other hand, the meteorological records are abundant around Lake Erie basins, and the basins are sampled at more frequent and regular intervals. Since the meteorological forcing is the direct cause of the thermal stratification in the lake, it is clearly essential that the definition of the hypolimnion be tied in with such weather records. One advantage is that the information on the thermal structures in any past year can be derived if the weather data are available. Alternately, if a long-term weather forecast becomes reliable, the lake thermal structures can be likewise forecast. Fortunately, over the past two decades, a sizeable body of knowledge has been gathered by physical limnologists on the thermal processes of lakes. While there are still major gaps of understanding in short-term turbulence processes, the simulation of the long-term seasonal behaviour of the stratification cycle has been made feasible by bulk parameterization using a one-dimensional laterally integrated model. This model is economical to use and is able to reproduce accurately the areally averaged vertical thermal profile for both the Central and Eastern basins of Lake Erie.

From the simulated daily temperature profiles, the dynamic positions and layer thicknesses of the epilimnion, mesolimnion and hypolimnion can be obtained. These are input into, on a daily basis, a segmented mass balance model of Lake Erie, consisting of the three basins with two or three vertical layers. That is, the layers are adjusted daily and the mass balance model permits the vertical entrainment and lateral water movements associated with the changes. In other words, the one-dimensional thermocline model and the six- or nine-box mass balance model together form the main frame of our new modelling approach. It is through such a systems approach that we are able to confirm Charlton's (1980) finding of the short-term weather-induced variations on the oxygen depletion rate and, at the same time, are able to detect the long-term influence on the sediment oxygen demand by nutrient loadings as reported by Rosa and Burns

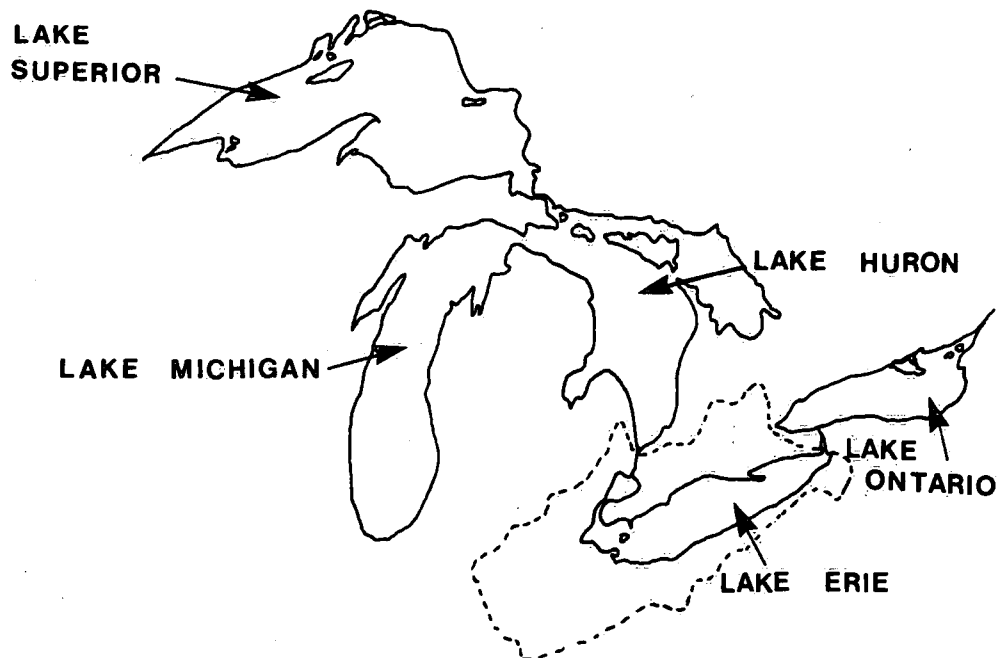


Figure 1.1. Lake Erie Basin in relation to the Great Lakes.

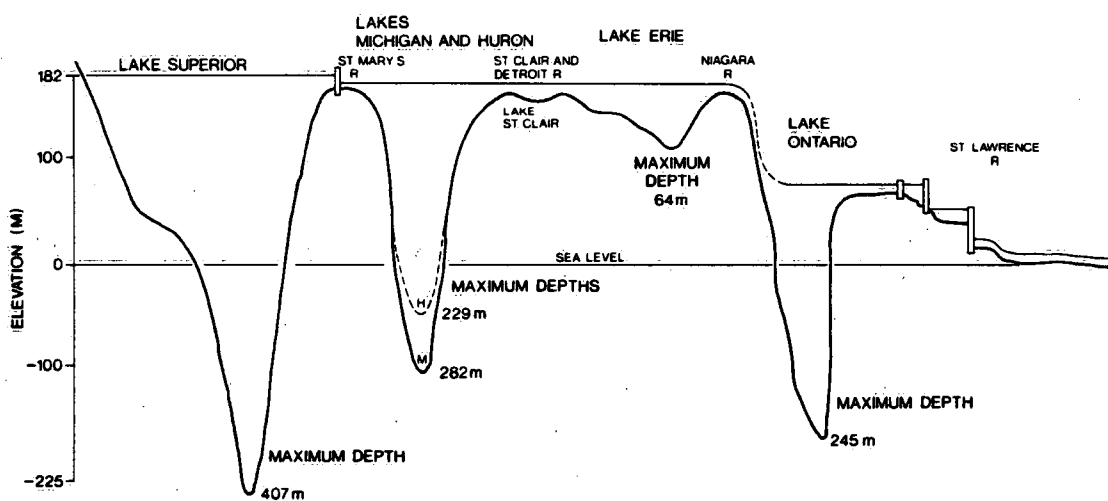


Figure 1.2. Profile of the Great Lakes.

(1981). The diagnostic and prognostic results of this modelling approach have been mentioned in the Summary and will be discussed in detail in the subsequent chapters. The content and order of appearance of these chapters have also been provided in the summary.

1.2 Physical Characteristics

Lake Erie forms the southernmost portion of the Great Lakes system (Fig. 1.1). It is centred on $42^{\circ}15'$ north latitude and $81^{\circ}15'$ west longitude. The Lake Erie Basin encompasses an area of $103\,000\text{ km}^2$ and lies within the Province of Ontario and portions of the states of Michigan, Indiana, Ohio, Pennsylvania and New York. Approximately one quarter of the basin area, $25\,320\text{ km}^2$, represents the lake itself. Compared with the other lakes within the system, Lake Erie lies completely above sea level, contains the smallest volume of water and is the shallowest (Fig. 1.2).

Physical characteristics of Lake Erie are given in Tables 1.1a and 1.1b. The lake is elongate, and has its major axis oriented approximately west-east at $N70^{\circ}E$. Its maximum length is 390 km with an average width of 70 km, and it reaches a maximum of about 90 km near the midpoint of the long axis. At low water datum, it contains a volume of 473 km^3 , has a mean geometric depth of 18.7 m and has a depth of half volume of 9.97 m.

Figure 1.3 shows Lake Erie bathymetry. Most of the lake is shallow. However, there is a progressive increase in depth from a maximum of 10 m in the west end to a maximum of 65 m in the east end of the lake. On the basis of bathymetry, the lake can be subdivided into three distinct physiographic regions: the Western Basin, the Central Basin and the Eastern Basin. The shallow Western Basin is separated from the relatively flat-bottomed Central Basin by a rocky

Table 1.1a. Physical Characteristics of Lake Erie

Low water datum (LWD)	173.3	m
Length	388	km
Width	92	km
Shoreline length	1 377	km
Total surface area	25 320	km ²
Volume at LWD	470	km ³
Mean geometric depth	18.7	m
Depth of half volume	9.97	m
Maximum depth below (LWD)	64	m
Maximum surface elevation (IGLD)	174.7	m
Conical ratio	0.29	

Table 1.1b. Physical Characteristics of Lake Erie Basins

	West	Central	East
Surface area (LWD)	2 912 km ²	16 736 km ²	5 672 km ²
Volume (LWD)	20 km ³	300 km ³	150 km ³
Maximum depth (LWD)	10 m	25 m	64 m

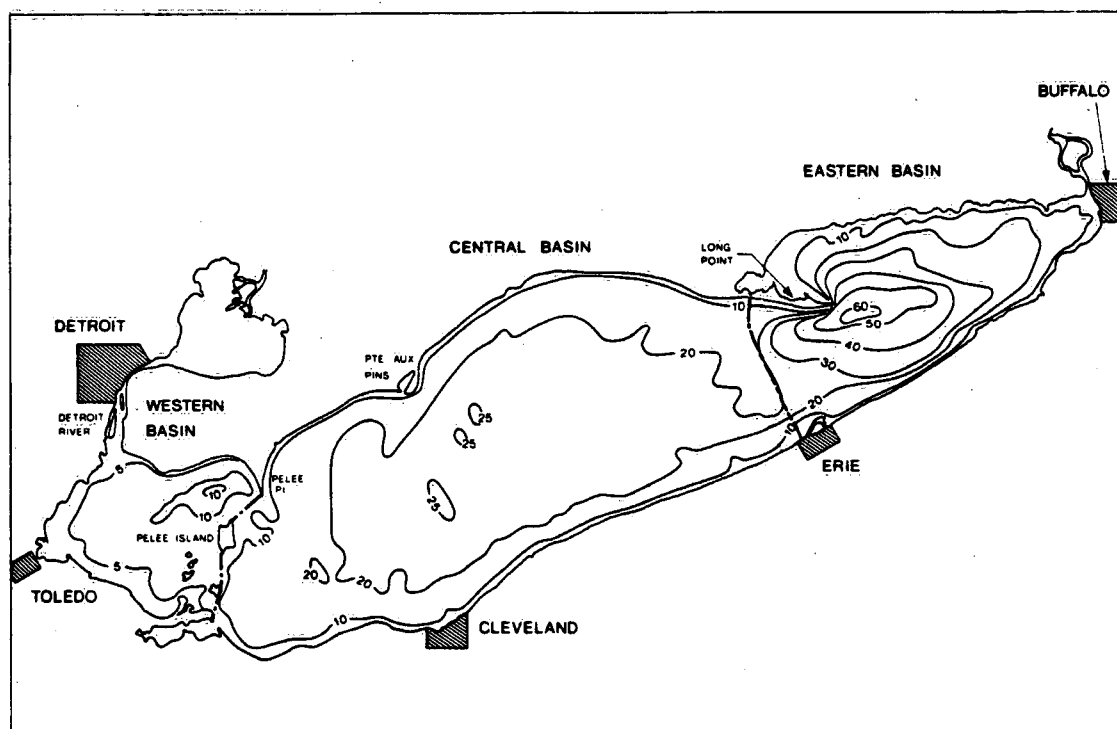


Figure 1.3. Lake Erie bathymetry (metres).

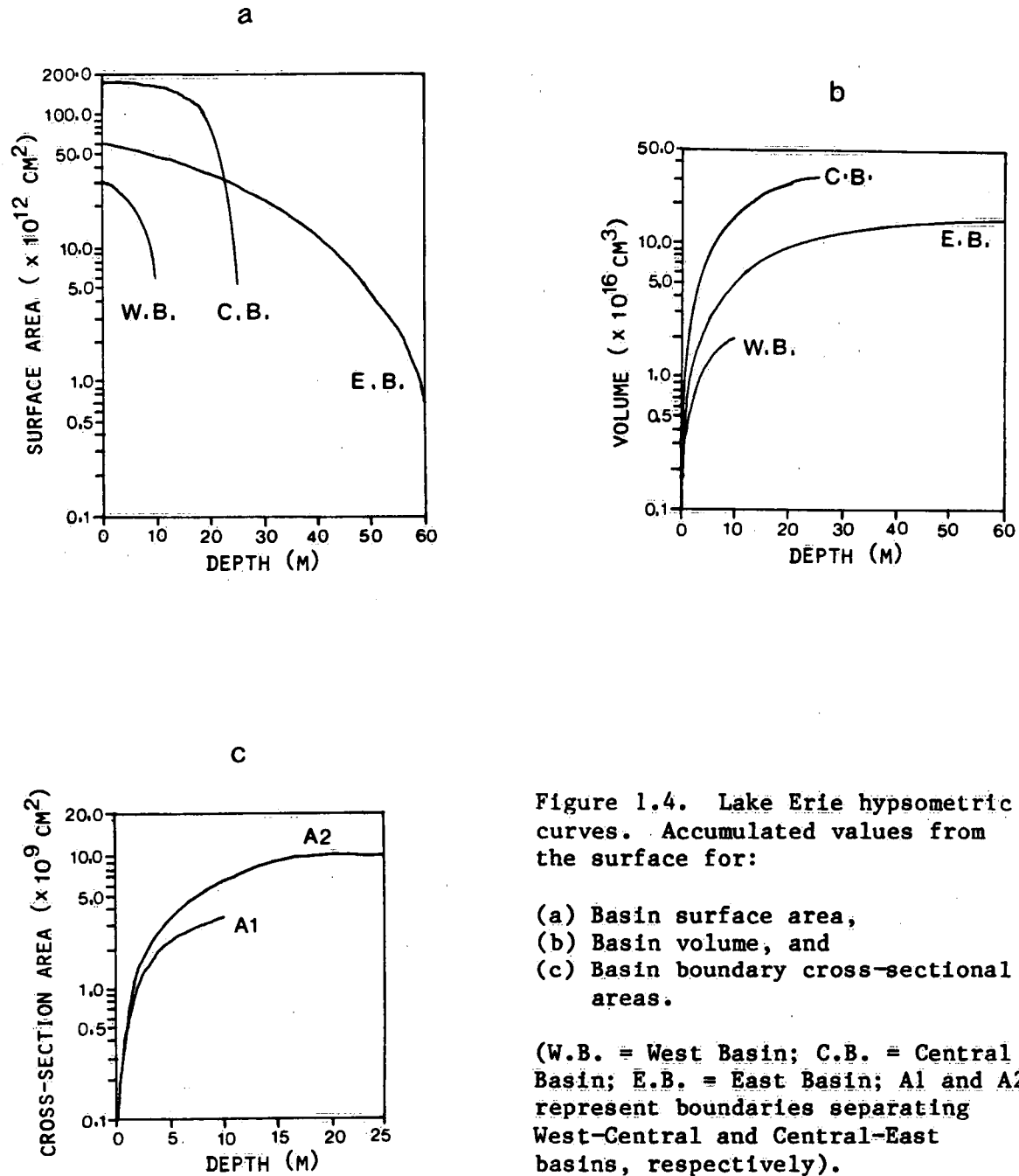


Figure 1.4. Lake Erie hypsometric curves. Accumulated values from the surface for:

- (a) Basin surface area,
- (b) Basin volume, and
- (c) Basin boundary cross-sectional areas.

(W.B. = West Basin; C.B. = Central Basin; E.B. = East Basin; A1 and A2 represent boundaries separating West-Central and Central-East basins, respectively).

island chain extending from Point Pelee, Ontario, to Marblehead, Ohio. A low wide submerged sand and gravel ridge called the Pennsylvania Ridge which extends from Long Point, Ontario, to Erie, Pennsylvania, separates the Central and Eastern basins. For computations in this report, the lake has been divided into three basins based on these physiographic features (Fig. 1.3).

A comparison of surface area and volume at corresponding depths from the surface is shown in Figures 1.4a and b for each basin. Cross-sectional areas for vertical boundaries separating the West-Central and Central-East basins are illustrated in Fig. 1.4c as a function of increasing depth from the surface. To facilitate computation of basin boundaries for each layer within mass balance models described in this report, functions were derived to approximate the hypsometric data. Boundaries are permitted to change with respect to mean daily water level movement.

Lake Erie Loading

2.1 Sources of Loading Data

In this study, the emphasis on loading data was placed upon obtaining where possible, both the flow and concentration data rather than accepting previously computed loads. Once obtained and evaluated, the data sets were uniformly subjected to the same loading calculation procedure. In some instances where data were not sampled or available, methods of estimation were employed. The purpose of this exercise is to attain some uniformity and consistency in the calculation and estimation of the chemical loading data. Without such a step, the choice of loading data determined previously by different methods would be difficult (Fraser and Willson, 1981; Dolan et al., 1981).

The raw data required for this study were obtained from many sources. The primary agencies involved in collecting the necessary data are the following:

- (1) Environment Canada/NWRI,
- (2) Michigan Department of Natural Resources,
- (3) New York Department of Environmental Conservation,
- (4) Ohio Environmental Protection Agency,
- (5) Ontario Ministry of the Environment,
- (6) U.S. Environmental Protection Agency,
- (7) U.S. Geological Survey,
- (8) U.S. National Oceanic and Atmospheric Administration.

The loading data are summarized according to source types, as described below.

2.1.1 Tributaries

Tributaries were defined as rivers and streams that flow directly into Lake Erie excluding the Detroit and Niagara rivers. Concentration data were obtained from the water quality monitoring station closest to the mouth of the river, and the corresponding flow data were obtained from the gauging station nearest to the water quality sampling site. No attempt was made to distinguish such sources as municipal plants or industrial outfalls that flowed into a tributary upstream from the water quality site.

Data for the Canadian tributaries were obtained from the Ontario Ministry of the Environment (MOE) for the period 1967-1974. To supplement these data for the years 1975 and 1976, additional data were acquired from PLUARG Canadian Task D. Similarly, data on flows and concentrations for the 14 U.S. tributaries studied were obtained from the USGS Water Resources publications for New York, Michigan and Ohio (1966-1976). These data were also supplemented by information retrieved directly from the U.S. STORET system that contains concentration and flow data for specified tributaries in the United States. For the years 1977 and 1978, data were obtained from the International Joint Commission.

2.1.2 Municipal and industrial loads

These sources are defined as point source dischargers to the lake or plants which discharged to a tributary downstream from the selected tributary water quality sampling station. In all cases both the concentration and the flow data were obtained from the monitoring point closest to the plant discharge.

Data for the eight Canadian municipal plants identified for the study were obtained for 1967, 1975 and 1976 from the International

Joint Commission reports (1969; 1976). Additional data were obtained for 1968, 1972, 1973 and 1974 from a report by Appelby (1977). Some of these data were incomplete and required estimation. As in the case for tributaries, the International Joint Commission provided data for the years 1977 and 1978.

The U.S. direct municipal dischargers included in this study are those identified in a report by the U.S. Army Corps of Engineers (1975). Flow and concentration data for the six plants in New York State were abstracted from the operating and maintenance files of the New York State Department of Environmental Conservation (NYDEC). Similarly, the data for 22 municipal dischargers from Ohio were obtained from the records on file with the Ohio EPA Northeast and Northwest district offices. The data for the three plants located in Michigan were released by the Michigan Department of Natural Resources (MDNR).

The availability of industrial nutrient and chloride data was severely limited, leading to the usage of the published material of the International Joint Commission (IJC: 1973, 1974, 1975, 1976). The industrial data obtained for the individual sites were included in the computations particularly with reference to the state of Ohio, which maintained excellent records with the major variable studied being chloride.

2.1.3 Atmospheric loads

Reliance was placed on published loads for atmospheric contributions. The total yearly loads for total phosphorus, chloride, and total nitrogen were taken from a study by Elder et al. (1977). Ammonia, nitrate plus nitrite, and Kjeldahl nitrogen loads were obtained from the work of Kuntz (1978). Atmospheric loadings were

assumed constant over the twelve-year period and spatially homogeneous (Elder et al., 1977; CCIW, 1977).

2.2 Connecting Channels

2.2.1 Detroit River

The Detroit River exhibits a complex structure with respect to water quality variable concentrations. In the region chosen for the computation of the loads out of the river (range DT 3.9), the horizontal concentration gradients for phosphorus and chloride vary substantially and in opposing directions across the transect (Fig. 2.1). This situation necessitates the subdivision of the transect into panels and weighting of the flow regime in order to compute representative loadings from the river. The panel weighting was made by considering a uniformly distributed flow at range DT 3.9 and by proportioning this flow by the panel areas.

The Detroit River range 3.9 which stretches between Lee Point in the United States and Bar Point in Canada has been segmented into 20 panels in a report by the U.S. Army Corps of Engineers (1975). For the purpose of this study a comparison was made between the sampling locations used over the ten-year period by the Ontario Ministry of the Environment and the Michigan Department of Natural Resources relative to the river segmentation. In this study the river range was segmented into 13 panels such that two water quality sampling sites would be located in each panel and that over the twelve-year study period there would always be at least one sampled station in each panel for each year (Fig. 2.2).

Daily flow records for the Detroit River from 1968-1978 were obtained from the U.S. Geological Survey using the computation made by

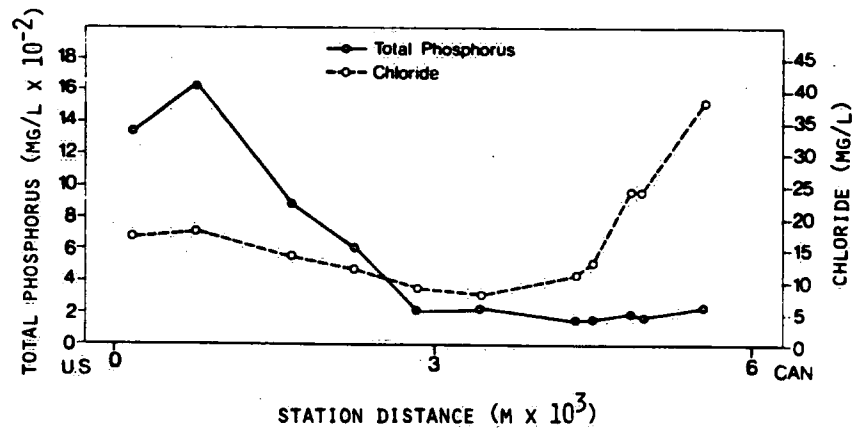


Figure 2.1. Detroit River concentrations (MOE data: June 3, 1976).

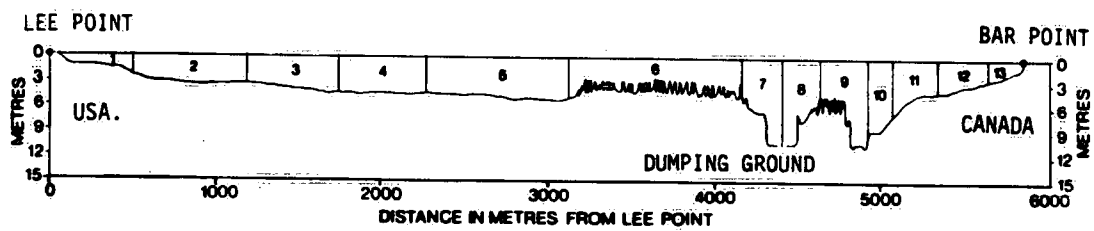


Figure 2.2. Lower Detroit River Bar-Lee section (range DT 3.9).

the National Oceanic and Atmospheric Administration based on variations in river and lake levels. These data were supplemented by additional records of flow for 1967 estimated from the mean monthly calculations reported by Derecki (1975).

The Canadian chemical data analysed by the MOE for the period 1967-1976 were summarized by PLUARG Canadian Task D. Similarly, data for the U.S. component were obtained from the U.S. "STORET" system operated by the U.S. Environmental Protection Agency. When these data were combined, a total of 22 sampling stations were available for the study period.

Computation of the Detroit River load was made by summing the contribution from each of the segments, which were treated as independent sections each with its own variable concentrations and flow. An unbiased estimator technique (Eq. 2.1) was used to compute the load from each segment.

2.2.2 Niagara River

A procedure similar to that used for the Detroit River was adopted for computing outflows through the Niagara River. The transect between Fort Erie, Ontario, and Buffalo, New York, was subdivided into nine area weighted panels. Flow data were obtained from the USGS water resources publications for the state of New York (1966-1978). The flows were measured as powerplant discharges plus an estimated flow over the Falls at Niagara. The chemical concentrations were obtained from the MOE and PLUARG Canadian Task D. Each panel segment had one sampling station at the cross section midpoint. As in the case of the Detroit River, each panel load was calculated independently using Eq. 2.1. Summation of individual loads at each panel provided the total load through the Niagara River.

2.2.3 Estimation method

The chosen estimator technique (Beale, 1962) utilizes the additional information where available for annual and monthly flows in the computation. Thus, some of the variance associated with perturbations in flow is removed, yielding an estimate with minimized variance associated with the flow component. This method has recently been evaluated by Dolan et al. (1981) as the most suitable for application in the Great Lakes basins.

The estimator $\tilde{\mu}_y$ is expressed (Tin, 1965; Kendall and Stuart, 1968) as follows:

$$\tilde{\mu}_y = \mu_x \cdot \frac{m_y}{m_x} \cdot \frac{\left(1 + \frac{1}{n} \cdot \frac{S_{xy}}{m_y m_x}\right)}{\left(1 + \frac{1}{n} \cdot \frac{S_x^2}{m_x^2}\right)} \quad (2.1)$$

where μ_x = mean daily flow for the year
 m_y = mean daily loading for the days for which concentrations were determined
 m_x = mean daily flow for the days for which concentrations were determined
 n = number of days for which concentrations were determined

$$S_{xy} = \frac{\sum_{i=1}^n X_i Y_i - n \cdot m_y \cdot m_x}{n-1}$$

$$S_x^2 = \frac{\sum_{i=1}^n X_i^2 - n \cdot m_x^2}{n-1}$$

and the X_i and Y_i are the individual measured flow and calculated loading, respectively, for each day for which concentrations were determined. The mean-square-error of this estimator may be estimated to terms of the order n^{-2} , assuming the population size is very large, by:

$$\begin{aligned} \hat{E} [(\tilde{\mu} - \mu_y)^2] = m_y^2 \cdot & \left[\frac{1}{n} \cdot \left(\frac{S_x^2}{m_x^2} + \frac{S_y^2}{m_y^2} - 2 \frac{S_{xy}}{m_x m_y} \right) \right. \\ & + \frac{1}{n^2} \cdot \left(2 \cdot \left(\frac{S_x^2}{m_x^2} \right)^2 - 4 \frac{S_x^2}{m_x^2} \frac{S_{xy}}{m_x m_y} \right. \\ & \left. \left. + \left(\frac{S_{xy}}{m_x m_y} \right)^2 + \frac{S_x^2}{m_x^2} \frac{S_y^2}{m_y^2} \right) \right] \quad (2.2) \end{aligned}$$

where S_y^2 is calculated analogously to S_x^2 .

2.3 Loading Estimates

Detailed loading computations for all sources of total phosphorus, soluble reactive phosphorus, total nitrogen, nitrate and nitrite, ammonia and chloride to Lake Erie, including estimates of the outflow load through the Niagara River, have been made for the years 1967 to 1978. Estimation procedures for these parameters are contained in a report by Fraser and Willson (1981).

2.3.1 Total phosphorus

Total phosphorus shows a marked decrease in the order of 50% over the period of study, with a clear dominance of the influence of

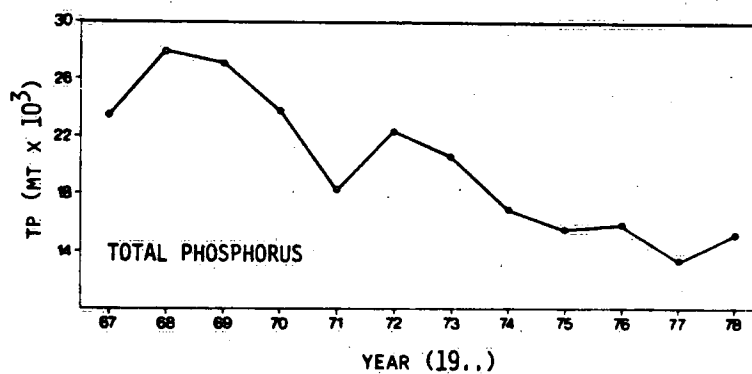


Figure 2.3. Total phosphorus loading to Lake Erie.

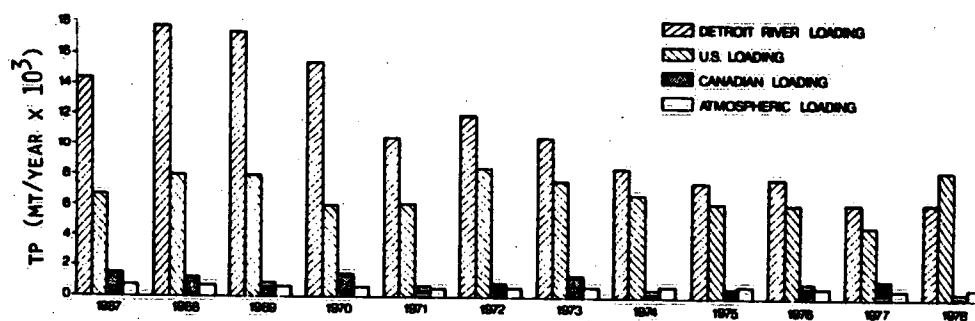


Figure 2.4. Source distribution of total phosphorus loading to Lake Erie.

the Detroit River component (Fig. 2.3). This one source represented an average of 56% of the total loading to the system. However, over the period of study (1967 to 1978), the total phosphorus loadings from the river dropped from 14 309 to 6205 MT. Similar reductions of approximately 50% are noted for the contributions from municipal and industrial sources. Reductions cannot be identified in the tributary component, because the tributary component shows more variability than the other components. Since tributaries reflect the activities occurring within their respective drainage basins, it should not be expected that these sources show signs of reduction until control measures on land use activities are implemented. Due to a transcription error, the 1975 Detroit River load was reported in Fraser and Willson (1981) as 6521 MT. This value has now been revised to 7521 MT, yielding a total load of 15 534 MT of phosphorus and a corresponding net load of 11 728 MT.

Examination of the loading results shows the dominant influence of the United States sources (Fig. 2.4). The distribution of major population centres within the Lake Erie Basin which heavily favours the United States is mirrored in the ratios between Canadian and U.S. tributary and municipal loads. Other than the Detroit River, the major source to the West Basin of Lake Erie is the Maumee River and Toledo, Ohio. Canadian sources to the Western Basin are minor in comparison with the U.S. sources, which account for 96% of the total basin load.

Over the period of study the highest loading of total phosphorus to Lake Erie occurred in 1968 (26 977 MT) coinciding with the highest Detroit River load of 17 822 MT. On a seasonal basis, the loading to the Western Basin generally follows a similar pattern from year to year. A significant increase in load occurs during the spring freshet in March, followed by relatively low loads during the summer. Autumn loads are slightly higher, being influenced by higher precipitation on the basin. This can be seen clearly in the 1967 and

1972 seasonal loadings (Fig. 2.5). Over the period of study, two incidents of flooding occurred in the Maumee Basin. In 1972, a large dam on the river was breached, resulting in a very high flow and load contribution. Much of this load to the West Basin was particulate in nature, and hence, settled out to the sediment very quickly. Similarly, in 1976, another flooding episode occurred causing abnormally high total phosphorus loads.

The Central Basin of the lake exhibits a loading distribution similar to that of the West Basin, with the major sources being the Cayahoga River and Cleveland, Ohio. The second most significant source to the Central Basin is the Black River, Ohio. Contributions from Canadian sources are relatively low but are approximately ten times greater than the West Basin levels. The Central Basin was dominated by the U.S. sources at the 89% level in 1967 and at the 79% level in 1978.

The overall load of total phosphorus to the Central Basin of the lake has been reduced from 60 MT/day in 1967 to an average load of 40 MT/day in 1978. This figure includes an estimate of the contribution from interbasin transport from the West Basin. The estimate is computed from the hydraulic flow, the cross-sectional area of the basin at the defined boundary, and the concentration of total phosphorus in the West Basin. As was the case, although not prominently, in the West Basin, relative increases in loading have been noted in the spring and fall seasons in the Central Basin (Fig. 2.5).

The Eastern Basin is dominated by the loading of the Grand River, Ontario, representing 62% of the total load to the basin. Indeed, the Grand River is the only major Canadian source to the entire lake. Located in this basin are two major municipal centres, Fort Erie, Ontario, and Buffalo, New York. These two cities are not considered as sources to the basin, as their municipal effluents

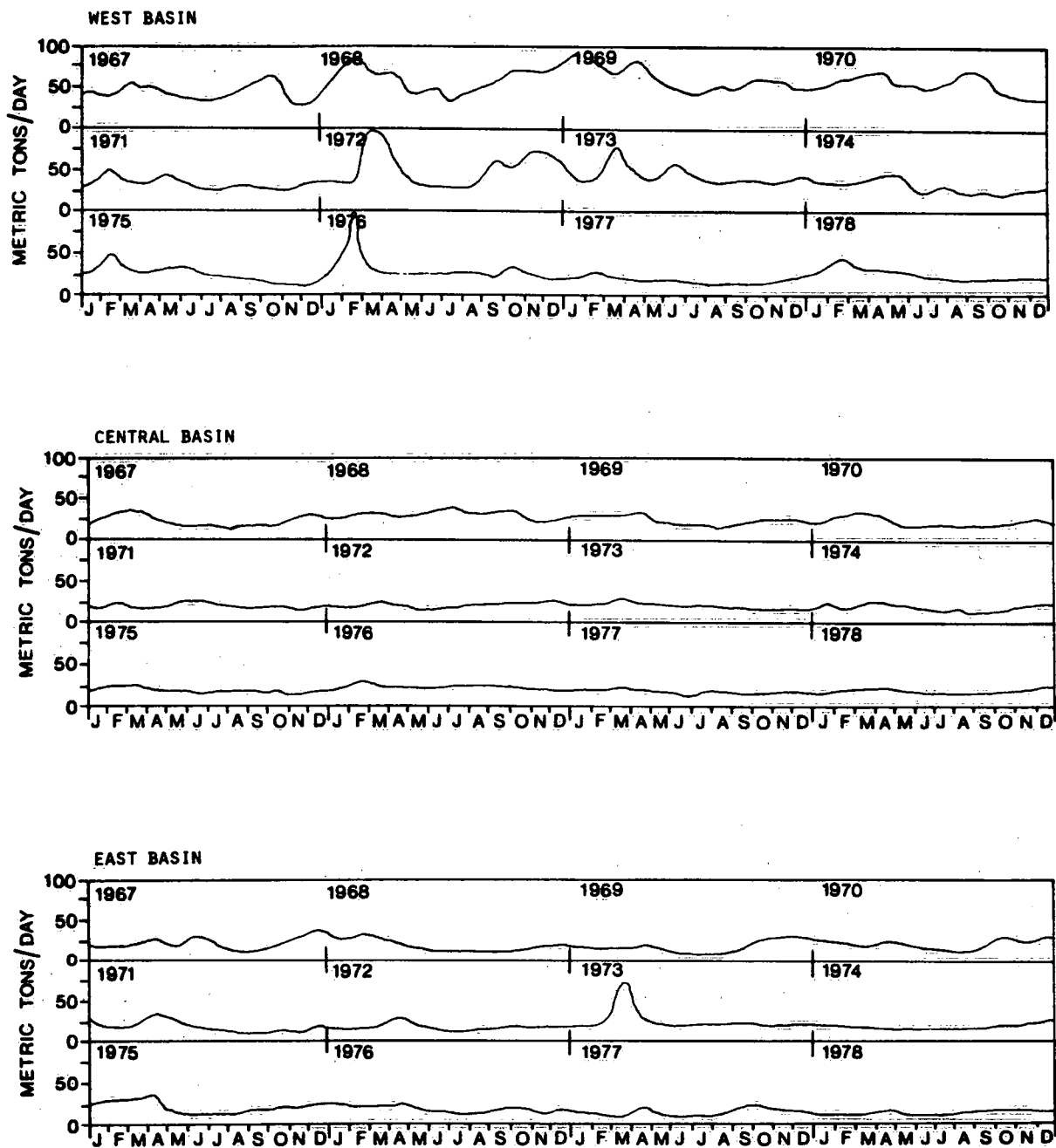


Figure 2.5. Total phosphorus loads to Lake Erie basins.

discharge into the Niagara River; the Buffalo River, however, is a tributary source.

Over the twelve years studied the load to the Eastern Basin has declined on an annual basis from a high of approximately 25 MT of total phosphorus per day in 1968 to 15 MT/day in 1977. As in the case of the Central Basin, the seasonal loads depicted here (Fig. 2.5) include a contribution for the transport from the Central to the Eastern Basin.

Seasonal effects are similar to those of the Central Basin, with slightly higher loads in the spring and fall. However, a significant event occurred in 1973 involving the Grand River, Ontario. This river reaches flood stage quite regularly during spring freshet. In 1973, flooding caused the total phosphorus load for March to exceed 70 MT/day, but the load material was largely inorganic unavailable phosphorus which settled quickly and contributed little to the lake concentration.

2.3.2 Soluble reactive phosphorus

Soluble reactive phosphorus, which may be considered to be the soluble inorganic form of phosphorus most readily available for biological use, shows loading patterns fairly similar to those of total phosphorus (Fig. 2.6). Although the magnitudes of the loads are considerably lower than those for total phosphorus (e.g. Eastern Basin summer load is about 2 MT/day), seasonal distributions are discernible. The dominance of the Detroit and the Maumee rivers in the Western Basin is again evident.

From lake-wide averaged figures, this form constitutes about 34% of the total phosphorus. The bioavailability associated with this form is an important factor in managing Lake Erie eutrophication

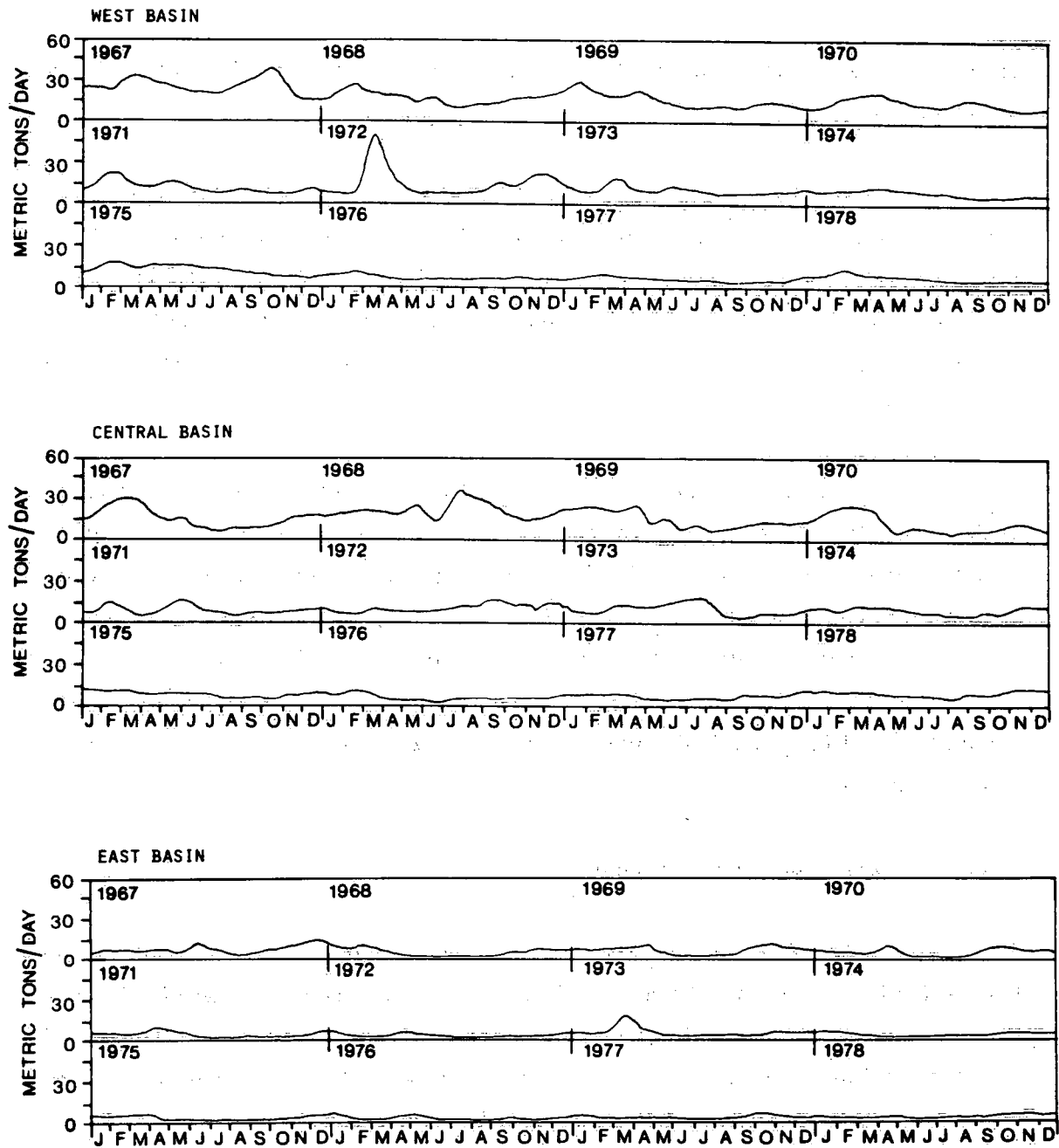


Figure 2.6. Soluble reactive phosphorus loads to Lake Erie basins.

problems. As demonstrated by Simons and Lam (1980), a reduction in the soluble reactive phosphorus load is more efficient in bringing down the in-lake phosphorus concentrations than an equivalent reduction in the particulate load. As shown in Fig. 2.7, the soluble reactive phosphorus load has declined quite drastically for the lake as a whole. The main reduction lies with the Detroit River, but additional reductions can be noted in the other sources also. The downward trend is particularly evident between 1967 and 1969. After 1969, the decline is about 740 MT/year.

Both the total and the soluble reactive phosphorus loads will be used in the mass balance models in this study. However, to offer some comparisons, the lake-wide annual loads of the following water quality variables are also provided.

2.3.3 Nitrogen

Total nitrogen loads to Lake Erie have been increasing, with significant increases beginning in 1972. The four nitrogen variables, total nitrogen, nitrate plus nitrite, Kjeldahl nitrogen, and ammonia, although related, display somewhat varied behaviour over the twelve years studied (Fig. 2.7). Nitrate plus nitrite, which constitutes the major soluble inorganic component of total nitrogen, has increased since 1967 at an average rate of 7800 MT/year. Examination of the load sources for nitrate plus nitrite indicates increases in the contributions from the Detroit River and tributary sources in concert with reductions in the municipal and industrial component. This factor can be related to the installation of municipal treatment plants which, although their design is to reduce organics and remove phosphorus, also remove an amount of nitrogen in the process. Thus treated effluents are likely to show reductions, whereas untreated sources may display increases.

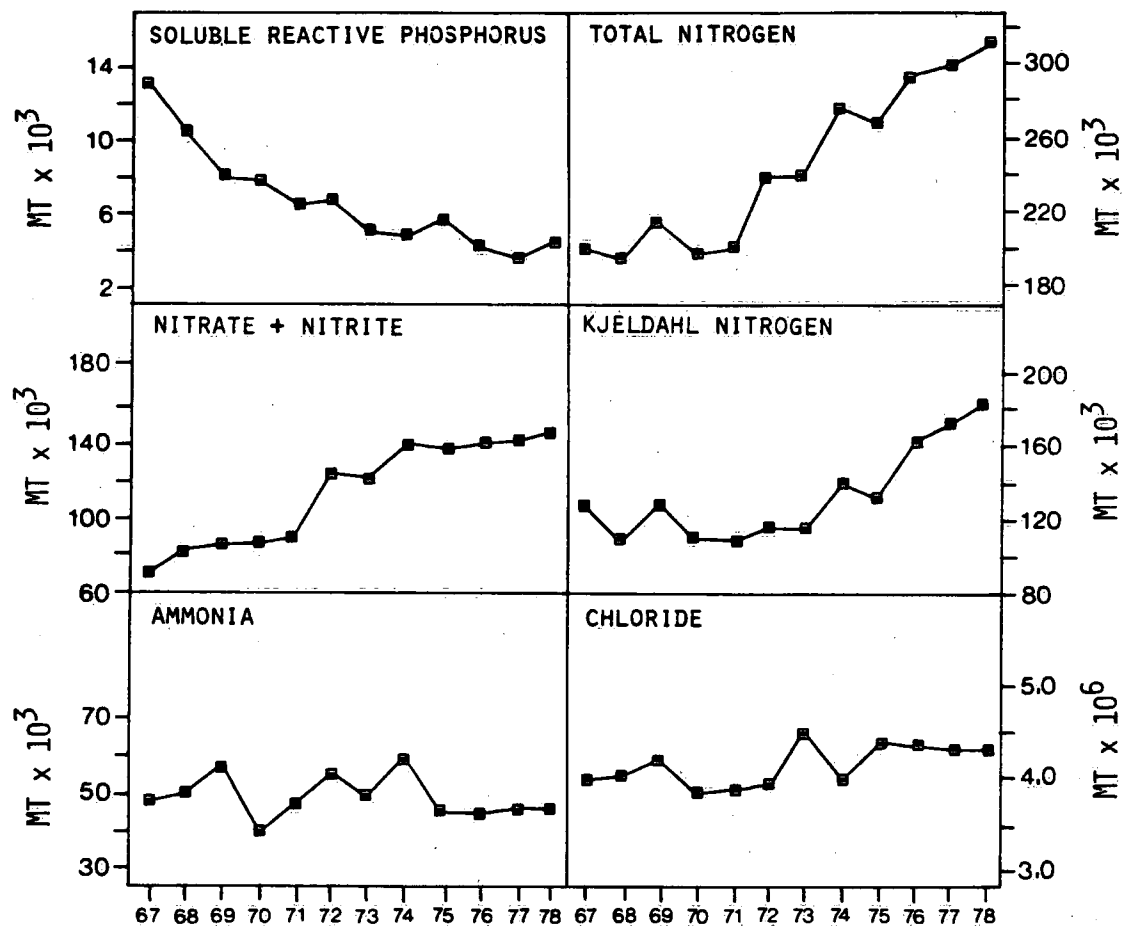


Figure 2.7. Chemical loadings to Lake Erie.

Kjeldahl nitrogen, which is a combined measure of the organic nitrogen and ammonia component, shows some variability from 1967 to 1970, with a levelling up to and including 1973, followed by an increase to 1978. In conjunction with the examination of the Kjeldahl nitrogen the ammonia loads show a larger variability with an average loading of approximately 47 000 MT/year over the study period. Of note here is the increase in the contribution of organic nitrogen from 1974 to 1978 attributed to the Detroit River and tributaries to the lake.

2.3.4 Chloride

The variable chloride was included in this study to act as a conservative substance within the lake chemistry. The loading of chloride (Fig. 2.7) displays some variability over the study period except in the latter years 1975 to 1978 where a higher than average load is noted. This increase is attributed primarily to the contribution coming from tributaries. It should be noted that as well as the load presented here, an additional load of 1.0 to 1.5 million metric tons of chloride is added to Lake Erie annually from road salting operations (Fraser, 1981).

Lake Chemistry

3.1 Introduction

As noted in Chapter 2, the Western Basin receives the highest input load of the three basins of Lake Erie. This basin is usually well mixed with respect to both temperature and chemicals. The basin is classified as eutrophic because of the large phosphorus load. Substantial quantities of chemical materials are also transported to the Central Basin from the Western Basin. The Central Basin supports a high productivity level and is thermally stratified in the summer. These conditions allow the formation of strong chemoclines for several water quality variables including dissolved oxygen and soluble reactive phosphorus. The thermocline inhibits significant oxygen transfer from the saturated epilimnetic waters to the hypolimnion, causing anoxia. Under anoxic conditions, redox potentials become very low and negative, leading to the onset of chemical reduction processes. The main results of the reduction are strong releases of available phosphorus and ammonia from the sediment.

Depending on wind and other weather conditions, a westward hypolimnetic current may, at times, bring oxygen-rich waters from the Eastern Basin into the Central Basin and relieve the anoxic condition somewhat. The net transport, however, is still from the Central to the Eastern Basin. Thus, the description of the lake chemistry must take into consideration the spatial differences of the basins. An example is offered by the basin-averaged concentrations of total phosphorus and chloride given in Table 3.1.

Table 3.1. Lake Erie Horizontal Gradients

Variable	Western Basin	Central Basin	Eastern Basin
Total phosphorus ($\mu\text{g P/L}$)	35.6	25.6	18.1
Chloride (mg Cl/L)	16.8	23.9	24.8

Total phosphorus displays the highest concentration in the West Basin, because of loading effects. As the material moves eastward, elements of the nutrient are subject to sedimentation processes such that, even with additional loads of phosphorus entering into each basin, a general decreasing west-east gradient is observed. On the other hand, the chloride ion, which is essentially a conservative variable, shows a gradient in concentration toward higher levels from west to east. This may be explained primarily by the additional sources of chloride loaded to the lake in each basin.

The existence of chemoclines and thermoclines also complicates the data analysis in the Central and Eastern basins. The hypolimnion in the Central Basin can be 2 to 4 m thick during the anoxic period and requires an accurate method to estimate chemical concentrations within that layer. In general, a data estimation method, which is capable of selecting homogeneous zones according to the thermoclines and chemoclines, is required for all the three basins. Such a method is discussed in detail in the Appendix. Briefly, at each data collection cruise, the observed temperature data will provide the vertical thermal structure at a given sampling station. The assumed structure forms the basis for vertically interpolating the water chemistry data at that station. Depending on the sampling station patterns, the vertically interpolated chemical data are then interpolated horizontally over chosen distances so that, desirably, the whole lake is covered. During the horizontal interpolation, only data from the same assumed thermal layer, e.g. top 1 m of the epilimnion, are

used for interpolation within that particular layer. The result is a three-dimensional array of interpolated data.

These interpolated lake chemistry data serve two purposes in this study. One purpose is to check diagnostically, from mass balance principles, whether the estimated chemical loads are consistent with the observed in-lake concentrations (Section 3.3). The other purpose is to verify the water quality models and to assess their predictive capability (Chapters 6 and 8). Thus, depending on the spatial complexity of these models, the three-dimensional data can be used either as they are, laterally averaged into a two-dimensional (longitudinal and vertical) representation, vertically integrated into an areal map, or averaged into two or three layers for each basin.

The accuracy of this data estimation method is affected, of course, by the station density and distribution and the availability of the thermal structure information. Over the period of 1967 to 1978, a total of 63 ship cruises were found to be adequate for the data estimation analysis (Table 3.2). Additional data from sources (e.g. Herdendorf, 1980) not identified in Table 3.2 have been used to supplement weak data sets. Such requirements were minimal, as the primary data set was of sufficient calibre.

Table 3.2. Primary CCIW Cruises Used in Lake Chemistry Analysis

67	68	69	70	71	72	73	74	75	76	77	78
101*	102	103	102	101*	101	101	101	101	101	102	103
102*	104	108	103	101	102	103	104	102	102	103	104
111	108	110	104	111	103	106		106		105	106
113	111		106	117	104	109		107		106	108
115	112		107		107			110		107	110
	105*		109		108			111		109	111
			111					112		113	114
			113								
			114								
			116								

*Great Lakes Institute

3.2 Two-Dimensional Interpolated Data

To summarize the interpolated water quality data over the twelve-year period given in Table 3.2, we have selected the laterally averaged two-dimensional version of the results for discussion. There are many interesting features among the 63 cruises, but they are sufficiently represented by the late summer cruises of 1968, 1970, 1975 and 1978 to cover years with high nutrient loads, thin hypolimnion, thick mesolimnion and reduced nutrient loads, respectively. Our discussions will centre on the relationships among water temperature, total phosphorus, soluble reactive phosphorus, and dissolved oxygen so that a conceptual model can be visualized. To supplement the discussions, the data of chlorophyll a, nitrate plus nitrite, ammonia and chloride will also be presented. In preparing the figures for these two-dimensional results, the vertical scale has been enlarged to enable clearer representation of contours.

3.2.1 Temperature

Detailed discussions of water temperature as a physical parameter are given in Chapters 4 and 5. Biologically, water temperature is a primary factor affecting the photosynthesis of phytoplankton. For example, the rise in water temperature in spring signals the growth of the diatom species. Chemically, it affects the kinetic rates. For Lake Erie, the lake chemistry is tied in closely to the thermal structures, particularly the thicknesses of the hypolimnion and mesolimnion layers.

Figure 3.1 shows the temperature distributions of the four years under discussion. In 1970, a sharp thermocline extends throughout both the Central and Eastern basins. The Central Basin hypolimnion is quite thin and extends fully to the basin boundaries.

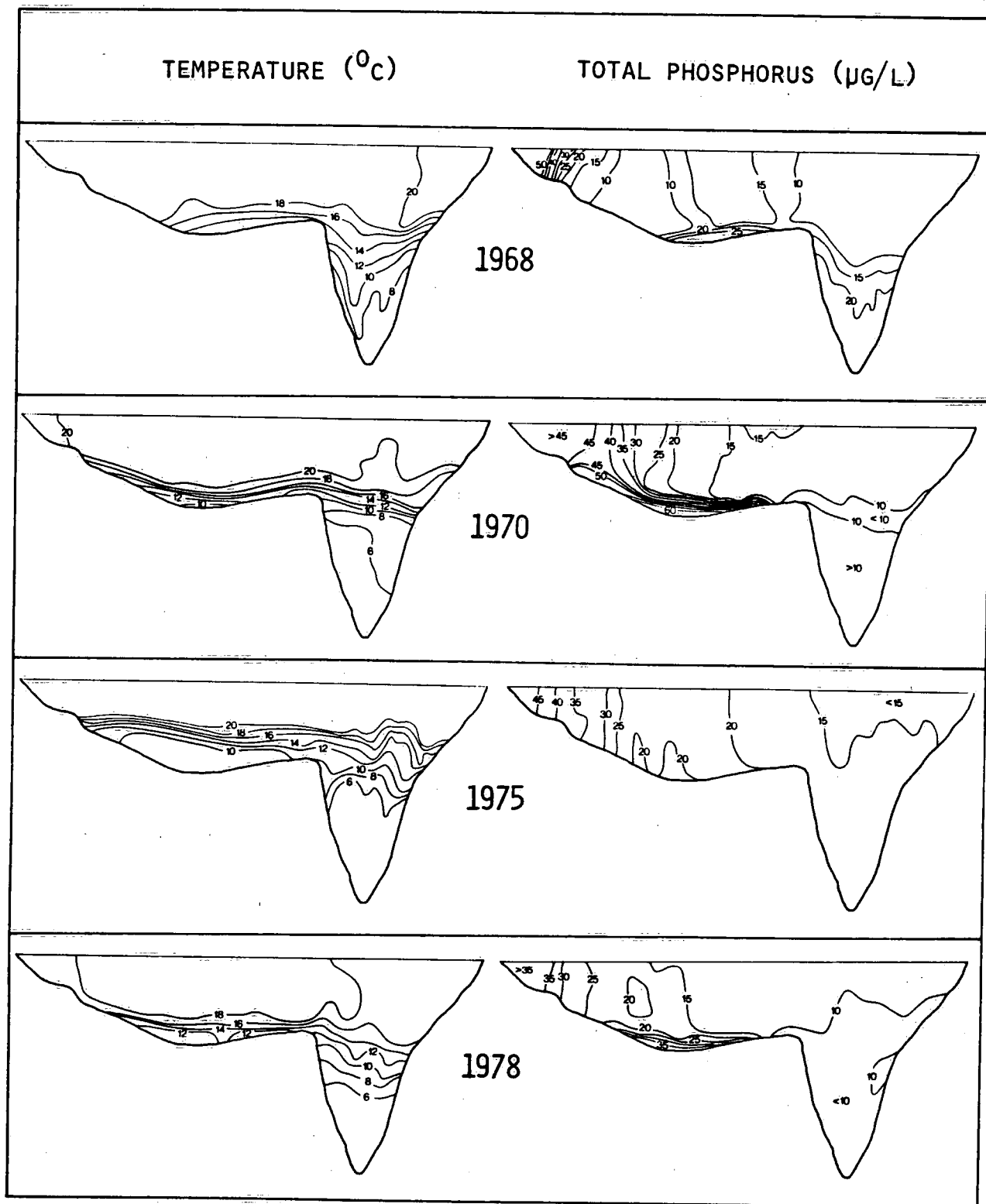


Figure 3.1. Two-dimensional representation of observed data for temperature and total phosphorus for the August-September period.

The case for 1978 is similar to that of 1970 with a slightly thicker hypolimnion in the Central Basin. The East Basin, however, shows deeper penetration of heat. In contrast, the 1975 situation is radically different, displaying very broad hypolimnion and mesolimnion layers in the Central Basin with the hypolimnion temperature 2°C below normal. The 1968 data also show a moderate stratification.

3.2.2 Total phosphorus

Total phosphorus represents both soluble and particulate forms of inorganic and organic phosphorus. The total phosphorus regimes for the late summer display significantly different lake effects (Fig. 3.1). Horizontally, a decreasing west-to-east gradient is apparent in all years. The Western Basin concentration, which is subject primarily to the loading influence of the Detroit River, is approximately 50 µg P/L in 1968. As the loading of total phosphorus has declined so has the basin concentration. In 1978, a value of 35 µg P/L is observed.

The Central Basin exhibits the strongest effect of stratification during the August to September period. The very shallow hypolimnion observed in 1970 is responsible for the large release of phosphorus from the sediment into the hypolimnion. In 1970, the gradient in total phosphorus was approximately 40 µg P/L over a thermocline thickness of one metre. Massive releases of nutrient material from the sediment occur under anoxic conditions in which the redox potentials are negative, thereby causing disruption of the stability of the surficial sediments. Of the other years presented in Fig. 3.1, 1968 and 1978 both show degrees of hypolimnion phosphorus regeneration but not of the magnitude observed in 1970.

Essentially, no increase in hypolimnetic phosphorus in the late summer of 1975 was noted. Although the Central Basin was stratified, both the hypolimnion and mesolimnion were of higher than average thickness. This indicates the presence of strong vertical diffusion which might have brought in more oxygen to the hypolimnion from the upper thermal layers. Thus, the oxygen demand of the sediment was satisfied and large-scale anoxia was precluded.

3.2.3 Soluble reactive phosphorus

This parameter is the soluble inorganic form of phosphorus most readily available for use as a nutrient in phytoplankton production. Although terminology implies that only one phosphorus form is considered, this parameter, in fact, is a representation of several phosphate (PO_4) species of the orthophosphate type.

During the winter isothermal period, whole lake concentrations of soluble reactive phosphorus are at their highest. The characteristic longitudinal gradient decreasing from west to east is also present as in the case of total phosphorus (Fig. 3.2). When warming begins in the spring, epilimnion concentrations of SRP rapidly decrease due to phytoplankton nutrient uptake. The degree of phosphate reduction is sufficient to yield extensive epilimnion concentrations between 1.0 and 2.0 $\mu\text{g P/L}$, exerting a limiting factor upon phytoplankton growth. The sediment release mechanism under anoxic conditions discussed previously is clearly shown for soluble reactive phosphorus in the late summer (Fig. 3.2). A comparison of relative concentrations of total and soluble phosphorus concentrations shows that of the material regenerated to the hypolimnion waters, between 60% and 80% is of the soluble reactive form. However, the duration of time that these high concentrations of soluble phosphorus remain in the hypolimnion is very short, implying a rapid loss mechanism in the Central Basin hypolimnion at this time.

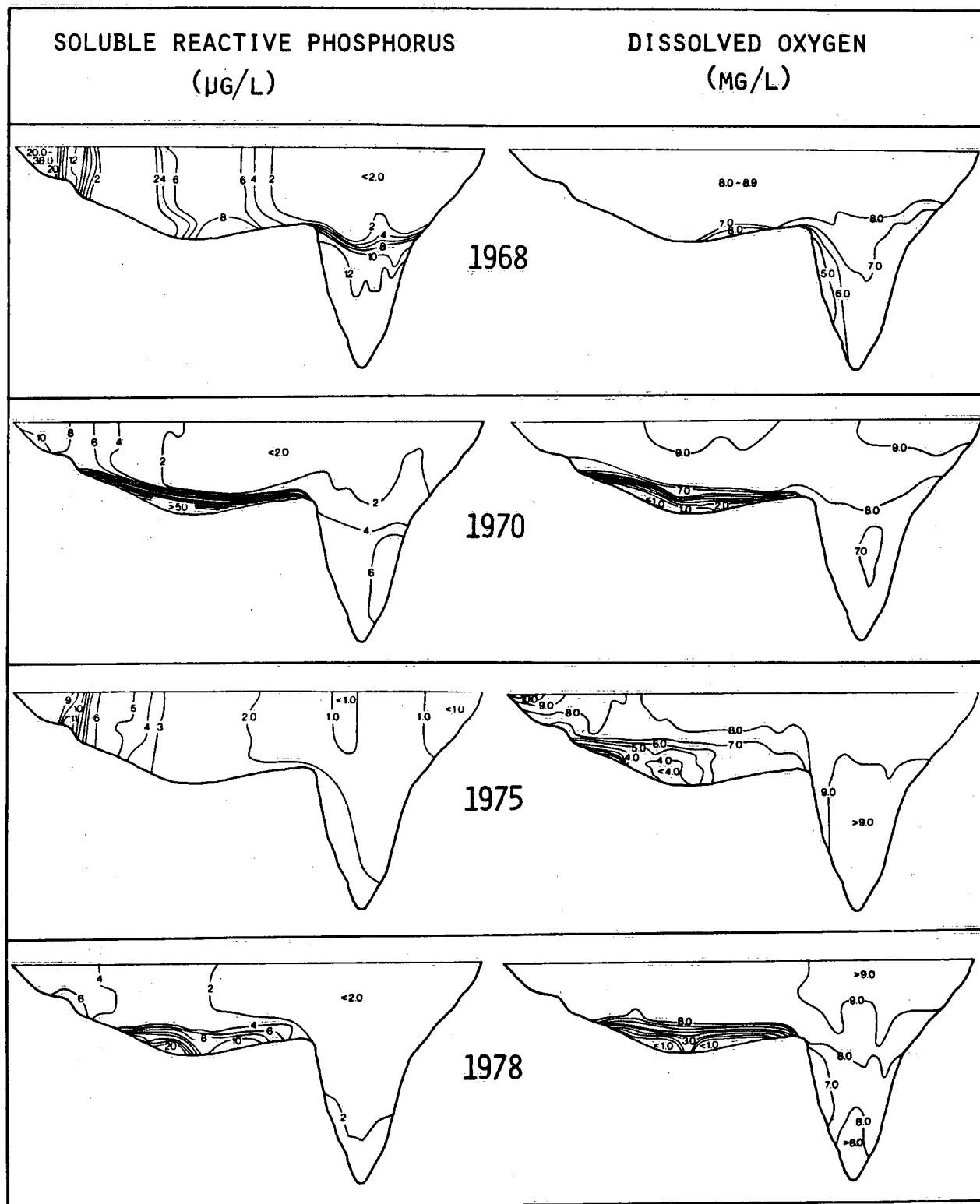


Figure 3.2. Two-dimensional representation of observed data for soluble reactive phosphorus and dissolved oxygen for the August-September period.

The regeneration of soluble phosphorus to the water column from the sediments represents a significant internal load of nutrient material to the lake. This contribution is unaccounted for in computations of loadings. However, the subsequent uptake and sedimentation followed by the onset of the fall mixing period may well offset much of the impact.

3.2.4 Dissolved oxygen

Concentrations of oxygen in aquatic systems are governed by many mechanisms. In epilimnetic waters the concentration is mainly controlled by ambient temperature and pressure. Under normal conditions there is sufficient oxygen present to establish 100% saturation at all times. Typically, during the winter-spring isothermal period, oxygen concentrations lie in the range 12 to 13 mg O₂/L. As the lake warms, the oxygen concentration in the epilimnion decreases but still maintains 100% saturation. Under fully stratified conditions and when the temperature in the epilimnion reaches 20°C, oxygen saturation is achieved with concentrations of 8 to 9 mg O₂/L (Fig. 3.2).

Chemical and microbiological oxidation processes occur continuously in both the water column and the surficial sediments of the lake. These processes comprise the water oxygen and sediment oxygen demand (Burns, 1976b). Hypolimnetic oxygen depletion in the Central Basin has been the centre of international concern for many years (IJC, 1969; Burns and Ross, 1972; Vollenweider, 1968). Anoxia occurs when aerobic decay processes acting on organic material consume the available oxygen in solution. Although anoxia technically is the absence of any oxygen, the International Joint Commission has accepted an analytical value of less than 0.5 mg O₂/L to be representative of the condition (IJC, 1978).

Since the thermocline prevents significant diffusion of oxygen from the epilimnion to the hypolimnion, the depth of the thermocline on the Central Basin is of prime importance in the evaluation of the relative severity of the anoxic conditions. Figure 3.2 shows different levels of oxygen depletion in the Central Basin hypolimnion for the four years. In the case of 1968, low oxygen values in this hypolimnion may be masked by higher concentrations which reside on the same transverse axis during the preparation of the two-dimensional representation.

The strong stratification of 1970 permitted a particularly severe episode of anoxia to occur which, as previously noted, released substantial amounts of nutrients into the hypolimnion. A similar though less severe situation was observed in 1978. Although some low oxygen concentrations were computed for the western end of the Central Basin in 1975, only a very small area was involved. The dominant feature of this latter year is the thickness and position of the thermocline relative to the basin morphometry (Fig. 3.1).

3.2.5 Chlorophyll a

Chlorophyll a is an indirect measurement of phytoplankton concentration in the water column from which estimates of the total algal biomass can be obtained. However, varying levels of chlorophyll a in phytoplankton and algae throughout the annual season mean that this parameter should be used primarily as an estimate of chlorophyll biomass. Despite these drawbacks, the parameter does yield useful information in regard to phytoplankton (Stadelmann and Munawar, 1974).

The two-dimensional results for chlorophyll a (Fig. 3.3) show generally higher concentrations in the Western Basin with a gradient to lower concentrations toward the east. This conforms with the nutrient distributions discussed previously and is indicative of

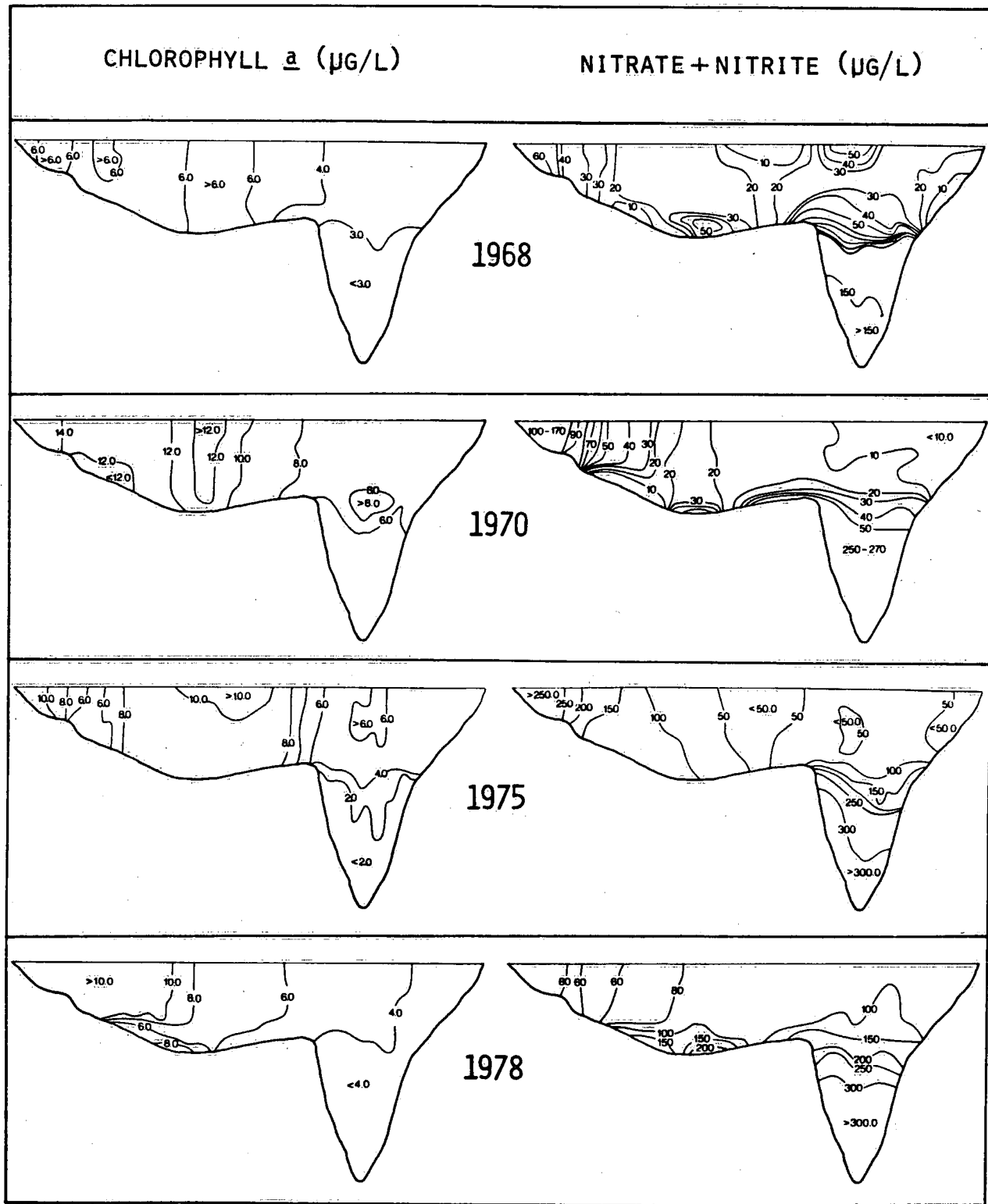


Figure 3.3. Two-dimensional representation of observed data for chlorophyll a and nitrate plus nitrite for the August-September period.

the influence of nutrient concentrations on phytoplankton within the lake. In the deeper waters of the Eastern Basin, concentrations of chlorophyll a do not rise beyond approximately 2 to 4 $\mu\text{g/L}$ due to light limitations. However, in the Central Basin, which has a mean depth of 19 m, sufficient light does reach into the hypolimnion to support chlorophyll phytoplankton growth. By the latter part of the summer season concentrations of chlorophyll a in the Central Basin range between 10 and 12 $\mu\text{g/L}$ over the water column from the surface to the bottom. Note that these high concentrations of chlorophyll a at the Central Basin hypolimnion are associated with the high anoxic regeneration of soluble reactive phosphorus (Fig. 3.2) in the case of 1970.

3.2.6 Nitrate plus nitrite

This parameter contains the two primary inorganic forms of nitrogen used as nutrients by algae within the lake. Nitrite (NO_2) represents only a small fraction of the total concentration. Generally, springtime concentrations in the lake average 300 $\mu\text{g N/L}$ with a strong horizontal gradient decreasing from west to east. Epilimnion concentrations of nitrate are depleted due to phytoplankton growth, yielding concentrations in the range 10 to 20 $\mu\text{g N/L}$ which are not uncommon in the late summer epilimnion waters (Fig. 3.3). East Basin hypolimnion waters do not show seasonal changes in the concentration of nitrate to the same degree as the waters in the upper layer and, therefore, are indicative of whole lake trends in the concentration over time. Over the twelve-year study period the deep water concentration has increased from approximately 150 $\mu\text{g N/L}$ to 300 $\mu\text{g N/L}$ between 1967 and 1978, respectively. This increase is a reflection of the increasing nitrate loadings noted in Chapter 2.

Vertical concentration gradients of nitrate are strongly related to the thermal structure. During periods of hypolimnion

anoxia in the Central Basin when sediment material is regenerated to the water column, nitrate concentrations increase in the same way as the phosphorus species discussed previously. The magnitude of the release, however, does not appear to be as large as the phosphorus release. Concentrations of nitrate plus nitrite were elevated from 10 µg N/L to 50 µg N/L at this time. Higher concentrations are noted in the hypolimnion as in 1978 (200 µg N/L) which are related to higher levels of nitrogen concentration in the epilimnion waters.

3.2.7 Ammonia

Except in very localized nearshore areas where the pH is low, the variable ammonia is in the aqueous form of the ammonium ion (NH_4^+). Ammonia is produced in the process of microbiological decay of organic material and as a constituent of excreta. Ammonia can be taken up as a nutrient directly by some phytoplankton, although a two-step aerobic bacterial process converts most ammonia into nitrite and subsequently from nitrite to nitrate. Ammonia concentrations display a horizontal gradient in Lake Erie again decreasing from west to east (Fig. 3.4). A strong hypolimnion increase is noted for the Central Basin corresponding to periods of anoxia. Under anaerobic conditions reduction occurs, producing ammonia from nitrate and nitrite. If the degree of reduction is severe enough, organic material in the sediments will be decomposed to methane. This situation has, as yet, not occurred in Lake Erie. However, as is noted for 1970 in particular and in 1978 to a lesser degree, reducing conditions have occurred sufficiently to produce high concentrations of ammonia (over 50 µg/L).

3.2.8 Chloride

Examination of the changes in the conservative element chloride shows a decreasing trend from concentrations of 24 mg Cl/L in 1968 to 20 mg Cl/L in 1978. The reduction in chloride concentration

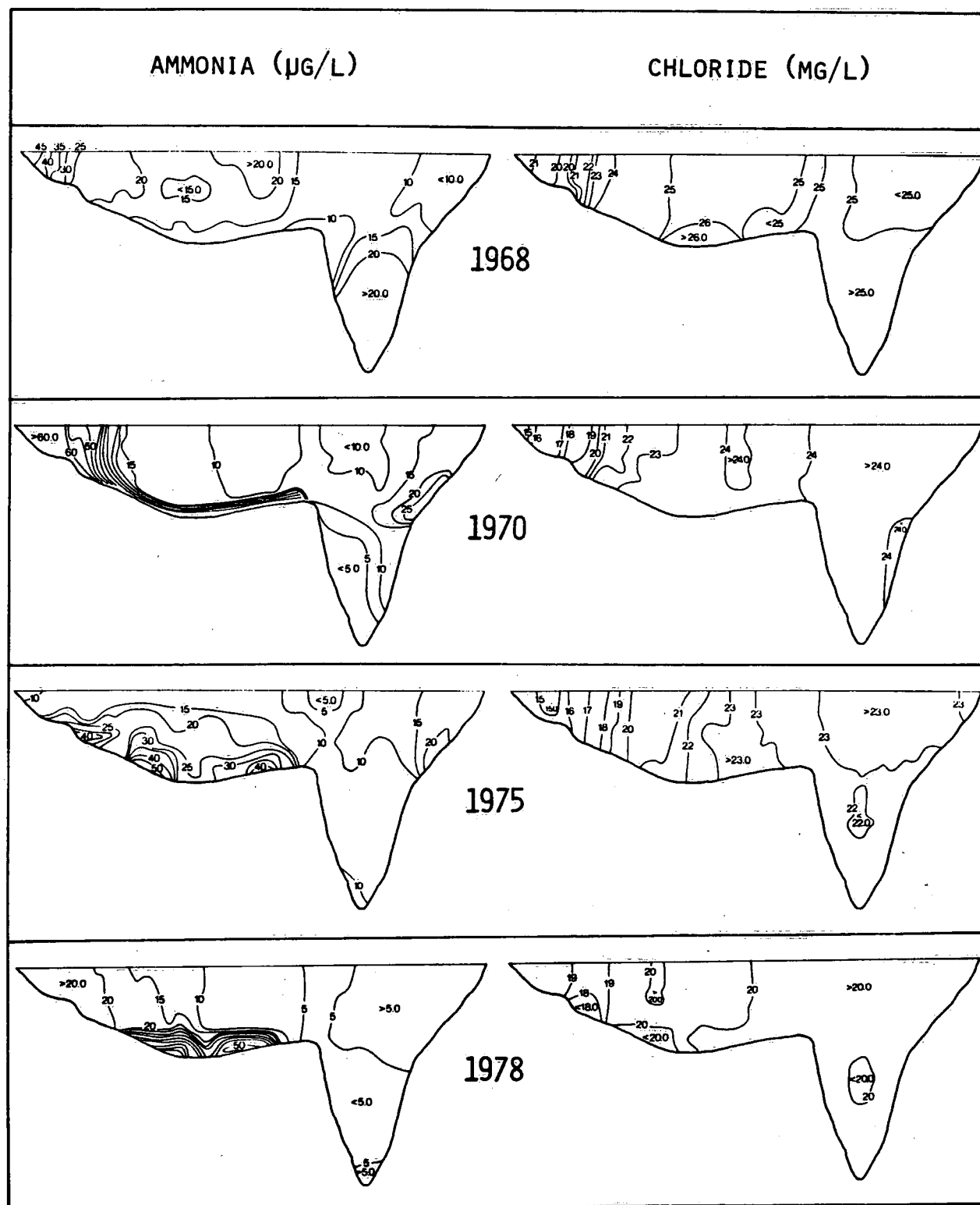


Figure 3.4. Two-dimensional representation of observed data for ammonia and chloride for the August-September period.

is primarily the result of dilution due to increased lake flushing during the study period (Bennett, 1976). Chloride concentrations are rather uniform vertically within the water column but display a distinctive horizontal gradient increasing from west to east (Fig. 3.4). This gradient is opposite in direction to the nutrient and biological parameters discussed previously.

3.3 Diagnostic Mass Balances

The discussions in Section 3.2 clearly point to a conceptual model in which both the loading and the thermal stratification influences play an important role in the temporal and spatial distributions of chemical variables in Lake Erie. Only after these influences have been quantified, can the kinetic transformation among the variables be established. An example of establishing kinetic rates by quantifying observed data with respect to thermal structures is the work of Charlton (1980) and Rosa and Burns (1981) on the sediment and water oxygen demands. Charlton (1980) used the observed position of the thermocline to derive the hypolimnion thickness which was then correlated to the oxygen depletion rate. Rosa and Burns (1981) used a three-layered structure to interpolate the oxygen concentration within each layer, which enabled them to correct for the vertical diffusion and entrainment effects. Furthermore, they considered essentially a mass balance budget for the Central Basin hypolimnion by incorporating the interbasin transports. The oxygen depletion rate was then obtained as the residual of the budget.

A more elaborate diagnosis can be achieved with the present three-dimensional interpolated data. Instead of a direct two-layered or three-layered interpolation, the three-dimensional data have been subjected to a fine vertical resolution (see Appendix), e.g. 25 layers for the Central Basin. This permits a more accurate vertical interpolation of the observed data, so that on reducing them back to the two- or three-layer representation, the incorporation of the vertical

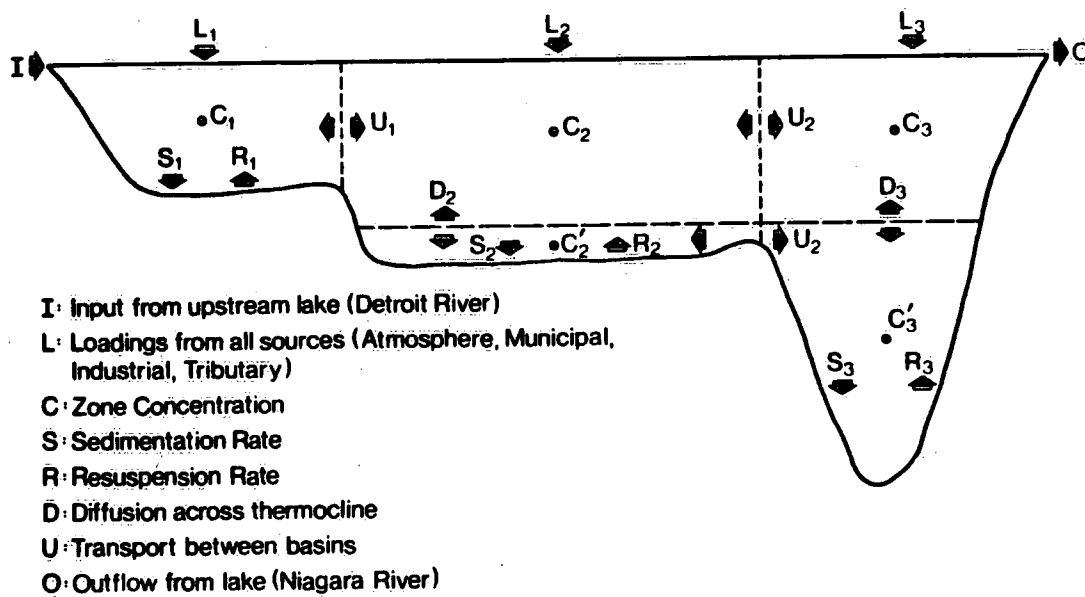


Figure 3.5. Schematic of Lake Erie dynamic mass balance model.

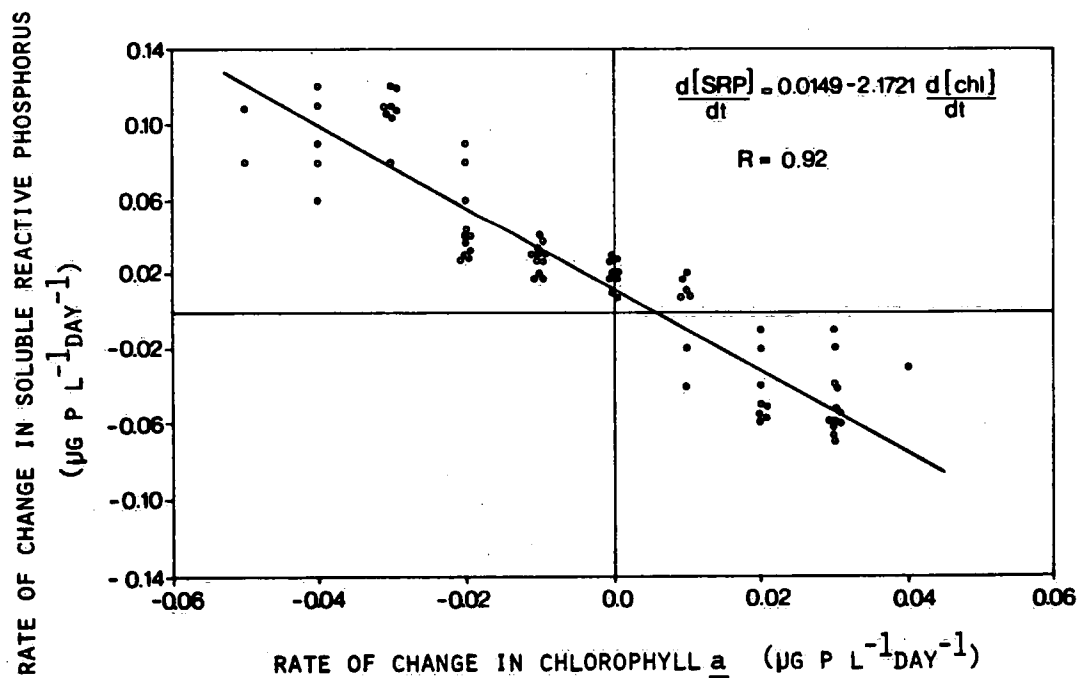


Figure 3.6. Rate correlation during growth phase in the Central Basin derived from the three-box representation of observed data.

distribution is more precise. Furthermore, the mass balances for all the layers and basins can be carried out, as the data are easily reducible. The detailed formulation of such a mass balance model is given in Section 5.5. For the present discussion, results diagnosing the sedimentation rate from the total phosphorus loading and concentration data will be given, as well as the kinetic rate for uptake and respiration from the soluble reactive phosphorus data. In both cases, the three-box and the six-box models are used in which the loadings, concentrations, advective diffusive and entrainment processes are all assumed known (Fig. 3.5). The rates in question are then obtained as residuals of the model equations (5.16 to 5.18 and 5.20 to 5.25). The oxygen depletion rate, however, will be addressed later in Subsections 6.2.4 and 6.3.3, using the prognostic approach.

3.3.1 Sensitivity of the lake concentration data

It is pertinent to include here a discussion of the sensitivity of the lake concentration data reduced to the three-, six- and nine-box representations used in this study. An example can be seen by examining day 275 of Tables 3.3 and 3.4. The Central Basin oxygen concentration is reported as 8.24 mg O₂/L for the whole basin (three-box). Splitting the basin horizontally at the midpoint of the thermocline (six-box) results in values of 8.76 mg O₂/L and 4.45 mg O₂/L for the top and bottom layers, respectively. Further elaboration to epilimnion, mesolimnion and hypolimnion (nine-box) results in values of 8.79 mg O₂/L, 7.43 mg O₂/L and 2.72 mg O₂/L, respectively. The degree of oxygen depletion in the hypolimnion is noted the most clearly in the latter case. However, there is an indication that lower oxygen levels are also present in the six-box model reduction but absent in the three-box.

Similarly, the sediment release of phosphorus is more evident in the nine-box representation on day 275 in the Central Basin (Table 3.3). Note that the three-dimensional interpolation scheme

Table 3.3. Total Phosphorus ($\mu\text{g P/L}$) Box Model Reduction

Day	C. Basin						E. Basin					
	W	T	B	E	M	H	W	T	B	E	M	H
151	14.35	13.79	15.06	13.35	15.04	15.00	15.51	15.30	15.63	14.95	16.09	15.59
S	1.51	1.40	1.36	1.34	1.15	1.34	2.10	2.82	1.74	2.99	1.83	1.76
172	12.77	12.53	13.59	12.29	13.37	13.35	14.05	14.30	13.77	14.37	13.86	13.83
S	1.72	1.77	1.41	1.52	1.88	1.11	2.26	1.39	2.69	1.35	1.39	2.91
196	14.43	13.36	18.13	12.79	17.03	18.78	14.55	13.63	15.63	13.49	14.54	15.91
S	3.73	3.32	2.11	2.96	2.83	1.90	1.93	1.47	1.74	1.41	1.54	1.70
233	14.99	14.21	18.36	13.67	16.52	20.07	13.46	12.97	14.10	13.05	12.66	14.42
S	3.75	3.12	3.36	2.01	3.91	3.35	2.55	1.14	3.05	1.14	1.06	3.14
259	15.91	16.02	15.29	16.07	15.35	15.38	10.80	11.15	10.28	11.22	10.29	10.31
S	4.81	4.16	3.29	5.11	4.81	2.12	0.87	0.95	0.56	0.95	0.45	0.59
275	16.76	16.41	19.32	16.51	16.00	21.49	10.48	10.80	9.96	10.87	9.93	9.98
S	4.89	4.17	6.48	4.23	3.91	6.89	1.42	1.01	1.61	1.02	0.37	1.68

W = Whole Basin (three-box) E = Epilimnion (nine-box)

T = Top Layer (six-box) M = Mesolimnion (nine-box)

B = Bottom Layer (six-box) H = Hypolimnion (nine-box)

S = Standard Deviation

Table 3.4. Dissolved Oxygen ($\text{mg O}_2/\text{L}$) Box Model Reduction

Day	C. Basin						E. Basin					
	W	T	B	E	M	H	W	T	B	E	M	H
151	12.44	12.84	11.94	12.70	12.87	11.70	13.74	14.21	13.44	14.26	14.02	13.35
S	1.15	0.65	1.30	0.60	1.13	1.20	0.57	0.52	0.38	0.59	0.28	0.34
172	9.55	9.53	9.62	9.62	9.42	9.72	11.12	10.93	11.35	10.89	11.15	11.38
S	0.86	0.82	0.94	0.50	1.17	0.65	0.73	0.48	0.80	0.42	0.58	0.85
196	8.76	9.02	7.85	9.22	7.97	7.76	9.91	9.62	10.25	9.59	9.72	10.42
S	1.23	0.94	1.42	0.42	1.65	1.17	0.72	0.24	0.76	0.18	0.62	0.66
214	8.35	8.81	6.76	8.99	7.60	6.61	9.01	8.95	9.08	8.99	8.67	9.26
S	1.35	0.56	1.51	0.13	1.38	1.45	0.87	0.18	1.09	0.15	0.45	1.10
233	7.76	8.37	5.11	8.76	6.28	4.86	8.20	8.39	7.94	8.43	8.10	7.95
S	1.97	1.28	1.52	0.38	1.96	1.36	1.07	0.43	1.35	0.42	0.66	1.40
259	7.62	8.27	3.99	8.37	6.15	2.15	8.50	8.70	8.21	8.70	8.64	8.13
S	2.47	1.00	2.67	0.73	2.50	1.77	0.52	0.12	0.63	0.12	0.15	0.66
275	8.24	8.76	4.45	8.79	7.43	2.72	8.67	9.11	7.95	9.12	8.90	7.82
S	2.29	0.26	2.99	0.18	1.71	2.56	0.81	0.10	0.73	0.09	0.24	0.70

W = Whole Basin (three-box) E = Epilimnion (nine-box)

T = Top Layer (six-box) M = Mesolimnion (nine-box)

B = Bottom Layer (six-box) H = Hypolimnion (nine-box)

S = Standard Deviation

(see Appendix) preserves the basin morphology. The hypolimnetic concentration in the nine-box model, therefore, can be at 23 or 24 m depth. Thus, the concentrations given in Tables 3.3 and 3.4 refer to different layer depths for different cruise days. The standard deviation associated with the concentration for a particular box is obtained from all the interpolated and observed data within that box. That is, it represents both interpolation and observational errors.

3.3.2 Diagnostic results using total phosphorus data

Both the loading and the lake concentration data were interpolated into daily values by time-series interpolation (Simons and Lam, 1980) over the period 1967 to 1978. The advective transport and the dynamic movements of the thermal layers were based on those used in Chapter 6, which were derived from heat budget (Chapter 5) and one-dimensional simulation of the thermocline (Chapter 7). It is important to note here that, given the uncertainties surrounding the time-series interpolation, the diagnostic results have been intended primarily as a preliminary check on the consistency of the loading data and the lake concentration data. If the diagnostic results on the sedimentation rate and the soluble reactive phosphorus kinetic rates are uniform over the twelve-year period, then the two data sets should be quite consistent and the estimated rates (e.g. Fig. 3.6) may even be useful to the subsequent prognostic investigation. Otherwise, explanation must be sought for those cases with anomalies.

For example, the Western Basin receives 60% of the total loading of phosphorus to the whole lake which shows seasonal variability. Sedimentation increases dramatically for some years (1967, 1969, 1970, 1972 and 1976) during the spring runoff period with rates between 60 and 100 MT/day (Fig. 3.7). This is particularly prevalent with flooding of the Maumee River. Summertime sedimentation rates are substantially lower. The high sedimentation associated with spring

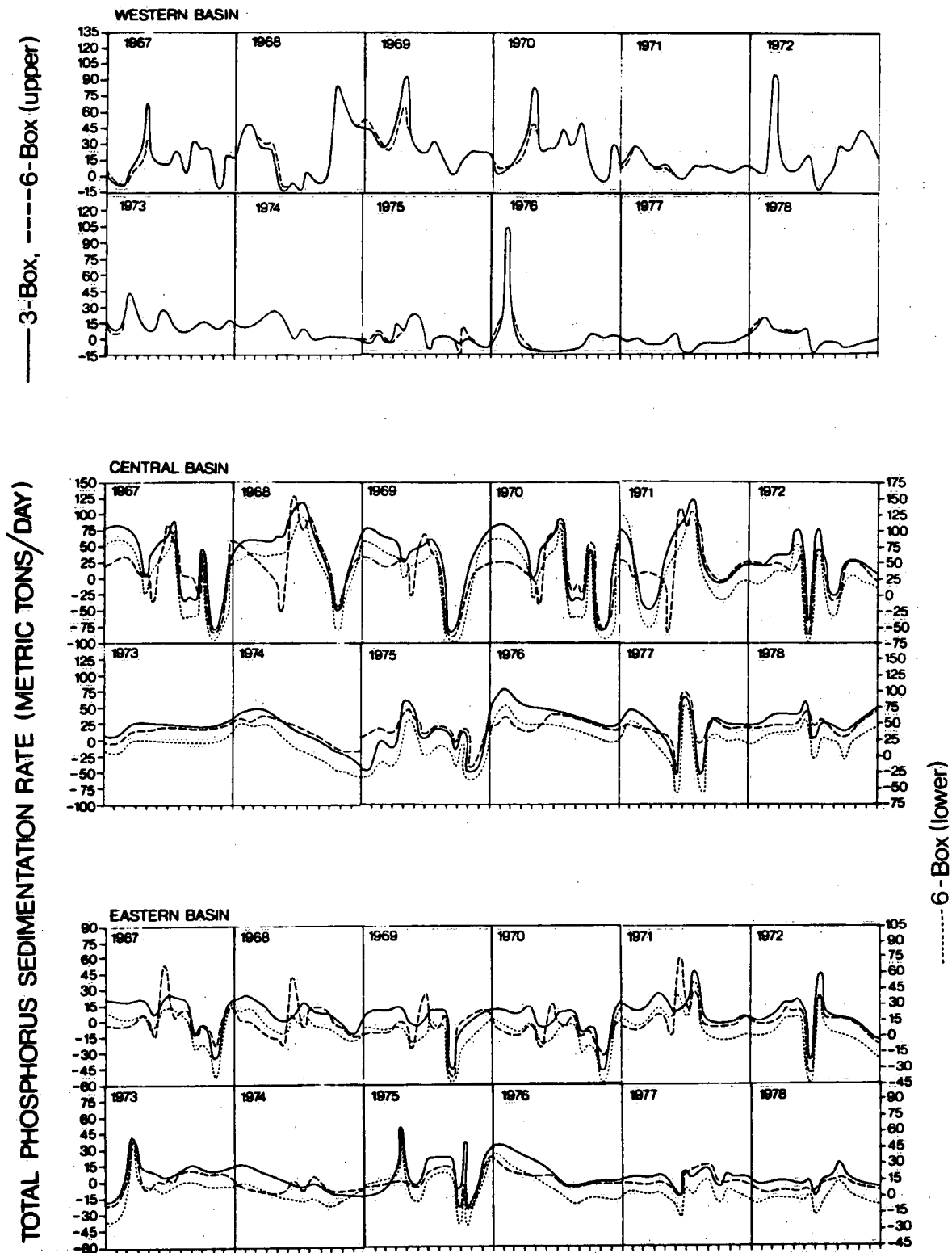


Figure 3.7. Net sedimentation rate of total phosphorus (MT/day) derived from diagnostic mass balances (negative values indicate significant returns from the sediment).

runoff implies that much of the phosphorus entering the West Basin is particulate in nature and is composed of non-available apatite phosphorus and phosphorus associated with clay particles. Such material will sediment out quickly, predominantly in the nearshore regions of the basin.

The Central Basin presents a more complex picture, as shown in Figure 3.7. During the late winter and early spring, the computed net flux of phosphorus towards the sediment is over 50 MT/day. This rate is larger than that of the Western Basin because the Central Basin is larger in volume. When the spring growth period commences, the net sedimentation rate begins to lower as more phosphorus material remains in the water column a result of uptake by phytoplankton. As the algae begin to die, sedimentation rates rise again until late September. If oxygen concentrations are depleted in the hypolimnion the net sedimentation curve swings rapidly to be negative as phosphorus is chemically regenerated to the water column from the sediments. As an example, in 1970, the net sedimentation rate for the Central Basin was -35 MT/day for the duration of the anoxia.

A major effect may be noted in June 1972, when a major storm (Hurricane Agnes) passed through the Great Lakes Basin. The effect on the net sedimentation curve is dramatic, moving from a rate of +80 MT/day to a rate of -80 MT/day and back to +80 MT/day. The storm significantly disrupted the physical structure and chemical mechanisms of the lake for a short duration of about a month. However, the significance of this event is not in the magnitude of the change in the rate, but rather in the effect upon the anoxic condition, so that much of the sediment return seen in Figure 3.7 is not due to chemical regeneration. The paucity of data in 1973, 1974 and 1976 produces rather monotone net sedimentation, which is a falsification due to the time interpolation.

Total phosphorus net sedimentation rates for the Eastern Basin were approximately 20 MT/day throughout most years up to the onset of fall overturn at which point mixing processes overshadow sedimentation, yielding either a balance between settling and sediment return or a negative sedimentation rate in favour of physical resuspension (Fig. 3.7). The hurricane of 1972 also affected the net sedimentation rate in the East Basin, causing large-scale sediment returns over a relatively short time span. In 1973, a flooding episode of the Grand River, Ontario, increased the sedimentation rate for the basin, doubling the average rate to 40 MT/day during March. The rapid increase in sedimentation in the spring is indicative of a particulate load which settles rapidly to the sediments.

3.3.3 Diagnostic results from soluble reactive phosphorus data

Biological considerations of phosphorus uptake can be approached from the relationship between the nutrient soluble reactive phosphorus (SRP) and the biomass indicator chlorophyll a. This relationship between phosphorus concentration and chlorophyll a is central to the discussion of biomass control in Lake Erie (Vollenweider, 1975; 1976; Simons et al., 1979).

During the spring, prior to the advent of any significant sediment effects from either chemical or physical sources, the uptake of SRP by phytoplankton can be seen in the relationship with chlorophyll a (Fig. 3.6). The correlation displays a slope of -2.17, indicating an inverse relationship in the growth curve of chlorophyll a biomass with phosphorus in the ratio SRP:CHL = 2:1. The ratio examined for the correlation was obtained from the three-box model results assessing the Central Basin only. In assessing only the spring period, while the surface waters begin warming, the growth relationship can be considered to represent growth conditions in the epilimnion throughout the lake as a whole.

As the annual cycle proceeds, the rate of change in soluble reactive phosphorus is affected by other factors of source and sink that are not directly related to chlorophyll a biomass growth. Biological uptake and respiration as well as sediment return of SRP may be expressed jointly in terms of phosphorus as a net uptake and regeneration rate B, as given by the following equation (Simons and Lam, 1980)

$$B = I - O - \frac{d[\text{SRP}]}{dt} \quad (3.1)$$

where I is input, O is output and t is time.

The Western Basin shows a strong uptake of phosphorus related to the spring period for the first six years studied, followed by a more uniform pattern in the latter years (Fig. 3.8). In most cases, independent of the spring growth period, phosphorus within the basin is depleted at a rate of between 5 and 10 MT/day. The smoothing of the uptake curve in the latter years of the study is related to the overall decrease in soluble phosphorus concentrations within the basin.

The uptake and regeneration episodes can be identified over the period of study for the Central Basin. In all of the years from January to May, the positive sign of the curve is indicative of biomass uptake at a rate of approximately 20 MT/day of phosphorus (Fig. 3.8). Following the initial uptake phase which, using 1970 as an example, is dominated by diatom species until early May (Munawar and Munawar, 1976), the uptake rate decreases as phosphorus concentrations within the basin tend to increase. This can be seen clearly in the years 1967, 1970, 1971 and 1972. In June the uptake curve increases again as the strong summer growth phase for phytoplankton species dominated by phytoflagellates and diatoms begins. Near the

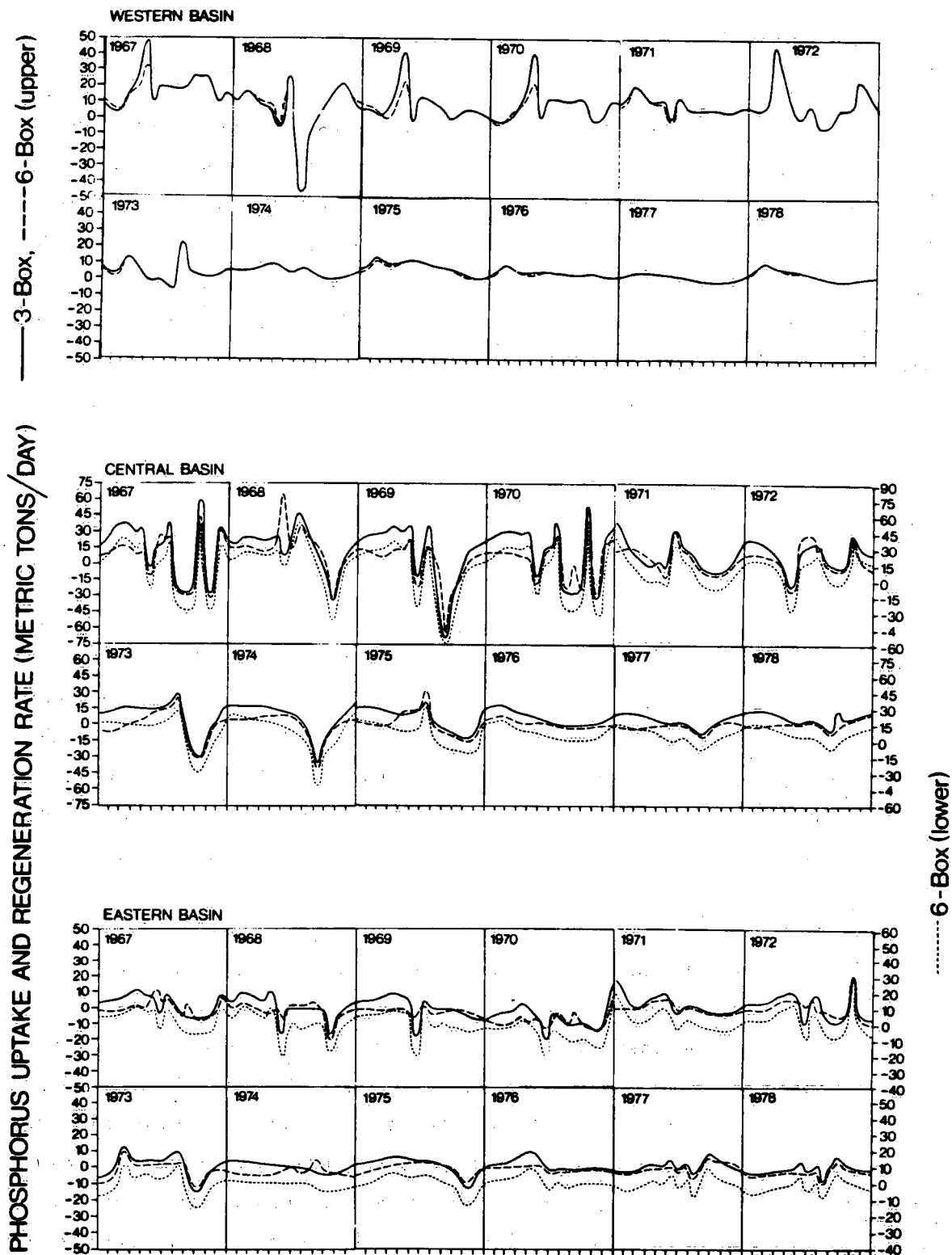


Figure 3.8. Phosphorus uptake and regeneration rate (MT/day) derived from diagnostic mass balances (positive values indicate significant uptake by algae).

end of summer (August to September) for most years, regeneration of soluble phosphorus from the sediments occurs. With low oxygen concentrations in the hypolimnion, the orthophosphate ions in the pore waters remain immobile associated with hydrated ferric oxide (Williams *et al.*, 1976). Under actively reducing conditions of anoxia, metal phosphate complexes are destroyed, liberating orthophosphate ions into the overlying hypolimnion waters. This ion migration is sufficient to represent an internal loading of soluble phosphorus detectable as the negative component presented for the late summer in Fig. 3.8. The magnitude of the release is directly related to the areal severity and duration of hypolimnion anoxia.

The third process which affects the uptake and regeneration curve are storm events, although resuspension of this type is less pronounced than corresponding effects to the total phosphorus component. This becomes evident in examining the 1972 June storm event, which produced very strong resuspension of total phosphorus (Fig. 3.7) and yet had little effect upon the soluble form (Fig. 3.8) indicating the dominance of the particulate fraction in strong physical resuspension episodes.

The Eastern Basin spring uptake rate has been reduced from approximately 10 MT/day to 5 MT/day over the study period with the decrease commencing in 1974 (Fig. 3.8). This is consistent with the reduction in total phosphorus concentrations. Seasonal patterns within the East Basin are reasonably consistent throughout the study period with an increasing uptake rate until June, at which point the uptake rate reduces for a short time prior to the onset of the summer growth period. The change in the uptake rate is again related to phytoplankton species composition for the East Basin in which the spring diatom population is reduced by early June (Munawar and Munawar, 1976). Evidence of fall uptake is noted in the upper layer representation from the six-box results, which is related to the increasing dominance of diatoms in the fall.

3.3.4 Sedimentation coefficient

A sedimentation coefficient (σ) can be computed from the net sedimentation rate (Fig. 3.7) as follows:

$$\sigma = \frac{S_r}{PP} \quad (3.2)$$

where S_r = net sedimentation rate for total phosphorus

PP = mass content of particulate phosphorus.

Particulate phosphorus is an estimate of phytoplankton biomass derived from the organic phosphorus fraction

$$OP = TP - SRP \quad (3.3)$$

By subtracting the inorganic fraction (SRP), total organic phosphorus remains along with a small quantity of unreactive inorganic phosphorus which is considered as being negligible. Total organic phosphorus represents both a particulate and soluble organic fraction. In general, the particulate phosphorus component represents approximately 75% of the total organic fraction with the difference assigned to the soluble organic component.

The coefficient of sedimentation is computed for the Central Basin for the years 1967 to 1978 (Fig. 3.9) in which it is apparent that seasonal cycles closely resemble those determined for the total phosphorus sedimentation curves (Fig. 3.7). An estimate of settling velocity for particulate phosphorus is determined from springtime values as

$$\sigma' = \sigma \cdot \frac{V}{A} \quad (3.4)$$

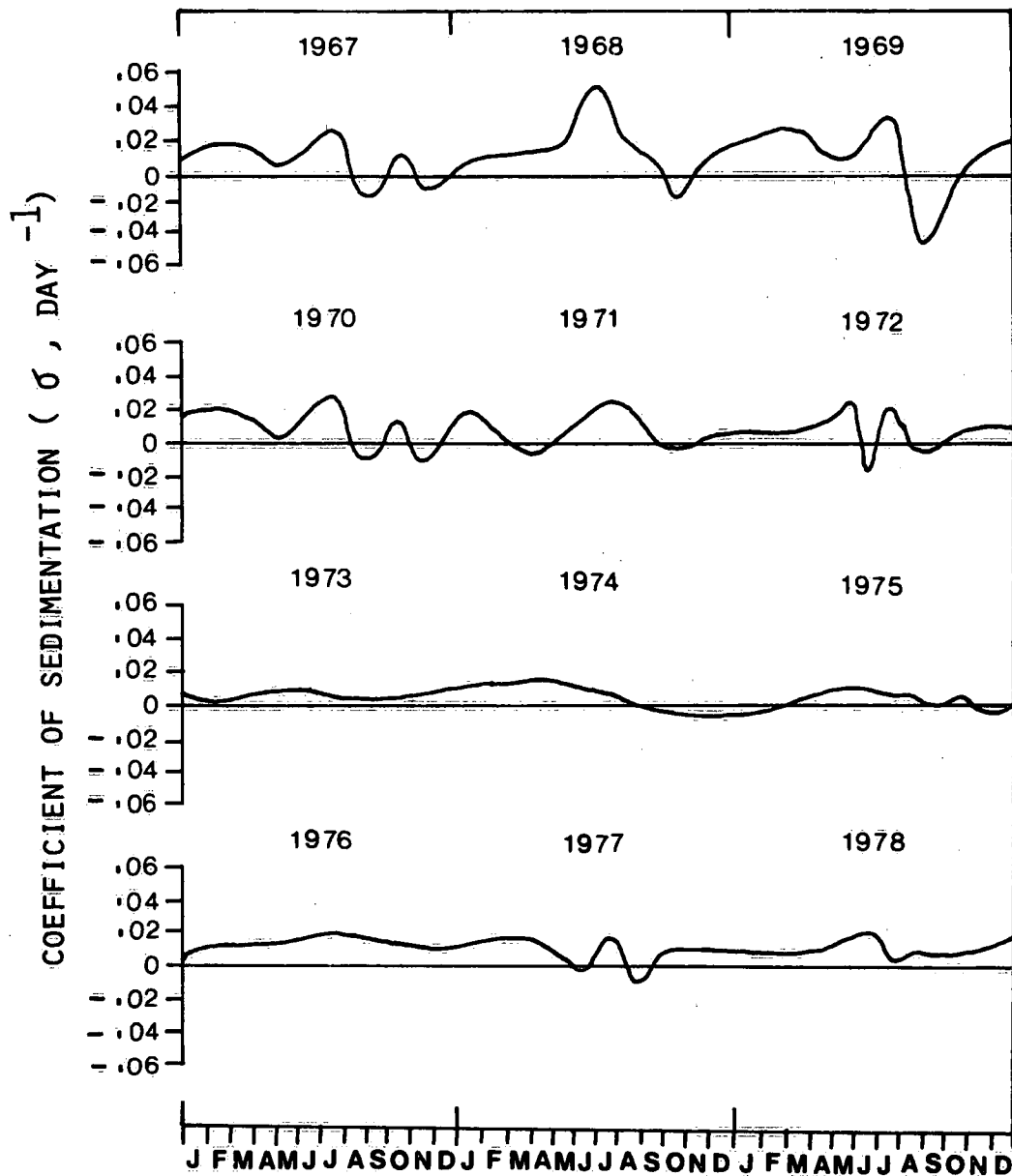


Figure 3.9. Sedimentation coefficient for the Central Basin (1967-1978).

where σ' = settling velocity (m/day)
 σ = sedimentation coefficient (day^{-1})
 V = volume (m^3)
 A = area (m^2).

Estimates for the coefficient of sedimentation (σ) are approximately 0.01 day^{-1} throughout the study period and correspond to a mean settling velocity for the basin of 0.2 m/day (Table 3.5). This average value is in agreement with estimates made for the Lake Ontario epilimnion computed with the Marquardt optimization procedure applied to a two-layer budget model (Simons *et al.*, 1979).

Table 3.5. Spring Values for Sedimentation Coefficient (σ) and Settling Velocity (σ')

Year	σ (day^{-1})	σ' (m/day)
1967	0.013	0.23
1968	0.010	0.18
1969	0.022	0.39
1970	0.011	0.19
1971	0.010	0.18
1972	0.008	0.14
1973	0.005	0.09
1974	0.013	0.23
1975	0.009	0.16
1976	0.011	0.19
1977	0.013	0.23
1978	0.012	0.21

In comparison, an annual averaged settling velocity of 0.11 m/day has been made for the Lake Erie Central Basin using data from 1970 (Burns, 1976a). The difference between the two estimates is due to the consideration in this study of the spring period only, and therefore the present value does not include summer regeneration events which would have the effect of lowering the estimate.

The largest deviations from the average settling velocity occurred in 1969 and 1973. These two years had sparse data sets covering the spring period and hence a larger deviation can be expected in these two years. The settling velocity can be used in this study as a check upon the loading estimate accuracy relative to the behaviour of the models. If the estimated load of total phosphorus was significantly different from the actual load, this would be reflected by proportionate deviations in σ' , i.e., if the estimate of load was high, σ' would be correspondingly higher than the mean. As can be seen from Table 3.5, the loading estimates may be considered reasonable.

To this point, emphasis has been placed upon the five major variables concerned with the study of eutrophication in Lake Erie: temperature, total phosphorus, soluble reactive phosphorus, dissolved oxygen, and chlorophyll a. The interdependence and interaction between these variables will be explored in detail later. Although consideration of the nitrogen forms (nitrate, nitrite and ammonia) has been made, these variables have been de-emphasized due to the requirement for additional evaluation and a more quantitative understanding of the dynamic interactions associated with them. This area is the subject of forthcoming research on the water quality problems of Lake Erie related to eutrophication.

Physical Data Base

4.1 Introduction

Several organizations within Canada and the United States are responsible for providing basic data pertinent to the Great Lakes and surrounding basin. A summary of supervisory agencies has been given in Section 2.1. Observation networks consist of a limited number of synoptic stations which provide hourly data. Other specialized stations provided periodic or seasonal observations ranging from three-hourly, daily or monthly averages. All the physical data are formed into daily observations by appropriate averaging or interpolation for the period from 1967 to 1978.

During this period, a total of 62 lake-wide surveys of physical variables were used, most of which also involved chemical measurements, as given in Table 3.2. The measurements were conducted primarily between the months of April and November corresponding to periods of lake stratification. The frequency of the surveys varied from a minimum of two to a maximum of eight per year. In general, the station density was of the order $1:400 \text{ km}^2$. Ship data were used in this analysis for approximation of water surface temperature, vertically integrated water temperature and mean vertical extinction coefficient. The extensive limnological data used in this report permit a more detailed analysis of Lake Erie and its basins. Previous studies were limited to few observations and reliance on water intake temperatures as predictors of lake temperature and heat content (Millar, 1952; Powers et al., 1959; Derecki, 1975).

Meteorological observations from land-based stations at the periphery of the lake (Fig. 4.1) were used to approximate over-lake

meteorological and radiation fields. There is a paucity of meteorological observations at close proximity to the lake on the Canadian shoreline. One consequence of this problem is the possible bias of lake-wide and basin averages to values along the southern shoreline. Mean daily observations of air temperature, dewpoint temperature, wind speed and direction, and sunshine duration were readily available from these stations within the 1967-78 period. Data from the lake-exposed stations Pelee Island and Long Point are particularly relevant to this study, especially for the computation of basin mass exchanges.

Meteorological buoy observations were not available for most of the study period except in the years 1977-78. Figure 4.1 shows the location of a meteorological buoy used to represent open-lake conditions. Meteorological data from the buoy have not been incorporated within the model framework, but are used for independent verification of computed over-lake meteorological fields.

Current meter measurements at the Pennsylvania Ridge in 1977-78 (Boyce et al., 1980; Chiocchio, 1981) formed the basis for basin transport computation for the mass balance models and for verification of model parameters.

4.2 Physical Data

The physical data described in this chapter are:

- (a) Water temperature,
- (b) Air temperature and vapour pressure gradients,
- (c) Wind speed,
- (d) Lake inflow and outflow,
- (e) Water level,
- (f) Mean vertical extinction coefficient,

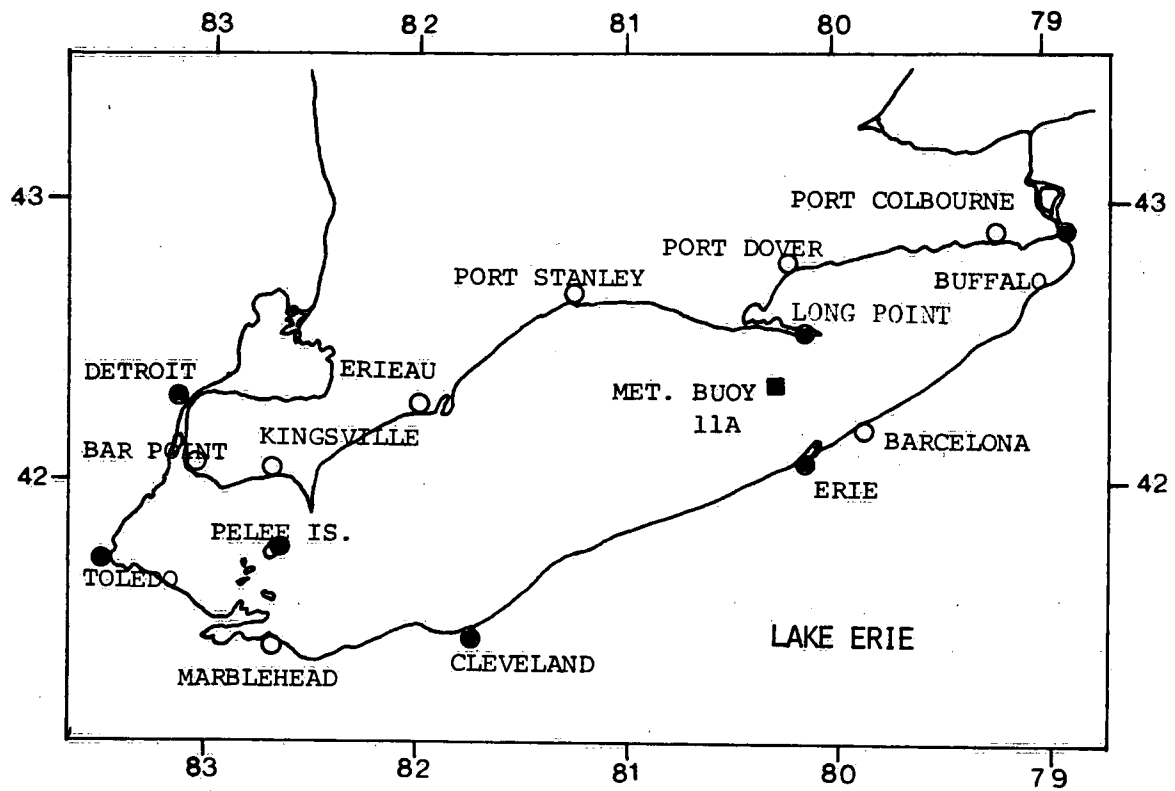


Figure 4.1. Location of meteorological stations (●), water level recording stations (○) and meteorological buoy (■).

- (g) Light for primary production, and
- (h) Heat content.

4.2.1 Water temperature

Water temperature at the surface and at depth was measured at a grid of stations over Lake Erie during the 62 cruises for the period 1967-78. Observations from electronic bathythermograph (EBT) and fixed temperature profilers (FTP) were digitized at CCIW and processed to derive estimates of water surface temperature and vertically integrated temperature. By interpolation techniques, similar to the Theisson polygon approach, lake-wide and basin temperature estimates were derived. Additional observations of water surface temperature were given by monthly ART surveys (AES, 1967-1978).

A composite of all cruise values of water temperature collected over the study period is given in Fig. 4.2. These graphs indicate a uniform and predictable water temperature increase for all basins during the heating season. However, the greatest variability in seasonal values occurs at maximum temperature and in the cooling season. The long-term data indicate temperature variation in the range of 2°C to 3°C.

Estimates of daily water temperatures utilized in this investigation were derived by recourse to two approaches. Under conditions of sufficient survey measurements and availability of ART observations, interpolation through these data would provide the best estimate of current year water temperatures. Water intake temperatures were not used. For the years in which cruise data were sparse, available data and ART values were supplemented by reference to long-term water temperature values. These were derived by polynomial fit through cruise data, over the study interval 1967 to 1978.

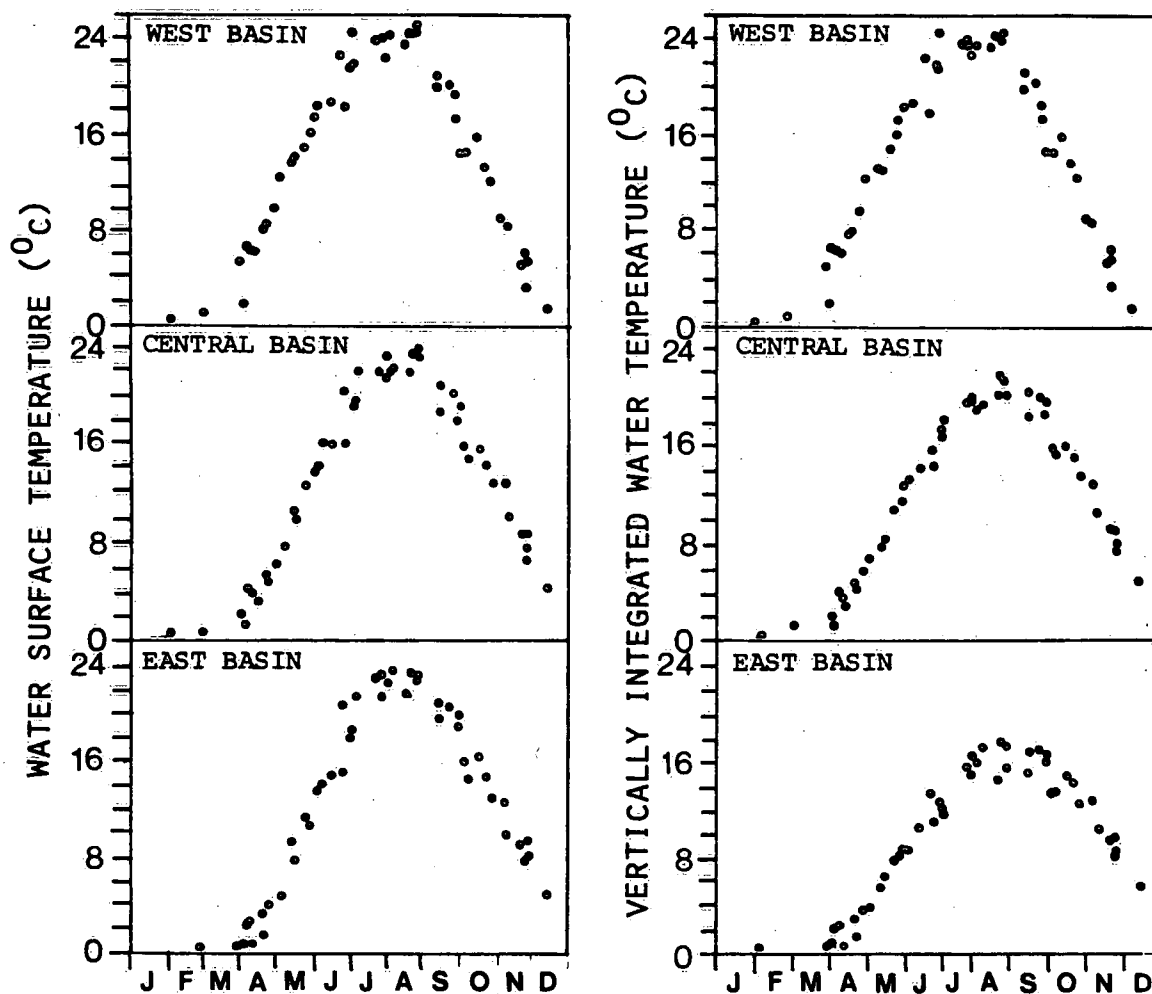


Figure 4.2. (Left) Basin surface water temperature and (right) vertically integrated water temperature averages computed from CCIW surveys in the period 1967 to 1978.

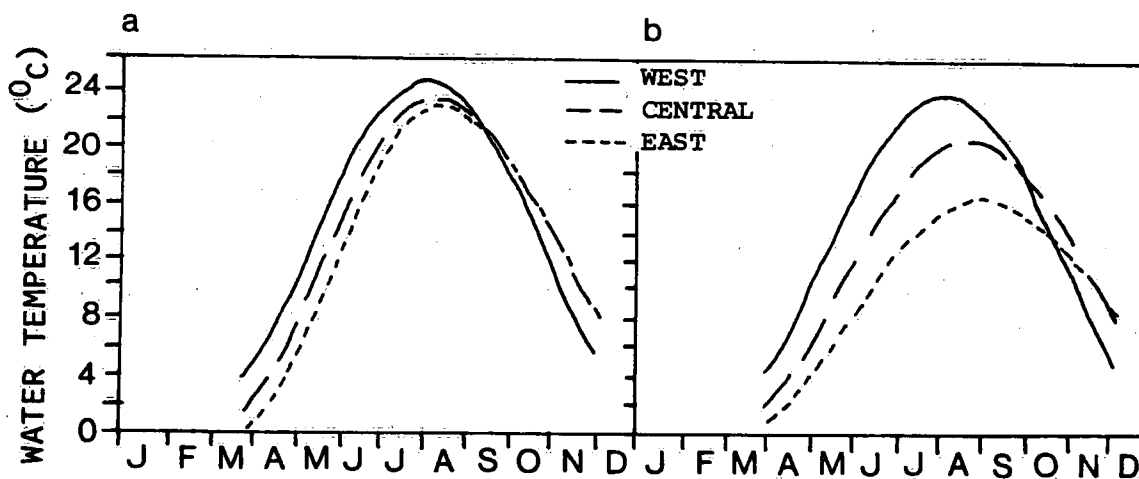


Figure 4.3. Polynomial fit to Lake Erie Basin (a) water surface temperature and (b) vertically integrated water temperature for the period 1967 to 1978.

Polynomial fit through the cruise data for basin and lake-wide cases is given in Fig. 4.3b. These curves clearly illustrate seasonal lags in the mean temperature and are related primarily to the heat storage capacity of each basin. The Western Basin is the shallowest basin and heats to maximum temperature at a faster rate than the other Lake Erie basins and cools at a higher rate due to the more efficient wind-induced mixing in the fall. The deeper Eastern Basin lags the Central Basin in the heating season but retains its heat in storage for longer periods during the cooling phase. Comparison of the surface water temperature and vertically integrated temperature for the Western Basin reveals nearly identical values, and hence demonstrates vertically mixed conditions throughout most of the year. Comparisons for other basins show substantial differences.

Large lakes have a tendency to moderate meteorological conditions over them and also over adjacent land areas. Through air-water interaction, air temperatures, winds and humidities are modified as the water acts as a heat source or sink. Since the water temperature varies substantially between basins, the implication is that Lake Erie cannot be treated uniformly. This has been demonstrated in terms of the bathymetry and also in terms of the thermal regime. The advantage of the present investigation is the availability of detailed data to account for such basin differences.

An indication of the variability of water temperature values is given by examining the scatter of values about the cruise data (Fig. 4.2). On the basis of these data, the expected error in water temperature estimate is in the range of $\pm 1.5^{\circ}\text{C}$. Absolute values of daily temperature departures from the mean may be much larger for shorter periods of time depending on the prevailing meteorological conditions.

4.2.2 Air temperature and vapour pressure gradients

Air temperature and vapour pressure are used in the computation of the lake energy balance. Daily values were observed at stations at the lake periphery, and as indicated previously, measurements may be biased to the southern shoreline (Fig. 4.1). Basin averages are determined as arithmetic means from station data nearest the basin boundaries.

Daily air temperature averages from shoreline stations were adjusted to over-lake conditions, according to Rodgers and Anderson (1961)

$$T_a = 0.25 T_L + 0.75 T_s \quad (4.1)$$

where $T_L(^{\circ}\text{C})$ is air temperature measured on land and $T_s(^{\circ}\text{C})$ is water surface temperature. Saturation vapour pressure (e_s) is determined by using the estimated water surface temperature ($T_s^{\circ}\text{C}$) (Dilley, 1968)

$$e_s = 6.1073 \exp \left[(17.269 \cdot T_s) / (T_s + 237.3) \right] \quad (4.2)$$

Ambient vapour pressure (e_a) was determined from daily estimates of dewpoint temperature at the lake perimeter. Over-lake vapour pressure was determined by applying lake/land corrections (Richards and Fortin, 1962). Figures 4.4a to c show summaries of the long-term air temperature, stability and vapour pressure values expressed as monthly means, respectively.

Air-water temperature difference is an indicator of atmospheric stability over the water surface. Fig. 4.4b summarizes the long-term average monthly stability conditions for Lake Erie.

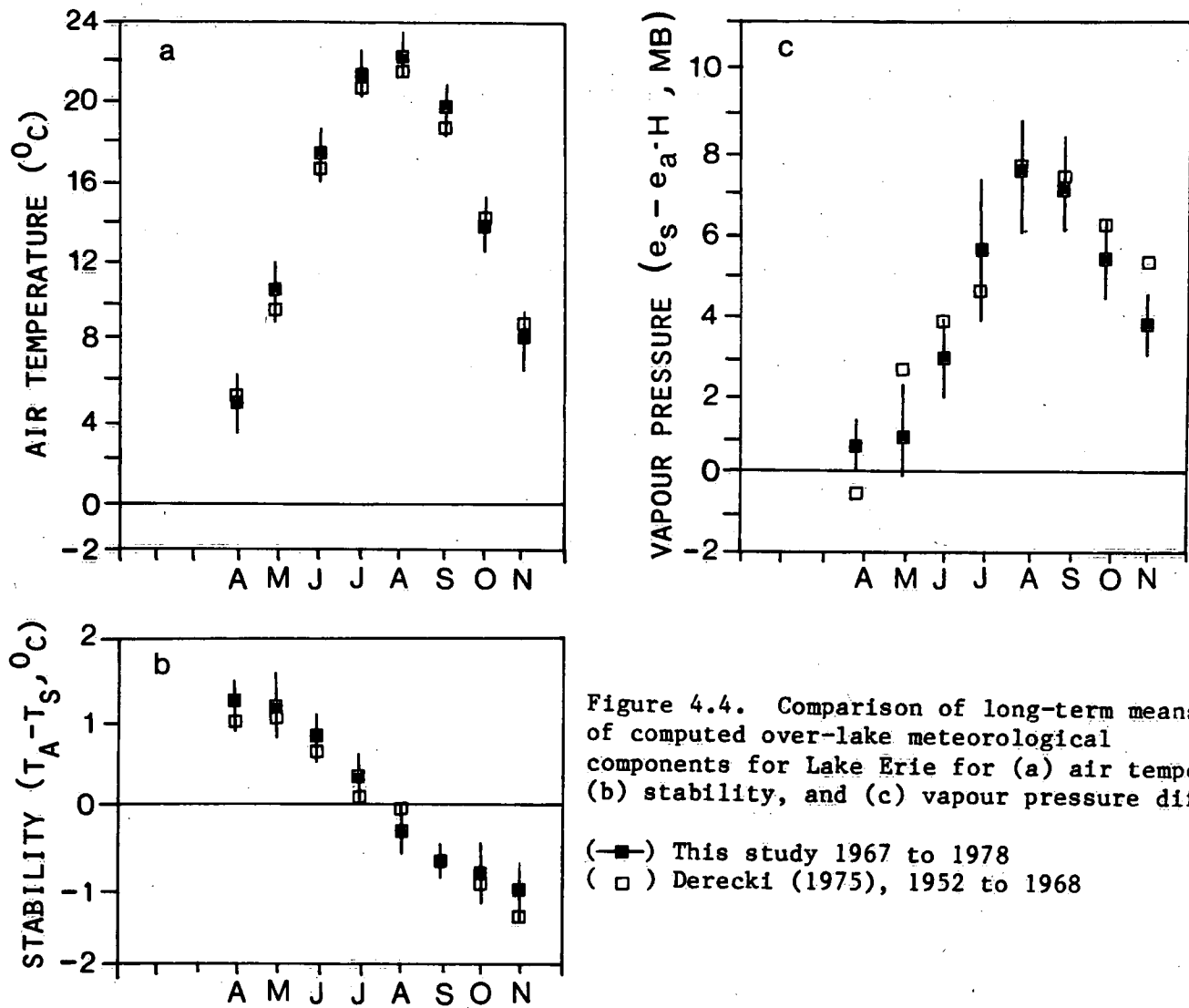


Figure 4.4. Comparison of long-term means of computed over-lake meteorological components for Lake Erie for (a) air temperature, (b) stability, and (c) vapour pressure difference.

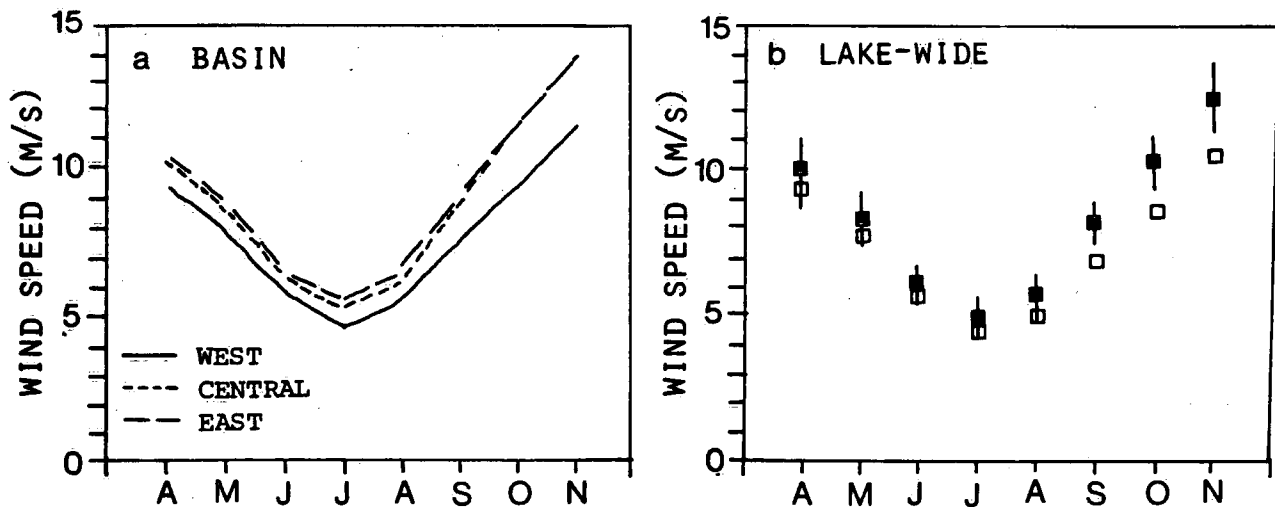


Figure 4.5. Comparison of long-term monthly mean over-lake wind speed for Lake Erie basins and lake-wide case (—■—) This study 1967 to 1978; (□) Derecki (1975), 1952 to 1968.

Under stable conditions, the air is warmer than the water surface, and the wind speed and evaporation tend to be lower. On the other hand, unstable conditions persist when the air is cooler than the water surface and the magnitude of such processes mentioned above tends to increase. As indicated, stable conditions tend to prevail in the period March to mid-July and unstable conditions exist for the rest of the year. Comparison with other long-term data (Derecki, 1975) shows good agreement.

Vapour pressure gradient is illustrated in Fig. 4.4c for long-term monthly means and standard deviation about the monthly means. For most months, comparison with other long-term data (Derecki, 1975) is reasonable. The comparison for spring and fall values is less impressive. As indicated previously, the present analysis utilized additional station data which were located at the lake periphery. Derecki (1975) reported that the lowest vapour pressures of the air occurred at London, Ontario, and this was probably due to its location farther from the lake, which eliminates possible lake effects. In this study, the London data were not used. Comparison of the present computations with mid-lake buoy data indicates acceptable results (Subsection 4.2.4).

Vapour pressure derived from land-based stations at the periphery of the lake is modified to represent over-lake conditions by adjustment coefficients (Richards and Fortin, 1962) or by regression techniques (Phillips and Irbe, 1978). The former technique was used in this analysis. The humidity ratio H is defined as $H = e_{ab}/e_{al}$ where e_{ab} is humidity over the lake surface and e_{al} is humidity over the land. Richards and Fortin (1962) used 525 matched ship and land observations to derive average humidity ratios. Observations for this analysis were derived from Lakes Huron, Ontario, Superior and Erie. The mean value of the ratios was 1.14 reduced seasonally to 1.13 and 1.15, respectively, for spring and summer.

Table 4.1 Comparison of Monthly Lake/Land Humidity Ratios

Richards and Fortin (1962)		Buoy data (1977)			This study
		H _C	H _E	Mean	
A	1.14	--	--	--	1.14
M	0.86	1.09	1.28	1.14	1.11
J	0.94	1.06	1.17	1.09	1.09
J	1.09	1.06	1.13	1.08	1.09
A	1.09	1.00	1.04	1.01	1.09
S	1.11	1.00	1.05	1.01	1.11
O	1.15	--	--	--	1.15
N	1.15	--	--	--	1.15

H_C = Humidity ratio computed using Buoy 11A and Central Basin average land-based vapour pressure.

H_E = Humidity ratio computed using Buoy 11A and Eastern Basin average land-based vapour pressure.

Table 4.1 presents a comparison of humidity ratios which are computed using average land-based values in 1977 and data from 1977 buoy records, with values of Richards and Fortin (1962). It shows a number of departures from the monthly estimates given by Richards and Fortin (1962). The most significant difference is that values in May and June are greater than 1.0, implying that for Lake Erie in 1977 over-water humidity at the buoy location was greater than average over-land humidity. Due to the tentative nature of these results only the values of ratios in May and June from Richards and Fortin (1962) are altered to reflect the buoy results. This has implications for evaporation and heat balance computations discussed further in the report (Subsection 5.2.3).

4.2.3 Wind speed

Winds constitute a principal force for driving Lake Erie currents (Simons, 1976a), for providing energy for lake setup (Hamblin, 1979) and for providing a mechanism for heat dissipation and mass transfer from the lake surface. Lake Erie is particularly susceptible to large-scale water level motions in response to wind events for the following reasons. The lake is relatively shallow and presents its long-axis along the direction of the prevailing winds which occur from the southwest quadrant for most of the year (Phillips and McCulloch, 1972). In addition, Lake Erie has records of the highest monthly wind speeds around the lake. Significant shoreline damage can occur in these circumstances, and the energy is sufficient in cases of high wind storms to perturb existing stratification in the Central Basin and to influence the interbasin transports (Boyce et al., 1980).

As indicated previously, wind speed was observed at meteorological stations at the periphery of the lake (Fig. 4.1). Hourly and three-hourly station data were formed into daily means. Land-based

averages were adjusted to over-lake conditions by application of lake/land wind ratios (R) determined by Lamire (1961) (Table 5.2). Basin wind speed averages were formed as arithmetic means of data from stations nearest to the basin boundaries.

Figures 4.5a and b show monthly mean wind speed for basin and lake-wide cases. In all basins minimum wind speed occurs in the summer months. Differences between Central and Eastern Basin monthly mean wind speed are small. However, the Western Basin experiences values averaging 0.5 to 2.0 cm/s lower. This implies a sheltering effect due to the surrounding land mass which is not evident in the other basins which have longer fetches. Variability of the monthly mean wind speed is shown for the lake-wide case in Fig. 4.5b. The greatest variation in wind speeds occurs in the spring and fall months.

A comparison of long-term monthly mean lake-wide wind speeds (Fig. 4.5b) with those derived by Derecki (1975) shows generally higher values in this study. The greatest departures occur in the fall months. Several factors contribute to these differences. Derecki (1975) adjusted wind speed measurements from stations at the periphery of the lake to a common height which modified observed wind speeds lower by approximately 10%. In addition, Derecki's computations were based on data from Buffalo, Cleveland, Toledo and London. In this study, London data are not considered representative of lake perimeter conditions, and the present investigation incorporated additional observations from presently available lake exposed stations, Pelee Island and Long Point, which tended to have higher wind speeds.

4.2.4 Comparison of meteorological data and buoy values

One major problem with computation of over-lake meteorological fields is the paucity of lake data for verification of computed

values. In the present study, buoy data for the period May to September 1977 are processed and are compared with calculated values from stations at the lake perimeter.

Figure 4.1 shows Buoy 11A located on the boundary between the Central and Eastern basins. This is a complex area of interchanging water masses (Boyce et al., 1980; Chioocchio, 1981) and the overlying air would be expected to be affected by changes occurring at the air-water interface. The buoy meteorological data are digital, and were recorded on magnetic cassette at 10-minute intervals and processed at CCIW. Data were formed into monthly means for comparison purposes.

Figures 4.6a, b and c show monthly mean temperature difference, vapour pressure difference and wind speed from the buoy data compared with Central Basin averages. The dashed lines represent standard deviation about the monthly mean Central Basin values. The comparison is reasonable, as both model and buoy values show similar seasonal trend and monthly variability.

4.2.5 Lake inflow and outflow

Detailed analysis of Lake Erie water balance components was conducted by Derecki (1975) in which it was determined that inflow and outflow volumes have a pronounced effect on Lake Erie hydrology. Inflow from the Detroit River is an order of magnitude greater than other components such as precipitation or runoff. On an annual basis, a 1% change in inflow or outflow produces approximately an 8% change in the evaporation, respectively.

Figure 4.1 illustrates locations of the stations at which basic inflows are determined. These data are coordinated by the Coordinating Committee on Great Lakes Basic Hydraulic and Hydrologic Data and are used in this analysis. Figure 4.7a summarizes average Lake

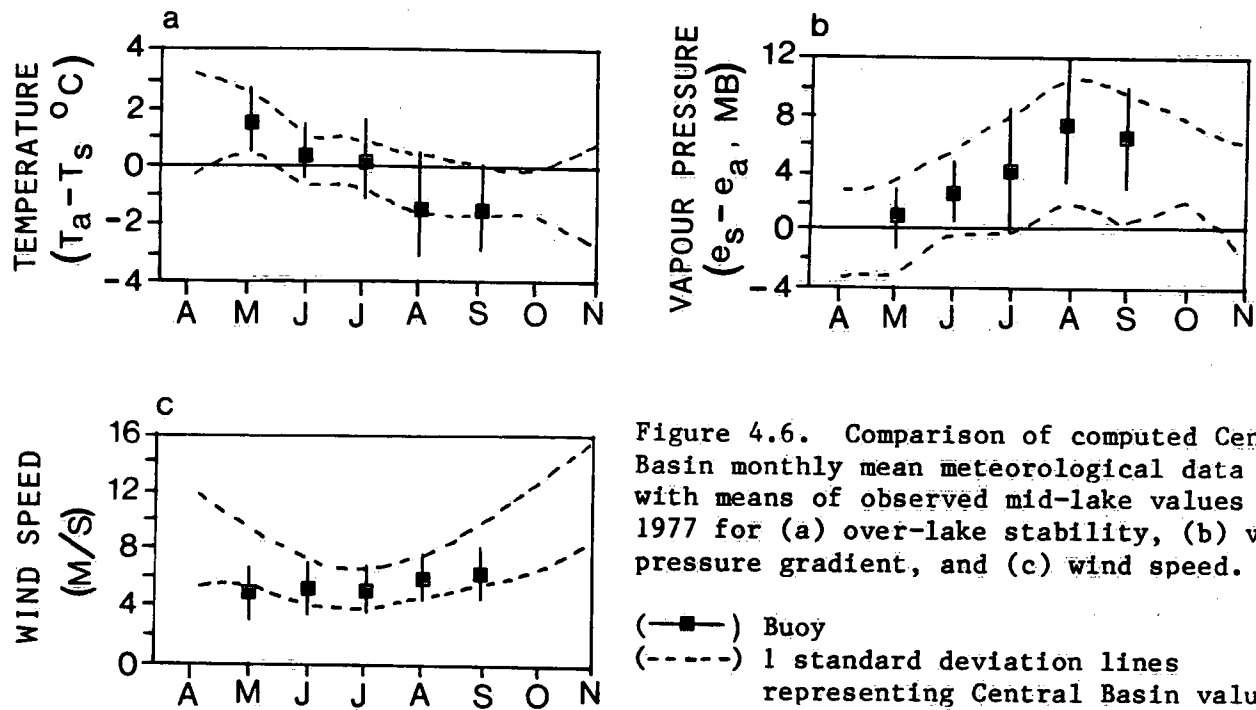


Figure 4.6. Comparison of computed Central Basin monthly mean meteorological data with means of observed mid-lake values for 1977 for (a) over-lake stability, (b) vapour pressure gradient, and (c) wind speed.

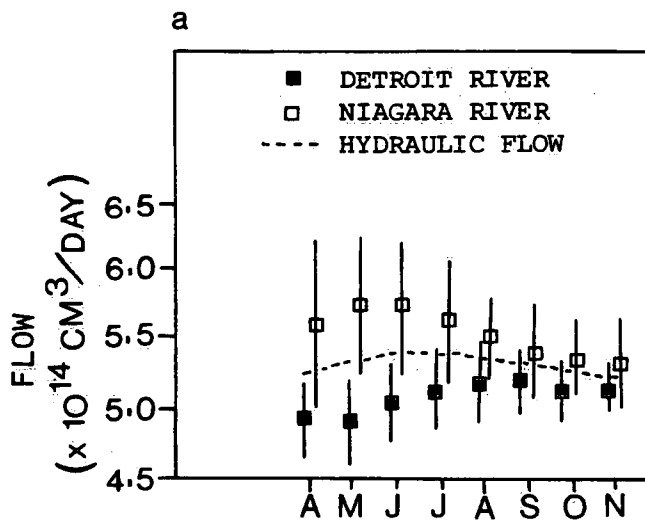
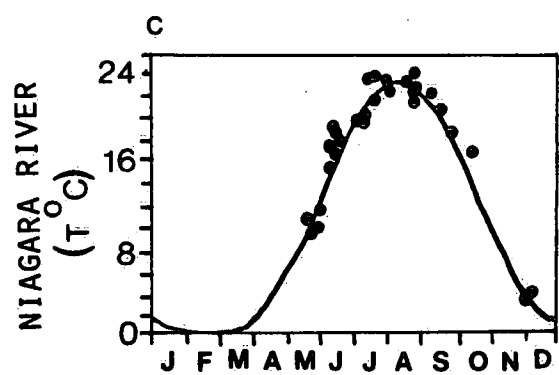
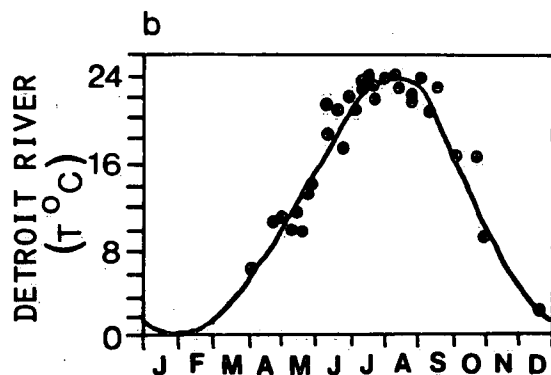


Figure 4.7. Detroit River and Niagara River inflow and outflow volumes and estimation of average river water temperatures for 1967 to 1978: (a) Detroit and Niagara River flow rates; (b) Detroit River temperature; (c) Niagara River temperature.



Erie inflow and outflow volumes for the period 1967-78 expressed as monthly means. As indicated, Detroit River inflows show a maximum in the summer months in response to the supply from sources outside its drainage basin. Niagara River outflows show a peak discharge occurring in spring and early summer months as a consequence of basin runoff. Discharge rates for the Detroit and Niagara rivers which correspond to the stratification periods over the period 1967-78 average 5.07×10^{14} and 5.52×10^{14} cm³/day, respectively. The Detroit River inflow averages approximately 90% of the Lake Erie outflow through the Niagara River. Variations about the monthly means for the Niagara River are nearly twice as large as those observed on the Detroit River. For purposes of mass balance models discussed later in the report, the average hydraulic flow is computed and represents the average of inflow and outflow volumes (Fig. 4.7a).

Average water temperatures and transects along the Detroit River and Niagara River in the period 1967-1978 were measured by the Michigan Department of Natural Resources (MDNR) and by the Ontario Ministry of the Environment (MOE). Discussion relating to the measurement and averaging techniques used for these and other measurements across the river transects is given in Fraser and Willson (1981). Available data for all of the years are given in Figures 4.7b and c. Polynomial fit through these data represents an estimate of the river temperature for computations involving heat inflow and outflow from Lake Erie.

4.2.6 Water level

Water level fluctuations are the result of lake volume changes. On Lake Erie, daily water level measurements are conducted at 12 shoreline stations (Fig. 4.1). These data are collected by MOE in Canada and the NOAA Lake Survey Center in the United States. For purposes of this investigation, reported monthly means from

observation stations were averaged and referenced to the midpoint of the month. Interpolation through the monthly means is used to represent mean lake level fluctuations. The plane of reference for Great Lakes water levels was established in 1955 and is called the International Great Lakes Datum (IGLD). The mean elevation according to the IGLD for Lake Erie is 173.31 m above sea level.

Figure 4.8 shows interpolated water levels for Lake Erie from 1967-78. The water level undergoes a seasonal cycle in which higher levels occur in the summer months and low values are prevalent in winter. The lowest water levels occurred in 1967, and high water years with average summer values greater than 174.5 m above sea level occurred in 1973 to 1976 inclusive. Mean daily water level changes are small. Average monthly water level changes are in the range of a few centimetres. On an annual basis, changes in water levels are relatively small due to the cyclic nature of the hydrological factors, but the amplitude of annual variations can be large. Large annual water level variations occurred in the years 1969, 1972, 1973, 1974, 1976 and 1977, the difference between maximum and minimum levels averaging approximately 0.5 m.

Digital bathymetry of Lake Erie was determined by Robertson and Jordan (1978) based on IGLD levels. Hypsometric functions were derived to approximate these values (Fig. 1.3). On the basis of these functions, hypsometric parameters for Lake Erie basins could be derived and extended to incorporate changes due to water level fluctuations.

4.2.7 Mean vertical extinction coefficient

The penetration of solar radiation into the water column is assumed to decay exponentially with depth at a rate dependent on the water transparency. On Lake Erie, Secchi disc (30-cm diameter) and

transmissometer data were collected on 67 cruises for the period 1967-78. In this analysis, Secchi disc values were used as the basis for the estimation of mean vertical extinction coefficient ϵ in the wavelength band 400 to 700 nm.

Details of the procedure for determining ϵ are given (Simons et al., 1979; Schertzer et al., 1978). In general, the diminution of light intensity between the surface and some depth follows the Beers=Lambert law. Spectrometer data which are measurements of irradiance are used directly to estimate ϵ for specific station locations (Vollenweider, 1955)

$$\epsilon = \frac{1}{n} \sum_{i=1}^n \left[\frac{1}{m} (\ln I_o - \ln I_z) \right]_i \quad (4.3)$$

where n denotes the number of successive layers of observations with depth. Extinction coefficients derived from spectrometer measurements were then regressed with inverse Secchi observations. Regressions formed from observations at corresponding locations in the period August to October 1975 (Jerome, personal communication) were used to derive the following

$$\epsilon = 0.97 (1/S) + 0.15 \quad n = 26 \text{ cruises} \quad (4.4) \\ r = 0.93$$

Using this regression relationship, ϵ was estimated for each basin and cruise 1967-78. A linear interpolation between cruise data for each year provided daily approximations of the mean vertical extinction coefficient. For the years with limited cruise data, subjective interpolation using long-term means was initiated.

Figure 4.9 is a composite of ϵ for the period 1967-78. Cruise means are plotted at the midpoint of the survey period which

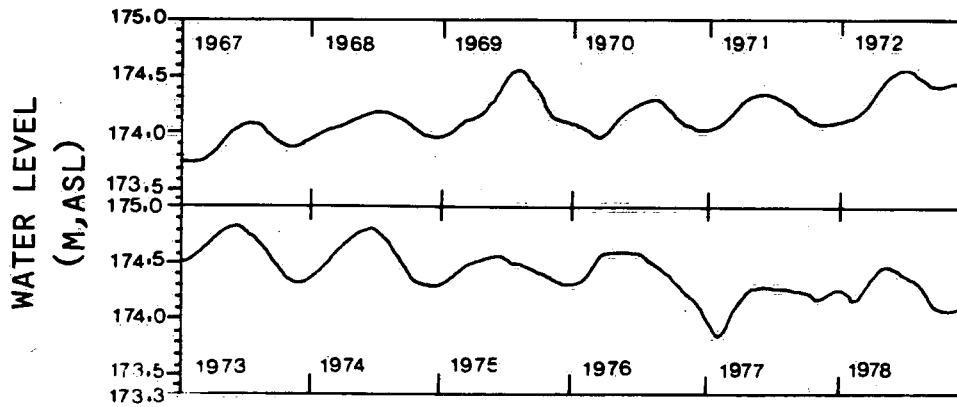


Figure 4.8. Lake Erie water level approximation.

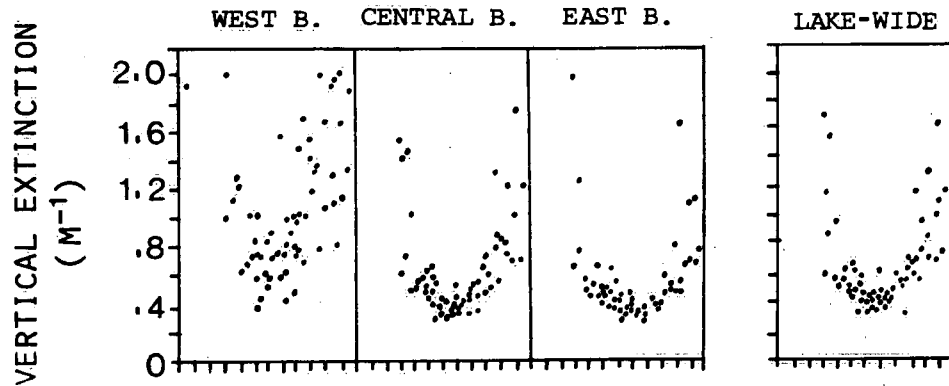


Figure 4.9. Lake Erie mean vertical extinction coefficient based on CCIW surveys in the period 1967 to 1978.

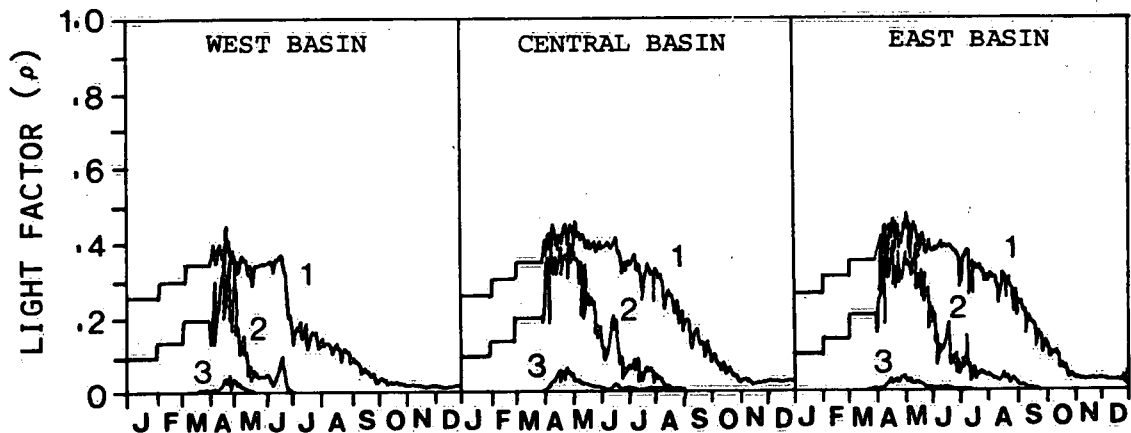


Figure 4.10. Light factor computed for Lake Erie basins for the (1) epilimnion; (2) mesolimnion; (3) hypolimnion layers for 1967.

usually lasted one to two weeks. The general trend for all basins is high extinction values in spring and fall months with a minimum occurring in the summer. The turbid nature of the Western Basin is quite evident, as indicated by the wide scatter of values.

4.2.8 Light and primary production

Surface radiation fluxes and extinction coefficients can be combined to estimate radiation as a function of depth. In turn, the radiation must be related to the optimum light intensity for phytoplankton growth. Effects of light on photosynthesis have been reviewed by Vollenweider (1970) and Platt *et al.* (1975). A convenient formula was suggested by Steele (1965), namely, $r = R \exp (1-R)$ where r is the relative photosynthesis and R is the solar radiation in the photosynthetic wavelength band expressed as a fraction of the saturation light intensity. In a homogeneous layer of water, the light intensity decreases with depth as $R = R_t \exp (-\epsilon Z)$ where R_t is the incident radiation at the top of the layer and ϵ is the extinction coefficient. Thus, Steele's function can be integrated immediately to give the depth-averaged light factor

$$\rho = \frac{1}{\epsilon \delta} (e^{1-R_b} - e^{1-R_t}) \quad (4.5)$$

where R_b is the radiation passing through the bottom of the layer and δ is the layer thickness.

The light factor, ρ , which will be directly incorporated in the photosynthesis formula (Table 6.2), was computed at hourly intervals from the Lake Erie data base and then averaged over each day. It was estimated that 6% of the incoming radiation is reflected and that 48% of the net radiation is contained in the photosynthetically active 400- to 700-nm band. The saturation light intensity, referred to this

band, was taken to be $4.75 \text{ cal/cm}^2/\text{m}$ by recourse to the light effect curves presented by Stadelmann et al. (1974). Figure 4.10 gives an example of the light factor p for the epilimnion, mesolimnion and hypolimnion layers.

4.2.9 Heat content

During the period 1967-78, a total of 62 temperature surveys were conducted at specific locations in Lake Erie at which vertical temperature profiles were derived by electronic bathythermograph. Using a nine-point digitization scheme and interpolation techniques, these data were processed to derive average temperatures for each 1-m layer from the lake surface and heat content. Heat content was derived for basin and lake-wide cases for each cruise period. A plot of all derived heat content over the study period is given in Figures 4.11 and 4.12, for the lake-wide and basin cases.

The greatest variability in the heat content is at the period of maximum heat content and in the cooling phase of the lake, as in the case of water temperature discussed previously. Variation of the lake and basin heat content from year to year is related to the interaction of various climatic and hydrological factors with heating and cooling processes in the lake. Meteorological factors contribute to the deepening of the surface layer, while hydrological processes cause temperature changes by horizontal movement of water. These factors do not operate uniformly on the lake from year to year and hence, detailed analysis (see Section 5.2) of surface heat flux is necessary for evaluation of the depth of the mixed layer.

Polynomial fit through the cruise data was conducted in an effort to generalize the relationship between basins. The results are given in Fig. 4.11. The largest range between maximum and minimum heat content occurs in the Central Basin and is attributable to its

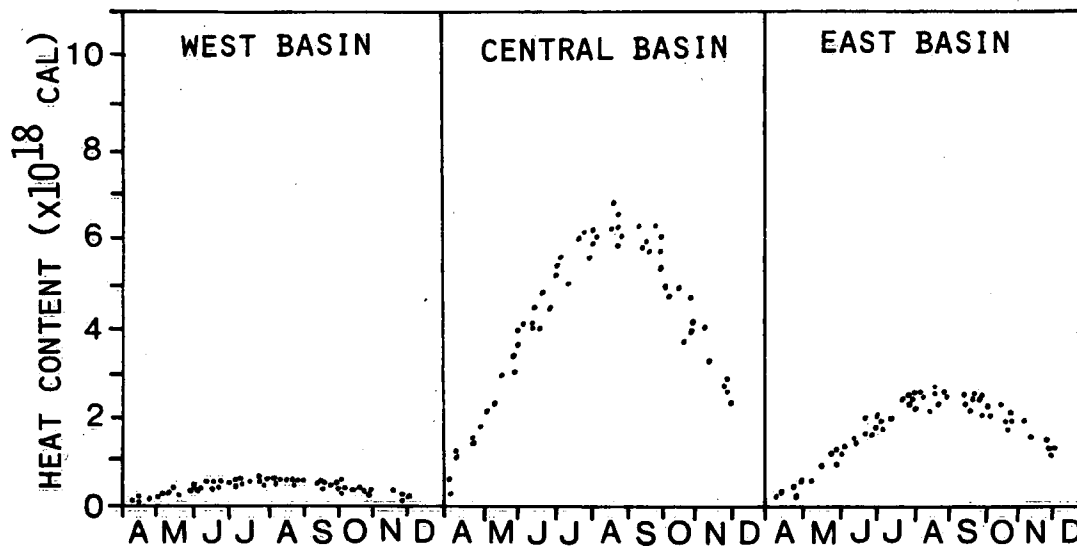


Figure 4.11. Lake Erie basin heat content based on CCIW water temperature surveys in the period 1967 to 1978.

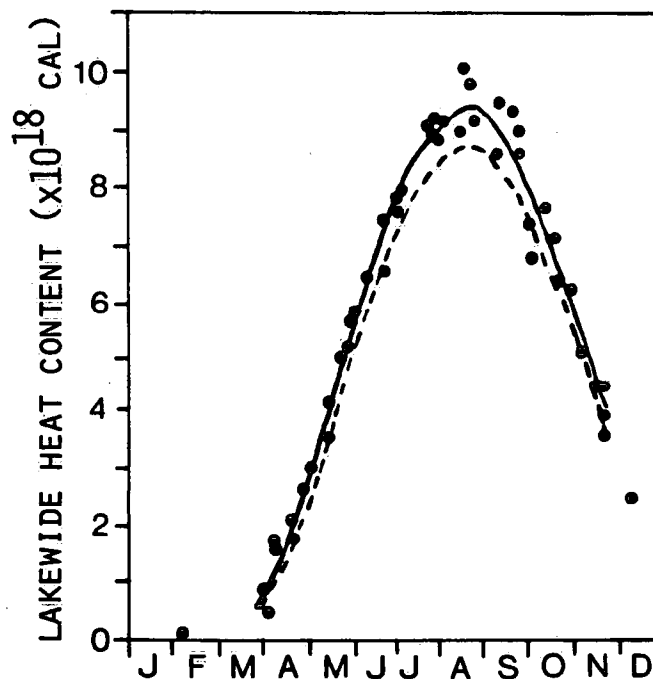


Figure 4.12. Lake Erie lake-wide heat content from CCIW water temperature surveys from 1967 to 1978 (●), and comparison of mean values derived from this study (—) with those of Derecki (1975) (- - - -) for the period 1952 to 1968.

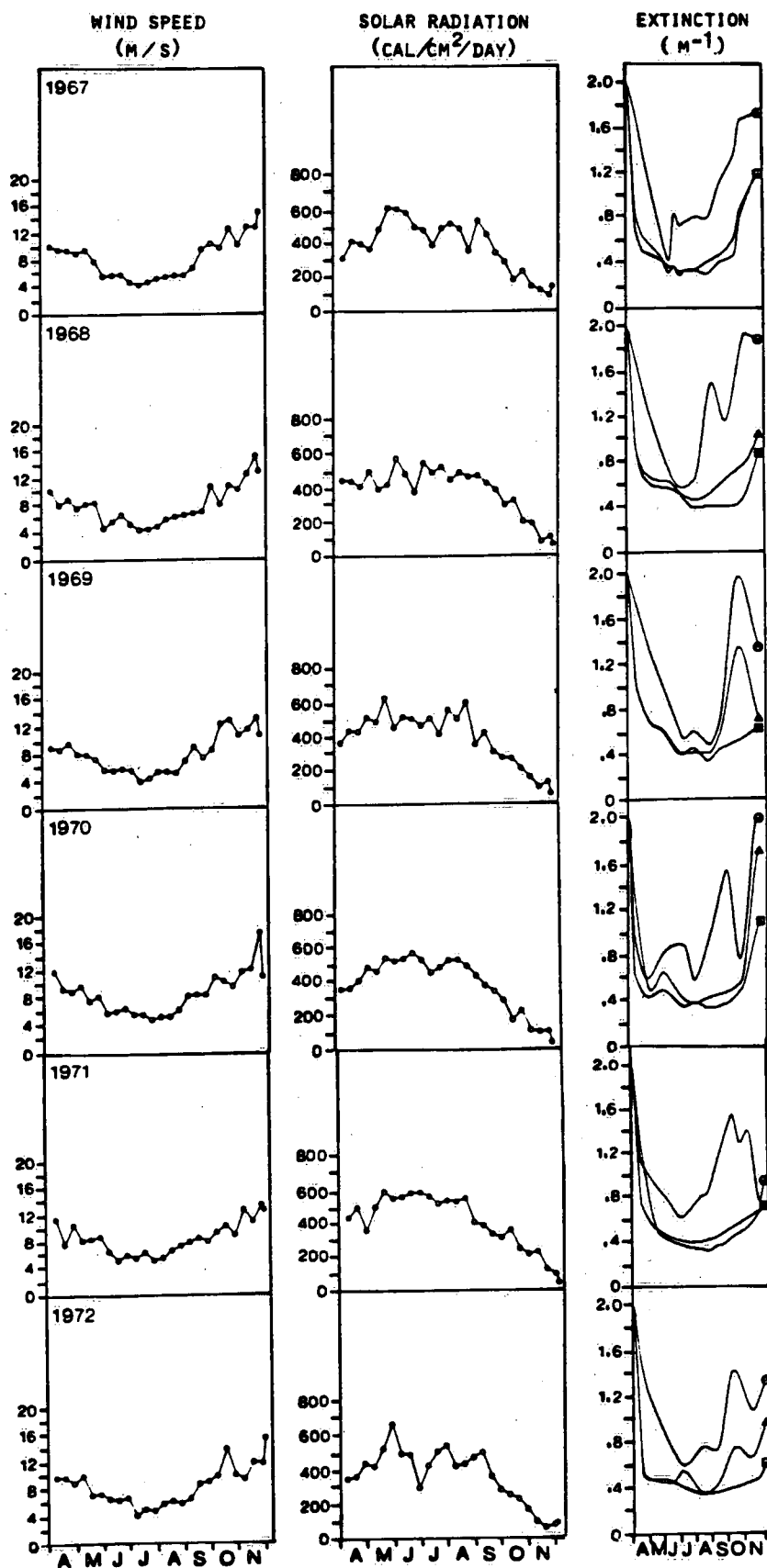


Figure 4.13. Ten-day means of lake-wide wind speed, solar radiation and basin-wide averages of mean vertical extinction coefficient for Lake Erie in the period April through November for 1967 to 1978.

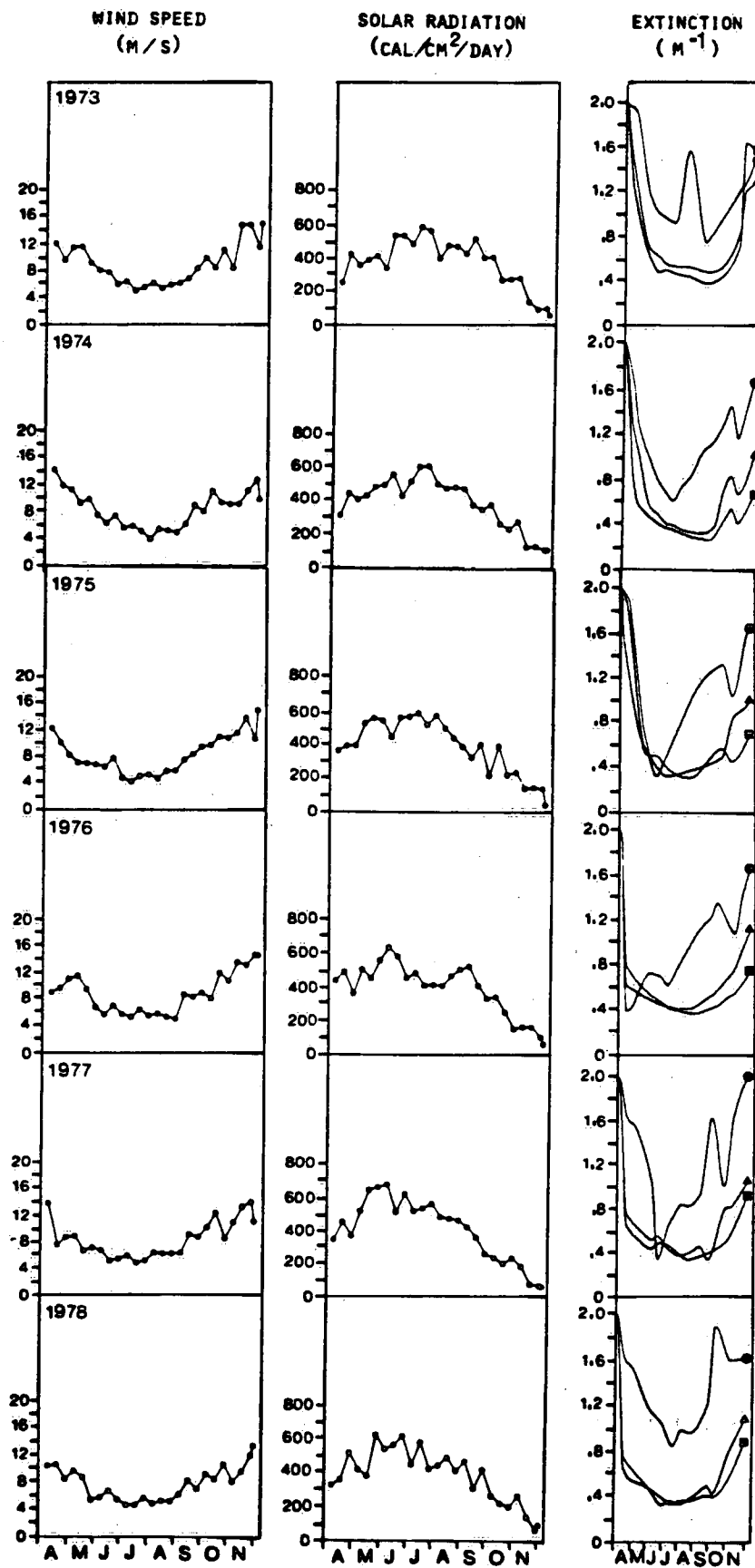


Figure 4.13. Continued.

bathymetric characteristics and larger volume of water. The Western Basin has the smallest range of heat content. As indicated in Fig. 4.11, times of occurrence of maximum and minimum heat content vary for all basins. Analysis of the long-term data shows that in the stratified period, the ratios of basin heat content to lake-wide heat content are relatively constant in the period April to November, approximately 0.06, 0.68 and 0.26 for the Western, Central and Eastern basins, respectively.

Previous investigation of Lake Erie heat storage was conducted by Derecki (1975; 1976) from limited survey data in which he used temperature profile data 1960-63 from the Great Lakes Institute (University of Toronto) for determination of average water temperature for various depths from the surface. By an adjustment procedure, these data were extended over the period 1952-68 and the heat content was estimated by summing energy contents at the pre-determined depths (Derecki, 1975). Figure 4.12 shows a comparison between results of the present long-term data 1967-78 which used cruise data with the approximation of Derecki (1975) for the period 1952-68. The figure shows a considerable departure between the two studies. Part of the difference may be in the fact that the present study incorporates data from high water years and the period 1952-68 had generally lower water levels. Heat content estimates for the period 1960-63 by Derecki (1975) agree much closer with the results of the present study.

Model simulations described in this report rely on detailed meteorological and limnological data such as described in the preceding sections. In particular, models of the lake thermal regime (see Sections 7.1 and 8.3) require estimates of wind speed, solar radiation and mean vertical extinction coefficient. Figure 4.13 illustrates these data for Lake Erie for the period 1967 to 1978.

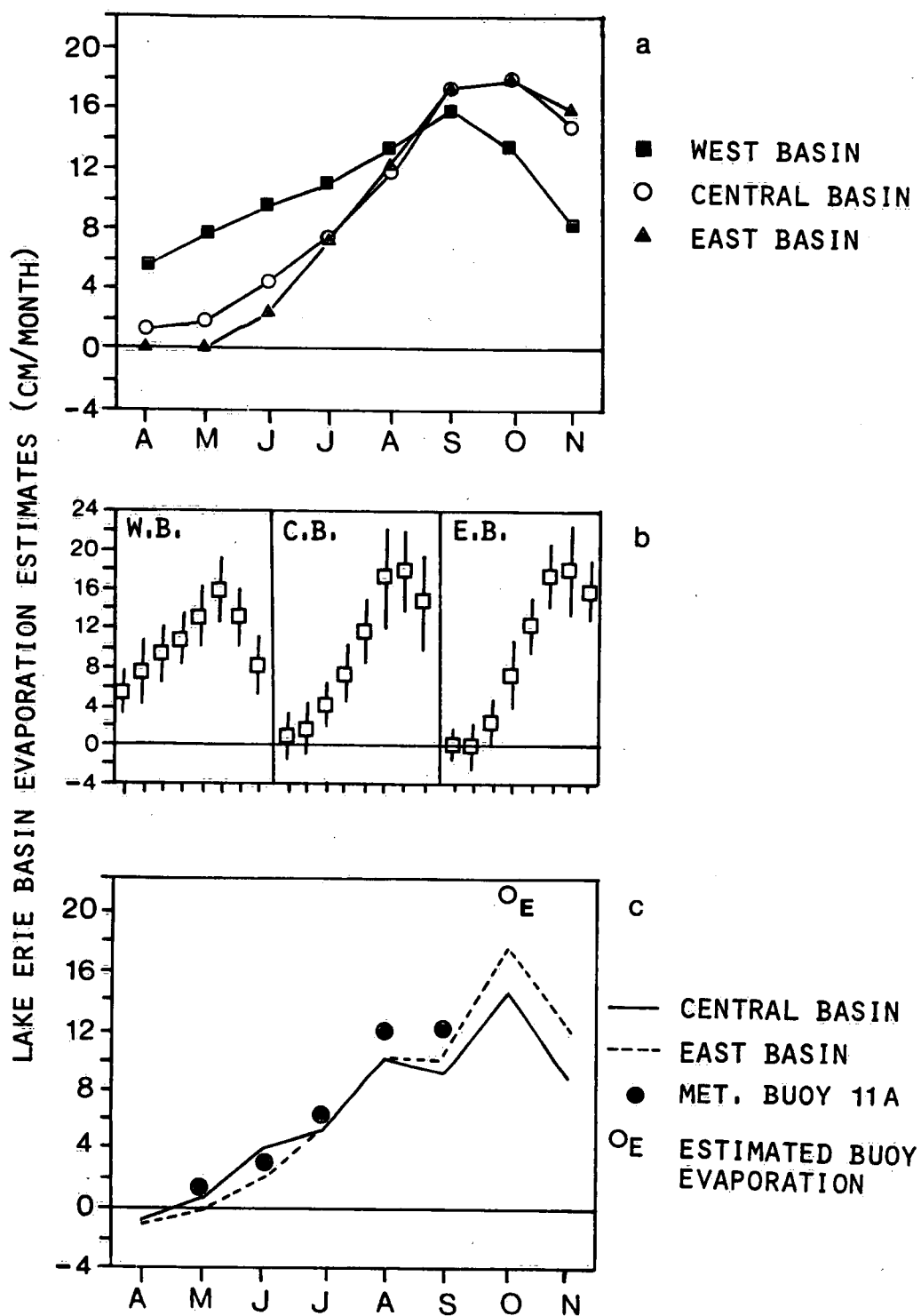


Figure 5.4. Average monthly evaporation for Lake Erie basins for the period 1967 to 1978 for the months April through November.

(a) Monthly mean basin evaporation rates; (b) variability of monthly mean basin evaporation rates; (c) comparison of 1977 computed Central Basin and East Basin evaporation with evaporation from mid-lake buoy, Buoy 11A.

of water masses resulting from the inflow-outflow balance. The magnitude of this component is of an order less than reflected solar radiation or sensible heat flux (Derecki, 1975) and is neglected in this analysis.

5.2.2 Radiation components

Lake-wide heat flux components were computed from relationships given in Table 5.1, incorporating values for various rate coefficients (Table 5.2). Computations were based on daily estimates of meteorological and limnological data. Figure 5.1 gives a summary of long-term monthly means for solar and longwave fluxes for the months April to November. Table 5.3 shows a comparison of long-term monthly mean net solar radiation and net longwave radiation in this study with that of Derecki (1975). These values show relatively good agreement for most months, considering the differences in the period of analysis and the differences in computational time scales.

5.2.3 Evaporation

The mass transfer approach to compute lake evaporation is based on the removal of water vapour from the water surface by turbulent diffusion and transport. Evaporation is derived by employing a modified version of the Lake Hefner relationship (U.S. Geological Survey, 1954; Derecki, 1975), which uses average wind speed and vapour pressure data adjusted to over-lake conditions (Table 5.2).

Figure 5.2 shows a comparison of long-term mean monthly evaporation derived in this study with mass transfer and water balance evaporation from Derecki (1975). Water balance values can be considered as a control with which other approaches can be compared. Figure 5.2 shows a number of departures from the results of Derecki (1975). In particular, it is apparent that the evaporation estimates

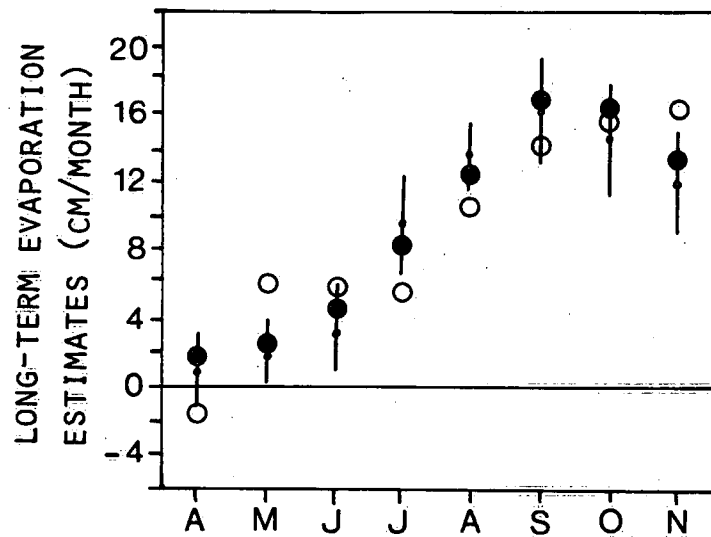


Figure 5.2. Comparison of long-term monthly mean lake-wide evaporation estimates for Lake Erie.

- (—●—) water balance 1937-68, Derecki (1975)
- (○) mass transfer 1937-68, Derecki (1975)
- (●) mass transfer 1967-78, This study

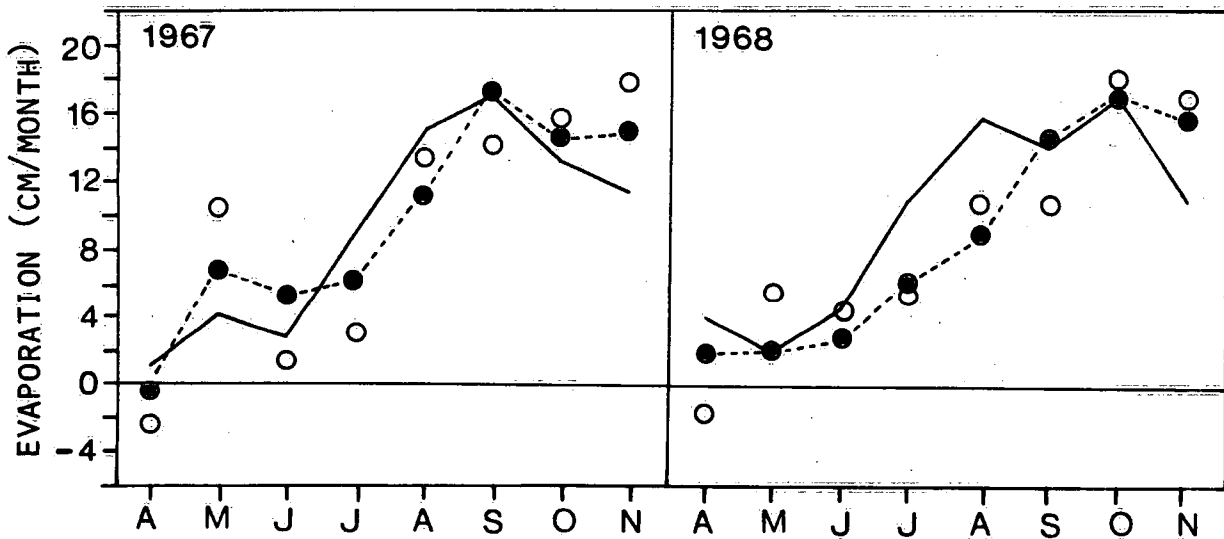


Figure 5.3. Comparison of 1967 and 1968 monthly mean evaporation from the mass transfer approach in the present study with values of evaporation computed by water balance and mass transfer (Derecki, 1975).

- (—) water balance, Derecki (1975)
- (○) mass transfer, Derecki (1975)
- (--●--) mass transfer, This study

Table 5.2. Meteorological and Radiation Factors

	(1)	(2)	(3)	(4)	(5)	(6)	
	R	H	α	A	CF	a	b
A	1.81	1.14	0.08	11	0.37	0.15	0.61
M	1.71	1.11*	0.08	8	0.61	0.22	0.56
J	1.31	1.09*	0.08	6	0.59	0.14	0.64
J	1.16	1.09	0.08	2	0.61	0.13	0.61
A	1.39	1.09	0.08	4	0.58	0.17	0.59
S	1.78	1.11	0.08	10	0.52	0.16	0.67
O	1.99	1.15	0.09	15	0.45	0.15	0.61
N	2.09	1.15	0.13	17	0.22	0.12	0.58

- (1) Lamire (1961)
 (2) Richards and Fortin (1962) (*This study, Table 4.1)
 (3) Davies and Schertzer (1975)
 (4) Anderson and Baker (1967); Derecki (1975)
 (5) Derecki (1975) modified in this study
 (6) Sanderson (1980) Pelee Island data

Table 5.3. Comparison of Lake Erie Radiation Flux Computations

(a) This Study 1967 to 1978

	A	M	J	J	A	S	O	N
K*	365	464	488	463	431	346	215	94
L*	-68	-121	-121	-142	-134	-122	-105	-58

(b) Derecki 1952 to 1967

K*	358	477	525	505	437	347	242	131
L*	-30	-117	-93	-130	-144	-137	-138	-99

$$K^* = Q_s - Q_r$$

$$L^* = Q_a - Q_{bs} - Q_{ar}$$

Table 5.1. Heat Balance Relationships

$$Q_s = Q_o [a + b (S_m/S_p)]$$

$$Q_r = \alpha Q_s$$

$$Q_a = \sigma T_a^4 - [228.0 + 11.16 (\sqrt{e_{sa}} - \sqrt{e_a}) - A] \cdot C_F$$

$$Q_b = \epsilon' \sigma T_s^4$$

$$Q_{ar} = (1 - \epsilon') Q_a$$

$$Q_e = [0.0097 (e_s - e_a \cdot H) u \cdot R] \cdot L$$

$$Q_h = \beta \cdot Q_e$$

$$Q^* = Q_s - Q_r + Q_a - Q_b - Q_{ar}$$

Q_o = extraterrestrial radiation ($\text{cal cm}^{-2} \text{ day}^{-1}$)
 S_m = measured sunshine (hours and tenths)
 S_p = potential sunshine (hours and tenths)
 T_a = air temperature ($^{\circ}\text{K}$)
 T_s = surface water temperature ($^{\circ}\text{K}$)
 T_d = dew point temperature ($^{\circ}\text{C}$)
 e_s = saturation vapour pressure at T_s (mb)
 e_a = ambient vapour pressure at T_d (mb)
 e_{sa} = saturation vapour pressure at T_a (mb)
 A = mean monthly station adjustment term (Anderson and Baker, 1967; Derecki, 1975) ($\text{cal cm}^{-2} \text{ day}^{-1}$)
 C_F = mean monthly atmospheric radiation correction factor
 u = mean wind speed (m/s)
 α = monthly mean surface albedo (Davies and Schertzer, 1975)
 σ = Stephan-Boltzmann constant
 ϵ' = emissivity at the water surface (0.97)
 β = Bowen ratio, $\beta = (T_s - T_a)/(e_s - e_a)$
 H = lake/land humidity ratio
 R = lake/land wind ratio
 L = latent heat of vaporization, $L = 596 - 0.52 (T_s)$ (cal cm^{-3})
 a, b = radiation constants

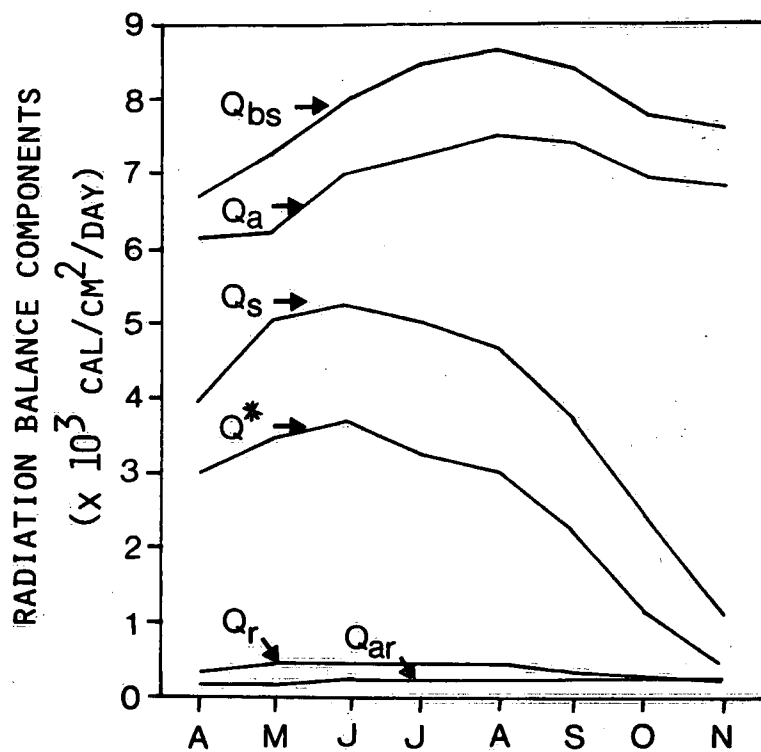


Figure 5.1. Monthly means of Lake Erie radiation components computed for 1967 to 1978.

balances are derived as a proportion of the lake-wide case. Finally, the basin heat balance is used to derive a first approximation of the horizontal heat exchange between basin boundaries.

A comprehensive analysis of lake-wide energy balance for Lake Erie has been conducted by Derecki (1975). It is interesting to compare the present analyses which utilize daily meteorological and limnological data with the results of Derecki (1975), who derived monthly mean values.

5.2.1 Lake-wide heat balance analysis

The exchange of thermal energy between the lake surface and the atmosphere involves parameterizations of heat sources and sinks

$$Q_s - Q_r + Q_a - Q_{ar} - Q_{bs} - Q_h - Q_e + Q_v = Q_t \quad (5.1)$$

where

- Q_s = incoming global solar radiation
- Q_r = reflected global solar radiation
- Q_a = incoming longwave radiation
- Q_{ar} = reflected longwave radiation
- Q_{bs} = outgoing longwave radiation
- Q_h = sensible heat flux
- Q_e = evaporative heat flux
- Q_v = net advected energy
- Q_t = surface heat flux.

Equation 5.1 disregards minor energy gains or losses such as from chemical or biological sources or from conduction through the lake bottom and transformation of kinetic energy. The component Q_v represents the net energy gained or lost by the lake due to exchange

Heat and Mass Balance Models

5.1 Introduction

The transfer of thermal and mechanical energy across the air-water interface is a primary mechanism for the formation and decay of lake thermal stratification. The surface heat flux is required as a boundary condition for simulation of vertical temperature distribution and as a thermocline position for input into mass balance models. The following section provides a description of the heat balance approach which produces a first approximation of the net horizontal exchange between Lake Erie basins. A more precise description of this horizontal exchange and other physical processes is given in the latter part of this chapter in the discussion of the mass balance model.

5.2 Heat Balance Model

Estimation of the surface heat flux can be approached from the equilibrium temperature concept (Edinger et al., 1974) which is dependent on accuracies in heat exchange coefficients, or by calculating the net heat flux to the lake directly (Di Toro and Connolly, 1980) which is dependent on detailed a priori knowledge of surface water temperature, or from detailed heat balance analysis. The detailed heat balance approach is used in this investigation, which involves parameterization of the relevant heat exchanges as a function of readily available meteorological data (Rodgers and Anderson, 1961; Derecki, 1975). Computation of the lake heat balance is a reasonably large undertaking. The approach used in this analysis is to derive the lake-wide heat balance from empirical relationships and to optimize the results based on the observed heat content. Basin heat

of the present study are in phase with months of maximum and minimum water balance evaporation. The most significant departure is that periods of high condensation at the lake surface in April are reduced and high values of evaporation in May do not occur. It is probable that this departure arises partly because of better water surface temperature estimates in the present study and partly because of the variation of the humidity ratios, as shown earlier in Table 4.1.

A further comparison between the evaporation results is given for overlapping years of study 1967 and 1968 (Fig. 5.3). Although agreement between results of the present study with the water balance estimates of Derecki (1975) is not as good as for the long-term case, the annual comparison shows a good correspondence in seasonal trend and the monthly values are generally in phase with the water balance evaporation.

Figure 5.4a shows evaporation estimates for Lake Erie basins. It is apparent that the rate of water loss is the greatest for the Western Basin in the spring and summer months, showing a significant difference from the other basins. Seasonal evaporation rates from the Central and Eastern basins are similar, but a seasonal lag in the basin evaporation rates in early spring and fall is related to differences in meteorological conditions such as air and water temperatures. The volume of water evaporated is the greatest from the larger surface area of the Central Basin.

The variation in monthly mean basin evaporation based on the period 1967-78 is shown in Fig. 5.4b. The evaporation rate for the Western Basin is predominantly positive, but periods of condensation on the lake surface can be expected to occur in the Central and Eastern basins during the early spring. These episodes appear more prevalent in the Eastern Basin. Maximum rates of evaporation occur in the Central and Eastern basins during the fall months, and these

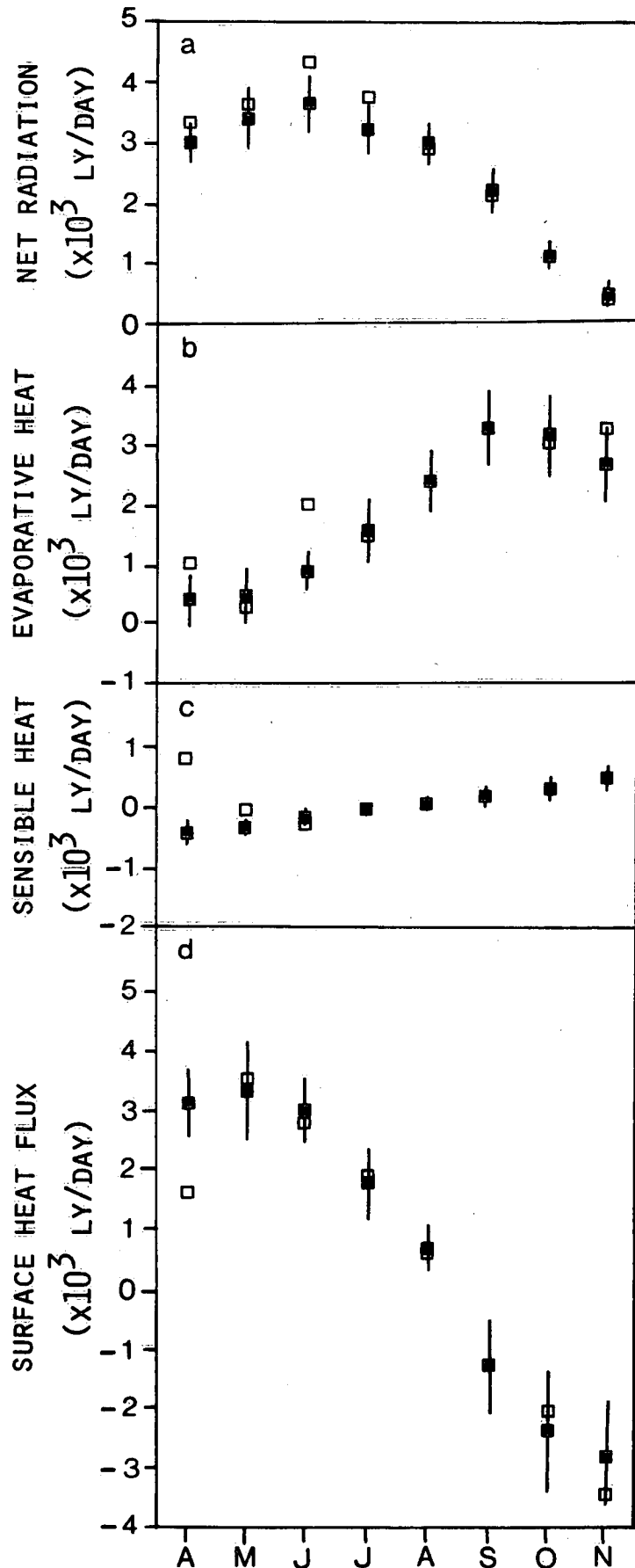


Figure 5.5. Lake Erie long-term monthly mean surface heat flux components and computed surface heat flux for the lake-wide case

- (a) Comparison of net radiation.
- (b) Comparison of evaporative heat flux.
- (c) Comparison of sensible heat flux.
- (d) Comparison of computed lake-wide surface heat flux.

(—■—) 1967-78, This study.
(□) 1937-68, Derecki (1975).

months also show the highest variation in evaporation. Comparisons of evaporation estimates from the Central and Eastern basins in 1977 with the buoy values (Fig. 5.4c) show good correspondence for the period of April to August. This is a verification of the present computations for that period. However, for the period of September to November, a large deviation occurs, indicating further research is needed.

5.2.4 Lake-wide surface heat flux

Computed daily heat flux components are summarized into monthly means for comparison purposes and expressed as a flux through the surface per day in Figures 5.5a to c. Standard deviation about the monthly mean is given for each component. For the period 1967-78 average monthly values of the net radiation flux are positive over the stratification period April to November. Evaporative heat flux is the lowest in the spring and increases to a maximum under unstable conditions in the fall. During the period April to July, sensible heat flux represents a gain to the surface and thereafter represents a loss. However, in comparison, the evaporative heat loss is significantly larger.

Figure 5.5d shows the lake-wide surface heat flux. In the period April to August, there is a net heat gain in the lake surface which results in temperature increases. The cooling phase of the lake begins in mid-August and progresses to minimum heat content in the winter months. Comparison of flux values with those derived by Derecki (1975) for the period 1952-68 shows good correspondence except for springtime evaporation and sensible heat flux. It appears that surface heat flux in April as derived by energy balance approach by Derecki (1975) is substantially too low in comparison with both the present values and with the heat content observations for the spring period (Fig. 5.5d).

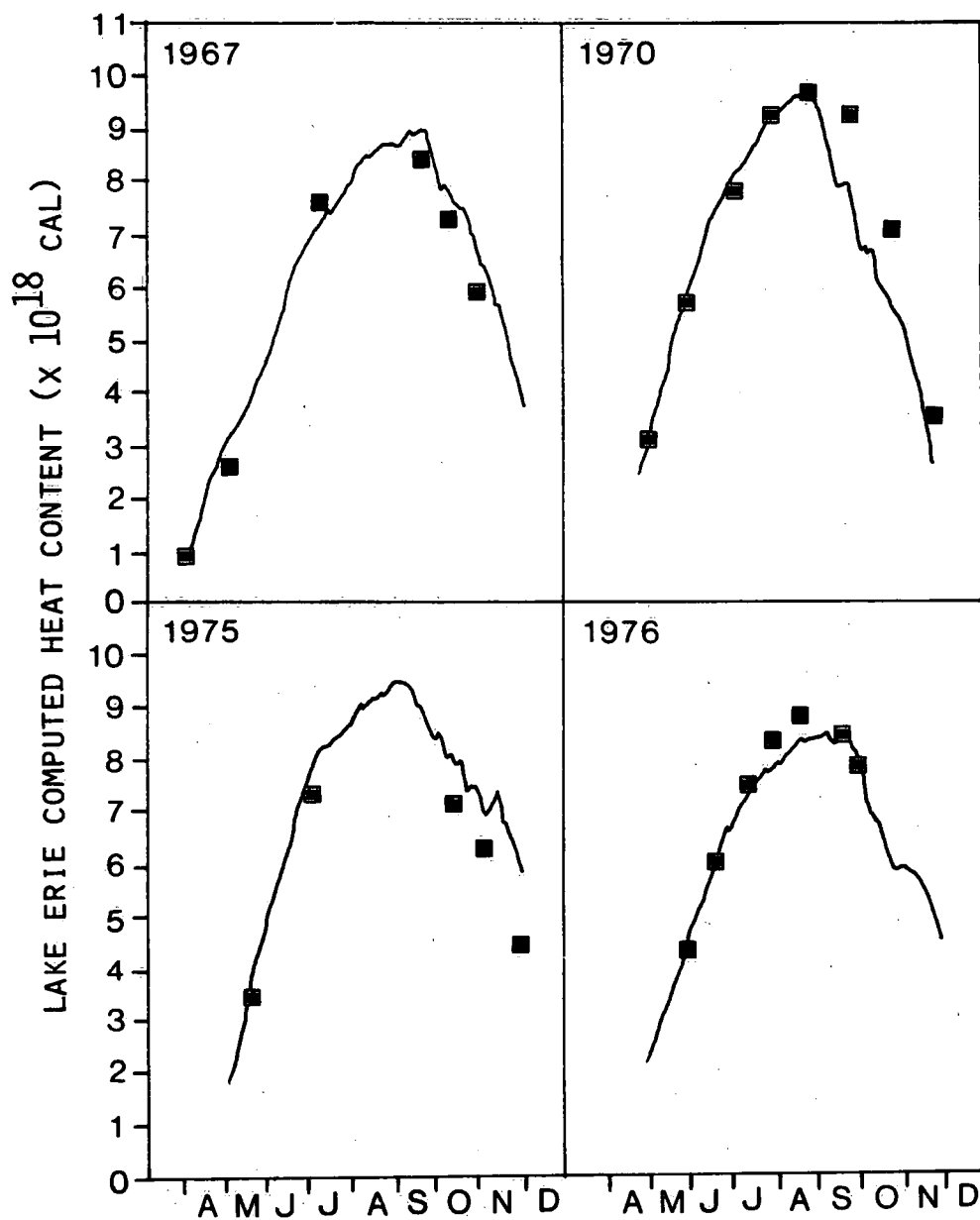


Figure 5.6. Examples of Lake Erie computed lake-wide heat content as the summation of computed lake-wide surface heat flux beginning at an initial value usually in April. Selected years of computation illustrate a range of accuracy due to the accumulation of errors through the heating and cooling season.

(—) Computed lake-wide heat content
 (■) Observed lake-wide heat content from CCIW temperature surveys.

5.3 Scaling and Interpolation Technique (SIT) for Optimizing the Lake-wide Heat Balance

The previous discussion detailed a first approximation to the lake-wide surface heat flux. Verification of the accuracy of the daily heat flux computations can be accomplished by direct comparison with over-lake flux values and/or by derivation of lake-wide heat content for comparison with measurements.

Summation of the daily surface heat flux, expressed as a quantity of heat from an initial minimum value usually at the first cruise in April inclusive to November, gives a computed heat content curve which can be compared with measurements. Figure 5.6 shows initial results for selected years as an example. Heat content derived from lake-wide survey values is plotted at the cruise midpoint. The agreement between measured and computed heat content for most years is reasonable for the heating portion of the year, but the largest departure occurs in the cooling phase due to the accumulation of errors in the summation from minimum heat content. Errors in the surface heat flux are due to inaccuracies of specifying over-lake meteorological and limnological data. Recall that surface water temperatures are derived as smooth interpolation through survey and ART data. One solution to minimize the inaccuracy is to contain the errors between consecutive cruise periods where such data are available and to distribute the total error over the inter-cruise interval. When cruise data are not available, recourse is to long-term mean heat content.

A first order adjustment of the heat content estimation is achieved by defining a scaling coefficient, γ , between each cruise interval:

$$\gamma = \frac{B - A - \sum_{j=1}^n (QDR - QNR)_j}{B' - A - \sum_{j=1}^n (QDR - QNR)_j} \quad (5.2)$$

where A = initial heat content at cruise midpoint
 B = measured heat content at the next consecutive cruise midpoint
 B' = estimated heat content at the next consecutive cruise midpoint
 QDR, QNR = heat inflow and outflow by Detroit and Niagara rivers, respectively.

Initial estimates of the daily surface heat flux for the lake-wide case, expressed as a quantity of heat between the specified cruise interval, are updated ($QF'_4 = \gamma \cdot QF_4$), and a new heat content curve, which must pass through the observed values, is derived. This adjustment procedure has the advantage of distributing the total inter-cruise error over the period of several days while maintaining the sense of the day to day meteorological influences. Errors in the procedure can occur at the period of maximum heat content where the flux values may be exaggerated.

Figure 5.7 shows a comparison of the new lake-wide heat content modified by the Scaling and Interpolation Technique (SIT) outlined above with observations. Differentiation of the modified heat content curve gives new estimates of daily surface heat flux. Figure 5.8 shows the difference between the modified and unmodified estimates of surface heat flux. The results indicate that for the period April to August, differences between the modified and unmodified results are relatively small, averaging $10 \text{ cal/cm}^2/\text{day}$. Larger differences occur in the period September to November in which the unmodified computations require greater heat loss from the lake surface in order to match measured heat content values.

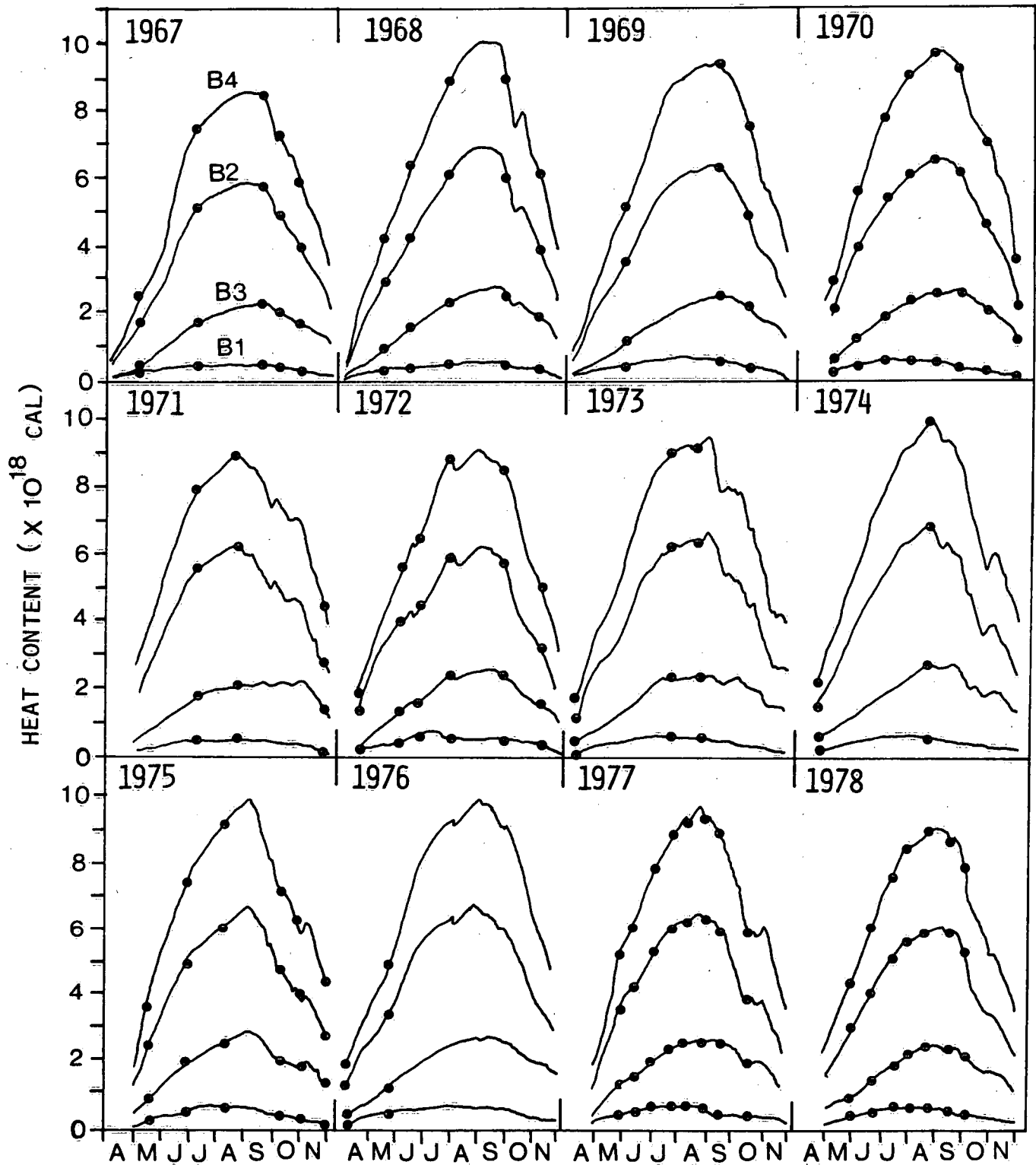


Figure 5.7. Computed Lake Erie lake-wide heat content modified through Scaling and Interpolation Technique and estimation of basin heat content as a proportion of the computed lake-wide heat content.

(●) Observed heat contents computed from CCIW temperature surveys;
 B1 = West Basin, B2 = Central Basin, B3 = East Basin, B4 = Lake-wide

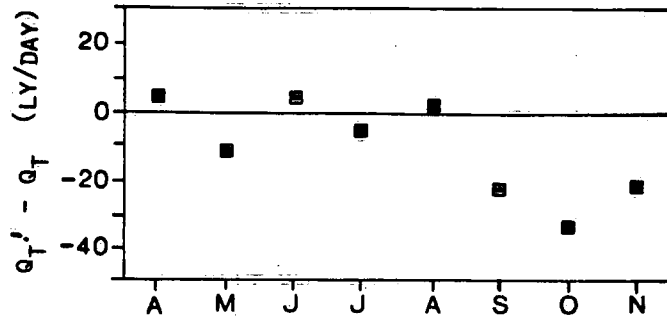


Figure 5.8. Average difference between lake-wide surface heat flux computations determined through modification by Scaling and Interpolation Technique ($Q_{T'}$) and with no modification (Q_T) for the period 1967 to 1978.

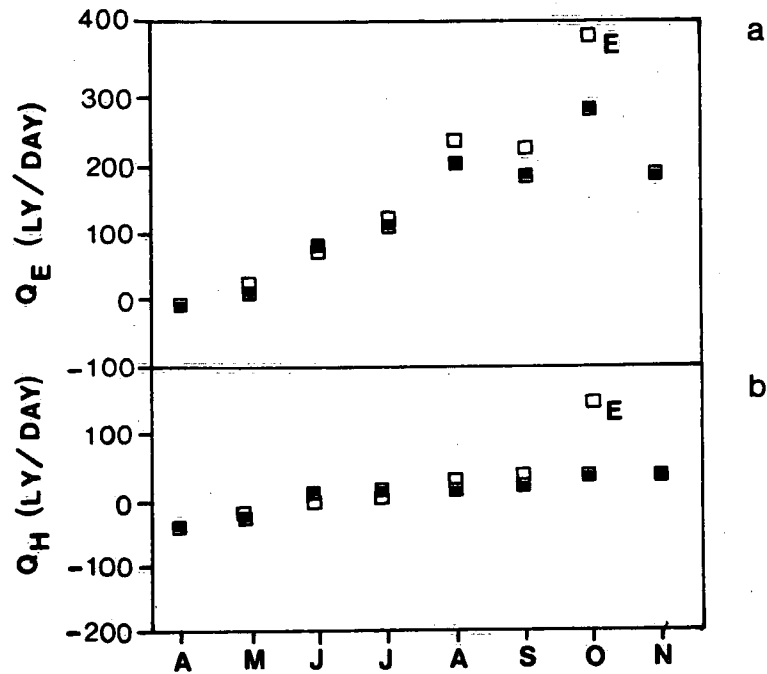


Figure 5.9. Comparison of computed Central Basin evaporative heat flux and sensible heat flux with Buoy 11A values for 1977.

- (a) Evaporative heat flux.
 (b) Sensible heat flux.

(■) Central Basin values; (□) Buoy 11A values;
 (E) Estimated Buoy 11A evaporation based on
 20 days of measurements.

These differences in the period September to November can be attributable to a combination of several sources. As indicated previously, some error exists in the approximation to over-lake conditions and the advective component Q_v is neglected. However, it is noted also that comparison with buoy values for the evaporation rate in 1977 shows that evaporative heat loss at the buoy location (Fig. 5.9) is greater than computed losses in September and October (cf. Subsection 5.2.3). The difference is of the order of the averaged adjustments (Fig. 5.8) to the unmodified surface heat flux for September and October 1967 to 1978.

5.4 Basin Heat Balance and Exchange Rates

A schematic of the components of Lake Erie basin heat exchange in the one-dimensional case is given in Figure 5.10. Whereas major inflow and outflow volumes and temperatures are observed, horizontal basin exchange rates are not measured. A first approximation to the exchange rates is derived from the heat balance. This requires the approximation of the basin heat storage and the heat flux at the air-water interface so that the net horizontal heat transfer may be calculated as a residual.

5.4.1 Approximation of basin heat storage

Uncertainties in components of the basin heat storage preclude direct computation. The approach used in the present analysis is to consider basin heat content as a proportion of lake-wide heat content. Previous analysis detailed the derivation of lake-wide heat content and lake-wide surface heat flux based on optimization procedures. Computations were based on daily meteorological data.

The proportionality factor p_i can be defined as, for $i = 1, 2, 3$:

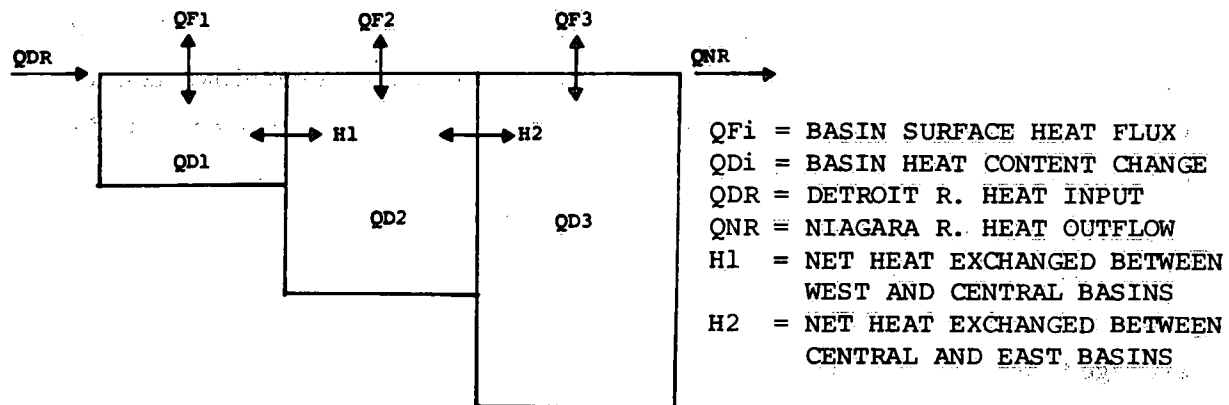


Figure 5.10. Schematic of components considered in the evaluation of the net heat exchanged between Lake Erie basins using a Heat Balance approach.

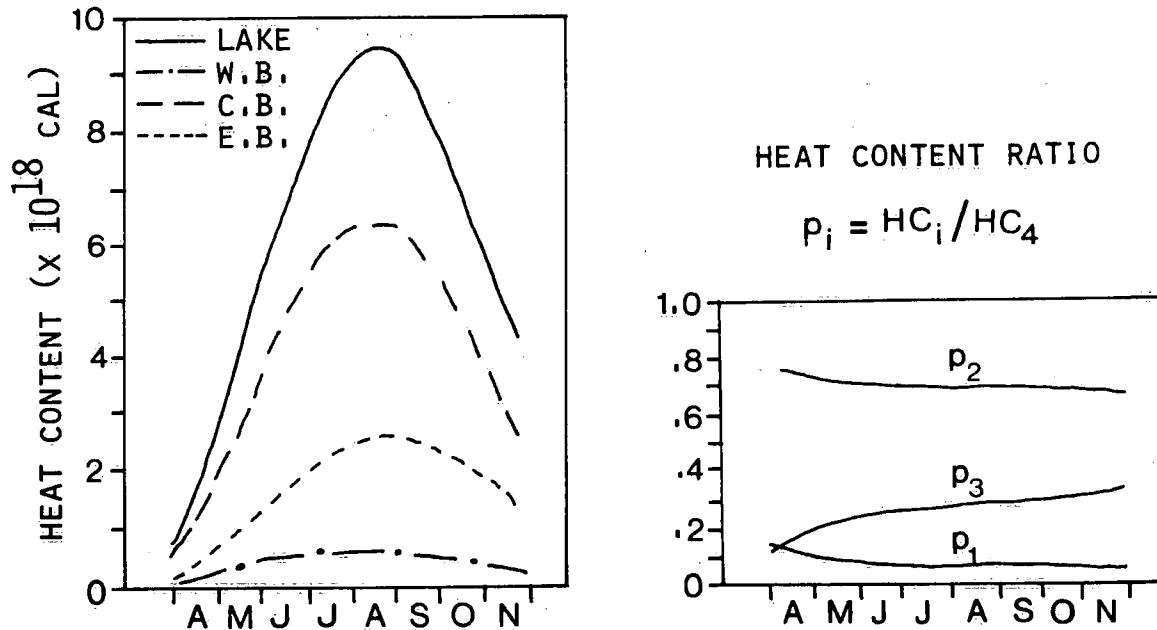


Figure 5.11. Ratio of basin to lake-wide heat content for Lake Erie based on polynomial fit through observations in the period 1967 to 1978.

- (a) Polynomial fit to long-term lake-wide and basin heat content observations.
 (b) Basin to lake-wide heat content ratios.

(p_i , $i = 1, 2, 3$ for West, Central and East basins, respectively).

$$p_i = HC_i / HC_4 \quad (5.3)$$

where HC_i is the heat content for the i th basin and HC_4 is the lake-wide heat content. Based on polynomial fit through long-term basin and lake-wide heat content (Fig. 5.11), it is apparent that the p_i 's are relatively constant over the period April to November (Fig. 5.9). Therefore, using proportions determined from long-term cruise data or from individual years when a sufficient number of cruises are available, daily basin heat content is derived as

$$HC_i = p_i \cdot HC_4 \quad (5.4)$$

and the basin heat content change is approximated as $\Delta HC_i / \Delta t$ where $\Delta t = 1$ day.

Basin heat content, modified by the Scaling and Interpolation Technique and the basin proportioning procedure outlined above, is also illustrated in Fig. 5.7 for the years 1967-78. Observed values of basin heat content based on temperature surveys are plotted at the cruise midpoint. The agreement between measured and computed basin heat content is dependent on the accuracy of the derived proportions.

5.4.2 Heat exchanged at the air-water interface

Heat exchange relationships used to determine first approximation to the heat flux at the air-water interface are given in Table 5.1. The unmodified (see Section 5.3) basin surface heat exchange is computed as

$$QF_i = (H_r - H_e - H_h)_i \quad (5.5)$$

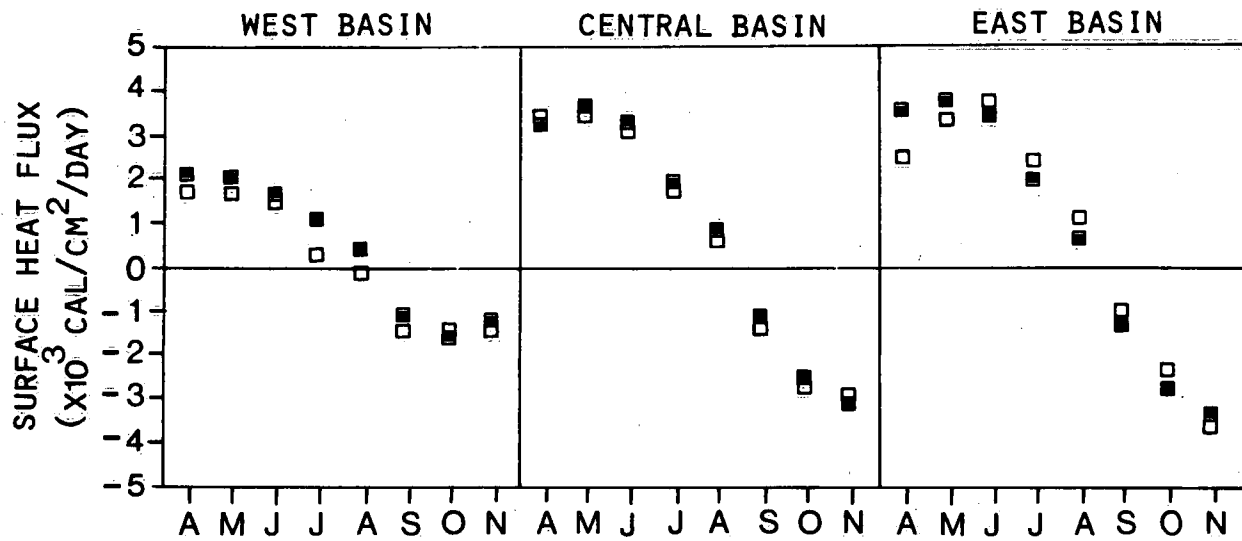


Figure 5.12. Comparison of long-term monthly mean surface heat flux modified through Scaling and Interpolation Technique (\square) with unmodified calculations (\blacksquare) for Lake Erie basins.

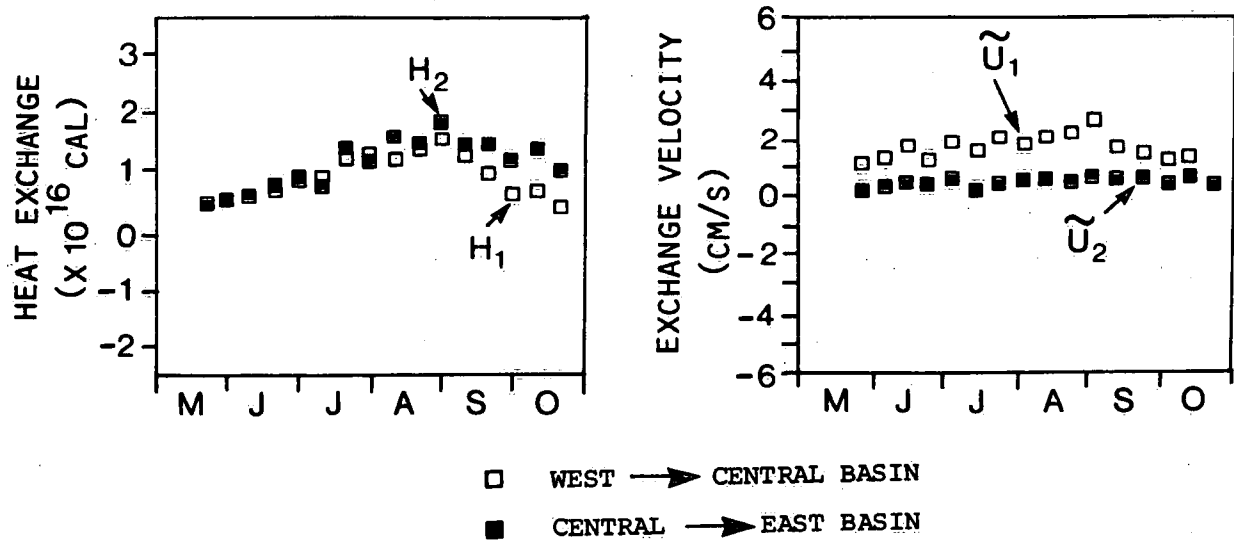


Figure 5.13. An example of the computed summertime net quantity of heat and net velocities exchanged across Lake Erie basins determined through Heat Balance approach for 1969 (ten-day means).

where QF = basin surface heat flux (unmodified)

H_r = total heat due to radiation exchanges

H_e = total heat due to evaporative exchanges

H_h = total heat due to sensible heat exchange

and the subscript i refers to the i th basin. Heat gains or losses from the Detroit or Niagara River are excluded.

A modified value (see Section 5.3) of the quantity of heat gained or lost from the air-water interface of the i th basin is derived by updating the initial basin estimates by the ratio of unmodified basin to unmodified lake-wide quantities of heat $R_i = (QF_i/QF_4)$. Modified values of surface heat exchange for the Western and Eastern basins are then formed as, respectively

$$QF'_1 = R_1 \cdot QF'_4 \text{ and } QF'_3 = R_3 \cdot QF'_4 \quad (5.6)$$

and consistency is maintained by forcing the Central Basin surface heat exchange to be the residual

$$QF'_2 = QF'_4 - QF'_1 - QF'_3 \quad (5.7)$$

Final estimates of the daily basin surface heat flux are determined by dividing the total daily basin heat change by the basin surface area. Figure 5.12 shows a comparison between unmodified and modified basin surface heat flux expressed as monthly means averaged for the period 1967 to 1978.

5.4.3 Basin net horizontal exchange

One-dimensional approximation of the net interbasin exchange using the heat balance approach required estimates of the total basin

heat storage change and the exchanges at the air-water interface only. The procedure for these computations was outlined in Subsection 5.4.2. Using estimates of these heat exchanges coupled with heat inflows or outflows through the Detroit River and Niagara River, e.g.

$$QDR = \rho c_p (V_r \cdot T_r) \quad (5.8)$$

where QDR = Detroit River heat inflow
 V_r = volume inflow
 T_r = mean water temperature of inflow volume (Fig. 4.7)
 ρ = density of water
 c_p = specific heat of water

the net exchange of heat between basins can be determined as a residual.

The net amount of heat exchanged between the West and Central basins of Lake Erie is approximated (Fig. 5.10) as

$$H_1 = QDR + QF'_1 - QD_1 \quad (5.9)$$

and similarly the exchange between the Central and Eastern basins becomes

$$H_2 = H_1 + QF'_2 - QD_2 \quad (5.10)$$

Heat loss through the Niagara River is determined as

$$CNR = H_2 + QF'_3 - QD_3 \quad (5.11)$$

where H_1 = heat exchanged between West and Central basins
 H_2 = heat exchanged between Central and East basins
 QF'_1 = West Basin surface heat exchange (modified by SIT)
 QF'_2 = Central Basin surface heat exchange (modified by SIT)
 QF'_3 = East Basin surface heat exchange (modified by SIT)
 QD_1 = West Basin heat storage change
 QD_2 = Central Basin heat storage change
 QD_3 = East Basin heat storage change
 CNR = computed Niagara River outflow.

Figure 5.13 shows the one-dimensional approximation of the net horizontal heat exchange between the Lake Erie basins. Using estimates of the basin net horizontal heat exchange, estimates of the net transport velocity in a one-dimensional sense can be derived as the following:

$$\tilde{U}_i = H_i / (\rho c_p A_i \cdot \bar{T}_{wi}) \quad (5.12)$$

where \tilde{U}_i = net horizontal transport velocity across basin boundaries ($i=1$, West to Central Basin; $i=2$, Central to Eastern Basin)
 H_i = basin mean heat exchange associated with V_i
 \bar{T}_{wi} = basin vertically integrated temperature (determined from long-term mean or cruise data within a particular year); \bar{T}_{wi} is dependent on the upstream flow direction, i.e. sign of H_i , e.g. \bar{T}_{w1} is Western Basin temperature if $H_i > 0$ and $i = 1$
 A_i = cross-sectional areas (cm^2).

Figure 5.13 also shows ten-day means of net horizontal transport velocities for the period 1967-78. Net exchange velocities determined by the heat balance approach are in the order of the approximations

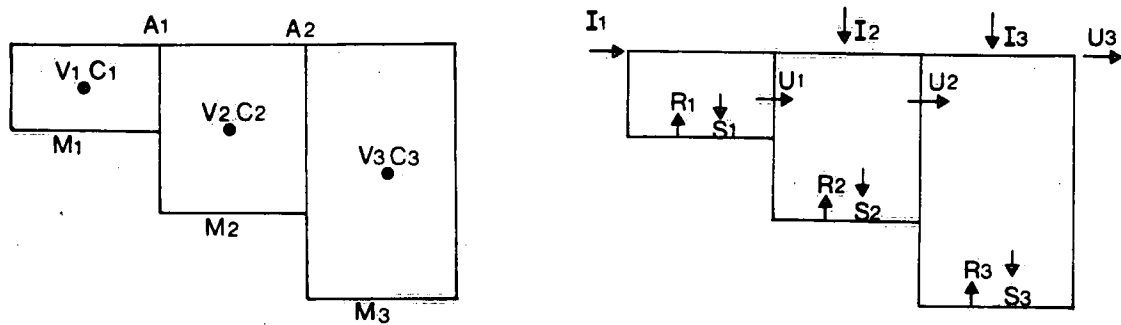


Figure 5.14. Basin boundaries and major components incorporated in the three-box mass balance model of Lake Erie.

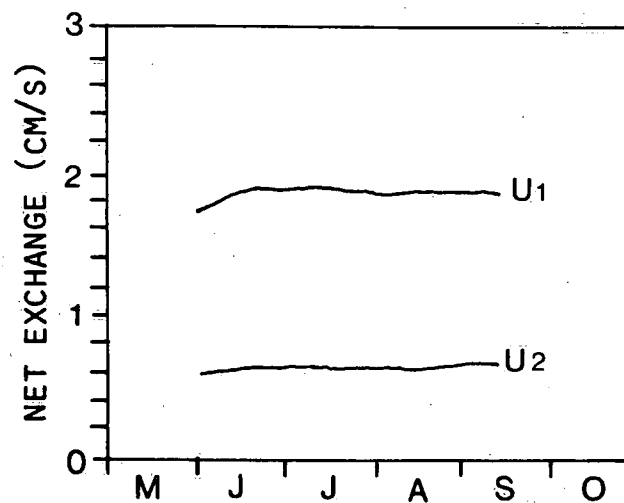


Figure 5.15. Computed net exchange rates between the West-Central (U1) and Central-East (U2) basins based on the hydraulic flows.

derived by considering the mean hydraulic flow based on the Detroit River (Q_1) and Niagara River (Q_2) flows

$$U_1 A_1 = U_2 A_2 = (Q_1 + Q_2)/2 \quad (5.13)$$

where U_1 = mean hydraulic flow rate (cm/s)

Q_1 = river flows (cm/s)

A_1 = cross-sectional areas (cm²).

Although Q_1 will vary seasonally, computations indicate that U_1 is about 2 cm/s and U_2 is about 0.5 cm/s. Since these velocities are derived from diagnostic heat balances, they are not statistically reliable to replace the interbasin exchange velocities, \tilde{U}_1 . Rather, the purpose here is to see whether they would reach some constant values, as an indirect check on the heat flux estimation. Such an interpretation of diagnostic model results has also been used in the discussion of the settling velocity of the particulate phosphorus (Subsection 3.3.4, Table 3.5).

5.5 Diagnostic Mass Balance Models

Vollenweider (1969, 1975) discussed the response of a lake to external loading using the concept of the input-output box model. For a substance such as total phosphorus, the model may be generalized as

$$\frac{dM}{dt} = L + S, \quad L = I - O \quad (5.14)$$

where the left-hand side represents the time rate of change of the total mass of the nutrient contained in the lake, I is the total nutrient input to the lake, O is the loss by river outflow, L is the net loading and S is the net contribution from the sediments to the water.

Simons and Lam (1980) have investigated the relative merits of the input-output box model. Whereas conventional prognostic models are used to produce time series solution of chemical concentration, the more profitable use of the input-output box model is to solve it diagnostically. That is, approximation of the unknown quantity is obtained as residual, assuming other quantities known from observational or interpolated data. An example is the estimation of the net sedimentation

$$S = L - \frac{dM}{dt} \quad (5.15)$$

On the other hand, the box model is somewhat limited in its ability to describe the complex interactions within the lake. Specifically, the net sedimentation term is usually not directly proportional to the total nutrient concentration and may be a function of the organic fraction which may vary considerably over time. As well, there are

limitations associated with parameterization of spatial variations such as the vertical gradients during summer stratification.

In mass balance models of the constantly stirred reactor (CSR) type, the interaction between the sediment and water is often assumed to occur at the bottom panel of a box which is used to represent a homogeneously mixed lake. However, large concentration gradients observed particularly in the stratified season necessitate increasing spatial complexity to describe the ongoing processes. While it is recognized that there are several forms of phosphorus which contribute differently to the total lake concentration, there are uncertainties associated with the kinetics between the different forms (Simons and Lam, 1980). Consequently, only one form of phosphorus is examined here, namely, total phosphorus.

The following section describes the formulation of and derivation of rate processes from box models of increasing complexity. Specifically, the three-box, six-box and nine-box mass balance models are discussed. Description of higher order multi-layered models of the prognostic type will be given in Sections 7.2 and 8.3 later. The emphasis here is placed on formulating the diagnostic approach of calculating the net settling and resuspension of total phosphorus in Lake Erie basins as a response to the effects of thermal stratification and interbasin transport. Preliminary results of this diagnostic approach have been discussed in Section 3.3 in conjunction with the lake chemistry data.

5.6 Three-Box Model

Lake Erie consists of three distinct basins such that the least complex mass balance formulation of the CSR type must consider at a minimum three basin compartments. The most general CSR case is a three-box model. Relevant basin boundary terms and major mass balance

components are shown schematically in Figure 5.14. The system equations describing the three-box model are

$$\frac{dV_1 P_1}{dt} = I_1 - U_1 A_1 P_1 - S_1 + R_1 \quad (5.16)$$

$$\frac{dV_2 P_2}{dt} = I_2 + U_1 A_1 P_1 - U_2 A_2 P_2 - S_2 + R_2 \quad (5.17)$$

$$\frac{dV_3 P_3}{dt} = I_3 + U_2 A_2 P_2 - U_3 P_3 A_3 - S_3 + R_3 \quad (5.18)$$

where for $i = 1, 2, 3$ representing the Western, Central and Eastern basins, respectively, P_i is the total phosphorus concentration, t is time, I_i is input loading, U_i and A_i are the transport velocity and cross-sectional areas between basins i and $i+1$ for $i=1$ and 2 , U_3 and A_3 are the transport velocity and cross-sectional area at the outflow, V is basin volume, S_i is the sedimentation of phosphorus from water to sediment and R_i is the resuspension of phosphorus from sediment to water.

The transport velocity in the three-box model must obey the hydraulic flow continuity constraint. As discussed previously, the hydraulic flow is defined from observations of Detroit River inflow (DR) and Niagara River outflow (NR) volumes, such that the hydraulic flow (Q_m) is computed as $Q_m = (DR + NR)/2$ on a daily basis. Consequently, the net horizontal transport velocities can be calculated as

$$U_i = Q_m / A_i \quad (5.19)$$

where $i=1, 2$ across the West-Central and Central-East basin boundaries. Alternatively, the transport velocity can be estimated as a

residual by rearranging Equations 5.16 to 5.18. Figure 5.15 shows the net horizontal transport velocity U_1 as determined from consideration of the hydraulic flow. Since the hydraulic flow is determined as the average between major inflow and outflow volumes, U_1 is relatively invariant (cf. Fig. 5.13). From long-term calculations, the average net velocity across the West-Central basin boundary is about 2 cm/s and across the Central and East basins is about 0.5 cm/s (cf. Subsection 5.4.3). In comparison with the net horizontal transport, which is approximated numerically by the upwind differencing scheme in Equations 5.16 to 5.18, the horizontal diffusion term is small and is neglected in this calculation.

In the diagnostic approach, the left-hand-sides of Equations 5.16 to 5.18 are assumed to be known from interpolated observational data. Consequently, unknowns can be selected from the right-hand-sides and solved for as residuals. The most uncertain components of the phosphorus model are the settling and resuspension terms. In general, S_1 is related to a settling rate σ_1 and a particulate form of phosphorus, PP_1 , so that the settling formulation, cf. Eq. 3.2, $S_1 = \sigma_1 PP_1$ holds. Conversely, R_1 represents the physical resuspension of phosphorus due to wind-wave interaction or the chemical regeneration from the sediment under anoxic conditions. Because R_1 is related to many external factors not parameterized here, it is treated as a general term of sediment return.

Rearrangement of Equations 5.16 to 5.18 gives net sedimentation ($S_1 - R_1$) such that a positive $S_1 - R_1$ represents net settling of total phosphorus, while a negative value indicates a net return amount. Long-term results of the three-box CSR mass balance model have been given in Section 3.3.

5.7 Six-Box Model

In the constantly stirred reactor model, the concentration is assumed to be homogeneous throughout the water column. Thus, in the case of chemical regeneration of phosphorus from the sediment under anoxic conditions, the regenerated phosphorus is added to the entire column. Such an assumption is of course not always true, because anoxic conditions usually occur in the presence of a shallow hypolimnion under a strong thermal stratification influence. Often, large density differences (Figures 3.1 to 3.4) between the upper and lower layers of water effectively restrict vertical mixing. Thus, in the realistic case, resuspended phosphorus at the sediment-water interface should remain within the hypolimnion until the existing stratification is perturbed and vertical mixing becomes effective again.

The simplest way to incorporate the thermal stratification phenomenon in a mass balance model is to divide the water column into two layers. The effect of considering a two-layer mass balance model framework is to increase the model complexity by requiring solutions to more compartments and by introducing additional processes and parameters into the model.

One possible formulation for achieving a two-layer model is to separate the lake at a chosen but fixed depth. By noting the interpolated/observed temperatures, the vertical mixing or exchange coefficient across the fixed compartment boundary can be calculated (Simons and Lam, 1980). A more preferable approach for Lake Erie is to permit the layer interface to coincide with the actual observed thermocline or with the computed thermocline position.

Computation of thermocline position can be accomplished using a one-dimensional (z) temperature model, as discussed in

Chapter 7. As indicated previously in Subsection 4.2.9, the temperature model is dependent on meteorological parameters such as the surface heat flux, and consequently, thermocline position can be estimated from year to year without detailed knowledge of the thermal structure. For the six-box model, the layer-interface for all three basins is constrained to correspond to the computed Central Basin values (see Fig. 6.3 and Sections 7.2 to 7.4).

Since the layer-interface is allowed to change dynamically in time, the vertical exchange coefficient should always be small, permitting minimum mixing across the interface. Moreover, since the upper and lower layers correspond more closely to the epilimnion and hypolimnion of the water column than in the case of a fixed position, the effects on the phosphorus concentration as a result of sediment-water interaction can be more precisely followed and monitored.

One additional complication arising from a two-layer variable interface formulation is the necessity to follow the changes in epilimnetic and hypolimnetic volumes and basin boundaries. Daily water level changes are also incorporated in the model. Figure 5.16 shows relevant basin boundaries and major components of the six-box mass balance model. Generalization of the three-box model system equations to the six-box case including the thermal stratification effects gives the following

$$\frac{d(V_{11}P_{11})}{dt} = I_1 - U_{11}A_{11}P_{11} + E_1AB_1(P_{12}-P_{11}) + W_1AB_1P_{12} - S_{11} \quad (5.20)$$

$$\frac{d(V_{12}P_{12})}{dt} = -U_{12}A_{12}P_{12} - E_1AB_1(P_{12}-P_{11}) - W_1AB_1P_{12} - S_{12} + R_1 \quad (5.21)$$

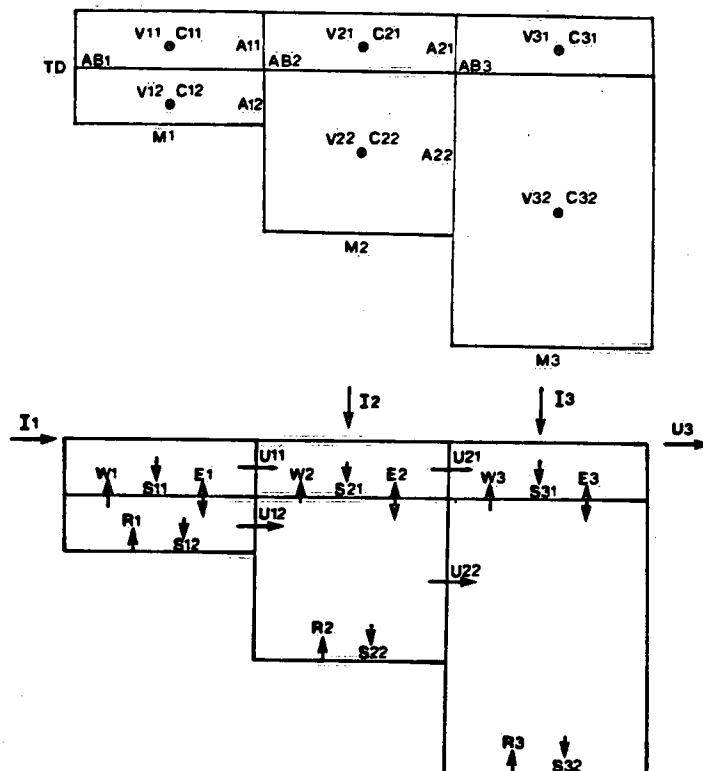


Figure 5.16. Basin boundaries and major components incorporated in the six-box mass balance model of Lake Erie.

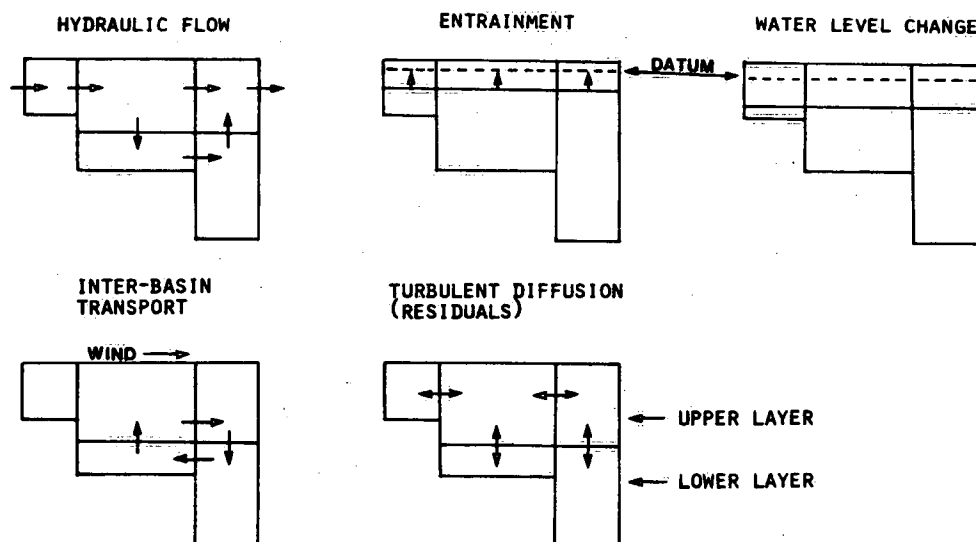


Figure 5.17. Schematic of the major processes parameterized in the six-box mass balance model of Lake Erie.

$$\frac{d(V_{21}P_{21})}{dt} = I_2 - U_{21}A_{21}P_{21} + U_{11}A_{11}P_{11} + E_2AB_2(P_{22}-P_{21}) + W_2AB_2P_{22} - S_{21} \quad (5.22)$$

$$\frac{d(V_{22}P_{22})}{dt} = -U_{22}A_{22}P_{22} + U_{12}A_{12}P_{12} - E_2AB_2(P_{22}-P_{21}) - W_2AB_2P_{22} - S_{22} + R_2 \quad (5.23)$$

$$\frac{d(V_{31}P_{31})}{dt} = I_3 + U_{21}A_{21}P_{21} - U_{33}A_{33}P_{31} + E_3AB_3(P_{32}-P_{31}) + W_3AB_3P_{32} - S_{31} \quad (5.24)$$

$$\frac{d(V_{32}P_{32})}{dt} = U_{22}A_{22}P_{22} - E_3AB_3(P_{32} - P_{31}) - W_3AB_3P_{32} - S_{32} + R_3 \quad (5.25)$$

where the symbols and notations are the same as in Equations 5.16 to 5.18, except that the second subscript 1 or 2 is used to denote the upper or lower layer, respectively. The vertical exchange coefficient is denoted by E_i and the vertical transport parameter and cross-sectional area at the thermocline interface by W_i and AB_i , $i=1,2,3$, respectively.

Figure 5.17 shows the major processes parameterized in the six-box mass balance model which include consideration of (a) hydraulic flow field, (b) vertical entrainment, (c) the water level variations, (d) interbasin transport, and (e) turbulent diffusion.

Estimation of the lake-wide daily averaged water levels was detailed in the physical data base section. The basin boundaries (Fig. 5.16) were computed from hypsometric curves referenced to the IGLD for Lake Erie, namely 173.31 m above sea level. Since limnological measurements and the thermocline computations (Section 7.3) are referenced with respect to the surface elevation, the increment in

water level, above or below 173.31 m, is added to the lower layer, and the measurements and computations are extrapolated to the added portion.

On the other hand, the layer positions are modified by the daily water level in such a way that they must be aligned with the daily surface level at the lake top, while the upper layer thickness remains unchanged as the whole thermal structure is shifted with respect to the lake bottom. Accordingly, the cross-sectional areas and volumes of each box in the model are affected by the water level changes. The cross-sectional areas, volumes and basin boundaries used in the following discussion are already modified by the daily water level variations.

5.7.1 Hydraulic flow

The lateral and vertical velocities are computed from the hydraulic flow continuity constraint and are based on observed inflow (DR) and outflow (NR) data. Note that the difference between inflow and outflow is largely responsible for the water level changes, which will be discussed in Subsection 5.7.3. For simplicity, we apportion the hydraulic flow, $Q_m = (DR+NR)/2$, for each cross-sectional boundary

$$U'_{11} = (A_{11}/A_1) \cdot Q_m \quad (5.26)$$

$$U'_{12} = Q_m - U'_{11} \quad (5.27)$$

$$U'_{21} = U'_{11} \quad (5.28)$$

$$U'_{22} = Q_m - U'_{21} \quad (5.29)$$

where U'_{ij} is the hydraulic flow at each vertical cross section $i=1,2$ and layer $j=1,2$. The sign convention is positive flow towards the Eastern Basin. Since the layer interface (thermocline) is constrained to follow the computed Central Basin values, all relevant components of the lower layer in the Western Basin are forced to zero

when the thermocline is below the maximum depth of the Western Basin. By no means can the velocities defined by Equations 5.26 to 5.29 completely represent the horizontal movements of water. If they are viewed as streamlines of the flow field, then some vertical transports (Subsection 5.7.3) are also required to maintain fluid continuity. In addition, internal flow gyres, in the form of vortex components (Subsection 5.7.2), must be used to augment these streamlines to define wind-driven circulations.

5.7.2 Interbasin transport

While internal flow gyres exist for both unstratified and stratified periods, a distinction is made here in reference to the parameterization of internal flows based on observations at the Pennsylvania Ridge (Boyce et al., 1980; Chiocchio, 1981). The convention adopted is that internal circulations between the Central and Eastern basins are considered only for the stratified period defined as the period of observation for Julian days 154 through 254.

Both hydrodynamical computations (Simons, 1976a; Lam, 1980) and observational data (Boyce et al., 1980) show deep exchange at the Pennsylvania Ridge in the direction from the East to the West basin. For example, data for 1978 have been processed (Chiocchio, 1981) and are reproduced in Fig. 5.18 as 48-hour averages. Boyce et al. (1980) have suggested that the hypolimnion flows at the Pennsylvania Ridge are related to and primarily opposed to the surface winds. Correlations show that indeed they are related, and they will be discussed in Section 5.8. These correlations then provide the daily mesolimnetic and hypolimnetic flows from meteorological data for the model computations.

Thus, for fully mixed periods, the horizontal transport velocities, U_{ij} , are simply those defined for hydraulic flow, i.e.

$$U_{ij} = U'_{ij}/A_{ij} \quad (5.30)$$

where cross-sectional areas $i=1,2$ and layers $j=1,2$ are as defined previously. For stratified periods, the net effective flow, FHV, is estimated by wind-flow correlations in the lower layer at the Pennsylvania Ridge. Note that the continuity of flow is not affected by adding an internal flow, going from Central to Eastern Basin in the lower layer, up from the lower to the upper layer in the Eastern Basin, then from Eastern to Central Basin in the upper layer, and back to the lower layer from the upper layer in the Central Basin. This internal gyre, resembling a vortex flow, is a simplified version of the flow pattern shown in the two-dimensional simulation (see Section 8.3 and Fig. 8.4). This internal flow is defined as CV, and is combined with the hydraulic flow, U'_{22} , to form the net effective flow, FHV, in the lower layer of the Central Basin

$$FHV = CV + U'_{22}$$

or

$$CV = FHV - U'_{22} \quad (5.31)$$

Thus, the horizontal transport velocities at the Pennsylvania Ridge are now defined as

$$U_{21} = (U'_{21} - CV)/A_{21} \quad (5.32)$$

$$U_{22} = FHV/A_{22} \quad (5.33)$$

The modification due to this internal flow on the vertical transport velocities will be discussed in Subsection 5.7.3. Note that the horizontal transport components are approximated by upwind weighted finite difference forms (Lam and Simons, 1976), and hence, the horizontal diffusion terms can be omitted in view of the numerical dispersion.

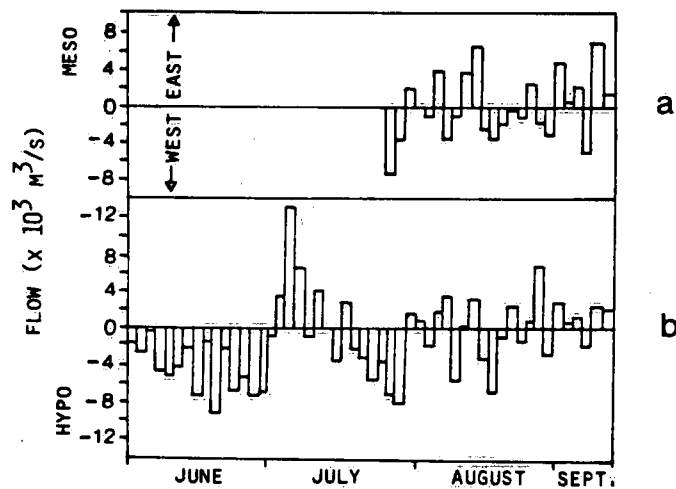


Figure 5.18. Mesolimnion and hypolimnion flow at the Pennsylvania Ridge computed as 48-hour averages for the period June through September 1978 (Chiocchio, 1981).

- (a) Mesolimnion flow at the Pennsylvania Ridge.
 (b) Hypolimnion flow at the Pennsylvania Ridge.

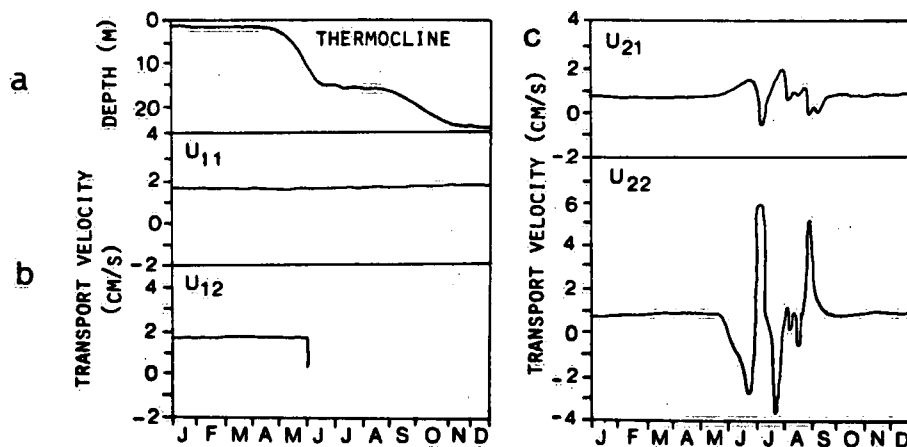


Figure 5.19. Time-series computed (five-day mean) plot of (a) the thermocline position; (b) the transport velocities U_{11} and U_{12} between the West and Central basins; and (c) the transport velocities U_{21} and U_{22} between the Central and East basins for Lake Erie, 1978 (positive values are directed eastwards).

Figure 5.19 shows a time-series plot of the 1978 thermocline position and the horizontal transport velocities. Note that there is sometimes a sizeable east to west component in the hypolimnion which may replenish the depleted oxygen in the Central Basin by transporting water containing relatively higher oxygen content from the Eastern Basin.

5.7.3 Effective vertical velocity parameter W_1 : entrainment, hydraulic flows, interbasin transports, and water levels

The daily temperatures computed by the one-dimensional thermocline model (see Section 7.3) for the Central and Eastern basins are based on a finer spatial resolution than the box models. In grouping the one-dimensional spatial details into a two-layer or three-layer structure, particularly where the layer thicknesses change dynamically with time, it is necessary to consider two types of vertical mixing mechanisms: entrainment and turbulent diffusion. Both of these mechanisms can be derived from the one-dimensional temperature results. The vertical entrainment will be discussed here, and the turbulent diffusion, in Subsection 5.7.4.

Movement of the thermocline downwards results in an entrainment of water from the lower layer to the upper layer and vice versa. Physically, this exchange of volume of water does not involve changes in horizontal transport, nor is there any actual vertical flow of water associated with it. From a modelling point of view, however, the objective is simply to redefine the thermocline for such a movement from one time step (Δt), to the next, effecting a gain of the entrained volume (and its content) to the upper layer and a loss of the same to the lower layer. Thus, it is possible to consider an effective vertical velocity parameter which will not only incorporate this effective exchange of entrained volume between the two layers but also combine with the vertical flow components in the hydraulic

flow (Subsection 5.7.1) as well as the vertical flows in the internal gyres (Subsection 5.7.2). It must be emphasized that the latter two physical movements are not related to the entrainment process. These three processes are presently linked because it is computationally convenient to combine them.

The contribution of entrainment to the effective vertical velocity parameter, W_1 , which has the dimension of a velocity (m/day), is $(dV_{1j}/dt)/AB_1$, where V_{1j} is the volume of the j th layer of the i th basin and AB_1 is the horizontal area at the thermocline. In other words, $\Delta t \cdot W_1 \cdot AB_1$ would be equivalent to the entrained volume $\Delta t \cdot (dV_{1j}/dt)$, i.e. $W_1 AB_j = dV_{1j}/dt$, had there been entrainment processes only. Indeed, if we rewrite, for example, the left-hand side of Eq. 5.23 as $d(V_{22}P_{22})/dt = V_{22}dP_{22}/dt + P_{22}dV_{22}/dt$, then $P_{22}dV_{22}/dt$ is equal to $-W_2 AB_2 P_{22}$ on the right-hand side. Since the same volume (and its content) is added to the upper layer (Eq. 5.22), the exchange of materials due to entrainment is effectively achieved.

Note that dV_{11}/dt also includes the change of water levels for the case of the upper layer. Again, it is computationally convenient to combine water level changes with the change of thermocline positions, because the thermocline positions are computed from the water surface, which changes with the water levels (Subsection 7.4.2). In unstratified periods, in order to retain a six-box model structure, the "thermocline" is artificially imposed at 1 m below the lake surface with a large vertical diffusivity (Subsection 5.7.4) to effect the fully mixed condition. Now, any change in water level will cause this artificial thermocline to move up or down in order to maintain a thickness of 1 m for the upper layer. Thus, vertical entrainment occurs because of such an artificial displacement and the effective vertical velocity parameter applies. During the stratified period, the computed thermocline positions reflect

adjustments due to actual physical processes, but the positions are still measured from the lake surface. Therefore, the effect of water levels is likewise incorporated through dV_{11}/dt and W_1 as in the unstratified case.

Recall that actual flows in the six-box model are decomposed to a streamline component and a vortex component, the horizontal portions of which have been discussed in Subsections 5.7.1 and 5.7.2, respectively. To complete the computations of the hydraulic flow and interbasin transports, W_1 must incorporate two additional contributions corresponding to the vertical portions of these flows. In the case of hydraulic flows, if the thermocline is above the maximum depth of the Western Basin, the vertical portions involve a vertical velocity of $-U'_{12}/AB_1$ at AB_1 and a vertical velocity of $+U'_{22}/AB_3$ at AB_3 (Fig. 5.16). If the thermocline (i.e. the thermocline of Central Basin; see Subsection 5.7.1) is below the maximum depth of the Western Basin, they become $-U'_{22}/AB_2$ at AB_2 and $+U'_{22}/AB_3$ at AB_3 . Of course, it is possible to adopt other hydraulic assumptions, but the constraint is that when combined with the wind-driven flow, the resultant vector of the hydraulic and wind-driven currents must be equal to the observed actual flow, FHV (Subsection 5.7.2). Under the present assumption, the contribution of the vortex component to W_1 is $-CV/AB_2$ for the Central Basin and $+CV/AB_3$ for the Eastern Basin.

In summary, the effective vertical velocity parameter, W_1 , is used to simulate the processes of entrainment, water levels, hydraulic flows and wind-driven currents through Equations 5.20 to 5.25. The time change rates of the layer volumes can be obtained from the computed layer thickness and the hypsometric curves (Fig. 1.4c). The effective velocity parameter is, for the fully mixed periods, defined as:

$$W_1 = \left(\frac{dV_{11}}{dt} - U'_{12} \right) / AB_1 \quad (5.34)$$

$$W_2 = \frac{dV_{21}}{dt} / AB_2 \quad (5.35)$$

$$W_3 = \left(\frac{dV_{31}}{dt} + U'_{22} \right) / AB_3 \quad (5.36)$$

For the stratified period, the additional volume of water as a result of the imposed internal gyre of flow strength, CV, is accounted for by redefining W_2 and W_3 as

$$W_2 = \left(\frac{dV_{21}}{dt} - CV \right) / AB_2 \quad (5.37)$$

$$W_3 = \left(\frac{dV_{31}}{dt} + CV + U'_{22} \right) / AB_3 \quad (5.38)$$

5.7.4 Turbulent diffusion

The term "turbulent diffusion" is often used loosely to denote the residual fluctuation component, when the averaged mean component is isolated from a turbulent flow field. In the context of the six-box or the nine-box model, if the entrainment velocity represents the averaged condition, then the vertical turbulent diffusion is the residual component obtainable by isolating the mean entrainment transport from the one-dimensional temperature results. Specifically, let T_{ij} denote the temperature in the i th basin and j th layer, $i=1,2,3$ and $j=1,2$, and let E_i denote the vertical turbulent diffusion velocity (m/day) at the i th interface. Furthermore, let \bar{E}_i denote the mean entrainment of heat, and let the symbol \sim denote quantities at $t+\Delta t$, where t is time and Δt is the

increment in time, say, one day. Then, consider the lower layer, i.e. $j = 2$, for the i th basin

$$\bar{E}_1 = (\tilde{V}_{12} - V_{12}) T_{12} \quad \text{if } \tilde{V}_{12} \leq V_{12} \quad (5.39)$$

$$\bar{E}_1 = (\tilde{V}_{12} - V_{12}) T_{11} \quad \text{if } \tilde{V}_{12} > V_{12} \quad (5.40)$$

The heat balance equation for the lower layer, assuming the lateral heat transport is negligible, is

$$\tilde{V}_{12} \tilde{T}_{12} = V_{12} T_{12} + \bar{E}_1 \Delta t - E_1 \cdot AB_1 (T_{12} - T_{11}) \cdot \Delta T \quad (5.41)$$

so that

$$E_1 = \left(\bar{E}_1 - \left(\frac{d(V_{12} T_{12})}{dt} \right) \right) / AB_1 \quad (5.42)$$

for $i=1,2,3$. Note that t is in days, T_{1j} in $^{\circ}\text{C}$, V_{1j} in m^3 , and AB_1 in m^2 , then the "heat" content is in $^{\circ}\text{Cm}^3$; to obtain units in calories, multiplication of the heat balance equation above by water density and specific heat is necessary. The turbulent diffusion velocity, E_1 , is mainly used in the six-box mass balance model to bring about the full mixing condition, in which case a value of 10 m/day has been taken as its arbitrary upper limit. During stratification, the vertical entrainment component, along with the vertical hydraulic and internal flow transport component, is more important. Indeed, the turbulent diffusion velocity approaches zero during this period and a restriction on negative values must be imposed.

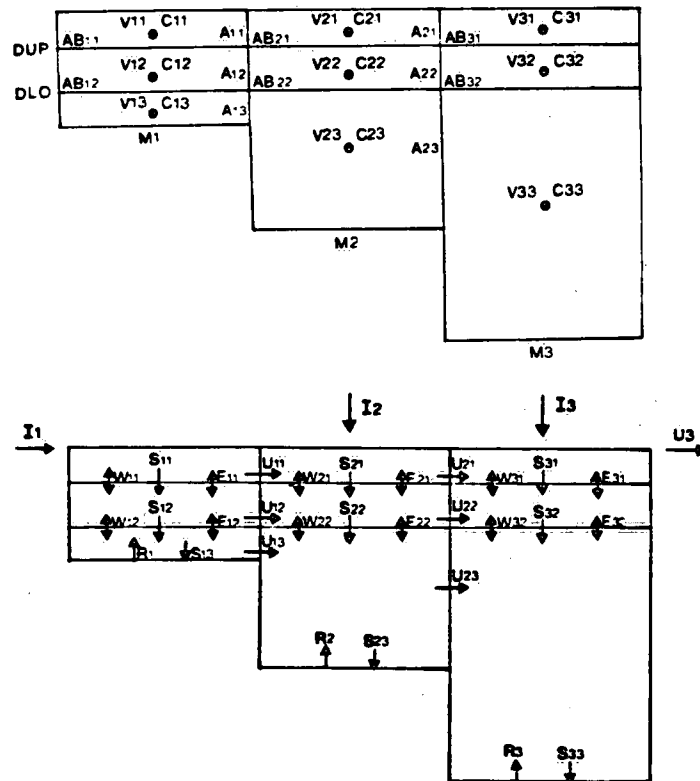


Figure 5.20. Basin boundaries and major components incorporated in the nine-box mass balance model of Lake Erie.

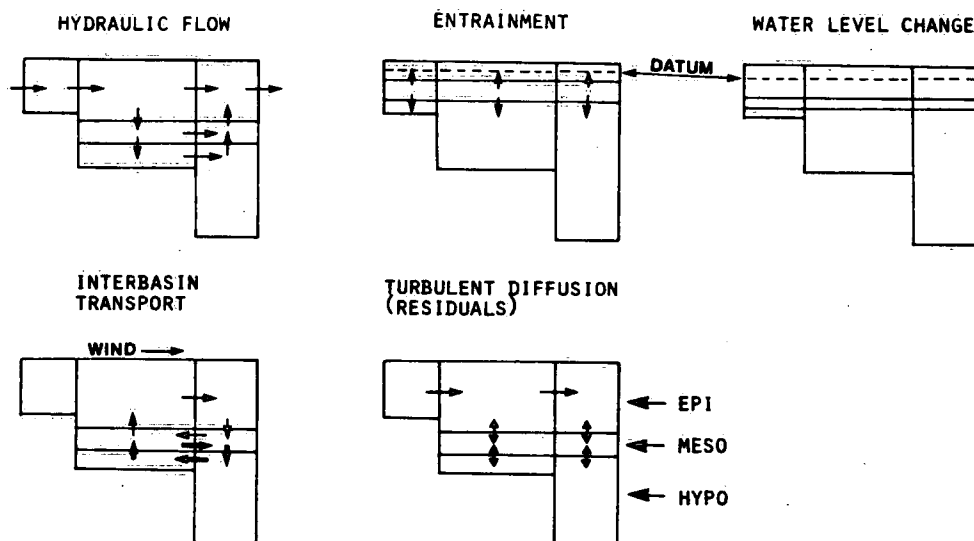


Figure 5.21. Schematic of the major processes parameterized in the nine-box mass balance model of Lake Erie.

5.8 Nine-Box Model

The six-box model for Lake Erie is the most general framework which incorporates a thermal stratification feature as well as the interbasin transports. To simulate the thermal structures with greater accuracy requires increasing model complexity with inclusion of more vertical detail. This is accomplished by including the feature of a mesolimnion by adding another layer between the epilimnion and hypolimnion, forming a three-layered nine-box model.

The six-box model allows consideration of processes in the presence of thermal stratification via separation of the water column by a one-layer interface analogous to a thermocline. However, the transports between the Central and Eastern basins mainly occur in the mesolimnia of these two basins compared with what has been defined as the hypolimnion in the six-box model. Thus, by inclusion of a middle layer, the transports can be more completely described.

Derivation of the upper and lower mesolimnion interface is accomplished with the one-dimensional thermocline model described in Chapter 7. It is assumed that the Central Basin thermal structure can be extended over all basins and that the vertical transport components will compensate for this simplification.

Basin boundaries (Fig. 5.20) between compartments are allowed to change with time in response to changes in mesolimnion interface depths, and as discussed previously, water level effects are added to the lower layer. The components of the nine-box mass balance model are given schematically in Fig. 5.20. The system equations describing the nine-box model are

$$\frac{d(V_{11}P_{11})}{dt} = I_1 - U_{11}A_{11}P_{11} + E_{11}AB_{11}(P_{12} - P_{11}) + W_{11}AB_{11}P_{12} - S_{11} \quad (5.43)$$

$$\frac{d(V_{12}P_{12})}{dt} = - U_{12}A_{12}P_{12} - E_{11}AB_{11}(P_{12}-P_{11}) + E_{12}AB_{12}(P_{13}-P_{12}) - W_{11}AB_{11}P_{12} + W_{12}AB_{12}P_{13} + S_{11} - S_{12} \quad (5.44)$$

$$\frac{d(V_{13}P_{13})}{dt} = - U_{13}A_{13}P_{13} - E_{12}(P_{13}-P_{12}) - W_{12}AB_{12}P_{13} - S_{12} + R_1 \quad (5.45)$$

$$\frac{d(V_{21}P_{21})}{dt} = I_2 - U_{21}A_{21}P_{21} + U_{11}A_{11}P_{11} + E_{21}AB_{21}(P_{22}-P_{21}) + W_{21}AB_{21}P_{22} - S_{21} \quad (5.46)$$

$$\frac{d(V_{22}P_{22})}{dt} = - U_{22}A_{22}P_{22} + U_{12}A_{12}P_{12} - E_{21}AB_{21}(P_{22} - P_{21}) + E_{22}AB_{22}(P_{23}-P_{22}) - W_{21}AB_{21}P_{22} + W_{22}AB_{22}P_{23} - S_{22} \quad (5.47)$$

$$\frac{d(V_{23}P_{23})}{dt} = - U_{23}A_{23}P_{23} + U_{13}A_{13}P_{13} - E_{22}AB_{22}(P_{23}-P_{22}) - W_{22}AB_{22}P_{23} - S_{23} + R_2 \quad (5.48)$$

$$\frac{d(V_{31}P_{31})}{dt} = I_3 + U_{21}A_{21}P_{21} - U_{31}A_{31}P_{31} + E_{31}AB_{31}(P_{32}-P_{31}) + W_{31}AB_{31}P_{32} - S_{31} \quad (5.49)$$

$$\frac{d(V_{32}P_{32})}{dt} = U_{22}A_{22}P_{22} - E_{31}AB_{31}(P_{32}-P_{31}) - W_{31}AB_{31}P_{32} - S_{32} \quad (5.50)$$

$$\frac{d(V_{33}P_{33})}{dt} = U_{23}A_{23}P_{23} - E_{32}AB_{32}(P_{33}-P_{32}) - W_{32}AB_{32}P_{33} - S_{33} + R_3 \quad (5.51)$$

Figure 5.21 shows the major processes parameterized in the nine-box mass balance model. Again, the lateral and vertical velocities are computed from the hydraulic flow continuity constraint. The hydraulic flow $Q_m = (DR + NR)/2$ is apportioned for each vertical cross section as:

$$U'_{11} = (A_{11}/A_1) \cdot Q_m \quad (5.52)$$

$$U'_{12} = (A_{12}/A_1) \cdot Q_m \quad (5.53)$$

$$U'_{13} = Q_m - U'_{11} - U'_{12} \quad (5.54)$$

$$U'_{21} = U'_{11} \quad (5.55)$$

$$U'_{22} = U'_{12} \quad (5.56)$$

$$U'_{23} = Q_m - U'_{21} - U'_{22} \quad (5.57)$$

where components and subscripts are as defined previously for basin and layers. Vertical transports required to maintain continuity are described later.

As in the case of the six-box model, the interbasin horizontal transport velocities are defined for each vertical cross section for the unstratified and stratified periods taken as Julian days 154 to 254 due to data constraints. Layer interfaces for the unstratified or weakly stratified periods are imposed for calculation conveniences only, and horizontal transports are defined from the hydraulic flow values as:

$$U_{ij} = U'_{ij}/A_{ij} \quad (5.58)$$

where U_{ij} represents the horizontal transport velocity and the other components are as previously given.

In the stratified period for 1978, observations were made of the mesolimnion and hypolimnion flow at the Pennsylvania Ridge (Fig. 5.18). In most cases, the deep flow opposes the hydraulic flow, and this is accounted for by imposing an internal circulation which represents a gyre restricted to rotate between the Central and Eastern basins about the mesolimnion boundaries. We define an internal circulation for the lower mesolimnion boundary as:

$$CV = FHV - U'_{23} \quad (5.59)$$

and for the upper mesolimnion boundary as:

$$BV = FMV - U'_{22} + CV \quad (5.60)$$

where CV and BV are flows and FHV and FMV represent observed transports for the hypolimnion and mesolimnion, respectively, at the Pennsylvania Ridge. Finally, horizontal transport velocities between Central and Eastern basins are redefined for the stratified period as:

$$U_{21} = (U'_{21} - BV)/A_{21} \quad (5.61)$$

$$U_{22} = FMV/A_{22} \quad (5.62)$$

$$U_{23} = FHV/A_{23} \quad (5.63)$$

Observation of the deep flow at the Central and Eastern Basin boundary was conducted only in 1978 for sufficient duration for application in the mass balance models. For analysis of the long-term period 1967 to 1978, relationships are formed to describe the general exchange at the Pennsylvania Ridge.

Boyce et al. (1980) and Chiochio (1981) formed consecutive 48-hour averages of temperature, wind and currents from meteorological buoy and EBT observations. The averaging period contained three full cycles of the dominant inertial frequency, and it was assumed that the averaged values would respond to major atmospheric forcings and to large-scale adjustments of the lake. Analyses of these data showed that flows in the deeper portions of the Pennsylvania Channel oppose the wind. One conclusion of these studies was that exchanges at the lower layers of the Pennsylvania Ridge are correlated with meteorological factors such as the strength and persistence of the down-lake (eastwards) component of the wind. In addition, the integrated effects of heat and momentum flux are also postulated as having an important role in determining the magnitude of the interbasin deep water exchange (Boyce et al., 1980).

As a first approximation to the deep exchange at the Pennsylvania Ridge, 48-hour averages of the 1978 estimated hypolimnion flow from June 1 to September 11 (Chiocchio, 1981) were plotted against two-day mean east component winds (along lake axis) determined from Long Point observations. Figure 5.22 shows all of the available data for the observation period. The large scatter of values is attributable to periods in which the flow field has not adjusted to the meteorological forcings at the lake surface. However, selection of events in which relatively high wind speeds and persistent wind directions occurred gives a general relationship between the surface winds and deep flow.

Analysis of the 1978 data at the Pennsylvania Ridge shows that mesolimnion velocities and flows are generally correlated to hypolimnion values. Consequently, if hypolimnion flows can be approximated from Long Point wind data, a first estimate of the mesolimnion flow can be derived (Fig. 5.23). In this manner, the layered mass balance box models can be extended over the years in which observations of the deep flow at the Pennsylvania Ridge are lacking.

As in the six-box model, movement of the layer interface downward induces a vertical transport of water upwards and vice versa. In the three-layer case, the interfaces may move in the same direction simultaneously without causing a volume change in the middle layer or, alternatively, movement of the interfaces may be such to increase or decrease mesolimnion volume. Volumes of the other layers will change accordingly. To account for these possibilities, the effective vertical transport velocity parameter W_1 (see Subsection 5.7.3) is computed from the lower layer upwards for each basin. For unstratified or weakly stratified periods, the vertical transport velocity parameter is computed for each layer as:

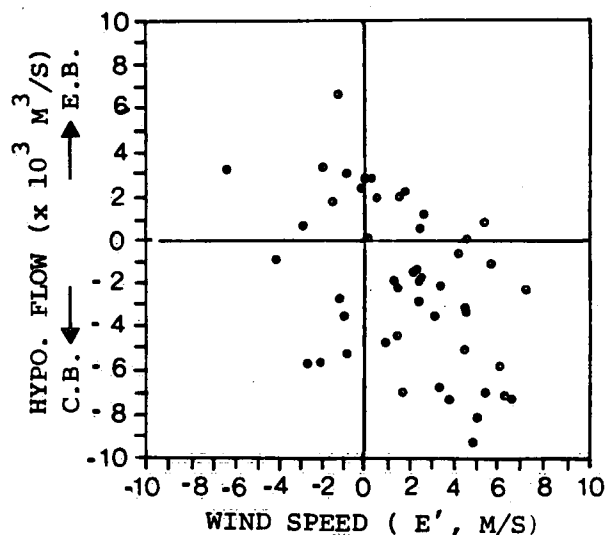
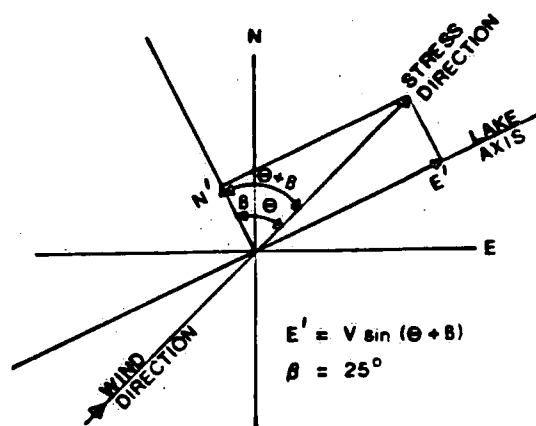


Figure 5.22. Relationship between two-day averaged east component winds from Long Point and two-day average hypolimnion flow at the Pennsylvania Ridge in the period June to September, 1978.

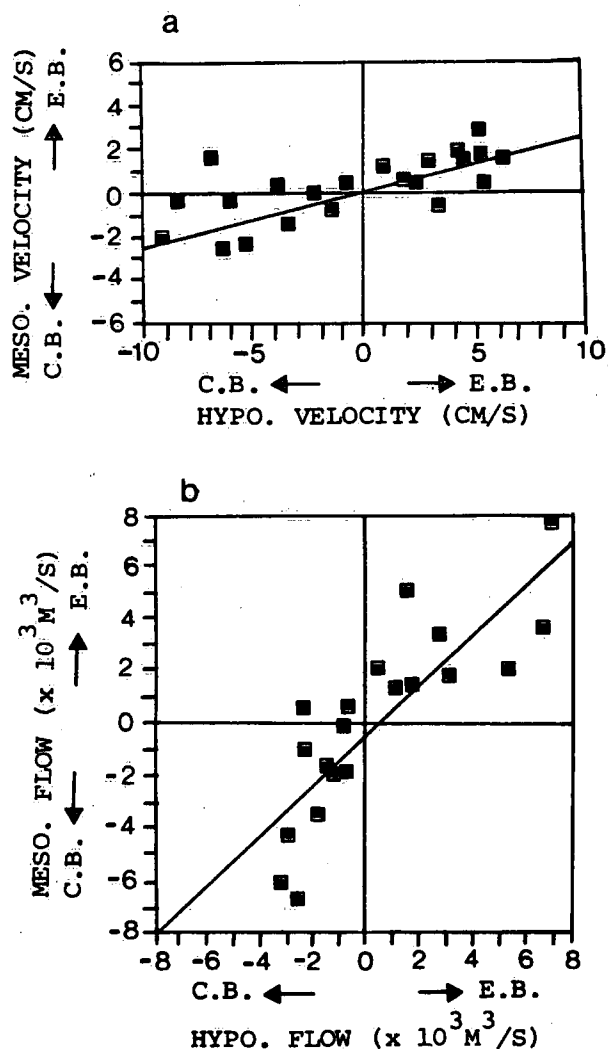


Figure 5.23. Relationship between 48-hour averages of (a) computed mesolimnion velocities to hypolimnion velocities and (b) computed mesolimnion flow to hypolimnion flow, at the Pennsylvania Ridge during the period June to September in 1978 (data: Chiocchio, 1981).

$$W_{12} = \left(-\frac{dV_{13}}{dt} - U'_{13} \right) / AB_{12} \quad (5.64)$$

$$W_{11} = \left(-\frac{dV_{12}}{dt} + W_{12} - U'_{12} \right) / AB_{11} \quad (5.65)$$

$$W_{22} = -\frac{dV_{23}}{dt} / AB_{22} \quad (5.66)$$

$$W_{21} = \left(-\frac{dV_{22}}{dt} + W_{22} \right) / AB_{21} \quad (5.67)$$

$$W_{32} = \left(-\frac{dV_{33}}{dt} + U'_{23} \right) / AB_{32} \quad (5.68)$$

$$W_{31} = \left(-\frac{dV_{32}}{dt} + W_{32} + U'_{22} \right) / AB_{31} \quad (5.69)$$

For stratified conditions, the additional volumes of water as a result of the internal circulations at the Pennsylvania Ridge are accounted for by redefining W_{ij} for the Central and Eastern basin boundaries as:

$$W_{22} = \left(-\frac{dV_{23}}{dt} - CV \right) / AB_{22} \quad (5.70)$$

$$W_{21} = \left(-\frac{dV_{22}}{dt} + W_{22} + CV \right) / AB_{21} \quad (5.71)$$

$$W_{32} = \left(-\frac{dV_{33}}{dt} + CV + U'_{23} \right) / AB_{32} \quad (5.72)$$

$$W_{31} = \left(-\frac{dV_{32}}{dt} - CV + W_{32} + U'_{22} \right) / AB_{31} \quad (5.73)$$

In terms of the eddy diffusion for the nine-box model, similar formulations can be made by extending those in the six-box model. Again, the computation should start from the bottom layer. Let E_{ij} and \bar{E}_{ij} denote the turbulent diffusion velocities and mean entrainment of heat for the i th basin and j th interface. Then, for the hypolimnion, for $i=1,2,3$

$$E_{i2} = (\bar{E}_{i2} - (\frac{d V_{i3} T_{i3}}{dt})) / AB_{i2} \quad (5.74)$$

$$E_{i1} = (\bar{E}_{i1} - \frac{d V_{i2} T_{i2}}{dt} + E_{i2} AB_{i2}) / AB_{i1} \quad (5.75)$$

Again, similar upper and lower bounds have to be imposed on the computed vertical diffusion coefficients, as in the case of the six-box model.

Prognostic Mass Balance Models

6.1 Introduction

The mass balance models discussed in Sections 5.5 to 5.8 refer to the diagnostic use of the mass balance equation as applied to individual water quality variables. The prognostic use of the mass balance models, on the other hand, assumes that the time change in concentration of the water quality variable is not known and must be obtained by solving the mass balance equation. To enable the solution to be found, not only would the input loading be assumed known but so would the biochemical kinetics, sediment-water interactions, and physical transports. The implementation of these limnological processes in the Lake Erie prognostic mass balance models will be the main discussion of this chapter.

The Lake Erie prognostic modelling approach has three salient features. The first feature is to allow the thicknesses of the epilimnion, mesolimnion and hypolimnion to change in time during the simulation, by using the results from a thermocline model (see Chapter 7). This implies that the homogeneous zones chosen as the boxes in mass balance calculations change in time, area and volume as the computations proceed, so that the limnological dynamics of the water quality variables are subject to less spatial inaccuracy. The second feature of the Lake Erie prognostic models is that the water temperature, interbasin transport, wind-wave turbulence and other physical processes used in the models are computed directly from meteorological parameters, external to the lake. This eliminates the need to use observed lake data of temperature or conservative tracers to establish such physical processes as turbulent eddy diffusion. Consequently, forecasts of lake water quality depend on projected

loading and long-term weather forecasts, rather than on the extrapolation of existing cruise data. There is, however, the option to utilize observed data to optimize the meteorological inputs, such as heat fluxes. The third feature is that the models are first calibrated with short-term data, i.e., those collected from the Central Basin and Eastern Basin of Lake Erie for 1978. This allows the subsequent verification, not only for these two basins but also for the Western Basin as an independent test case. The data collected at CCIW for 1967 to 1977 are then used for the long-term verification to establish the predictive capability of the models.

In this chapter, the calibration and verification results of a six-box model will be presented, i.e., by dividing the lake into three basins, each of which consists of two layers separated by the thermocline. The two-component phosphorus model (Simons and Lam, 1980) developed for Lake Ontario is adopted for Lake Erie, with a new component of dissolved oxygen added to it. Thus, there are six boxes representing the homogeneous zones of the lake, and there are three variables - soluble reactive phosphorus, organic phosphorus and dissolved oxygen - in each of the boxes. To investigate the advantages and disadvantages of increasing the spatial complexity of this model, we extend the six-box model to a nine-box model which also consists of three basins, but each of which is now composed of three layers: epilimnion, mesolimnion and hypolimnion. The number of water quality variables remains unchanged in this nine-box model. Of course, it is possible to include other variables, e.g. nitrogen and silica, but there are already several major uncertainties with the phosphorus system (Simons and Lam, 1980).

In Section 6.2, the six-box model will be discussed with emphasis on the dynamic features of the thermocline and its effects on the water quality variables. In Section 6.3, the nine-box model is shown to have a better spatial resolution, and the effects of dynamic

thermal layers will be further explained. The results of calibration and verification of those two models will be contrasted, particularly in their capability to simulate the loading and meteorological effects on total phosphorus concentration and the oxygen depletion conditions. Sensitivity analysis, relative errors, application and senario tests of the models will be discussed later in Chapter 9. The incorporation of finer spatial details, e.g. nearshore-offshore transports and sediment-water interactions, will be discussed in Chapter 8.

6.2 Six-Box Three-Variable Model

In Simons and Lam (1980), a phosphorus model was developed for Lake Ontario and verified with data for 1972 through 1977. The lake was divided into upper and lower layers separated at the thermocline, corresponding approximately to, but not exactly being the same as the epilimnion and hypolimnion. Two forms of phosphorus were considered, namely soluble reactive phosphorus (SRP) and organic phosphorus (OP). The total phosphorus (TP) was considered as the sum of (SRP) and (OP), while the particulate phosphorus (PP) was obtained from an empirical relationship, $(PP) = (OP) - 5$, expressed in $\mu\text{g/L}$. It was shown that the conversion of SRP to OP, and vice versa, depends on a critical balance of uptake and regeneration. Apparently, there were many possible ways of formulating these factors. Nevertheless, apart from this uncertainty of formulation, the two-compartment model appeared to explain the seasonal cycles and the six-year (1972-1977) downward trend of the phosphorus concentrations in Lake Ontario quite satisfactorily. The application of this two-layered two-compartment model to Lake Erie, however, requires a number of major modifications.

Because of the basin topography (see Section 1.2), it is not possible to use the lake-wide mean concentrations. A six-box or

nine-box model is required for Lake Erie. Another major change is to allow the thicknesses of the upper and lower layers to vary in time. This change is necessary because, for example, the thickness of the lower layer can vary from 1 m to 24 m in the Central Basin, whereas the maximum depth is only 25 m. The error due to excessive diffusion would be large in Lake Erie models, if the thermocline were fixed at only one depth, as in the case of the Lake Ontario model (Simons and Lam, 1980). This error can be avoided by using the concept of vertical entrainment. That is, when the thermocline moves downward, the volume of water traversed in the lower layer by the thermocline is entrained to the upper layer, and vice versa, when the thermocline moves upward. The detailed mechanisms of the entrainment and other physical processes for the six-box model have been discussed in Subsection 5.7.3 for a single variable, such as total phosphorus. In prognostic models, these processes are simulated for all of the model variables.

The other modification to the model of Simons and Lam is the inclusion of the dissolved oxygen as a variable in the model, since oxygen depletion, particularly in the Central Basin hypolimnion, has been considered as a major water quality problem of the lake. There has been some controversy over the causes of oxygen depletion in Lake Erie. Charlton (1980) correlated oxygen depletion rate to the hypolimnion thickness, Rosa and Burns (1981) stressed the effects of interbasin and vertical transports, and Di Toro and Connolly (1980) proposed the reduction of oxygen depletion by reducing total phosphorus loading. Thus, it seems inevitable to include dissolved oxygen as the third variable in the Lake Erie model. Since the Lake Erie model has now encompassed all these different aspects of oxygen depletion, careful calibration and verification of the model will clarify these controversies (see also Section 9.4) .

6.2.1 Model structure

Figure 6.1 shows the schematic for the biochemical kinetics of the three variables for a typical basin with a two-layered structure. It is understood that the physical processes such as entrainment, advection, diffusion and interbasin transports have been calculated. Table 6.1 contains the equations for the kinetics depicted in Figure 6.1. At the upper layer, the oxygen is produced by photosynthesis and reaeration at the lake surface, with plankton respiration and some sediment oxygen demand as removal processes. Most of the time, oxygen is saturated or even supersaturated in the upper layer and the saturation is a function of the water temperature. At the lower layer, photosynthesis can occur, since this layer may still be within the photic zone, particularly at the early part of the stratification period. As in the case of Lake Ontario, plankton respiration activity is reduced in the lower layer because of lower temperature and smaller particulate particle size. While there is no reaeration of oxygen in the lower layer, there is a persistent sediment oxygen demand as well as a water oxygen demand mainly resulting from plankton respiration. The sediment oxygen demand is formulated as in Snodgrass (1982) with a rate of $k_s = 0.5 \text{ g/m}^2 \text{ day}$ and a half-saturation oxygen concentration of $K_o = 1.4 \text{ mg/L}$ (Table 6.1a). For the two phosphorus forms, again because of the dynamic change in layer thickness, uptake and respiration can occur in both upper and lower layers. The loadings of soluble reactive phosphorus and organic phosphorus are assumed to enter the upper layer of each basin. A return component for soluble reactive phosphorus is included for the detrital decay at the sediment-water interface. The return rate, r_p , is usually small ($0.0001 \text{ g/m}^2 \text{ day}$) and could be considered as part of the plankton respiration activities but becomes large ($0.0044 \text{ g/m}^2 \text{ day}$) during anoxic conditions (Nriagu and Dale, 1974). Because of the two-layered structure, anoxia is assumed to occur at 1.5 mg/L oxygen in the lower layer. Settling of the particulate phosphorus may

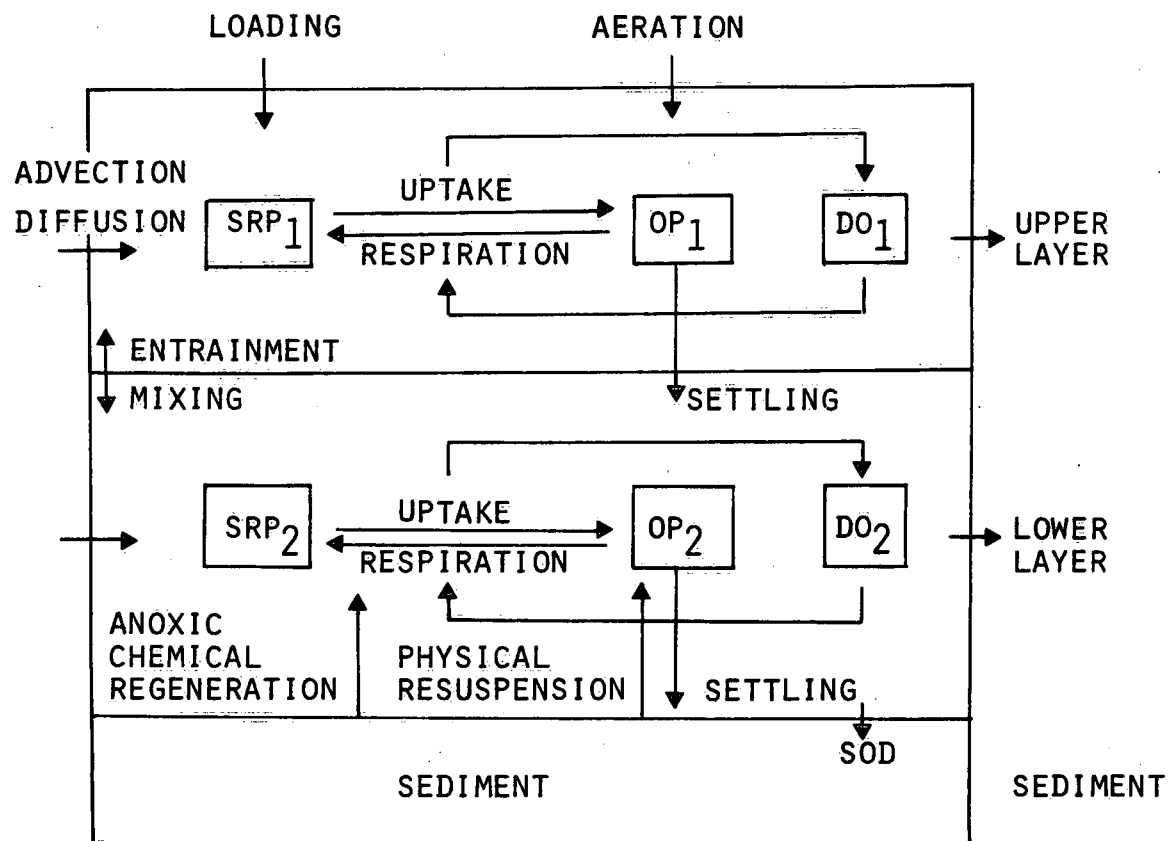


Figure 6.1. Model structure of the six-box three-variable model in a typical water column.

Table 6.1a. Equations of Six-Box Three-Variable Model

$$\frac{d(V_1)(SRP_1)}{dt} = F_1(SRP_1) - U_1 + R_1 + r_p(AB_0 - AB_1)$$

$$\frac{d(V_2)(SRP_2)}{dt} = F_2(SRP_2) - U_2 + R_2 + r_p AB_2$$

$$\frac{d(V_1)(OP_1)}{dt} = F_1(OP_1) + U_1 - R_1 + r_w(AB_0 - AB_1) - \sigma_1 AB_0(OP_1 - 5)$$

$$\frac{d(V_2)(OP_2)}{dt} = F_2(OP_2) + U_2 - R_2 + r_w AB_2 + \sigma_1 AB_1(OP_1 - 5) - \sigma_2 AB_1(OP_2 - 5)$$

$$\frac{d(V_1)(DO_1)}{dt} = F_1(DO_1) + [f_{po}(U_1 - R_1) - k_s(AB_0 - AB_1)] \frac{DO_1}{DO_1 + K_o} + r_A AB_0(DO_s - DO_1)$$

$$\frac{d(V_2)(DO_2)}{dt} = F_2(DO_2) + [f_{po}(U_2 - R_2) - k_s AB_2] \frac{DO_2}{DO_2 + K_o}$$

Note: The subscripts 1 and 2 denote first and second layers; the subscript 0 denotes surface quantity; SRP, OP and DO are concentrations of soluble reactive phosphorus, organic phosphorus and oxygen, respectively; T is temperature in °C; AB and V are area and volume; F is physical and loading source term; U and R are uptake and respiration in plankton; r_p is phosphorus return from sediment per area; r_w is phosphorus resuspended by wind waves; σ is settling velocity; f_{po} is phosphorus to oxygen ratio in photosynthetic production of chlorophyll; k_s is sediment oxygen demand; K_o is half-saturation coefficient for oxygen; DO_s is saturated oxygen concentration; r_A is reaeration coefficient.

Table 6.1b. Constants and Formulas of Six-Box Three-Variable Model

$$U_1 = 0.43 \rho_1 (1.07)^{T_1} \frac{SRP_1}{SRP_1 + 0.5} (OP_1 - 5) V_1 \quad (\rho = \text{light factor, Eq. (4.5)})$$

$$U_2 = 0.6 \rho_2 (1.07)^{T_2} \frac{SRP_2}{SRP_2 + 0.5} (OP_2 - 5) V_2$$

$$R_1 = 0.02 (1.07)^{T_1} (OP_1 - 5) V_1$$

$$R_2 = 0.002 (1.07)^{T_2} (OP_2 - 5) V_2$$

$$\sigma_1 = 0.2; \sigma_2 = 0.4 \text{ (m/day)}$$

$$r_w = 0.001 W/W_s; W_s = 5 \times 10^5 \text{ m/day}; W = \text{wind speed (m/day)}; (r_w = \text{g/m}^2\text{day})$$

$$r_A = 2 \text{ m/day}; k_s = 0.5 \text{ g/m}^2\text{day}; K_o = 1.4 \text{ mg/L}; f_{po} = 140;$$

$$r_p = 0.0001 \text{ g/m}^2\text{day} \text{ (0.0044 g/m}^2\text{day if } DO_2 < 1.5 \text{ mg/L)}$$

occur to the sides of the basin (since the surface area, AB_0 , may not be the same as the interfacing area, AB_1 , at the thermocline), and may also occur through AB_1 and enter the lower layer. Because the layer thicknesses change with time, so would the interfacing area AB_1 , so that the portion of particulate phosphorus which settles on the sides may increase as the thermocline moves downward. To account for the physical resuspension (r_w) of phosphorus from the sediment, a simple formula (Somlyódy, 1979) based on the study of Lam and Jaquet (1976) is used in the model (Table 6.1b).

6.2.2 Calibration

The data collected at NWRI from seven cruises for the year 1978 are used for calibration of the six-box three-variable model. Measurements in this year were conducted primarily in the Central and Eastern basins, with the purpose of an extensive analysis of the water quality in these two basins. The absence of data for the Western Basin in 1978 should not affect the calibration of the model and actually can be left as an area for verification using data from previous years. The model constants are given in Table 6.1 after calibration with 1978 data. Essentially, those constants which originated from the Lake Ontario model (Simons and Lam, 1980) are kept the same, e.g. the settling velocities σ_1 and σ_2 are 0.2 and 0.4 m/day for the upper and lower layers, respectively. The uptake and respiration coefficients for the upper layer are the same as the Lake Ontario model, but changes were made to improve the uptake rate and to suppress respiration at the lower layer. The phosphorus regeneration rate from the sediment is based on the values reported for oxic and anoxic condition in Project Hypo (Burns and Ross, 1972). The sediment oxygen demand required to contribute to the oxygen depletion in the six-box model is $0.5 \text{ mg O}_2 \text{ m}^{-2} \text{ day}^{-1}$. It was believed that most of the sources of oxygen due to physical transport, entrainment and diffusion have been more appropriately accounted for by using the

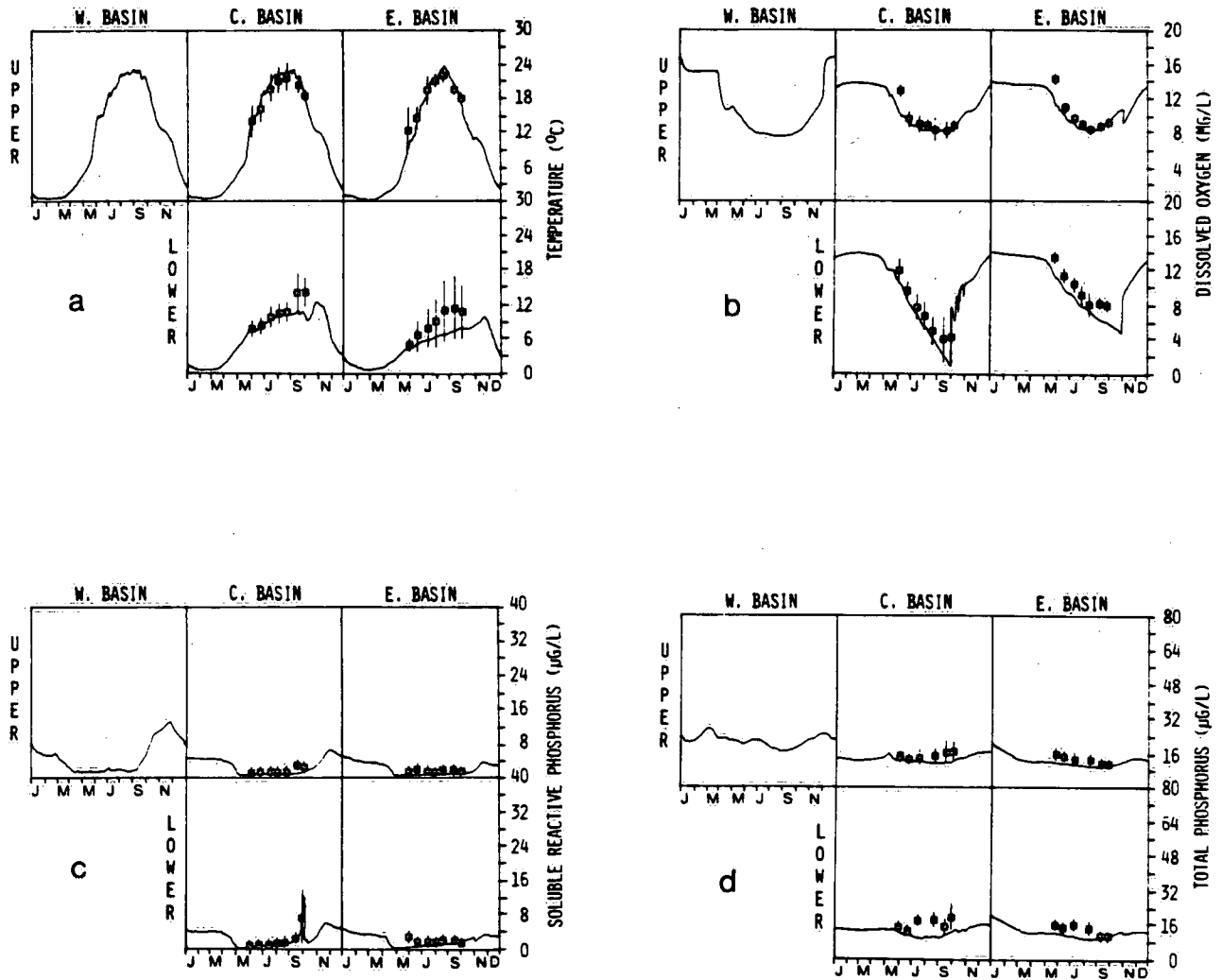


Figure 6.2. Calibration of the six-box model using 1978 data:

(a) temperature; (b) dissolved oxygen; (c) soluble reactive phosphorus; (d) total phosphorus.

(—■—) observed values
(——) computed values

dynamic thermal layers approach than by using the fixed layer approach. However, as discussed later in the nine-box model (Section 6.3), this sediment oxygen demand is probably too high, because extraneous sources of oxygen still exist mainly through "leaky" diffusive processes in the six-box model. All the meteorological data such as air temperature, wind and solar radiation are observed daily values for 1978 (Fig. 4.13) and used in the model. The phosphorus loading data for 1978 (Figures 2.5 and 2.6) are used in the simulation. Figures 6.2a,b, c and d show, respectively, the calibrated results for 1978 for temperature, dissolved oxygen, soluble reactive phosphorus and total phosphorus. The results for the Western Basin hypolimnion are not shown, because it is too shallow and exists only briefly. The temperature is volume-averaged, obtained from the one-dimensional thermocline model (see Chapter 7) and is based on the computed thicknesses of the upper and lower layers from the same model. All observed data are interpolated values, using the chemical interpolation program, TWIST, as described in the Appendix, and are averaged over the computed layer thicknesses. As shown in Fig. 6.2a, the computed temperature agrees satisfactorily with the observed data, but is over-predicted in the Eastern Basin lower layer. The computed oxygen concentration (Fig. 6.2b) compares well with the observed data in the upper layer. Note that the variations measured by the standard deviation of the observed oxygen data in the upper layer are rather small, indicating the homogeneity of the data in this layer. A large variation on the observed oxygen can be seen in the lower layer, and the computed oxygen concentration is within the standard deviations except for the Eastern Basin. Thus, the predicted oxygen is rather sensitive to the predicted temperature. The soluble reactive phosphorus concentrations (Fig. 6.2c) are rather low, about 1 to 2.5 $\mu\text{g/L}$, during the stratification period for both the computed and the observed values for all layers. While this is expected for the upper layer because of active uptake, the low values for the lower layer

indicate that photosynthesis or a rapid loss mechanism may occur as discussed in Subsection 3.2.3. There is a brief period of anoxic condition, as reflected in a sediment regeneration of soluble reactive phosphorus and low oxygen concentration, towards the end of September. For the total phosphorus simulation, as the sum of SRP and OP, the computed values agree well with the observed data (Fig. 6.2d). Note that the level of total phosphorus concentration is about 15 $\mu\text{g/L}$ for the stratified period, as compared with the SRP concentration of 1 to 2.5 $\mu\text{g/L}$.

6.2.3 Long-term simulation: 1967 to 1978

The data discussed in Chapter 3 for 1967 to 1977 are used for verification of the six-box three-variable model. The model constants are all kept the same as calibrated, but the interpolated loading data for total phosphorus and soluble reactive phosphorus are used as discussed in Subsections 2.3.1 and 2.3.2 for the eleven-year period. Furthermore, the meteorological data prepared as daily values for each of the three basins, including wind, air temperature, water level, inflow and outflow, solar radiation, heat inputs and light factor for primary production (Eq. 4.5), as discussed in Section 4.2, are all used in the model. These meteorological data are also used in the one-dimensional model and produce the computed water temperatures as averaged daily values for all the dynamic layers or boxes. Thus, the water temperature so computed is dependent on the daily meteorological inputs only, without the dependence on measured water temperature (see Chapter 7). An important output from the meteorologically driven thermocline model is the computed thermal layer thicknesses. As will be discussed in Section 7.2, the thermal eddy diffusivity used in the thermocline model is composed of three segments: the wind mixing and thermal buoyancy regime, the internal wave oscillation regime, and the bottom turbulence regime. Recognizing that definition of thermal layers in the lake is rather subjective and sometimes difficult or ambiguous, these three physically defined regimes offer

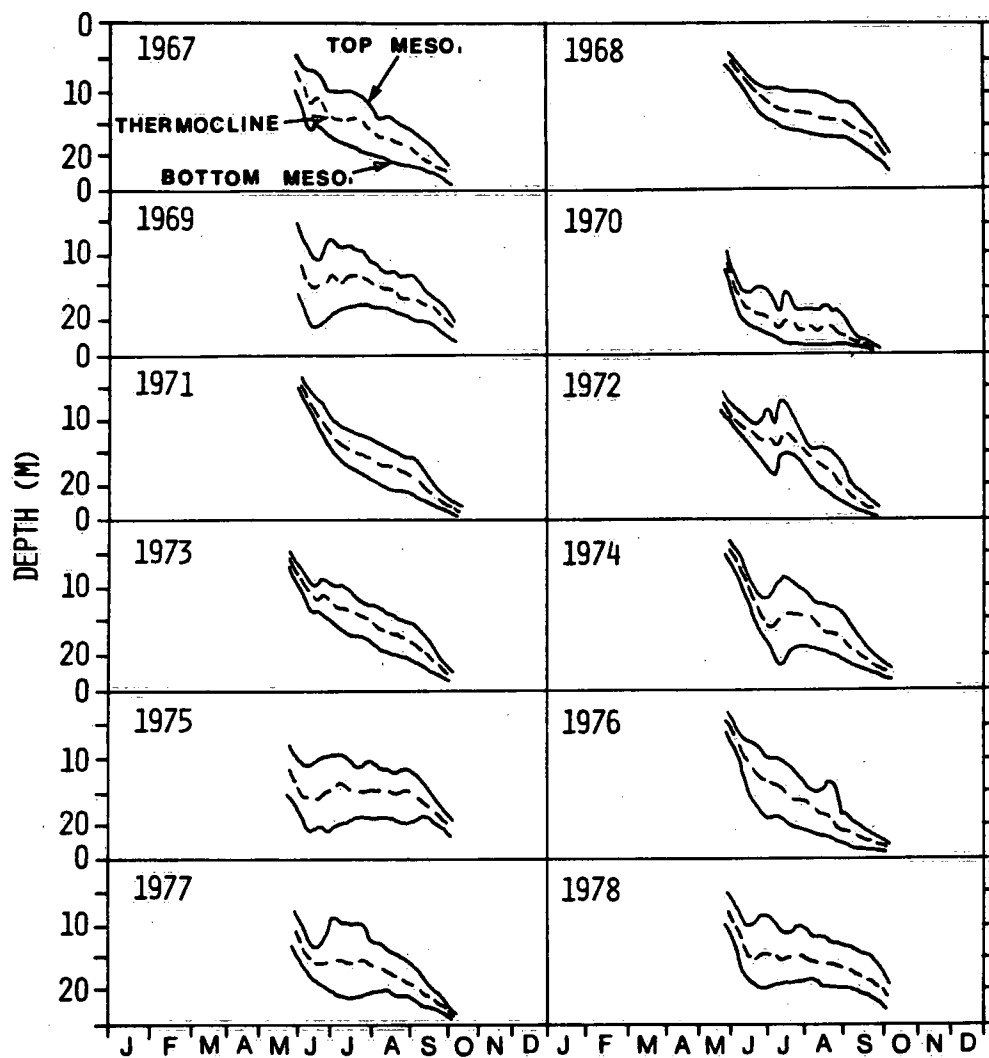


Figure 6.3. Computed positions of the thermocline (dashed lines), and the upper and lower mesolimnion boundaries (solid lines) of the Central Basin for 1967 to 1978. (This figure is the same as Figure 7.10.)

conveniently and objectively the definition for epilimnion, mesolimnion and hypolimnion. As will be seen in Section 7.2, the thermal eddy diffusivity is defined by solving iteratively the nonlinear heat balance equation over the water column of a basin, and the three regimes are matched according to daily meteorological forcing functions. The layer thicknesses so defined respond more correctly to meteorological conditions than those obtained without using meteorological inputs. However, the six-box three-variable model does not use a three-layered structure for each basin, but rather the two layers separated by the thermocline. Figure 6.3 shows the computed thicknesses for the three layers, as well as the position of the thermocline computed as the midpoint of the mesolimnion, for 1967 to 1978 for the Central Basin. The thermocline depth, measured from the surface, has been verified with observed data (see Fig. 7.9 and Subsection 7.4.1). Because anoxia often occurs in the Central Basin hypolimnion, the dynamic curve of the thermocline of the Central Basin is used as the interface of the lower and upper layers for all basins with adjustment as part of the vertical diffusive transport for the Western and Eastern basins (Subsections 5.7.1 and 5.7.4).

The dynamic changes in the thermal layer structure in the Central Basin during the twelve-year period from 1967 to 1978 are shown in Fig. 6.3. Three types of thermocline dynamics can be identified for explaining the six-box model results. First, the "normal" type, as shown in 1967, 1968, 1971, 1973 and 1976, shows a gradual, almost monotonic, downward movement of the thermocline (dashed line, Fig. 6.3), e.g., dropping from a depth of 7 m in early June to a depth of 16 m at the end of July in 1967. Secondly, the "shallow hypolimnion" type, as shown in 1970, 1975, 1977 and 1978, shows a relatively shallow hypolimnion over most of the stratification period and a rapid initial lowering of the thermocline, e.g., lowering from 12 m to 20 m over the month of June in 1970. Thirdly, the "reversal entrainment"

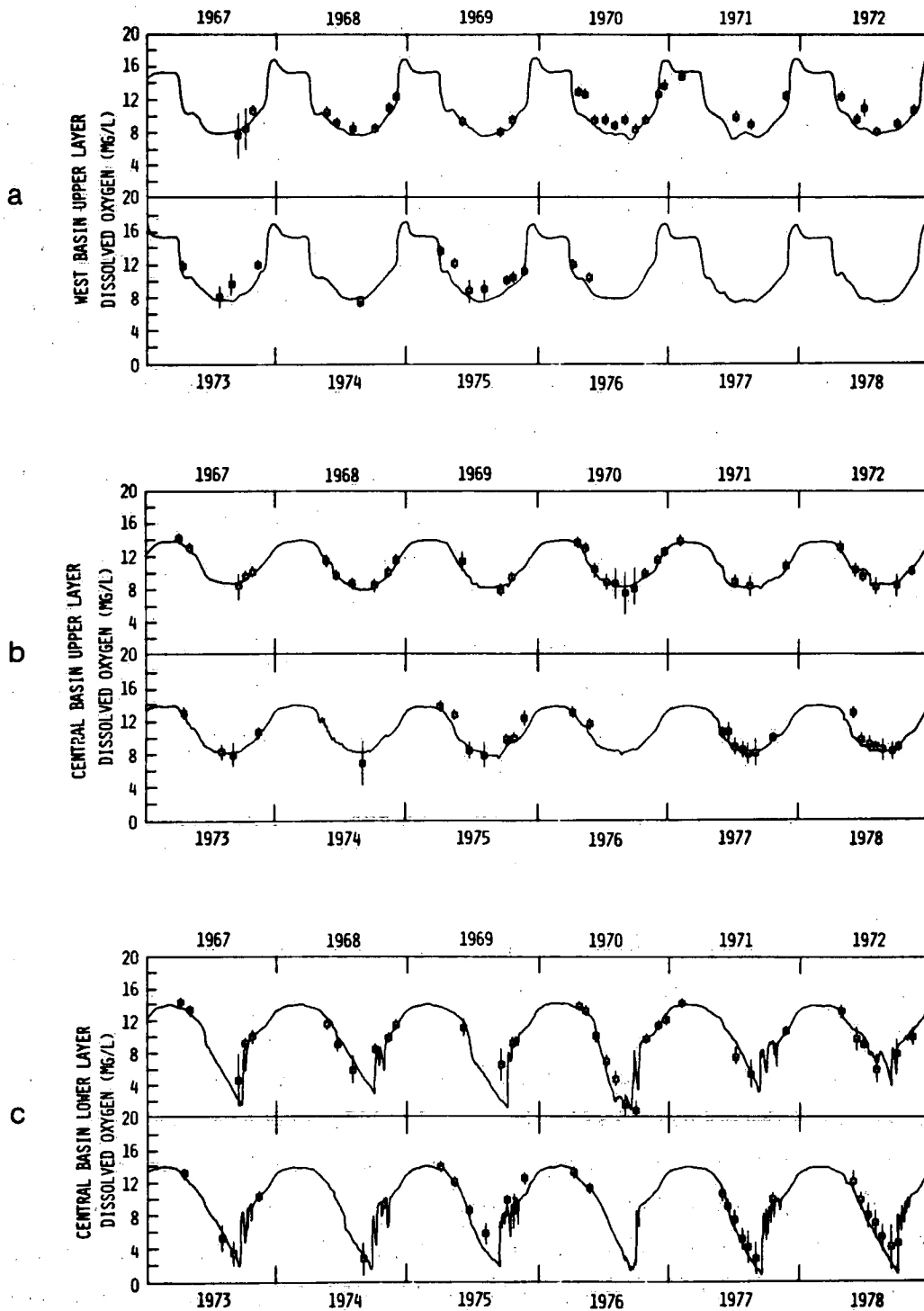


Figure 6.4. Verification of the six-box model for Lake Erie basins for dissolved oxygen, 1967 to 1978.

(—) computed values, (—■—) observed values

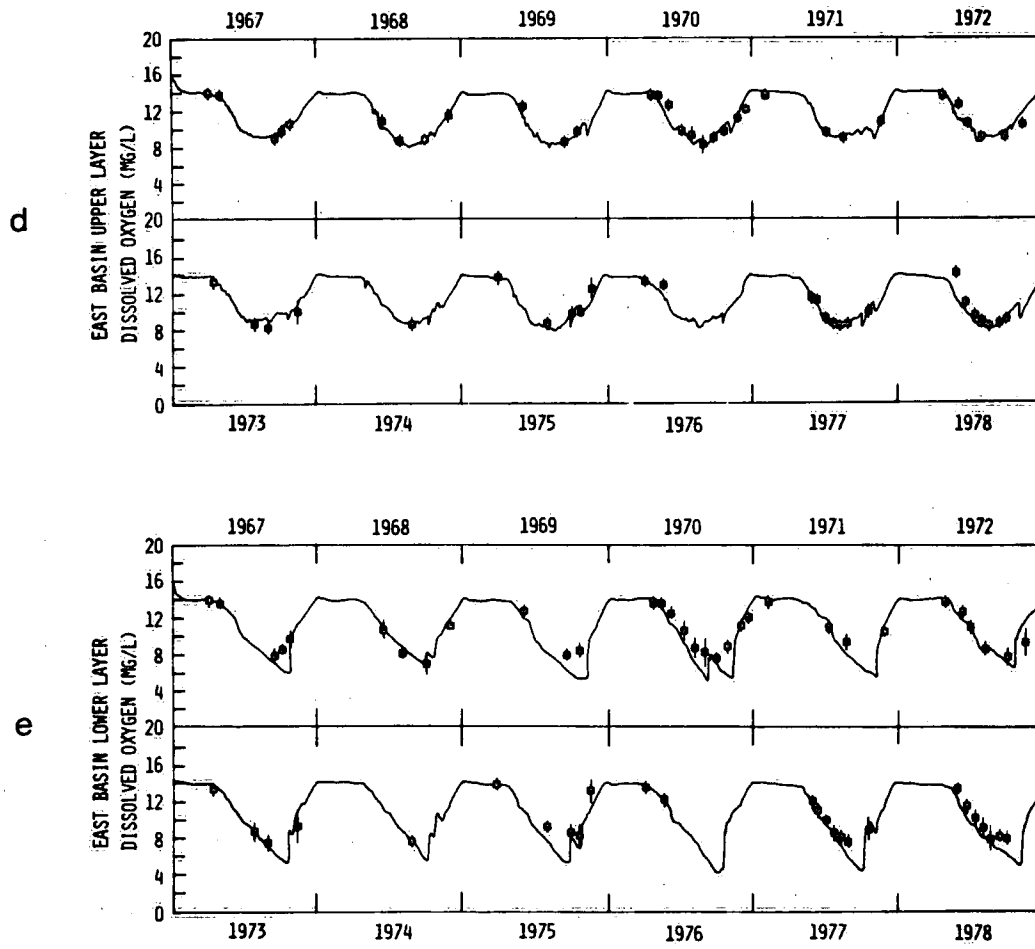


Figure 6.4. Continued.

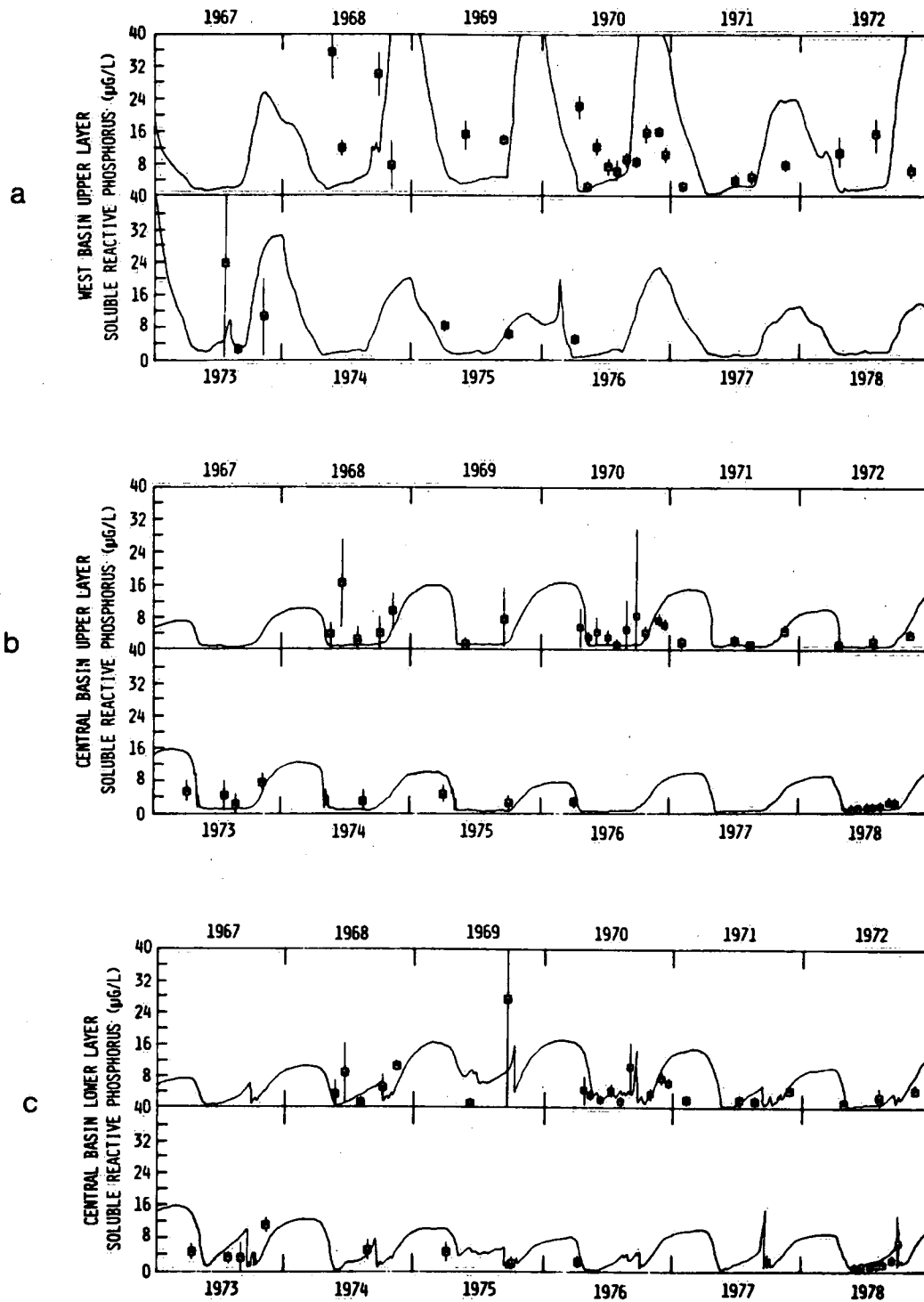


Figure 6.5. Verification of the six-box model for Lake Erie basins for soluble reactive phosphorus, 1967 to 1978.

(—) computed values, (—■—) observed values

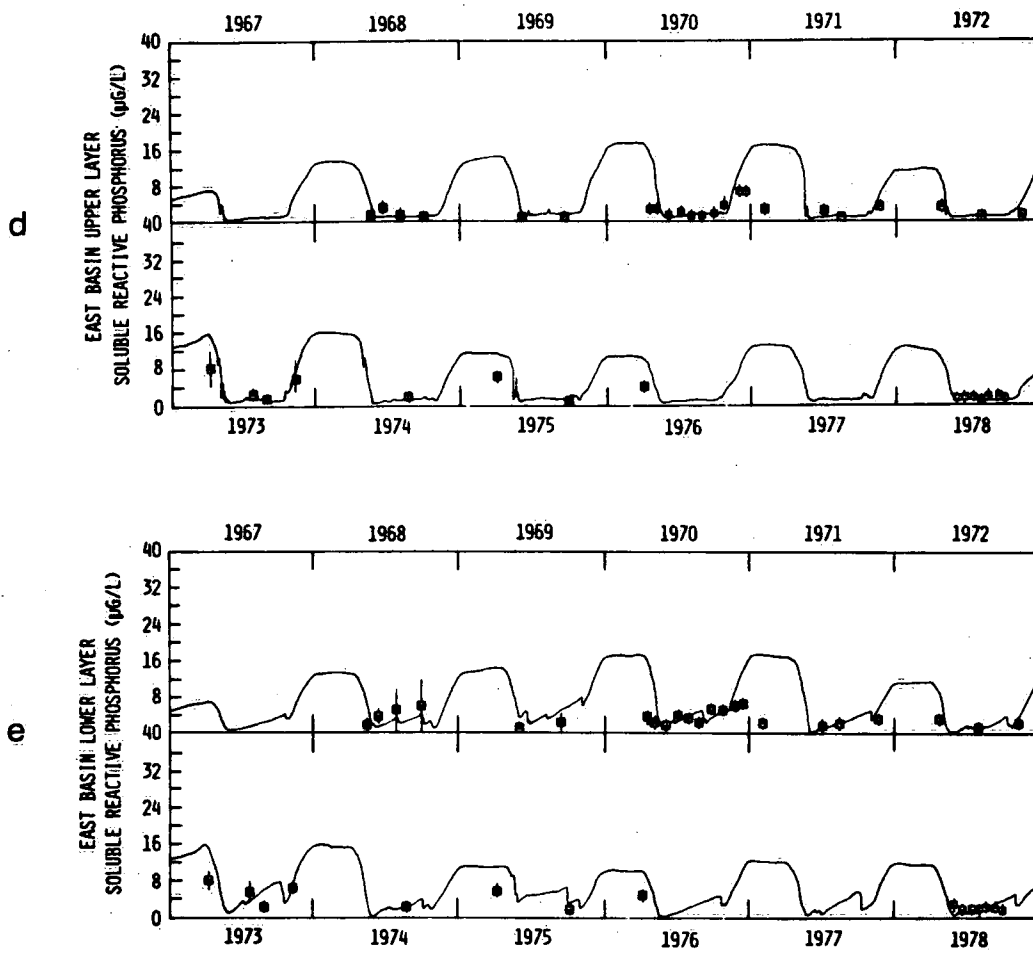


Figure 6.5. Continued.

type as shown in 1969, 1972 and 1974, shows substantial upward movement of the thermal layers during the stratification period, e.g., in 1972 there were major storms in June and in August causing the thermal layers to rise and fall in rapid succession, reflecting instability of the balance between wind mixing and thermal buoyancy. These three classes of thermal layer thickness play quite different roles in affecting the dynamics of the three water quality variables in the six-box model.

6.2.4 Dissolved oxygen: verification, 1967 to 1977

Figures 6.4a to e show the computed and observed results for dissolved oxygen for 1967 to 1977 (with 1978 results also attached for comparison) for the upper layer, Western Basin; the upper and lower layers, Central Basin; the upper and lower layers, Eastern Basin, respectively. From Figures 6.4a, b and d, in which the upper layer results are shown, the predicted dissolved oxygen concentration agrees very well with the observed. As mentioned in the discussion of the model structure of the six-box three-variable model, the dissolved oxygen in the upper layer is almost always saturated and hence is a function of the surface temperature. The good fit of computed and observed oxygen results at the upper layer for all the basins is therefore more of an indication for correctly predicting water temperature than an indication for accurate photosynthesis and reaeration formulae. Furthermore, since the agreement in the Western Basin is as good as the other two basins, the dissolved oxygen component of the six-box model is verified to apply equally well for the Western Basin. As the Western Basin has a maximum depth of 10 m, only the results of the upper layer, which represent the whole basin most of the time, are given in Fig. 6.4a. As for the results in the lower layers, for the Central and Eastern basins, the comparison of computed versus observed values is quite satisfactory. While both basins

exhibit oxygen depletion in the lower layer, the computed and observed oxygen concentration is seldom depleted to less than 4 mg/L in the Eastern Basin (Fig. 6.4e). On the other hand, the dissolved oxygen concentration in the lower layer of Central Basin can reach to less than 1 mg/L. Even though the thickness of the thermal layers is permitted to change dynamically, the lower layer may still include a portion of the mesolimnion, as dictated by the two-layered structure in the six-box model. Hence the computed oxygen concentration does not often go below the level of 0.5 mg/L during anoxia, as discussed in Subsection 3.2.4. In the model, anoxic condition is assumed to occur when oxygen concentration drops below 1.5 mg/L. If this definition is accepted, then, for the "normal type" of thermal layers (e.g. 1967, 1968, 1971, 1973 and 1976), anoxia seldom occurs, or occurs only for a brief period, as shown in Fig. 6.4c. However, for the "shallow hypolimnion" type of thermal structure (e.g. 1970, 1977 and 1978), anoxia can occur for two weeks or more. Because of the fast drop of the thermocline at the onset of thermal stratification for this type of thermal layer, little replenishment of oxygen is obtainable from the upper layer and the sediment and water oxygen demand gradually depletes the oxygen in the lower layer. In 1975, although there has been a fast drop of the thermocline depth in May, there is enough wind mixing during summer (Fig. 4.13) to induce diffusion across the layers in the Central Basin and hence no anoxia is observed. As for the "reversal entrainment" type of thermal layers, such as in the case of 1972, there is a sufficient supply of oxygen entrained from the upper layer to the lower layer because of the upward movement of the thermocline and hence the dissolved oxygen level in the lower layer stays at above 4 mg/L. Such large entrainment appears to be associated with storm events; similar but weaker entrainment occurrence, as in the case of 1969 and 1974, is not so successful in preventing the occurrence of anoxia. Thus the classification of different types of thermal layers provides only a general guideline or a rule of thumb concerning the effect of meteorological factors on oxygen depletion.

The study of thermal layer thicknesses alone does not always satisfactorily explain all occurrences of anoxia. Associated with the changes in layer thicknesses are vertical diffusion and interbasin transport which can alter the oxygen depletion scenarios indicated by the different types of thermal layer thickness. Based on the agreement between computed and observed oxygen concentrations for 1967 to 1978, it is strongly indicated that the meteorological effects dominate the seasonal variations of the oxygen concentration in both the upper and the lower layers of the basins. The effect of nutrient loading, be it an increase or reduction, on oxygen depletion cannot be seen immediately, particularly in the presence of highly fluctuating meteorological effects. For example, the fact that anoxia does not occur in 1972, but does occur in 1978, is explainable by meteorological factors, but not explainable by the total or soluble reactive phosphorus loading reduction between 1972 and 1978 (Figures 2.3 and 2.7). Therefore, it seems that the phosphorus loading effects on oxygen depletion, however small, are long-term and related largely to the sediment oxygen demand quite beyond the detection of the six-box model and the data represented by the two-layered structure.

6.2.5 Soluble reactive phosphorus: verification, 1967 to 1977

Figures 6.5a to e show the computed and observed results for soluble reactive phosphorus for 1967 to 1977 (with 1978 included for comparison) for the upper layer of the Western Basin, the upper and lower layers of the Central Basin, and the upper and lower layers of the Eastern Basin. For the Western Basin, the soluble reactive phosphorus concentration is strongly affected by the loading. For example, in Fig. 6.5a, the observed data in 1968 show a measured value of about 12 $\mu\text{g/L}$ in May, and a value of 62 $\mu\text{g/L}$ in July. Since the loading for the same period is only an approximate estimate (see Subsection 2.3.2), the seasonal variation is not simulated correctly. In general, the winter values are predicted too high for 1967 to 1973,

but the overall computed values for summer are within the observed errors. Note that both the computed and observed values of soluble reactive phosphorus in spring come down from a range of 30 to 40 $\mu\text{g/L}$ from 1967 to 1973 to about 20 $\mu\text{g/L}$ for 1974 to 1978. This decline of available phosphorus is in line with the reduction of total and soluble reactive phosphorus loading in the Detroit River. As for the upper layers of the Central and Eastern basins, the summer-uptake and fall-regeneration patterns are satisfactorily modelled. In 1971, however, the value measured in early February seems to be rather low and cannot be properly accounted for by the model. Otherwise, the agreement of computed and observed SRP values is rather close for the upper layers (Figures 6.5b and d). The lower layers are interesting in that both computed and observed values show active uptake of phosphorus during April to May for the Central Basin, and during May to June for the Eastern Basin. Of course, note also that because of the dynamic changes allowed in the lower layer thickness, the lower layer may include a portion of the photic zone. During the calibration, photosynthesis is allowed in this layer and regeneration is suppressed, leading to the low level of SRP in this layer, i.e., about 1 to 2 $\mu\text{g/L}$ in the summer for both basins. The other feature also noticeable is the sediment regeneration of SRP during anoxic condition. The anoxic conditions in 1969, 1970 and 1977 produce a relatively large amount of SRP in September, whereas for other years such as 1978, the regenerated amount is not as large (Fig. 6.5c). In general, the model underpredicts the amount because of the two-layered structure used by the model. That is, the lower layer has included a portion of the mesolimnion in it, which tends to bring down the concentration due to averaging and vertical diffusion. In general, the decline of SRP concentration in the Central and Eastern basins is not as large as that in the Western Basin.

6.2.6 Total phosphorus: verification, 1967 to 1977

Figures 6.6a to e show the corresponding comparison for total phosphorus. Again, the loading dominates the changes in total phosphorus concentration in the Western Basin. The loading data seem to be quite consistent with the computed and observed total phosphorus, e.g. in 1970 to 1974. The model underestimates total phosphorus in 1975 for the Western Basin. In early spring of 1976, there was a large pulse of total phosphorus loading from the Maumee River; both the computed and the observed concentration show an increase at about the same time. For the upper layers in the Central and Eastern basins (Figures 6.6b and d), the agreement is as satisfactory as for soluble reactive phosphorus. The effect of settling after algal growth is reflected as a decrease in the total phosphorus in August in the upper layer. Again, the drop in total phosphorus concentration is more pronounced in the Western Basin than in the upper layers of the Central and Eastern basins. For example, the computed January value of total phosphorus is about 65 $\mu\text{g/L}$ in 1970 and about 32 $\mu\text{g/L}$ in 1977 in the Western Basin, but the computed January value is about 24 $\mu\text{g/L}$ in 1970 and about 15 $\mu\text{g/L}$ in 1977 in the Central Basin. The observed values also show similar trends, and hence are in support of the loading reduction estimate given in Chapter 2. As for the lower layers, the settling activity also causes a decrease in the total phosphorus concentration around August, as shown in both the computed and observed values. In winter, the wind resuspension of particulate phosphorus brings the concentration level up in almost every year for all the basins, and all the layers, due to full mixing. However, these particulate phosphorus materials probably do not participate much in the biochemical kinetics, but rather settle back to the sediment quickly. This is particularly so in the Western Basin (Fig. 6.6a).

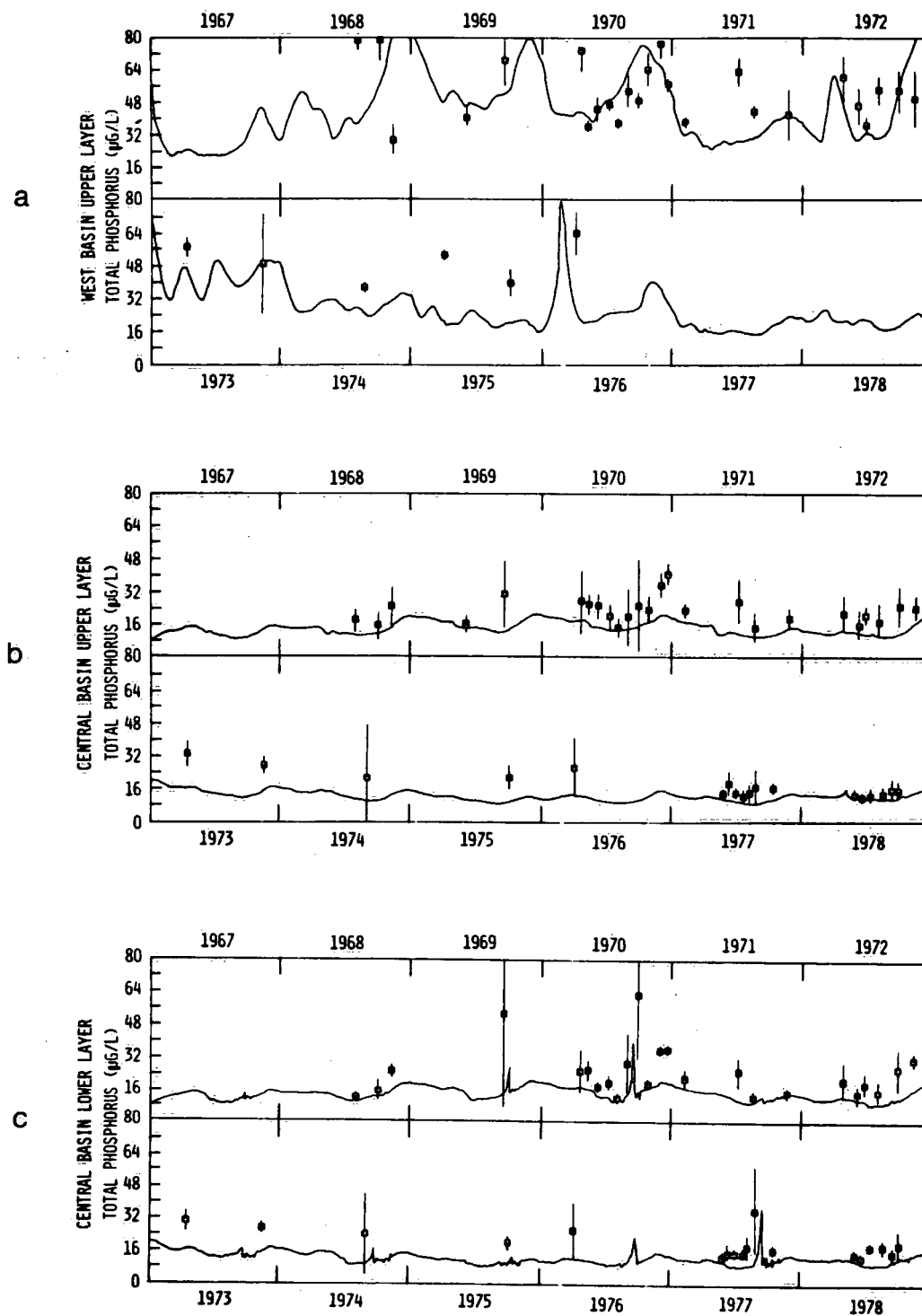


Figure 6.6. Verification of the six-box model for Lake Erie basins for total phosphorus, 1967 to 1978.

(—) computed values, (—■—) observed values

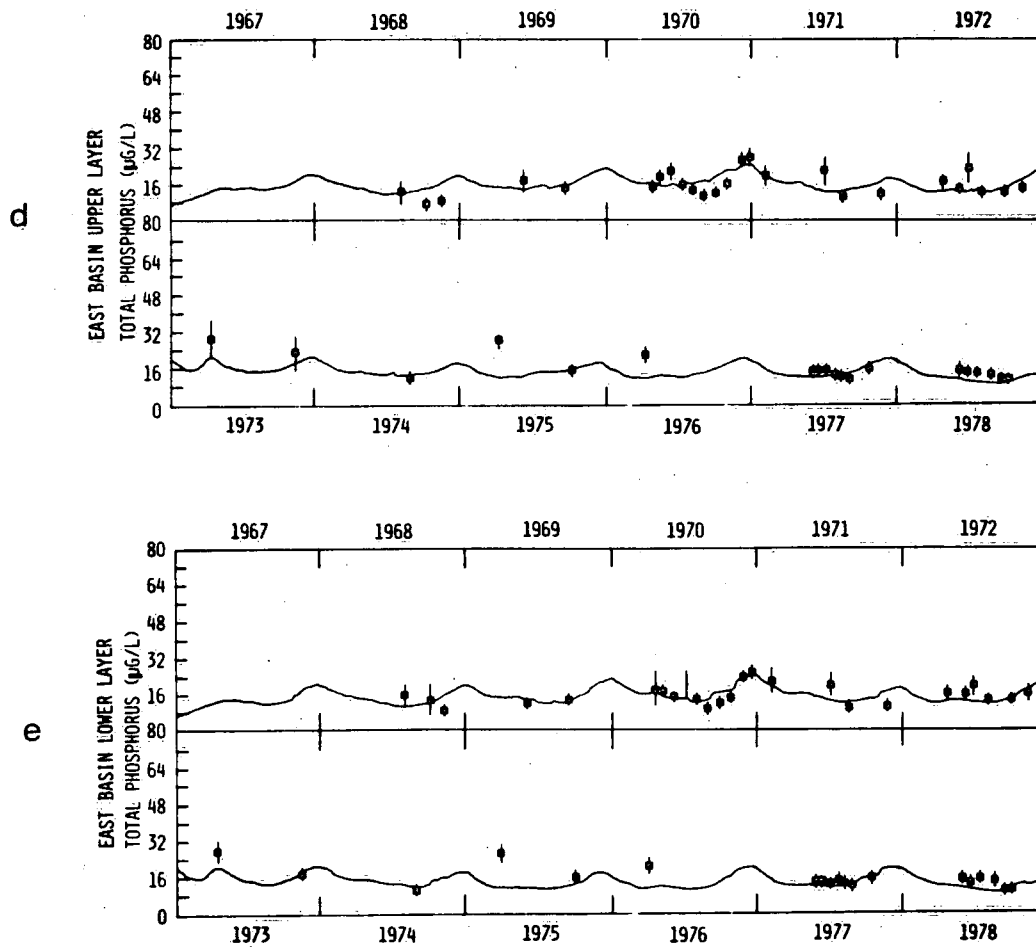


Figure 6.6. Continued.

From the twelve-year comparison, the model results seem to simulate the general seasonal behaviour of the dissolved oxygen, soluble reactive phosphorus and total phosphorus in the lake. The limitation to better simulations seems to be that of the ability to acquire more reliable loading estimates. The meteorological seasonal forcing seems to be far better simulated, as shown in the oxygen simulation.

6.3 Nine-Box Three-Variable Model

The addition of a middle layer, or mesolimnion, to the two-layered structure of the six-box model has two main advantages. From the physical point of view, the change in temperature from upper layer to lower layer is gradual, considering that the temperature data are averaged by volume-weighting to produce a mean basin-wide vertical profile. Intrinsic in the averaging process is the constraint of horizontal thermal layers. In reality, a thermocline consists of troughs, crests and convolutions and is never a flat plane. Thus, to assume that there is a flat thermoclinic plate separating the upper and lower layers adds to the inaccuracy of the assumption of homogeneous zones. An example of this inaccuracy is reflected in the six-box model simulation (Fig. 6.5c) of the sediment regenerated phosphorus in the lower layer of Central Basin. Further examples of this data representation problem have been discussed in Subsection 3.3.1 (Tables 3.3 and 3.4). If the spatial irregularities of the thermocline depths are confined in the mesolimnion, one finds that the upper layer now represents more of the epilimnetic condition, and the lower layer, the hypolimnetic condition. The other advantage of including the mesolimnion in model simulation is that epilimnetic particulate materials settle immediately to the lower layer in the two-layered model and the regeneration process, which consumes oxygen, occurs mostly in the lower layer. The addition of a mesolimnion therefore creates a

buffering volume, where some detrital decay and oxygen consumption take place, so that the apparent increase of oxygen consumption in the hypolimnion can be eliminated. As illustrated in Fig. 6.2, the thicknesses of the epilimnion, mesolimnion and hypolimnion have been computed by the thermocline model. The physical definition of the mesolimnion used in the thermocline model (see Chapter 7) involves the concept of internal wave oscillations, which are affected by meteorological forcing and, more important, are consistent with the averaging procedure based on lake thermal structures as outlined in Section 3.1. Thus, the computed thermal layer thicknesses are used to define the three layers for each of the three basins, forming a nine-box model. Note that to avoid confusion, the terms "upper layer" and "lower layer" are used to describe the two layers in the six-box model; and the terms "epilimnion", "mesolimnion" and "hypolimnion", the three layers in the nine-box model.

6.3.1 Model structure

The model structure is basically unchanged from the six-box model. The addition of the mesolimnion involves a straightforward extension of the physical transport, entrainment and diffusion processes, and is adequately discussed in the diagnostic design of the nine-box mass balance model in Section 5.8. However, two points of caution are worth re-mentioning here. Because of the presence of the mesolimnion, the interbasin transport across the boundary between Central Basin and Eastern Basin consists of two basic wind-driven flow patterns, one circulating within the epilimnion and mesolimnion of the two basins and the other circulating within the mesolimnion and hypolimnion of the two basins. This restriction is imposed in the nine-box model because as in the case of the six-box model, the thermal layer thicknesses of Central Basin are used for all the basins, so that the epilimnetic water of one basin flows only to the epilimnetic water of the adjacent basin, and so on. In reality, the thermal layer

thicknesses differ in adjacent basins. For example, the hypolimnetic water in the Central Basin may flow directly to the mesolimnetic water of the Eastern Basin; in the model simulation, this is achieved indirectly through combination of the two basic flow patterns discussed in Subsection 5.8 (Fig. 5.21). Of course, one can allow differences in layer thicknesses for different basins in the model, but this kind of spatial detail cannot be handled adequately in box models and must be simulated by using models of higher resolution (see Chapter 8). The other remark is that the mesolimnion is relatively thinner than the epilimnion or the hypolimnion, most of the time. To derive the vertical entrainment velocity for this middle layer, care must be exercised not to allow dynamic volume changes and water level changes to accumulate in the mesolimnion. In other words, any excess or deficiency of water in the water budget of the basin should be balanced with water from the epilimnion or hypolimnion, but not from the mesolimnion.

Figure 6.7 shows the schematic of the nine-box three-variable model, and Table 6.2 contains the model equations for the biochemical kinetics. Essentially, the kinetics for the mesolimnion are the same as those for the hypolimnion, which in turn resemble those of the lower layer in the six-box model (cf. Fig. 6.1 and Table 6.1). Note that the surface area, AB_0 , of a typical basin is larger than the interfacing area, AB_1 , between the epilimnion and mesolimnion, which is larger than the interfacing area, AB_2 , between the mesolimnion and hypolimnion. The bottom area, AB_3 , is assumed to be the same as AB_2 . As in the case of the six-box model, these areas change dynamically in time, and can alter the pathways of settling particulate materials, from water-bound to sediment-bound.

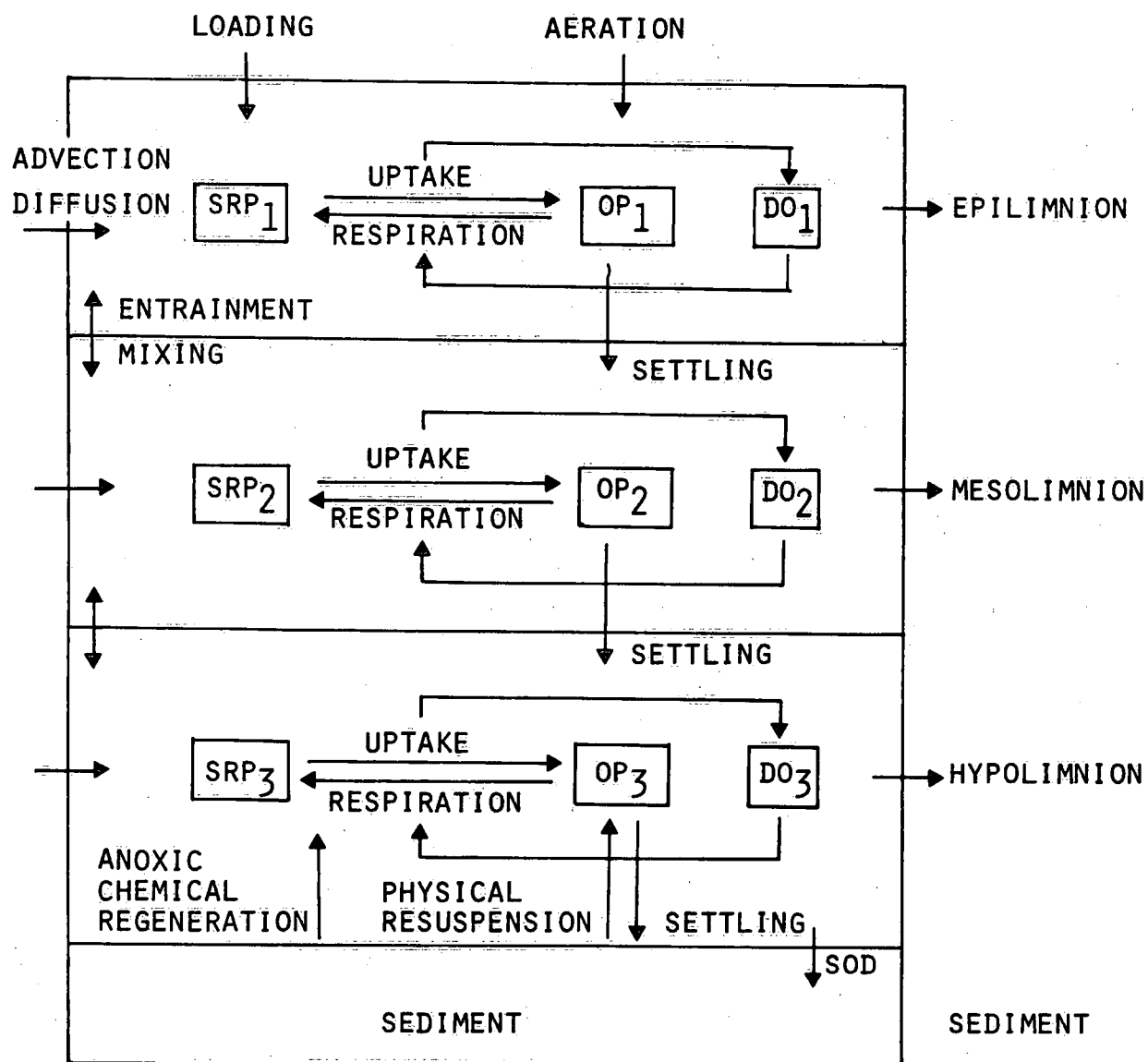


Figure 6.7. Model structure of the nine-box three-variable model in a typical water column.

Table 6.2a. Equations of Nine-Box Three-Variable Model

$$\frac{d(V_1)(SRP_1)}{dt} = F_1(SRP_1) - U_1 + R_1 + r_p(AB_0-AB_1)$$

$$\frac{d(V_2)(SRP_2)}{dt} = F_2(SRP_2) - U_2 + R_2 + r_p(AB_1-AB_2)$$

$$\frac{d(V_3)(SRP_3)}{dt} = F_3(SRP_3) - U_3 + R_3 + r_p AB_3$$

$$\frac{d(V_1)(OP_1)}{dt} = F_1(OP_1) + U_1 - R_1 + r_w(AB_0-AB_1) - \sigma_1 AB_0(OP_1-5)$$

$$\frac{d(V_2)(OP_2)}{dt} = F_2(OP_2) + U_2 - R_2 + r_w(AB_1-AB_2) + \sigma_1 AB_1(OP_1-5) - \sigma_2 AB_1(OP_2-5)$$

$$\frac{d(V_3)(OP_3)}{dt} = F_3(OP_3) + U_3 - R_3 + r_w AB_3 + \sigma_2 AB_2(OP_2-5) - \sigma_3 AB_2(OP_3-5)$$

$$\frac{d(V_1)(DO_1)}{dt} = F_1(DO_1) + [f_{po}(U_1-R_1) - k_s(AB_0-AB_1)] \frac{DO_1}{DO_1+K_o} + r_A AB_0(DO_s-DO_1)$$

$$\frac{d(V_2)(DO_2)}{dt} = F_2(DO_2) + [f_{po}(U_2-R_2) - k_s(AB_1-AB_2)] \frac{DO_2}{DO_2+K_o}$$

$$\frac{d(V_3)(DO_3)}{dt} = F_3(DO_3) + [f_{po}(U_3-R_3) - k_s(AB_2-AB_3)] \frac{DO_3}{DO_3+K_o}$$

Note: The subscripts 1,2,3 denote first, second and third layers, 0 denotes surface quantity; SRP, OP and DO are concentrations of soluble reactive phosphorus, organic phosphorus and oxygen, respectively; T is temperature ($^{\circ}\text{C}$); AB and V are areas and volume; F is physical and loading source term; U and R are uptake and respiration in planktons; r_p is phosphorus return per area; r_w is phosphorus resuspended by wind-waves; σ is settling velocity; f_{po} is phosphorus to oxygen ratio in photosynthetic production of chlorophyll; k_s is sediment oxygen demand; K_o is half-saturation coefficient for oxygen; DO_s is saturated oxygen concentration; r_A is reaeration coefficient.

Table 6.2b. Constants and Formulas of Nine-Box Three-Variable Model

$$U_1 = 0.43 \rho_1 (1.07)^{T_1} \frac{SRP_1}{SRP_1 + 0.5} (OP_1 - 5) V_1 \quad (\rho = \text{light factor: Eq. 4.5})$$

$$U_2 = 0.6 \rho_2 (1.07)^{T_2} \frac{SRP_2}{SRP_2 + 0.5} (OP_2 - 5) V_2$$

$$U_3 = 0.6 \rho_3 (1.07)^{T_3} \frac{SRP_3}{SRP_3 + 0.5} (OP_3 - 5) V_3$$

$$R_1 = 0.02 (1.07)^{T_1} (OP_1 - 5) V_1$$

$$R_2 = 0.002 (1.07)^{T_2} (OP_2 - 5) V_2$$

$$R_3 = 0.001 (1.07)^{T_3} (OP_3 - 5) V_3$$

$$\sigma_1 = 0.2; \sigma_2 = 0.4; \sigma_3 = 0.4 \text{ (m/day)}$$

$$r_w = 0.001 W/W_s; W_s = 5 \times 10^5 \text{ m/day}; W = \text{wind speed (m/day)}; r_w = \text{g/m}^2\text{day}$$

$$r_A = 2 \text{ m/day}; k_s = 0.15 \text{ g/m}^2\text{day}; K_o = 1.4 \text{ mg/L}; f_{po} = 140;$$

$$r_p = 0.0001 \text{ g/m}^2\text{day} \text{ (0.0044 g/m}^2\text{day if DO}_3 < 1.5 \text{ mg/L)}$$

6.3.2 Calibration

Figures 6.8a to d show the calibrated results of temperature, dissolved oxygen, soluble reactive phosphorus and total phosphorus, using the 1978 observed data. In general, the agreement is as satisfactory as the agreement shown in the six-box model results (Figures 6.2a to d). The model constants (Table 6.2) are essentially the same as for the six-box model (Table 6.1); the constants for the mesolimnion are assigned the same as the lower layer values of the six-box model. For example, the settling velocities for the epilimnion, mesolimnion and hypolimnion are 0.2, 0.4 and 0.4 m/day, respectively (cf. Table 3.5). One major change in the coefficients used is the sediment oxygen demand rate: in the six-box model, a rate constant of $0.5 \text{ g O}_2 \text{ m}^{-2} \text{ day}^{-1}$ is used; in the nine-box model, calibration required $0.15 \text{ g O}_2 \text{ m}^{-2} \text{ day}^{-1}$ to produce better fit with the data. An explanation for this discrepancy may be as follows. In the six-box model, there are sources of oxygen in the lower layer which are due to the inclusion of mesolimnion in the lower layer. Light is available for photosynthesis, at least when the lower layer is thick, e.g., a thickness of 15 m in May or June. Because of the omission of the mesolimnion, more vertical diffusion of oxygen from the upper layer is required to compensate for the spatial heterogeneity lost in the averaging processes. The lower layer of the six-box model is always thicker than the hypolimnion in the nine-box model (Fig. 6.3); hence there is more oxygen content in the lower layer of the six-box model than in the hypolimnion of the nine-box model. Although the sediment area in the lower layer of the six-box model is larger than that in the hypolimnion of the nine-box model, the net effect is that the lower layer of the six-box has more oxygen to consume before anoxia can be reached. By contrast, because of the deeper position of the hypolimnion in the nine-box model, these extraneous oxygen sources are not as great. Furthermore, as remarked earlier, the hypolimnetic

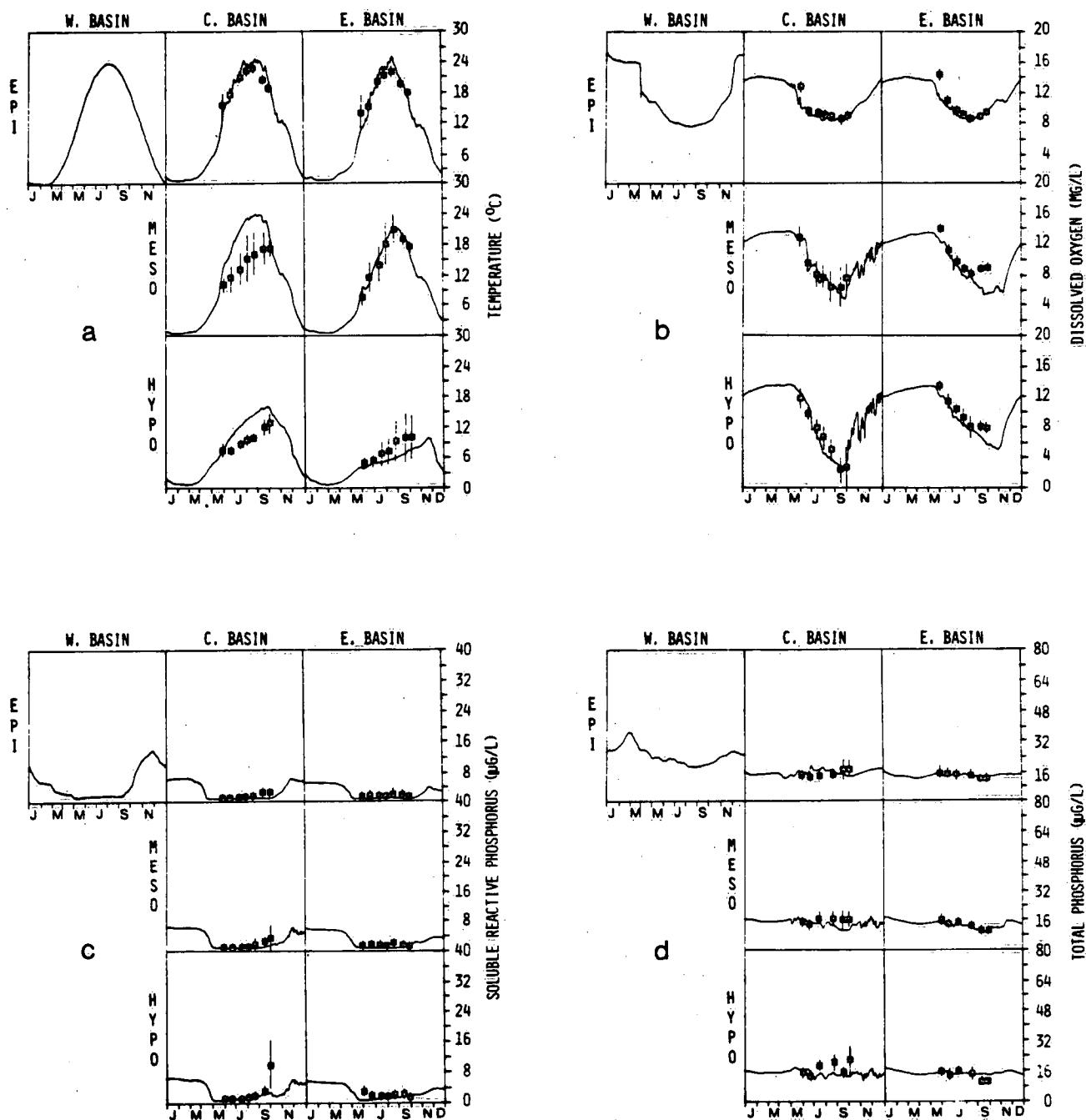


Figure 6.8. Calibration of the nine-box model using 1978 data:

(a) temperature; (b) dissolved oxygen; (c) soluble reactive phosphorus; (d) total phosphorus.

(—■—) observed values
(—) computed values

water in the Central Basin flows to the hypolimnetic water in the Eastern Basin. The direct interbasin transport of oxygen supply from the hypolimnion of Eastern Basin can be cut off if the hypolimnia of the basins are lower than the Pennsylvania Ridge separating the two basins. Beyond that point, any replenishment will be indirect and move from the mesolimnion of the Eastern Basin, to the mesolimnion of the Central Basin and then to the hypolimnion of the Central Basin. As discussed in Section 5.8, the occurrence of this indirect supply depends on the wind speed and direction and other meteorological factors. In all, the hypolimnion of the nine-box model has fewer extraneous oxygen sources which are due to improper model structure and hence requires a smaller value of sediment oxygen demand.

All of these differences move the nine-box model closer to reality, and in support of this idea, we note that the sediment oxygen demand rate of $0.15 \text{ g O}_2 \text{ m}^{-2} \text{ day}^{-1}$ is rather close to the values reported by Mathias and Barica (1980) for ice-covered lakes. Since for ice-covered lakes the sources and sinks of oxygen are more easily accountable, the measurements should be more accurate. Burns (personal communication) also found that the sediment oxygen demand rate should be around $0.1 \text{ g O}_2 \text{ m}^{-2} \text{ day}^{-2}$ for the Central Basin by carefully accounting for the various oxygen sources and sinks from known data. Therefore, by including the mesolimnion as an integral part of the thermal layer structure, and by allowing for the physical processes associated with a three-layered model framework, the simulated sediment oxygen demand is brought closer to the observed value.

Figure 6.8a shows close agreement between computed and observed temperature in the mesolimnion and epilimnion of the Central Basin and Eastern Basin; hypolimnetic temperatures for both basins, however, are underpredicted. As for oxygen, epilimnetic values are calibrated closely with the data. In the mesolimnion, dissolved oxygen is depleted in both the Central and Eastern basins. However,

when each is compared with the depletion of oxygen in the hypolimnion, an interesting observation can be made. In the Central Basin, the depletion is less rapid in the mesolimnion than in the hypolimnion, as demonstrated by both computed and observed values (Fig. 6.8b). In the Eastern Basin, the oxygen in the mesolimnion is consumed at a slightly faster rate than the oxygen in the hypolimnion. For example, the observed Eastern Basin oxygen concentration in late July of 1970 is 7.8 mg/L in the mesolimnion, but it is 8.7 mg/L in the hypolimnion and 9.3 mg/L in the epilimnion. The computed values also show a similar trend. This mesolimnetic oxygen minimum can be attributed to more active algal decay in the mesolimnion than in the hypolimnion, since the particle size is larger in the mesolimnion, or, somewhat less convincingly, can be due to the physical transport of relatively low oxygenated water (e.g. 5.1 mg O_2 /L) from the mesolimnion of the Central Basin.

Both forms of phosphorus (Figures 6.8c and d) are calibrated to the same degree of agreement as in the case of the six-box model. Whereas the seasonal variations are more pronounced in the computed and observed total phosphorus in the mesolimnia, the soluble reactive phosphorus is again at very low concentration levels, about 1 to 2 $\mu\text{g/L}$, during the stratified period for all basins. There is a slight sediment regeneration of SRP for a brief anoxic period by the end of September, and the increase in concentration is not significantly higher than that shown in the lower layer of the Central Basin for the six-box model (Fig. 6.2c).

6.3.3 Dissolved oxygen: verification, 1967 to 1977

Figures 6.9a to g show the computed and dissolved oxygen concentration for 1967 to 1977, for the epilimnion of the Western Basin, and the three layers of the Central and Eastern basins. It is assumed that the epilimnion of the Western Basin is representative of

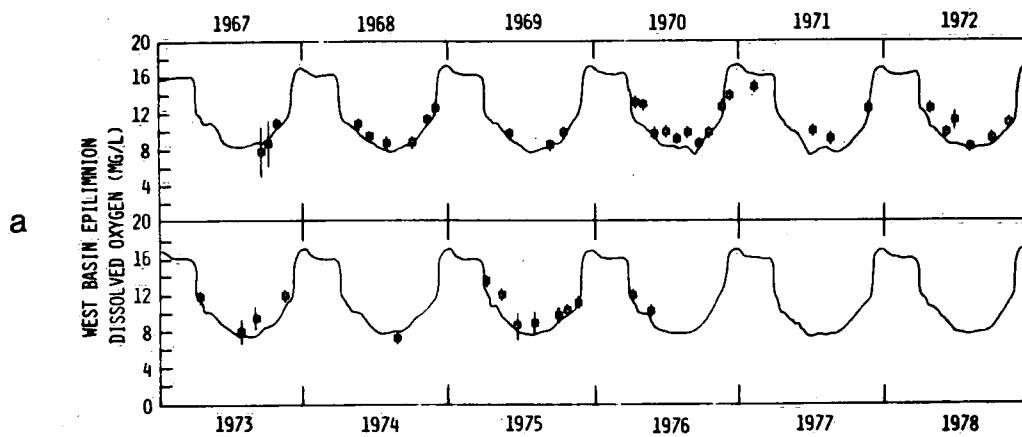


Figure 6.9. Verification of the nine-box model for Lake Erie basins for dissolved oxygen, 1967 to 1978.

(—) computed values, (—■—) observed values.

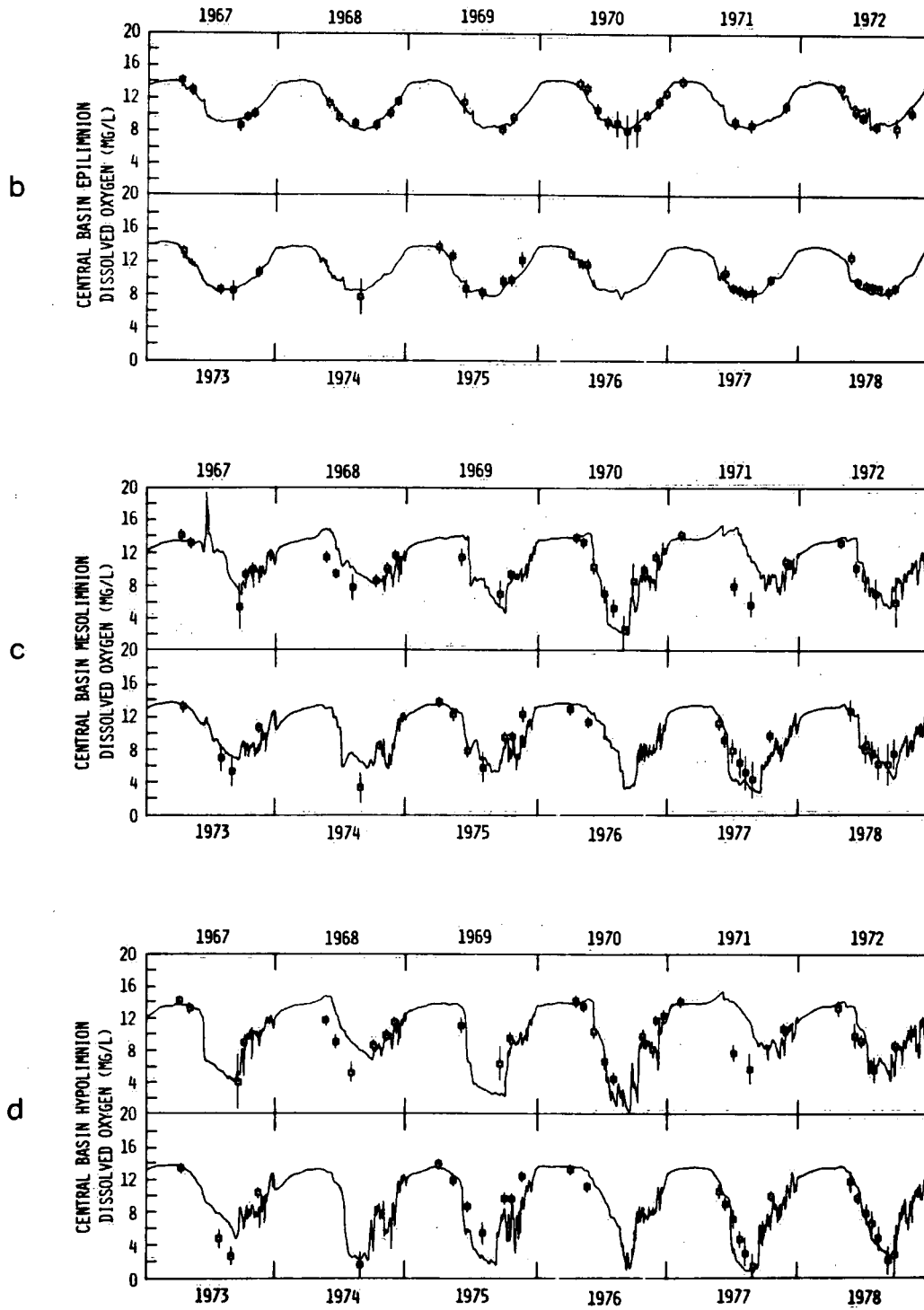


Figure 6.9. Continued.

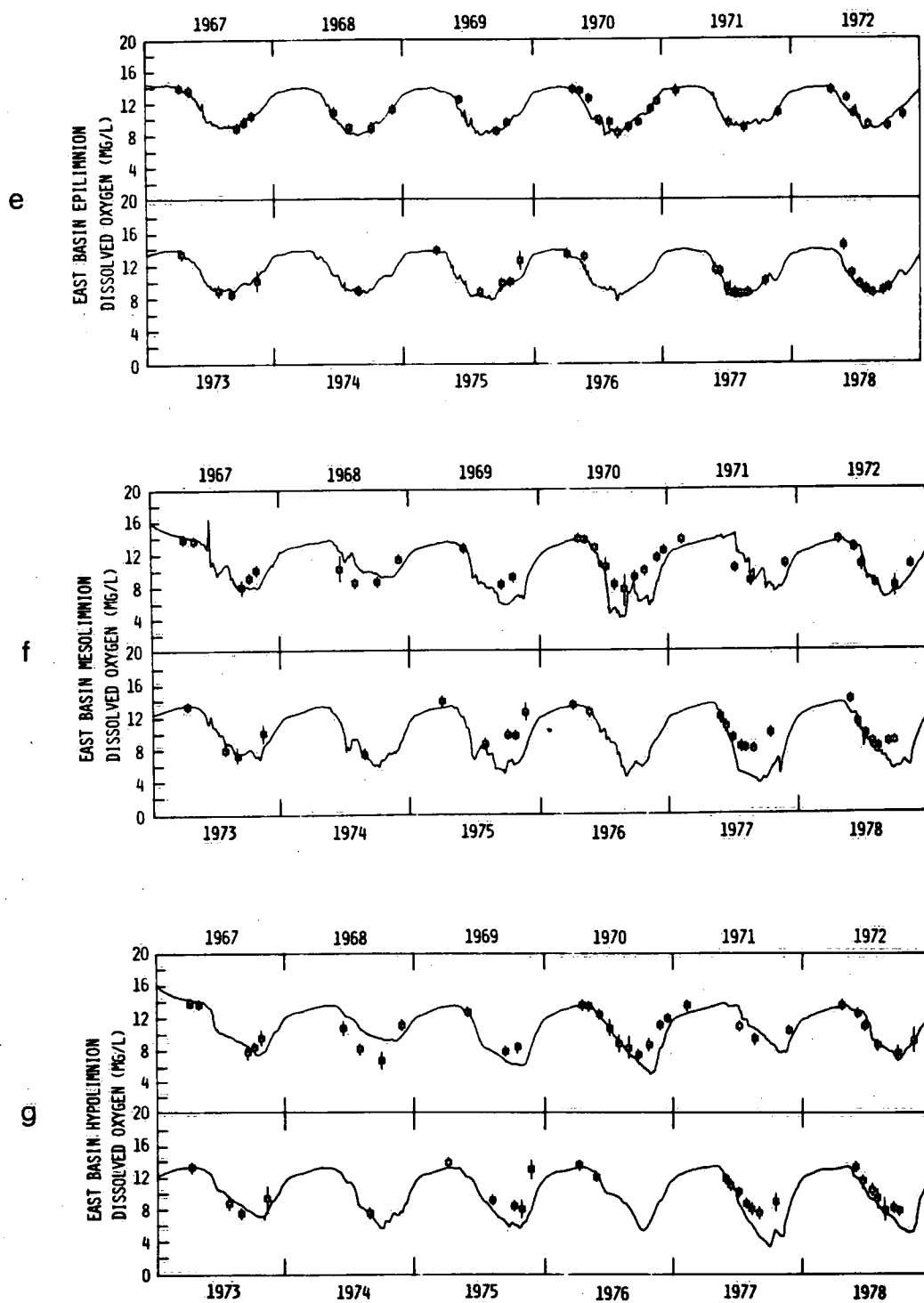


Figure 6.9. Continued.

the basin in terms of the water quality condition. For the epilimnion of all three basins, the agreement between computed and observed oxygen concentration is very good. As in the case of the six-box model, the dissolved oxygen is saturated most of the time in these surface layers (Figures 6.9a, b and e), and therefore depends on the water temperature. The goodness of fit for oxygen data is then a reflection of the goodness of fit in the temperature calculations.

On the other hand, the mesolimnion oxygen concentration displays different seasonal dynamics in different basins. For the Central Basin, the mesolimnetic oxygen concentration, either computed or observed, is almost always higher than the hypolimnetic oxygen concentration. According to the classification of thermal layer thicknesses given in Section 6.2, for the "shallow hypolimnion" type, e.g., 1970, 1977 and 1978, the mesolimnetic oxygen is depleted to less than 4 mg O₂/L (Fig. 6.9c). For the "reversal entrainment" type, e.g., 1972 and 1974, the depletion prevails for the months May and June, but the upward entrainment processes due to the meteorological conditions prevent further loss of oxygen. In the case of the "normal" type of hypolimnion thickness, e.g., 1967, 1968, 1971, 1973 and 1976, the mesolimnetic oxygen remains at about 8 mg/L or higher during the months of May, June and July, as seen in both the computed and observed values. In 1971, the nine-box model over-predicts the oxygen concentration in the Central Basin mesolimnion.

The computed and observed mesolimnetic oxygen concentrations in the Eastern Basin (Fig. 6.9f) provide evidence that oxygen concentration minima often occur in the mesolimnion. For example, in 1967, as a typical case of the "normal" layer thickness type, the computed mesolimnetic oxygen concentration for the Eastern Basin in early July is about 9 mg/L, but is about 10 mg/L in the epilimnion and hypolimnion. Interestingly, the mesolimnetic oxygen computed in the Central

Basin is about 11.5 mg/L. For this year at least, it appears that the mesolimnetic oxygen minimum in the Eastern Basin is caused mainly by phytoplankton respiration and sediment oxygen demand on the "sides" of the layer because the interbasin transport and the vertical mixing processes do not explain this phenomenon. For the "shallow hypolimnion" type, e.g., in 1970, this computed mesolimnion minimum is more pronounced, but, at the same time, the mesolimnetic oxygen in the Central Basin is also low. It is possible that the mesolimnion oxygen minimum is also caused by the transport of lower oxygen concentration from the Central to the Eastern Basin. In 1977, the nine-box model underpredicts the mesolimnetic oxygen in the Eastern Basin, probably because of a more excessive Central-to-Eastern interbasin transport than that used in 1970. In the case of "reversal entrainment", e.g., in 1972, upward movement does not seem to hold back this oxygen mesolimnetic minimum, as shown by the computed and observed values for June and July (Fig. 6.9f).

The computed hypolimnetic oxygen concentration shown in Fig. 6.9d shows a faster decline than the six-box model result (Fig. 6.4c) with the "shallow hypolimnion" type of thermal layers, such as in 1970 and 1977. In the case of "reversal entrainment", e.g., in 1972 and 1974, oxygen depletion is essentially interrupted by the supply of oxygen due to the increase in thickness in the hypolimnion (Fig. 6.3), at about mid-July. As for the "normal" layer thickness type, e.g., 1967, 1968, 1973 and 1976, the anoxic condition is either absent or lasts for a brief period only. Again, the nine-box model over-predicts the oxygen concentration in the Central Basin hypolimnion. On the other hand, the prediction for the Eastern Basin hypolimnetic oxygen (Fig. 6.9g) shows the same degree of goodness of fit between computed and observed concentration as the six-box model results for the lower layer of the Eastern Basin.

6.3.4. Soluble reactive phosphorus: verification, 1967 to 1977

Figures 6.10a to g show the computed and observed results for soluble reactive phosphorus in the nine-box model for 1967 to 1978. Only the epilimnion results for the Western Basin are given in Fig. 6.10a, in which the computed summer concentration is quite close to the observed data except for large discrepancies occurring in the winter months and for the entire year 1968. One explanation is that part of the particulate phosphorus returned by wind resuspension from the sediment is not completely biologically available. For example, in 1971, whereas the predicted total phosphorus concentration (Fig. 6.11a) is close to the observed data for February and November, the predicted SRP values for the same periods are not as good, indicating an inadequacy in the treatment of particulate phosphorus.

The computed epilimnetic values of SRP in the Central and Eastern basins (Figures 6.10b and e) agree well with the observed data, with a fairly consistent seasonal cycle. Note that the summer epilimnetic level of SRP in the Western Basin is higher in 1970 than in 1976 and 1977, whereas the computed and observed summer values in the other two basins are quite low, about 1 to 2 $\mu\text{g/L}$ only throughout 1967 to 1977. In the mesolimnion, photosynthetic uptake of the soluble reactive phosphorus is possible and gives rise to a similar seasonal cycle in the SRP for both the Central and Eastern basins (Figures 6.10c and f). In 1970, there was a large return of SRP from the sediment during the anoxic period (Figures 6.9c and d), and there is a significant pulse of increase of SRP in the mesolimnion (Fig. 6.10c).

More significant is the sediment return of SRP in the hypolimnion in September, 1970, as shown both by the computed and observed results (Fig. 6.10d). A similar anoxic regeneration can be seen in

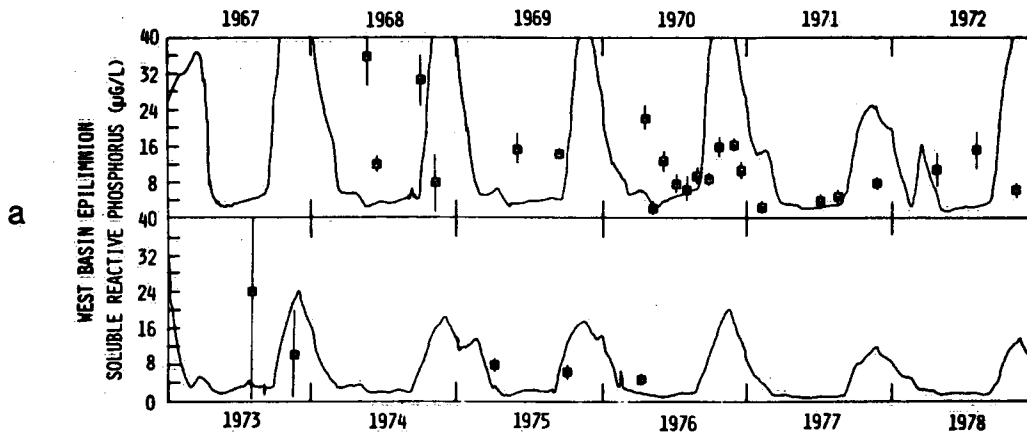


Figure 6.10. Verification of the nine-box model for Lake Erie basins for soluble reactive phosphorus, 1967 to 1978.

(—) computed values, (—■—) observed values

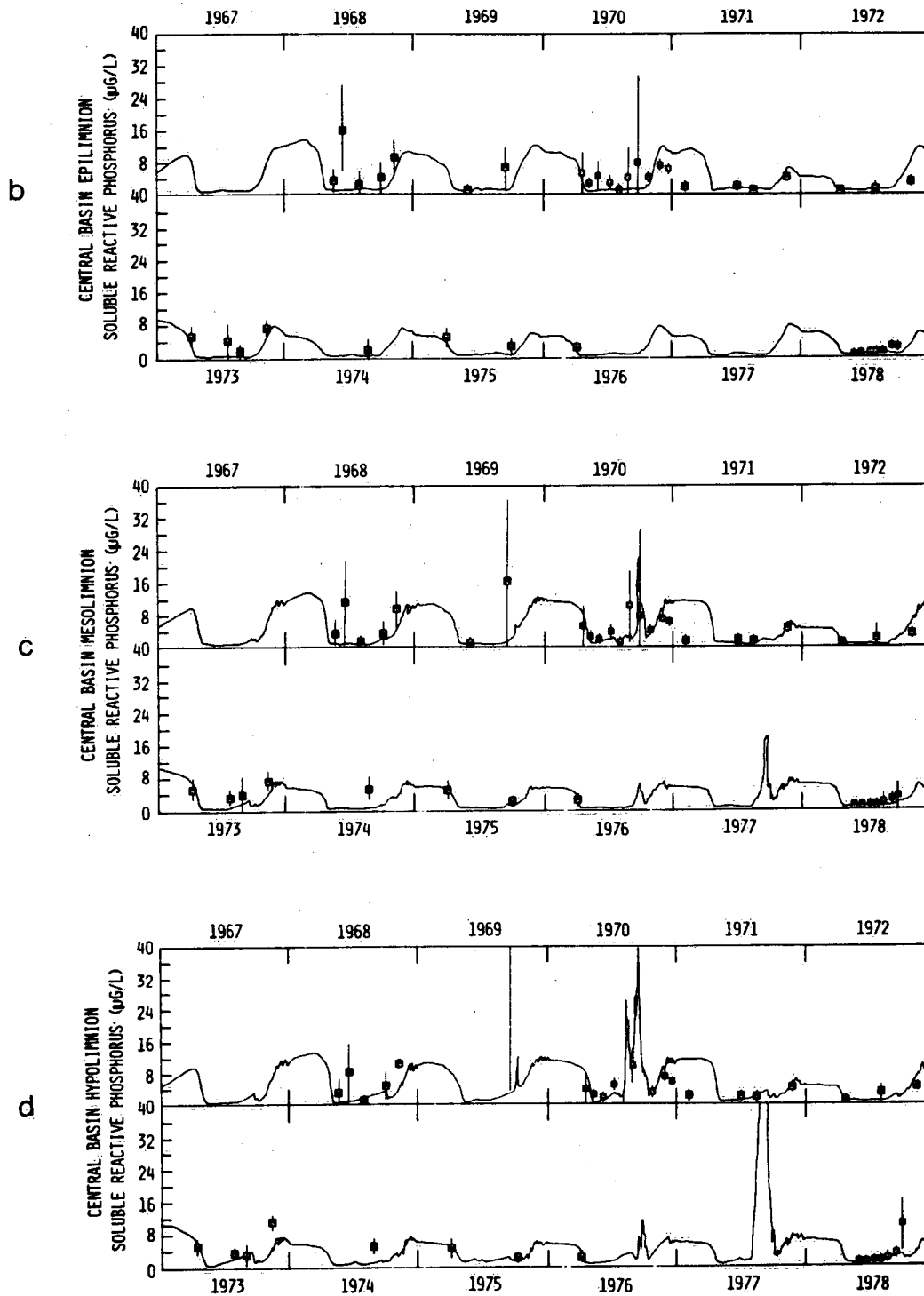


Figure 6.10. Continued.

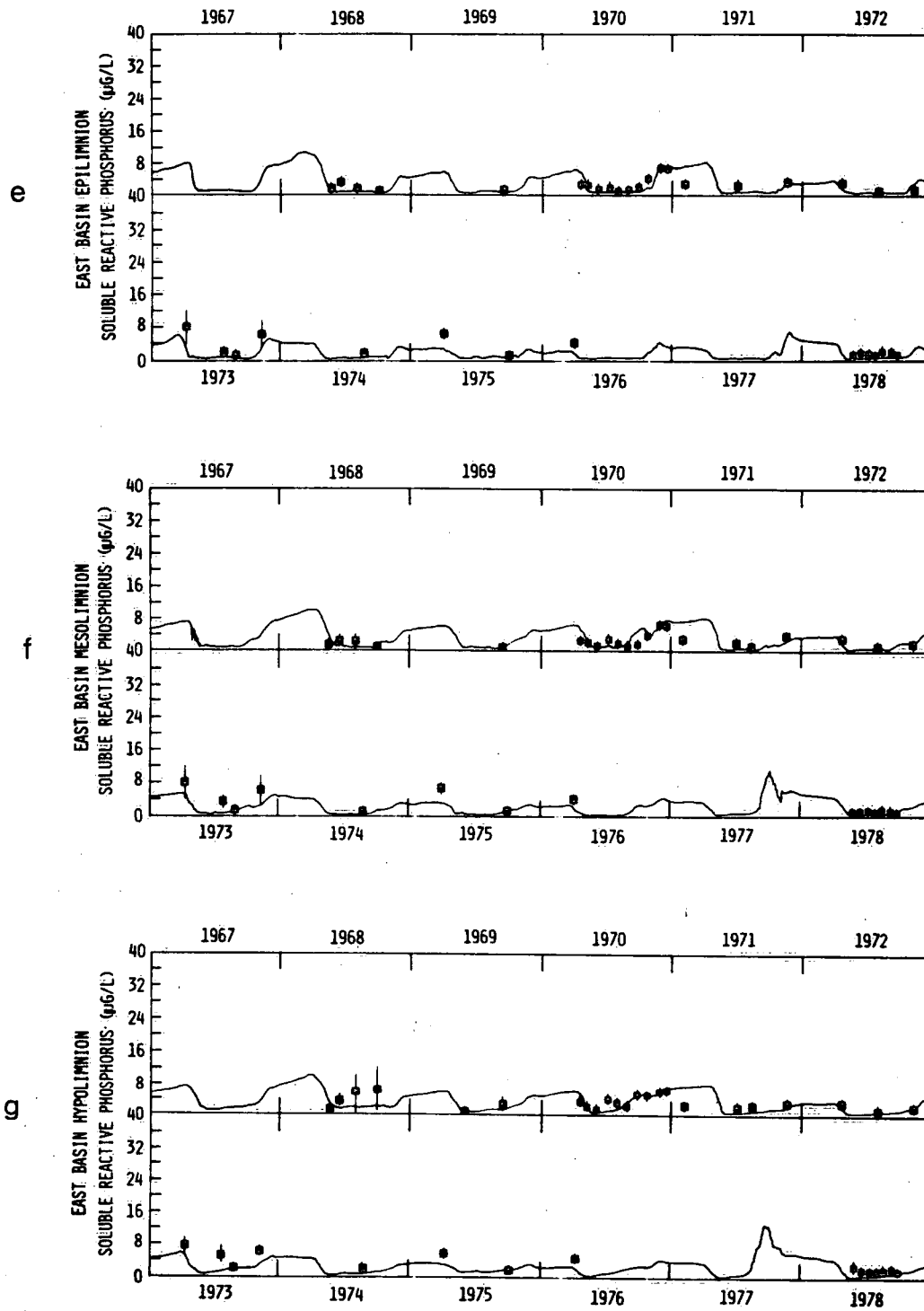


Figure 6.10. Continued.

1977 in the computed result. Both 1970 and 1977 have been classified as "shallow hypolimnion" type for the thermal thicknesses (Fig. 6.3). Compared with the six-box model results, the anoxic sediment return for 1970 and 1977 is higher and the SRP concentration is closer to the observation in the nine-box model. This ability to simulate pulse-like sediment return in 1970 and 1977 can be attributed to the shallower layer thickness in the hypolimnion in the nine-box model (Fig. 6.3). However, the pulse observed in September 1969 is underestimated. This underestimation leads to speculation that the sediment oxygen demand in 1969 should have been greater (see Eq. 9.2, Section 9.2).

6.3.5 Total phosphorus: verification, 1967 to 1977

Figures 6.11a to g show the corresponding comparison for total phosphorus. Essentially, the same satisfactory comparison between computed and observed total phosphorus concentration is shown in the nine-box model results as in the case of the six-box model. The uncertainties associated with the seasonal variation of the total phosphorus loading have caused large deviations from the observation in the Western Basin epilimnion than in the epilimnion of the Central and Eastern basins. The underestimation in 1975 is still obvious in these epilimnetic concentrations in the nine-box model results (cf. Figures 6.6a, b and d; Figures 6.11a, b and e). The same downward trend of total phosphorus concentration during 1967 to 1978 can be seen in the computed results.

As for the mesolimnetic and hypolimnetic total phosphorus concentration (Figures 6.11c, d, f and g), they exhibit larger seasonal variations than the six-box model results. For example, the persistent lower concentrations in these layers in July and August, for almost all the years from 1967 to 1978, indicate that settling occurs after algal growth takes place. In the Eastern Basin, this

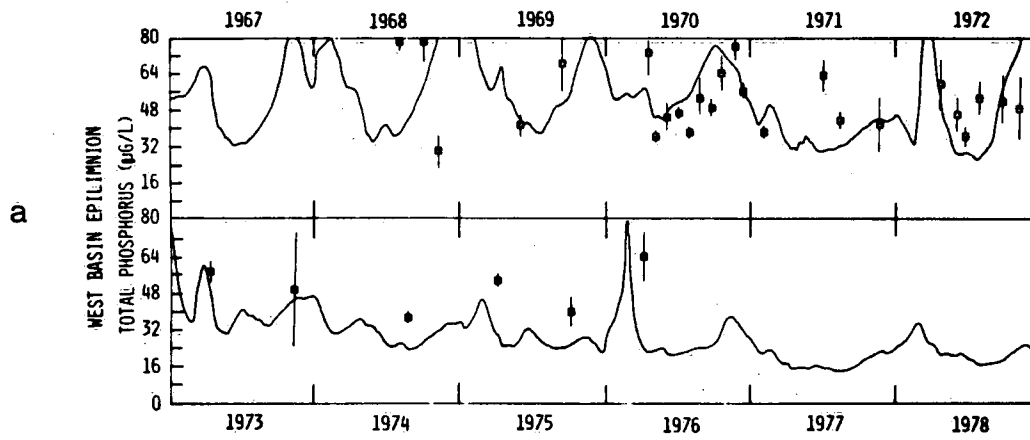


Figure 6.11. Verification of the nine-box model for Lake Erie basins for total phosphorus, 1967 to 1978.

(—) computed values, (—■—) observed values

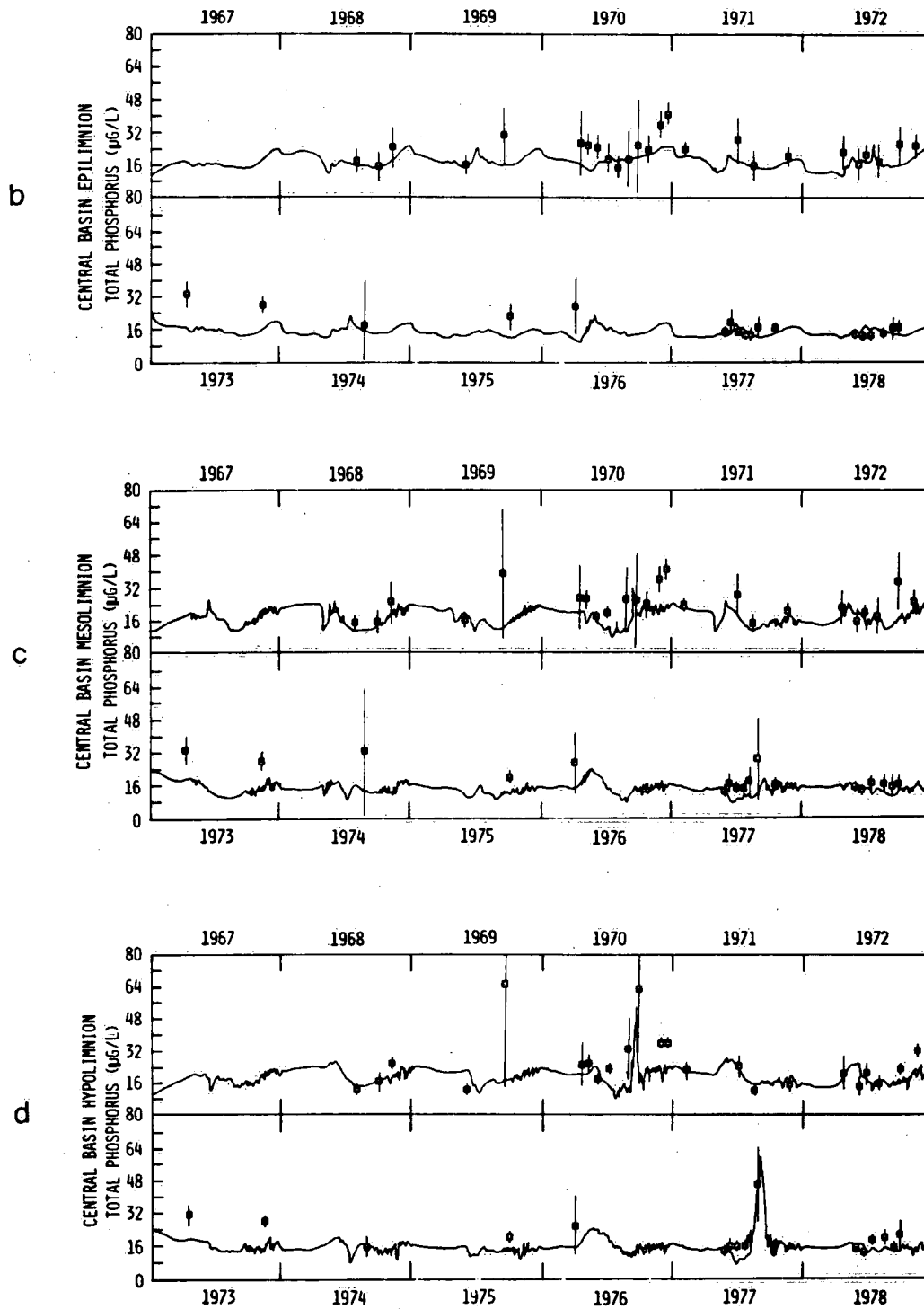


Figure 6.11. Continued.

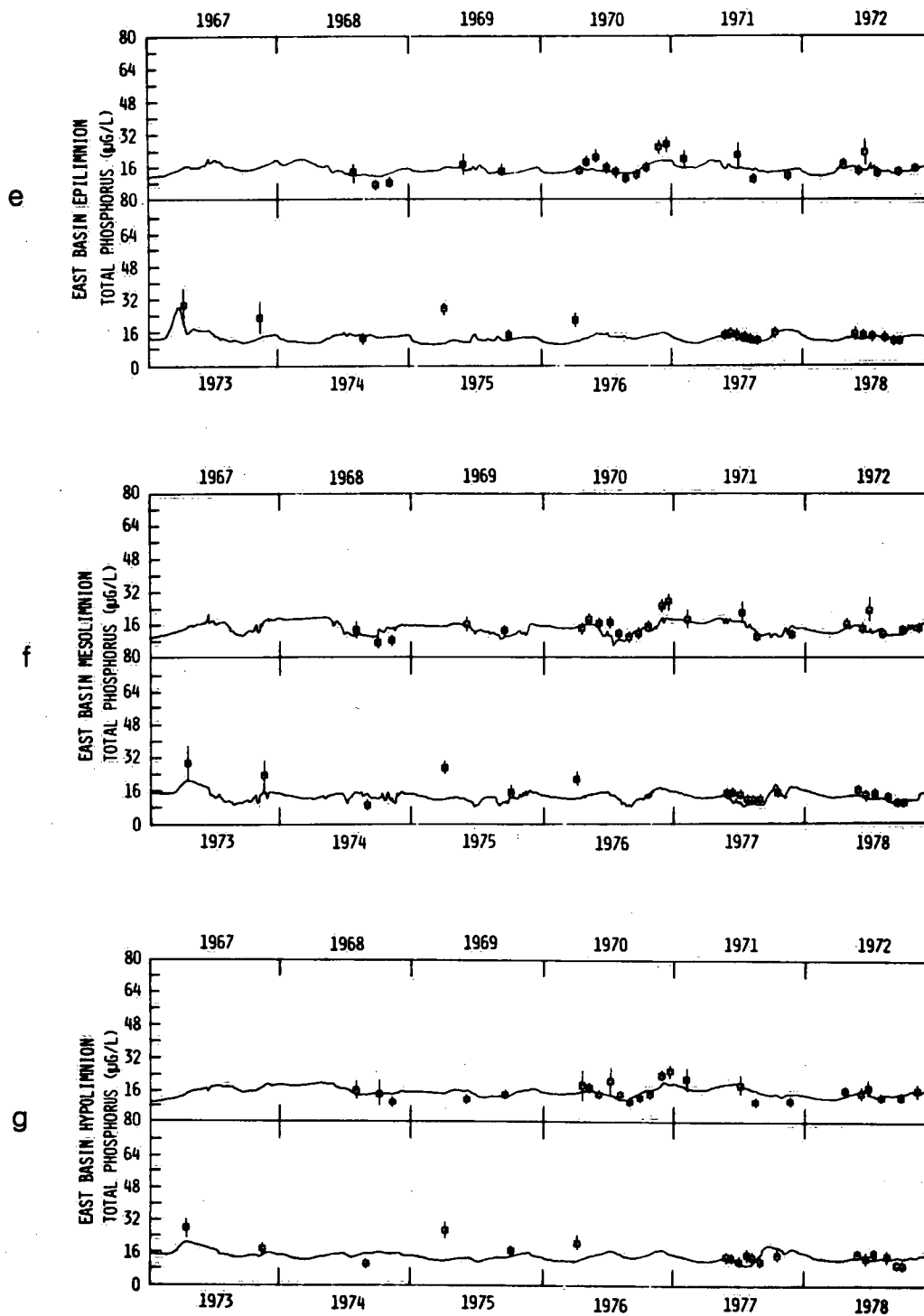


Figure 6.11. Continued.

drop in total phosphorus is more prominent in the mesolimnion than in the epilimnion or hypolimnion (Figures 6.11e to g).

In conclusion, the addition of the mesolimnion provides the spatial details necessary to discern the effects of the sediment oxygen demand rate. The model results are more sensitive to daily meteorological fluctuations. However, unlike the six-box model, a constant sediment oxygen demand in the nine-box model does not seem to simulate the oxygen depletion in the Central Basin hypolimnion for all of the years, e.g. 1969. The sensitivity and error analysis of the effects of loadings and meteorological factors on lake concentration response will be discussed in Chapter 9.

One-Dimensional Thermocline Model

7.1 Introduction

The Lake Erie basins are sensitive to changes in meteorological factors. Two important physical processes are directly influenced by the meteorological forcing: the lake-wide hydrodynamic circulation and the distribution of heat energy. The lake-wide hydrodynamics will be discussed in Chapter 8. In this chapter, the thermodynamic processes in the lake are discussed.

Whereas the hydrodynamic circulation influences on "lake-wide mean" concentrations of water quality variables are found to be slight (Simons, 1976b; Simons and Lam, 1978), the thermal structure exerts dominant effects on the dynamics and spatial distribution of these variables in Lake Erie (Section 3.2) because of the shallowness of the lake. The thermal structure of the lake not only defines the number, size and characteristics of its homogeneous compartments but also, within each compartment, the temperature of the water influences the biological and chemical processes. For example, oxygen depletion, denitrification, and anoxic regeneration of available phosphorus are among the more significant hypolimnetic processes affected by the lake thermal structures.

More important, a mechanism for the accurate thermal structure description provides the direct linkage of such meteorological factors as wind, solar radiation and air temperature to the seasonal response of the lake ecosystem. These seasonal variations often cause large short-term oscillations in the concentrations of dissolved oxygen and soluble reactive phosphorus in the hypolimnion, and almost completely mask the effect of long-term nutrient loading

(Section 6.3). However, to investigate the long-term effects of nutrient loading, detailed thermal structure computations, such as the three-dimensional spatial distribution of temperature, are not pertinent. What is required is an efficient and stable algorithm to compute the seasonal changes of the mean vertical temperature distribution over each of the basins over a long period.

There are a number of such one-dimensional thermocline models (Kraus and Turner, 1967; Sundaram and Rehm, 1973; Mellor and Durbin, 1975; Walters *et al.*, 1978; Simons, 1980); each has its area of application and turbulence closure submodels. However, verification of these models against long-term basin-wide mean temperature data has not been attempted. In this chapter, the one-dimensional thermocline model developed by Lam and Schertzer (1980) will be verified with twelve years of temperature data from Lake Erie. Specifically in Section 7.2, the model structure and the model formulation are discussed with respect to the parameterization of the physical processes in the heat diffusion equation. In Section 7.3, the numerical methods for solving the model equation and the calibration of the model coefficients will be discussed. In Section 7.4, observed data of temperature for 1967 to 1978 are compared with the predicted results for the Central and Eastern basins. Computed and observed layer thicknesses for the Central Basin in 1978 are also shown.

7.2 Physical Processes and Model Structure

The main purpose of developing a one-dimensional thermocline model, in the context of long-term simulation of water quality variables, is to compute the basin-wide mean temperature, the dynamic formation and changes of thermal layers, and the seasonal thermal structure cycle, in response to various types of meteorological forcing. Typically, the seasonal cycle starts with a springtime heating of the surface layers by solar radiation, resulting in thermal expansion and

a decrease in water density. Wind-generated turbulent mixing forces the warmer surface waters downward, in an attempt to overcome the buoyancy resistance of the colder and denser underlying waters. This process continues until the initial isothermal profile is modified to a stable stratification structure, consisting of three distinct vertical layers, i.e. the epilimnion, mesolimnion and hypolimnion. These equilibrium layers are so thermally stable that vertical transport and turbulent diffusion are all but suppressed across their interfaces, particularly across the thermocline where the vertical temperature and density gradients are the largest. Throughout the summer period, the positions of these layers change and their thicknesses expand or contract, according to the meteorological conditions. In the late fall, increased wind-generated turbulence, decreased thermal heat input, and excessive convective heat loss from the water surface as a result of cooler air temperature and lower humidity activate a rapid return to the homothermic condition. This process is usually known as the "fall overturn". The fall overturn marks the end of the stratification period and restores high oxygen level to the entire water column. The precise timing of fall overturn is an important element in deciding the duration of a shallow hypolimnion, if present, during the late summer. In the wintertime, Lake Erie is often partially ice-covered. A reverse but weak stratification may occur, because water at 4°C is at maximum density and tends to sink to the lake bottom, while the surface water is chilled to 0°C. Thus, the lake waters may become warmer at the bottom than at the top; the cycle again repeats itself at springtime.

The stratification phenomenon also occurs laterally. As the lake is warmed up in early spring, the nearshore zone, particularly the shallow regions, may be heated up faster than the offshore zone. Between the warmer nearshore waters and the colder (at 0°C) offshore waters, there exists a sharp frontal band of 4°C water. This sharp band, at maximum density, acts as a lateral thermal barrier to the

transverse transport and dispersion between the nearshore and offshore zones. This horizontal "thermal bar" phenomenon (Rodgers, 1965) usually disappears in a matter of weeks as the frontal band moves farther out to the offshore regions, becomes less stable and dissipates. However, differences in the horizontal distribution of temperature do occur thereafter from time to time during the vertical stratification period. Thus, the thicknesses of the vertical thermal layers vary at different locations in the lake, e.g. nearshore vs. offshore locations; the thermocline surface is never a flat plane, but rather a surface with troughs and crests. The simulation of the temporal and spatial details of the temperature distribution requires accurate knowledge of the physical processes and models with very fine resolution (see Chapter 8).

As an example, Figure 7.1 shows the observed hourly mean temperature profile collected at a fixed station with a depth of 20 m in the Central Basin of Lake Erie. The diurnal cycles can be readily traced in the oscillation of the thermocline position. Data are also obtained from ship surveys which typically sample the whole lake in a period of a week. Figure 7.2 shows typical ship surveillance data, interpolated over a two-dimensional (x-z) (along the longitudinal axis and depth) representation of Lake Erie (see also the Appendix for the method of interpolation). That is, the interpolated data along the transverse axis (y) are combined and averaged for each point on the x-z plane. Note that the isotherms are not straight lines parallel to the lake surface after the averaging. Figure 7.3 shows the same data set, plotted as a one-dimensional representation for each of the basins. This one-dimensional data representation is obtained by further collapsing the two-dimensional data of Fig. 7.2 along the longitudinal axis (x) of the lake. Obviously, the one-dimensional representation (Fig. 7.3) loses some of the temporal (Fig. 7.1) and spatial (Fig. 7.2) details. This also shows some of the limitations of the one-dimensional model.

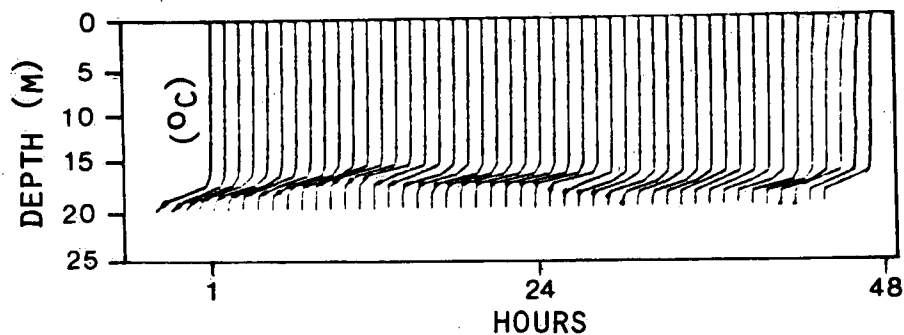


Figure 7.1. Hourly averaged temperature profiles.

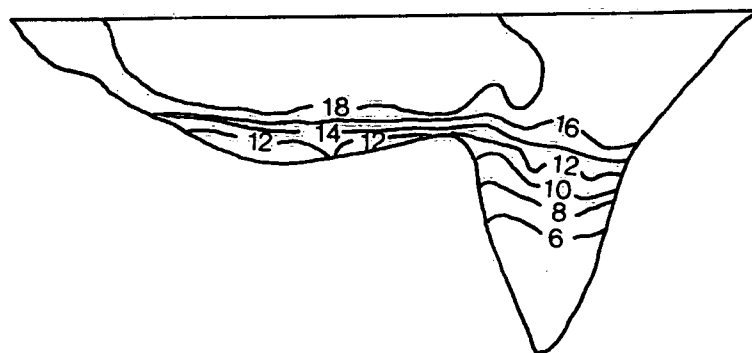


Figure 7.2. Two-dimensional (x-z) contours generated by interpolation (Program TWIST) of ship cruise temperature data (September 13-19, 1978).

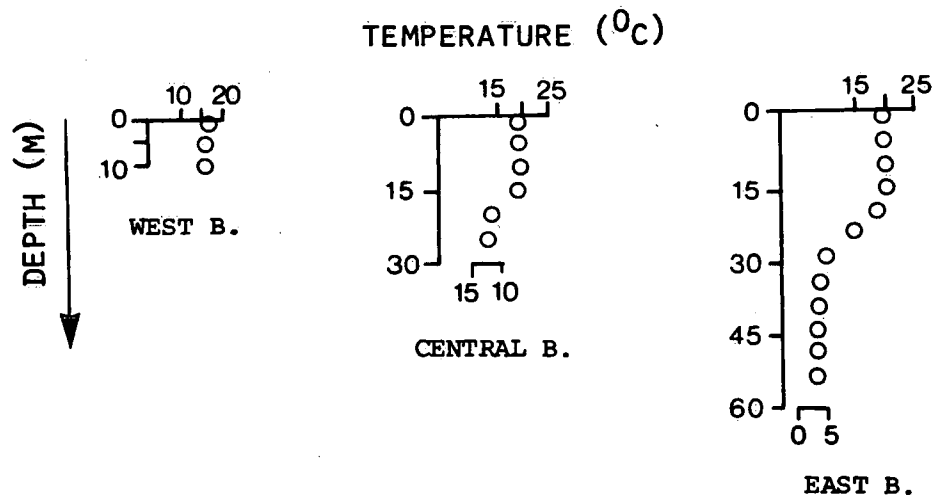


Figure 7.3. One-dimensional volume-weighted averaged temperature profiles obtained from results of Figure 7.2 for calibrating the one-dimensional thermocline model.

The heat balance equation for a water column or a lake basin is given by

$$\frac{\partial T}{\partial t} = \frac{1}{A} \frac{\partial}{\partial z} (AK_v \frac{\partial T}{\partial z}) + s \quad (7.1)$$

where T is temperature; t is time; z is depth measured from lake surface; A is cross-sectional area; K_v is vertical turbulent diffusivity; s is a source term. The diffusivity, K_v , can be a function of wind mixing, Coriolis force, buoyancy effects, internal-wave frequencies, and even molecular diffusion. The following formulation has been tested with Great Lakes data and has produced satisfactory results. Briefly, the vertical diffusivity is defined over the three layers

$$\text{Epilimnion: } K_v = K_0(1 + \sigma R_1)^{-1} - \gamma \partial \rho / \partial z \cdot \frac{g}{\rho} \quad (7.2)$$

$$\text{Mesolimnion: } K_v = K_{TC} (N_{TC}^2 / N^2)^{1/2} \quad (7.3)$$

$$\text{Hypolimnion: } K_v = K_B - \gamma \partial \rho / \partial z \cdot \frac{g}{\rho} \quad (7.4)$$

where K_0 is the air-water diffusion parameter; K_B is the bottom diffusion parameter; σ , γ are model coefficients, g is gravitational acceleration; ρ is water density; R_1 is the Richardson number; N is the Brunt-Väisälä frequency; TC denotes the value at the thermocline, where maximum temperature gradient occurs. The main concept here is that the diffusion at the epilimnion is controlled by the balance between the wind mixing and buoyancy effect as well as the effect of free, penetrative convective mixing. At the middle layer, the magnitude of diffusivity is the smallest at the thermocline but increases to a value limited only by the bottom turbulence induced by wind events. This limiting value of the eddy diffusivity is defined as

$K_B = \beta K_{TC}$ and remains constant throughout the hypolimnion, but can be changed as the air-water diffusion parameter, K_0 , changes.

This definition of vertical eddy diffusivity shows the three distinct phases of the balance of wind-mixing and thermal buoyancy, which can be adapted for designing the layer structures in mass balance box models (Sections 5.7 and 5.8). The switching from one phase to another, as defined in Equations 7.2 to 7.4, is accomplished by mathematically matching the continuity of the diffusivities so defined. Note that the physical parameters, R_1 , N and ρ , are all functions of temperature and hence Eq. 7.1 is a highly nonlinear, partial differential equation, and must be solved by appropriate and numerically stable methods (Section 7.3).

To allow for the variation of the cross-sectional areas, $A = A(z)$, of the water column or lake basin at different depths, the equation accounts for the diffusive fluxes across varying areal interfaces. This areal dependence sets the model apart from those which assume uniform cross-sectional area. The variation of the cross-sectional area as a function of depth is given in Fig. 1.4. The heat source and sink term, s , is a general term which includes the surface heat flux (Subsection 5.2.1) and the solar radiation as computed in Chapter 4 (Fig. 4.13). If the lateral heat transfer from adjacent water columns or basins can be disregarded, then the surface heat flux, Q_t , can be applied at the air-water interface as part of the surface boundary condition

$$-K_0 \left(\frac{\partial T}{\partial z} \right)_{\text{surface}} = (Q_t - R_t) / \rho c_p \quad (7.5)$$

where c_p is the specific heat of water and R_t is that part of the incoming solar radiation which is within the photosynthetic wavelengths of 400 to 700 nm (Subsection 4.2.8). After entering the water column, R_t is attenuated by the extinction coefficient, ϵ , such that the radiation R_z at a depth z is given by:

$$R_z = R_t \exp(-\epsilon z) \quad (7.6)$$

Thus, the radiation, R_z , is distributed in an exponentially decreasing manner over the entire water column. The incorporation of Eq. 7.6 as part of the source term, s , in Eq. 7.1 has been discussed in Walters et al. (1978) for different numerical schemes. The bottom boundary condition is simply the no flux condition.

$$\left(\frac{\partial T}{\partial z}\right)_{\text{bottom}} = 0 \quad (7.7)$$

The numerical solution of Equations 7.1 to 7.7 and the calibration of model coefficients will be discussed as follows.

7.3 Model Calibration

The calibration of the one-dimensional thermocline model Equations 7.2 to 7.7 is based on the observed data for 1970 for the Central Basin and the Eastern Basin of Lake Erie. The Western Basin is 10 m deep and thermal stratification only lasts for a short duration. It is also assumed that the horizontal transport of heat can be neglected among these basins (cf. Fig. 5.13). It must be pointed out here that the model requires information of the flow structure. Indeed, some turbulence closure models (e.g. Mellor and Durbin, 1975) are based on both thermal energy and momentum conservation equations

$$\frac{\partial T}{\partial t} = \frac{1}{\rho c_p} \frac{\partial R}{\partial z} + \frac{\partial}{\partial z} \left(-\overline{w'T'} + K_m \frac{\partial T}{\partial z} \right) \quad (7.8)$$

$$\frac{\partial \vec{V}}{\partial z} = f \vec{V} \times \hat{k} + \frac{\partial}{\partial z} (-\overline{w'\vec{V}'} + \nu_m \frac{\partial \vec{V}}{\partial z}) \quad (7.9)$$

where the symbols are the same as those in Equations 7.1 to 7.7, except that the prime symbol denotes fluctuations and \vec{V} is the deviation of the horizontal current from the geostrophic value; w and \hat{k} are the vertical velocity and vertical unit vector; f is the Coriolis parameter; K_m and ν_m are molecular thermal diffusivity and viscosity, respectively.

The advantage of the two-equation turbulence closure model is in the interaction between flow field and the thermal regime from linking terms like $\overline{w'T'}$ and $\overline{w'\vec{V}'}$. However, for practical and efficiency considerations (e.g. Walters *et al.*, 1978; Simons, 1980), the solution of Eq. 7.8 alone, with some reasonable assumption of the flow field, could also provide satisfactory results for the seasonal dynamics of lake temperature.

Thus, Eq. 7.1 is derived from Eq. 7.8 by the application of the gradient diffusion hypothesis

$$-\overline{w'T'} = K_v \frac{\partial T}{\partial z} \quad (7.10)$$

and, similarly, for the momentum equation:

$$-\overline{w'\vec{V}'} = A_v \frac{\partial \vec{V}}{\partial z} \quad (7.11)$$

where K_v is the eddy thermal diffusivity and A_v , the eddy viscosity.

The most common flow profile shape used in the one-dimensional thermocline model is the boundary-layer approximation with logarithmic velocity shear

$$\frac{\partial u}{\partial z} = \frac{U_*}{\kappa z} \quad (7.12)$$

where $U_* = (\tau/\rho)^{1/2}$ is the friction velocity, τ is the wind stress, u is horizontal velocity, and κ is von Karman's constant. The wind stress is obtained from

$$\tau = C_D \rho_a W^2 \quad (7.13)$$

where C_D is the surface drag coefficient, ρ_a is air density and W is wind speed. This assumption of profile shape given by Equations 7.12 and 7.13 removes the dependency on velocity in the definition of the Richardson number, which can be considered as a measure of thermal buoyancy to the wind mixing

$$R_i = \frac{g}{\rho} \frac{\partial \rho}{\partial z} / \left(\frac{\partial u}{\partial z} \right)^2 \quad (7.14)$$

where g is gravitational acceleration. If the thermal expansion approximation for water is incorporated as

$$-\frac{1}{\rho} \frac{\partial \rho}{\partial T} = \alpha_w (T - 4) \quad (7.15)$$

where α_w is thermal expansion coefficient and T is water temperature in °C, then Eq. 7.14 becomes

$$R_i = -g \alpha_w (T-4) \frac{\partial T}{\partial z} / \left[\frac{C_D \rho_a}{\rho} \cdot \left(\frac{W}{\kappa z} \right)^2 \right] \quad (7.16)$$

The air and water densities, ρ_a and ρ , should be functions of air and water temperature, but constant values are used for Eq. 7.16, see Table 7.1. In Eq. 7.2, the first term on the right-hand side uses Eq. 7.16 and the empirical formulation (Walters et al., 1978)

$$K_0 = 0.0045 W$$

where W is in cm/s, K_0 is in cm^2/s ; the last term can be approximated as

$$- \gamma \frac{\partial \rho}{\partial z} \cdot \frac{g}{\rho} = \gamma g \alpha_w (T-4) \frac{\partial T}{\partial z} \quad (7.17)$$

where γ is a model coefficient. Equation 7.17 is designed to make K_v large and positive to effect a rapid mixing for the unstable case in which $\partial \rho / \partial z$ is large but negative. The use of R_i in Eq. 7.2 has a similar effect but is often too slow for very unstable conditions such as the fall overturn. In Eq. 7.3, the squared Brunt-Väisälä frequency, N^2 , is approximated by

$$N^2 = \frac{g}{\rho} \frac{\partial \rho}{\partial z} = - g \alpha_w (T-4) \frac{\partial T}{\partial z} \quad (7.18)$$

Thus, the Equations 7.2 to 7.4 are now expressed in terms of either the water temperature or the water temperature gradient, so that Equations 7.1 to 7.7 form a closed system, with only one known, namely the temperature.

Table 7.1 shows the value of the model constants used for computing K , as defined by Equations 7.2 to 7.4. Note that there are essentially three adjustable constants, σ , γ and β . These values are based on calibrating Lake Erie observed data for 1970, which have been averaged, using the method of three-dimensional weighted interpolation

Table 7.1. Constants Used in One-dimensional Thermocline Model

Constants	Units
$K_0 = 0.0045 \text{ W}$	K in cm^2/s , W in cm/s
$\sigma = 0.03$	--
$\gamma = 4.6 \times 10^3$	cm^2/s
$\beta_{\text{C.B.}} = 2$	--
$\beta_{\text{E.B.}} = 5$	--
$\kappa = 0.4$	--
$g = 981$	cm/s^2
$\rho = 1$	g/cm^3
$\rho_a = 1.25 \times 10^{-3}$	g/cm^3
$C_D = 1.5 \times 10^{-3}$	--
$\alpha_w = 13.6 \times 10^{-6}$	$^\circ\text{C}^{-2}$
$c_p = 1$	$\text{cal}/\text{g}/^\circ\text{C}$

using the structure of temperature (see Chapter 3). As shown in Figures 7.1 to 7.3, different methods of combining the temporal and spatial details result in different degrees of smoothness in the temperature profile. Hence the model constants depend on the data and averaging method used (Henderson-Sellers and Lam, 1982). They also depend on the averaging method used in the heat flux estimation, e.g. the daily averaged scalar wind speed was used in Chapter 4. For example, the value of σ is 0.03 for Lake Erie in this study; Walters *et al.* (1978) reported $\sigma = 0.048$ for Lake Washington; and Sundaram and Rehm (1973) used $\sigma = 0.1$ for Cayuga Lake. The other adjustable constant in the Lake Erie model is γ , the coefficient which controls the rate of adjustment from unstable to neutral conditions. Referring to Eq. 7.2 for unstable conditions ($R_1 < 0$), the last term becomes large and induces a large effective diffusion to mix the unstable regime. A similar term Eq. 7.17 is added to Eq. 7.2 to speed up the fall overturn. Both coefficients σ and γ are held constant for both the Central and Eastern basins. However, it is found necessary to assign different values to the third adjustable coefficient, β , for the Central and Eastern basins, as $\beta_{C.B.}$ and $\beta_{E.B.}$, respectively. This coefficient, β , defines the limiting value for the eddy diffusivity, K_B , of the bottom layer, as a function of the diffusivity, K_{TC} , at the thermocline. It is therefore conjectured that the values of β may be also related to the geometry of the basins, such as the depths and aspect ratios.

Both the finite difference and the finite element methods (Lam, 1980) can be used to solve the heat balance equation, Eq. 7.1, with the boundary conditions given by Equations 7.5 and 7.7. The two methods give slightly different results because of the treatment of the surface boundary conditions (Eq. 7.5) and the solar radiation source (Eq. 7.6). However, these differences are within the uncertainties arising from the heat flux estimation, and hence both methods are applicable. The following results were computed by the

finite-difference method. Basically, the semi-implicit, Crank-Nicholson time-differencing scheme and an iterative procedure (Lam, 1980) are used to handle the nonlinear terms. A time step of 1 day and grid spacing, $\Delta z = 1$ m, are used. Because of the moderately coarse spatial resolution, it was necessary to force the computed eddy diffusivity, K_{TC} , to a smaller value, e.g. 0.2 times K_{TC} in the iteration procedure. Figure 7.4a shows the computed and observed temperature for the Central Basin in 1970 and Fig. 7.4b, the computed eddy diffusivity. Figure 7.5 illustrates the computed and observed thermocline positions for the Central Basin in 1970. For the chosen spatial grid resolution, the computed results appear to compare well with the observation.

7.4 Verification: Temperature, 1967 to 1978

Figures 7.6 and 7.7 show the verification results of the one-dimensional thermocline model for the Central and Eastern basins, respectively, for 1967 through 1978. To start the numerical integration of a typical year, a fully mixed temperature profile for May 1, or the profile of the first cruise in each year is used. The difference in the results of using either type of profiles is not significant as long as the total heat content is the same. The numerical integration then proceeds to cover the months of May through November. For the purpose of long-term water quality simulation, full mixing is assumed for December to March for each year. Thus, the model can be used repeatedly from year to year, using the daily heat fluxes and solar radiation inputs shown in Fig. 4.13.

Figure 7.6 shows the results for the Central Basin. Because of its relative shallowness, the Central Basin often develops a thick epilimnion (10 m) in June or July; the hypolimnion becomes shallow as September approaches and usually reaches a minimum (1 or 2 m) just before the complete fall overturn in October. The exception is 1972;

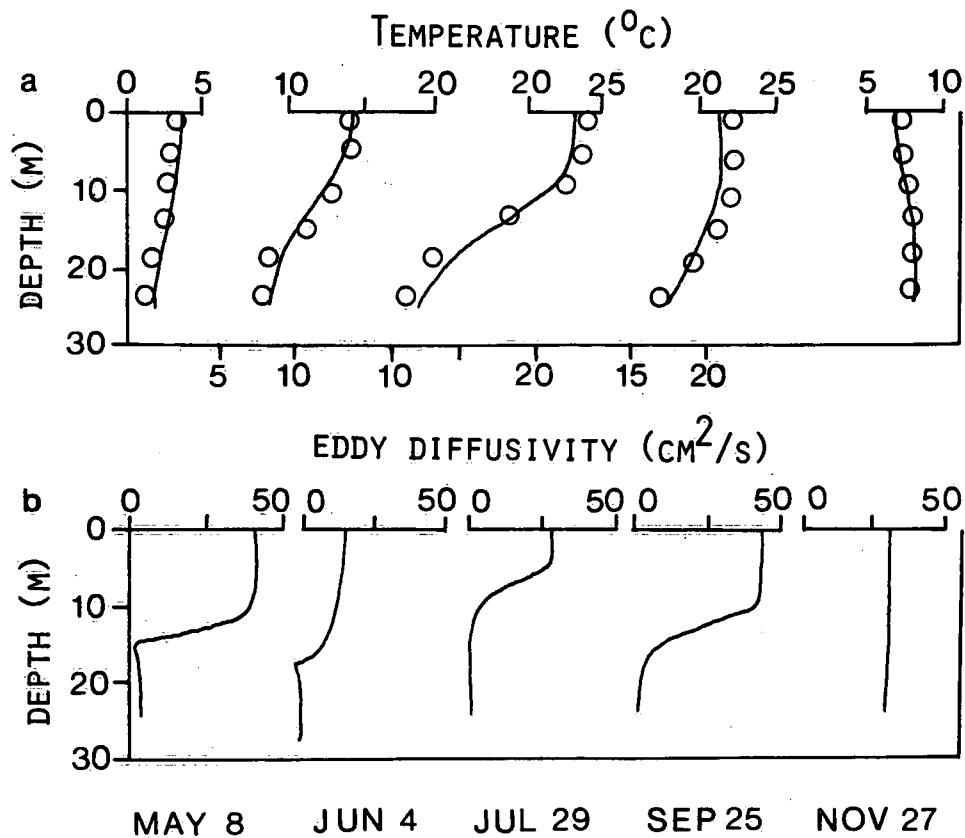


Figure 7.4. (a) Computed (lines) and observed (dots) temperature and (b) computed eddy diffusivity for the Central Basin, 1970.

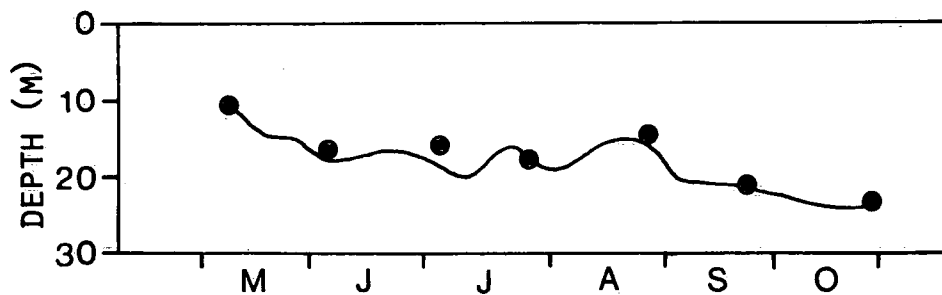


Figure 7.5. Computed (line) and observed (dots) thermocline positions for the Central Basin, 1970.

the stratification was interrupted in June and the temperature profile was straightened by storm events, and then became stratified again in August. However, it is clear, for example, that the hypolimnion is shallower in 1970, than, say, 1978. In general, the fall overturns were also fairly well simulated, as reflected in the transitions of stratified profiles to fully mixed profiles in the months of October and November.

Figure 7.7 shows the results for the Eastern Basin: the thermocline development in this basin is rather periodic. Because of its depth, the basin often starts with a smooth but slightly stratified temperature profile in June (e.g. June 2, 1969; June 4, 1970); it develops into a distinct three-segment stratification in August or September (e.g. August 27, 1970; September 18, 1978); then it proceeds rapidly with downward penetrative mixing in October (e.g. October 17, 1969; October 29, 1975); and the full mixing is usually completed in November or December. There are some exceptions to this cycle. For example, in 1972 there were two major storms which disrupted the thermal stratification and the epilimnion was only about 10 m deep in August, compared with the normal thickness of 20 m. Thus, the epilimnion in the Eastern Basin can vary anywhere from 1 or 2 m in May from the surface to 50 to 60 m in November.

In general, then, computed temperatures of both the Central and Eastern basins show good agreement with the observations. The error analysis of the verification results will be discussed in Chapter 9.

7.4.1 Verification: thermocline positions, 1978

As a result of its shallowness, the Central Basin has a less distinct three-layer structure, particularly if the layers are to be established from the observed data alone (Fig. 7.6). The definition of the eddy diffusivity (Equations 7.2 to 7.4), however, provides a

CENTRAL BASIN

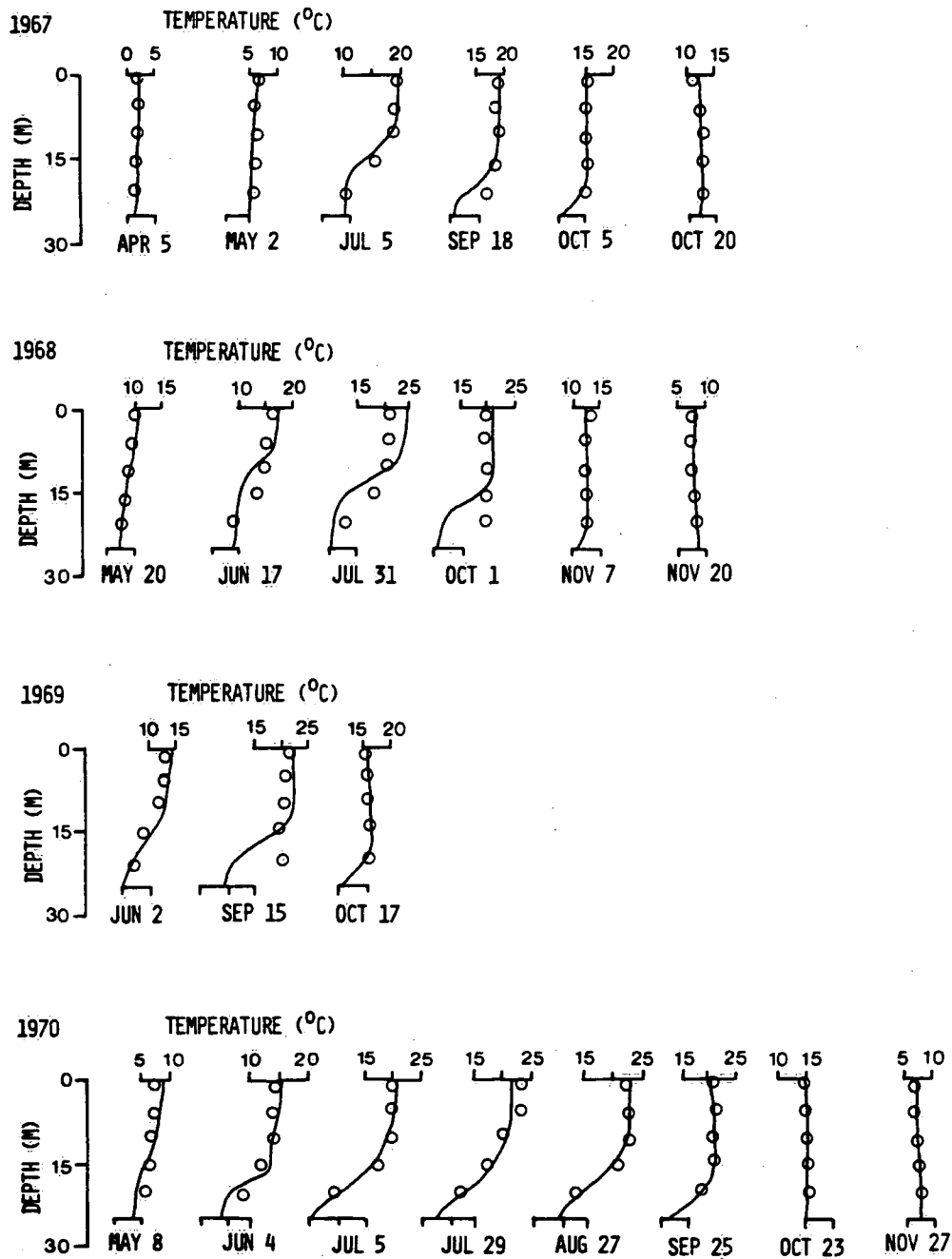


Figure 7.6. Computed (—) and observed (\circ) temperature for the Central Basin of Lake Erie.

CENTRAL BASIN

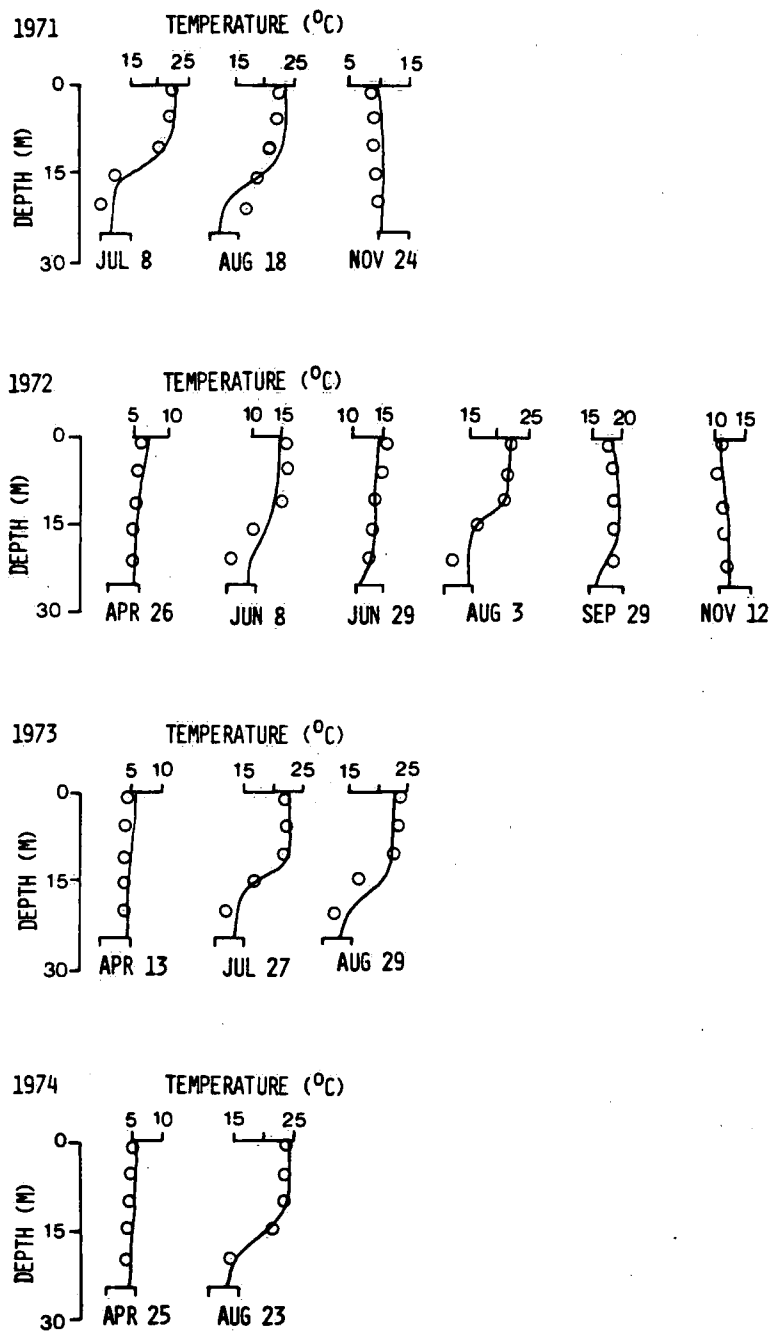


Figure 7.6. Continued.

CENTRAL BASIN

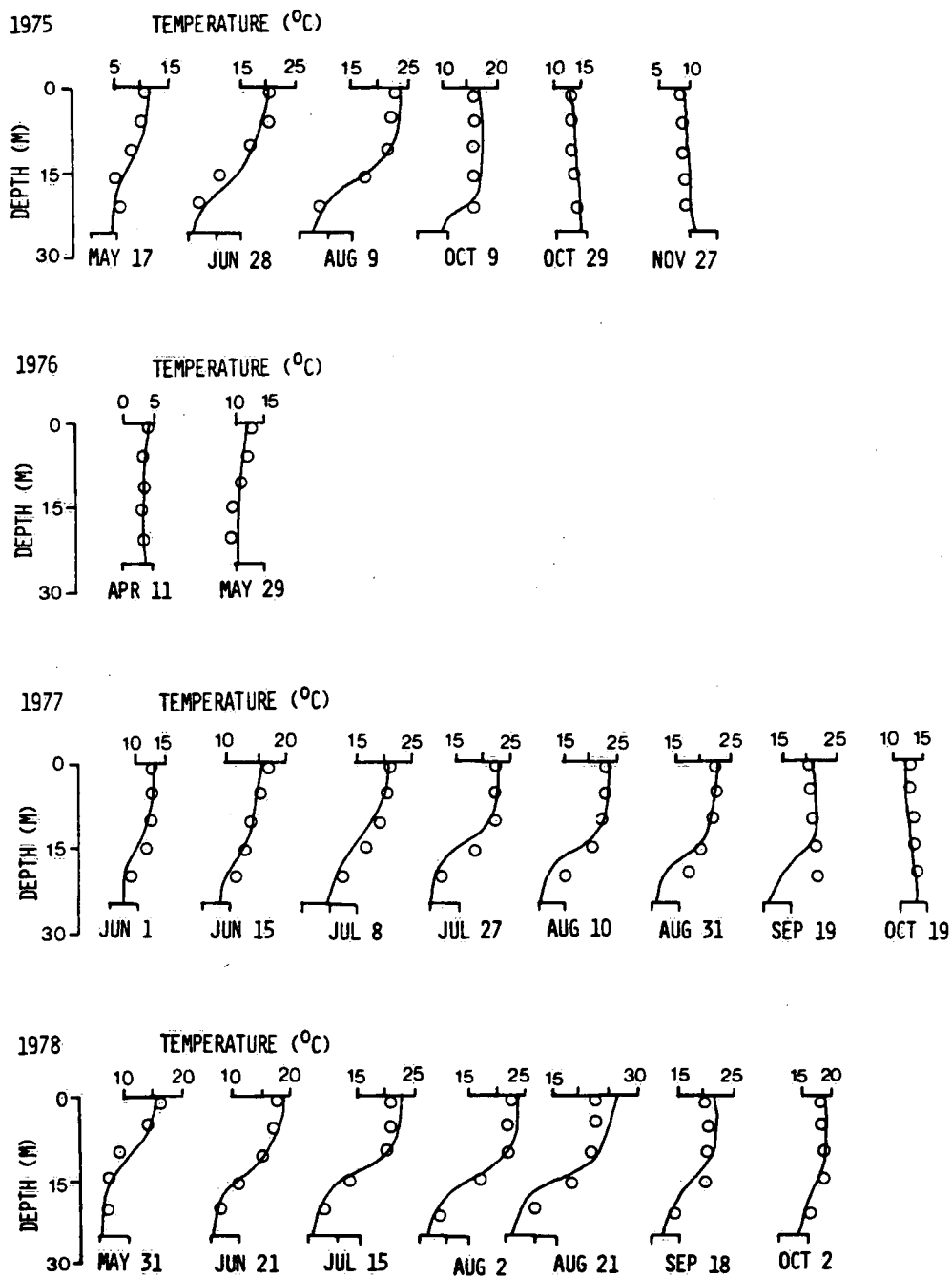


Figure 7.6. Continued.

EAST BASIN

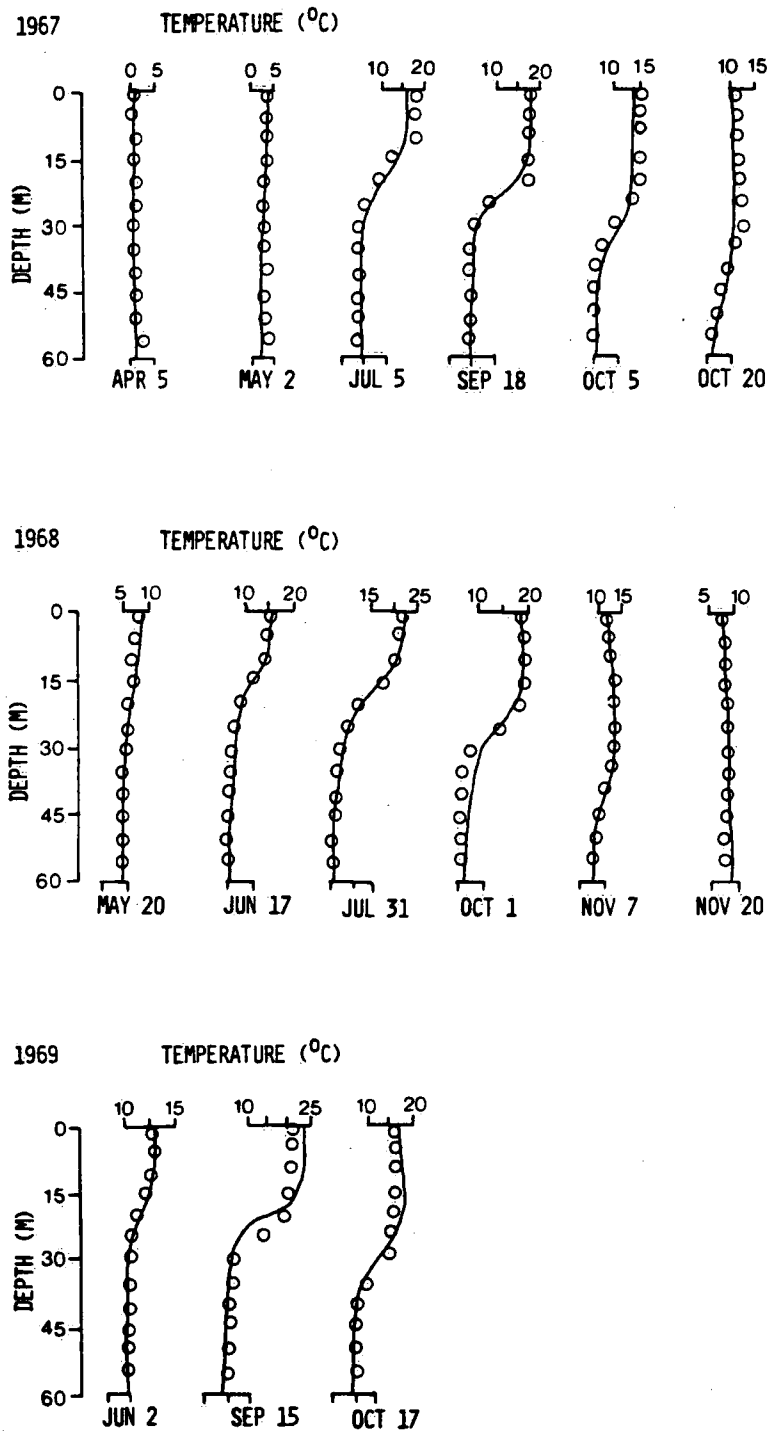


Figure 7.7. Computed (—) and observed (O) temperature for the East Basin of Lake Erie.

EAST BASIN

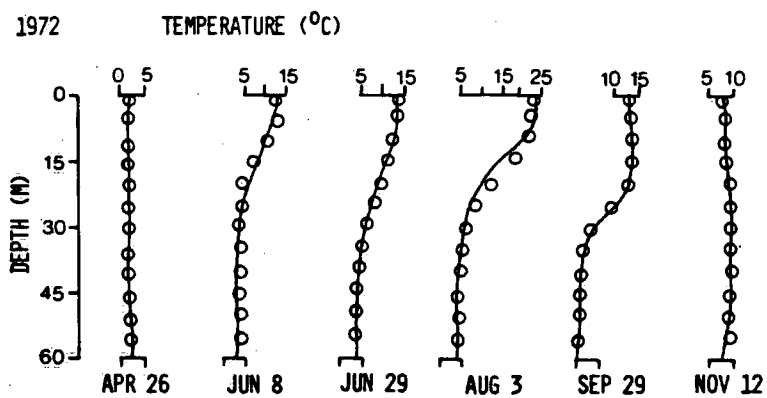
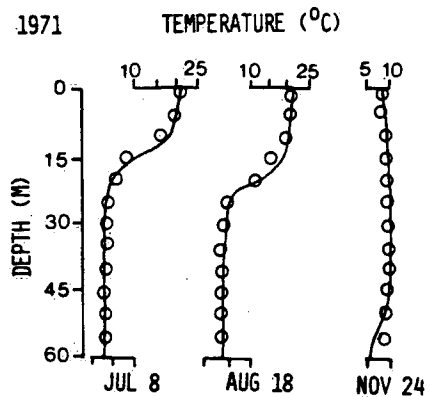
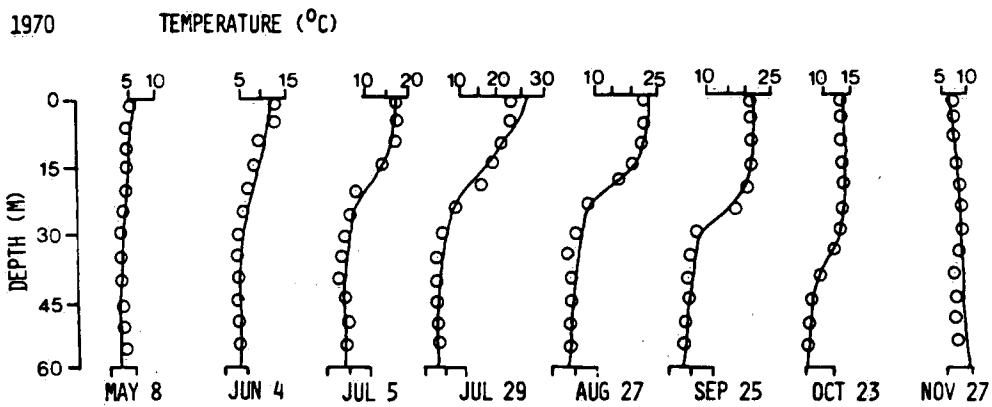
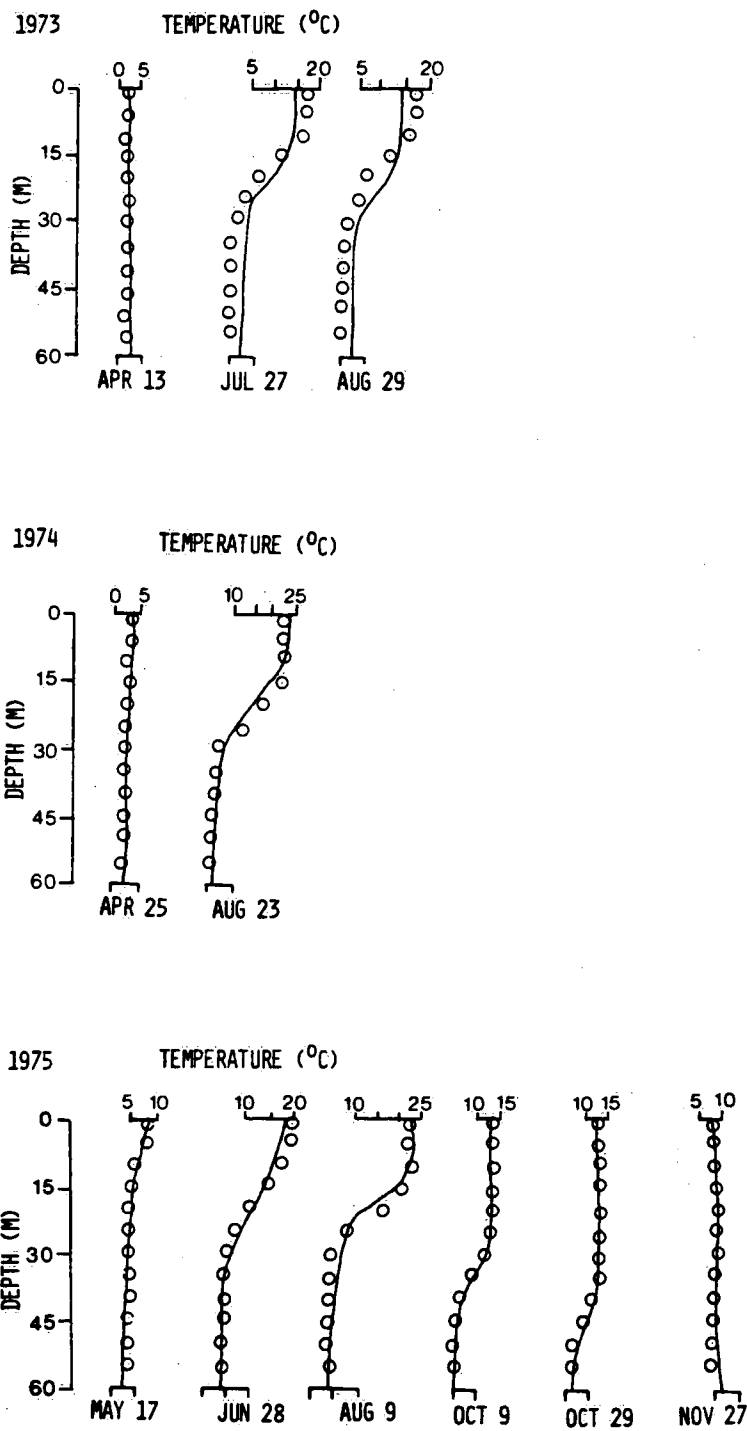


Figure 7.7. Continued.

EAST BASIN



EAST BASIN

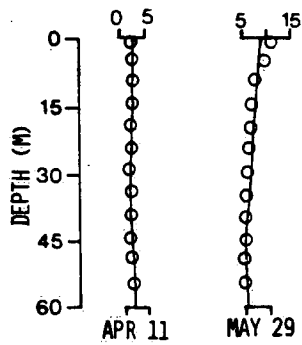
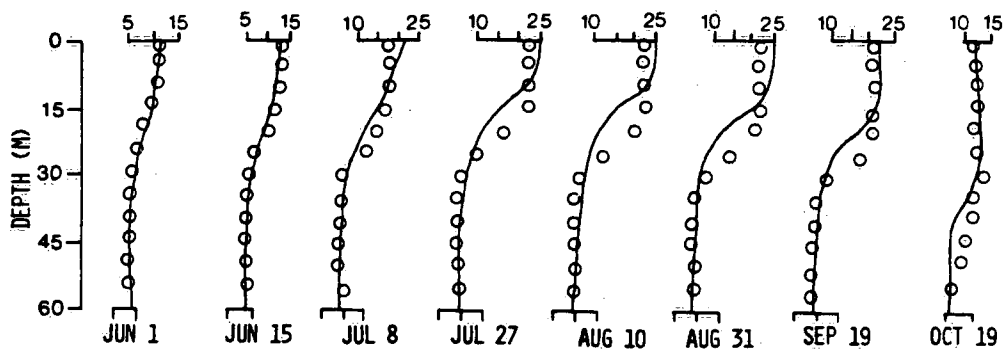
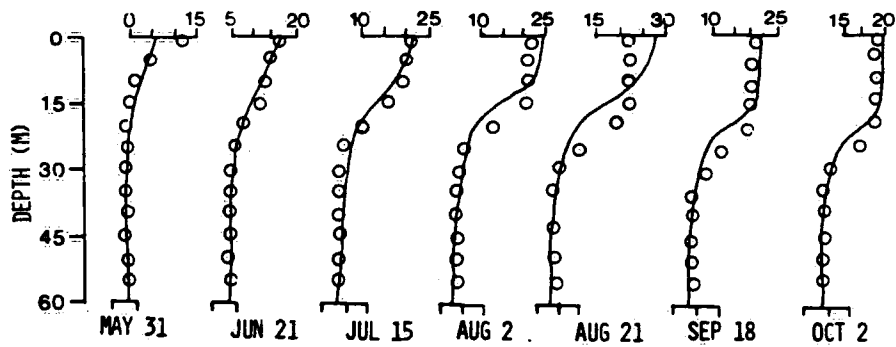
1976 TEMPERATURE ($^{\circ}\text{C}$)1977 TEMPERATURE ($^{\circ}\text{C}$)1978 TEMPERATURE ($^{\circ}\text{C}$)

Figure 7.7. Continued.

convenient alternate method of defining the layer thicknesses. The following is a description of this alternate procedure.

Using daily estimates of surface heat flux and wind speed, daily mean vertical temperature profiles were produced for the Central and Eastern basins. Based on these profiles, initial estimates of the upper and lower mesolimnion boundaries were made at the points of matching diffusivities (see Equations 7.2 to 7.4). Objective determination of the basin thermal structure was accomplished by application of a numerical procedure based on an extension of Newton-Taylor least-square fitting method (Papadakis, 1981). The method is an iterative technique which allows the determination of the best least-squares fit of three line segments to the computed temperature data. The intersection points of three linear segments define the upper and lower mesolimnion boundaries, and hence the thicknesses of the three layers. In general, the layer positions defined by Equations 7.2 to 7.4 are good initial guesses and therefore the convergence of the Newton-Taylor method is fast.

For purposes of mass balance models, smoothed daily estimates of layer thicknesses are derived by interpolation through five-day means. Only the values for the stratified period from Julian days 160 through 278 are chosen from this procedure. For computational convenience, values for the unstratified season are determined subjectively. The results of these boundaries for the Central Basin for 1967 to 1978 have been shown and discussed in Fig. 6.3 (same as Fig. 7.10 in this chapter) in conjunction with the mass balance box models. Central Basin thermocline values for the six-box model are determined as the average between upper and lower mesolimnion bounds.

To verify these computed thermocline positions for the Central Basin, the observed values at the boundary between the Central and Eastern basins for 1978 are used. During the stratified season of

1977-78, a network of current meters, meteorological buoys and thermistor arrays was installed (Boyce et al., 1980; Chiocchio, 1981) at the Pennsylvania Ridge. These measurements were augmented by weekly temperature surveys. The intensive studies were initiated to measure the hypolimnion exchange flow between the Central and Eastern basins.

Figure 7.8 shows the measurement network employed in 1978. Based on temperature profile data, isotherms were produced in vertical cross section across the ridge. These were drawn representative of 48-hour means. Using these isotherms, estimates of the mesolimnion boundaries could be determined. Figure 7.9 gives the range between maximum and minimum depths of the upper and lower mesolimnion boundaries and midpoint of the mesolimnion for the stratified period. These maximum and minimum depths are due to the variations in the transverse (y) direction of the lake, i.e. from station 1 to station 12 in Fig. 7.8. Superimposed on these values are the mean positions of the mesolimnion boundaries determined from the Central Basin based on the thermocline model and objective analysis discussed earlier. As indicated, there is reasonably good correspondence between measured Pennsylvania Ridge thermal structure and computed one-dimensional (z) profile values of the Central Basin. Topographic effects of the Pennsylvania Ridge are obvious from these figures. Maximum depth of the Pennsylvania Ridge is 21 m, whereas the Central Basin has a maximum depth of 25 m. These effects reflect some of the inaccuracies inherent in the six-box and nine-box mass balance models, in which the layer positions and thicknesses for Central Basin are used, if appropriate, for the other two basins. To simulate these spatial details, a finer grid resolution in both the y and z directions is required (see Section 8.3).

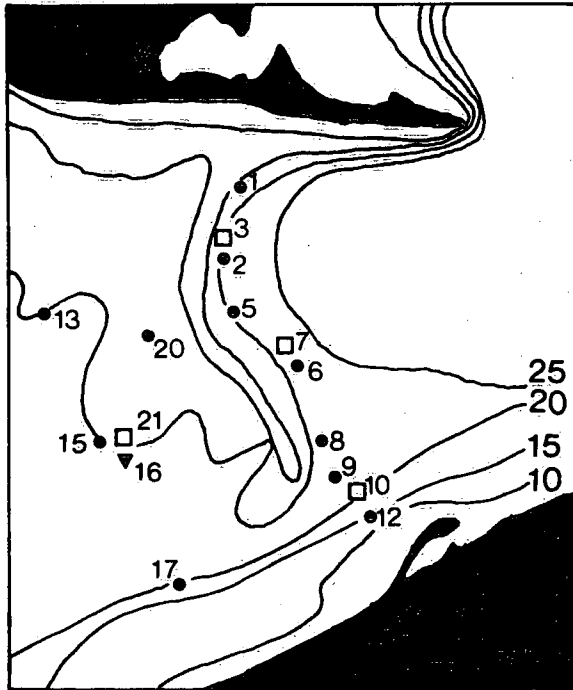


Figure 7.8. Sampling network near the Pennsylvania Ridge, Lake Erie, 1978.

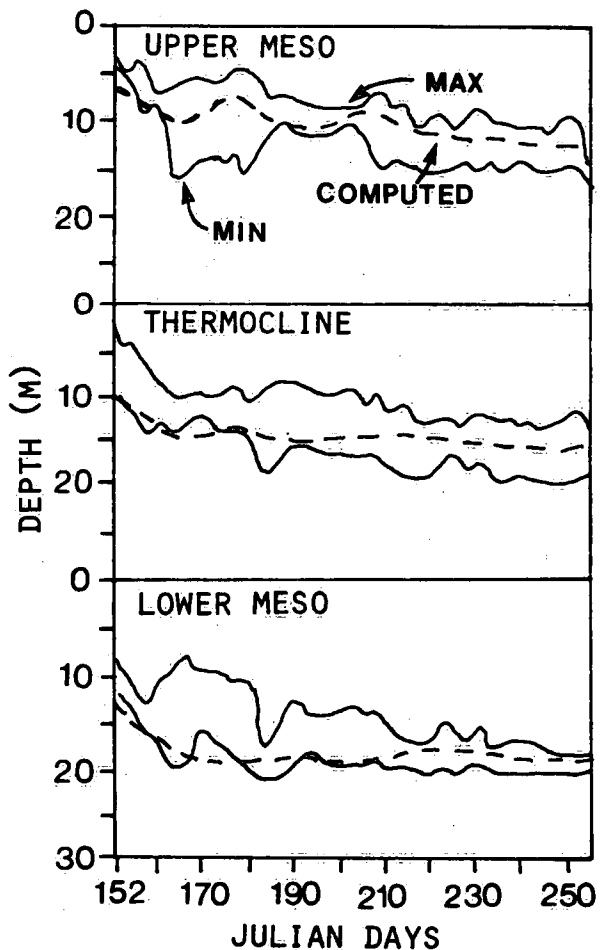


Figure 7.9. Computed mean depth (---) for the Central Basin and observed minimum and maximum positions (—) for the Pennsylvania Ridge of (a) the upper mesolimnion boundary, (b) the thermocline, and (c) the lower mesolimnion boundary.

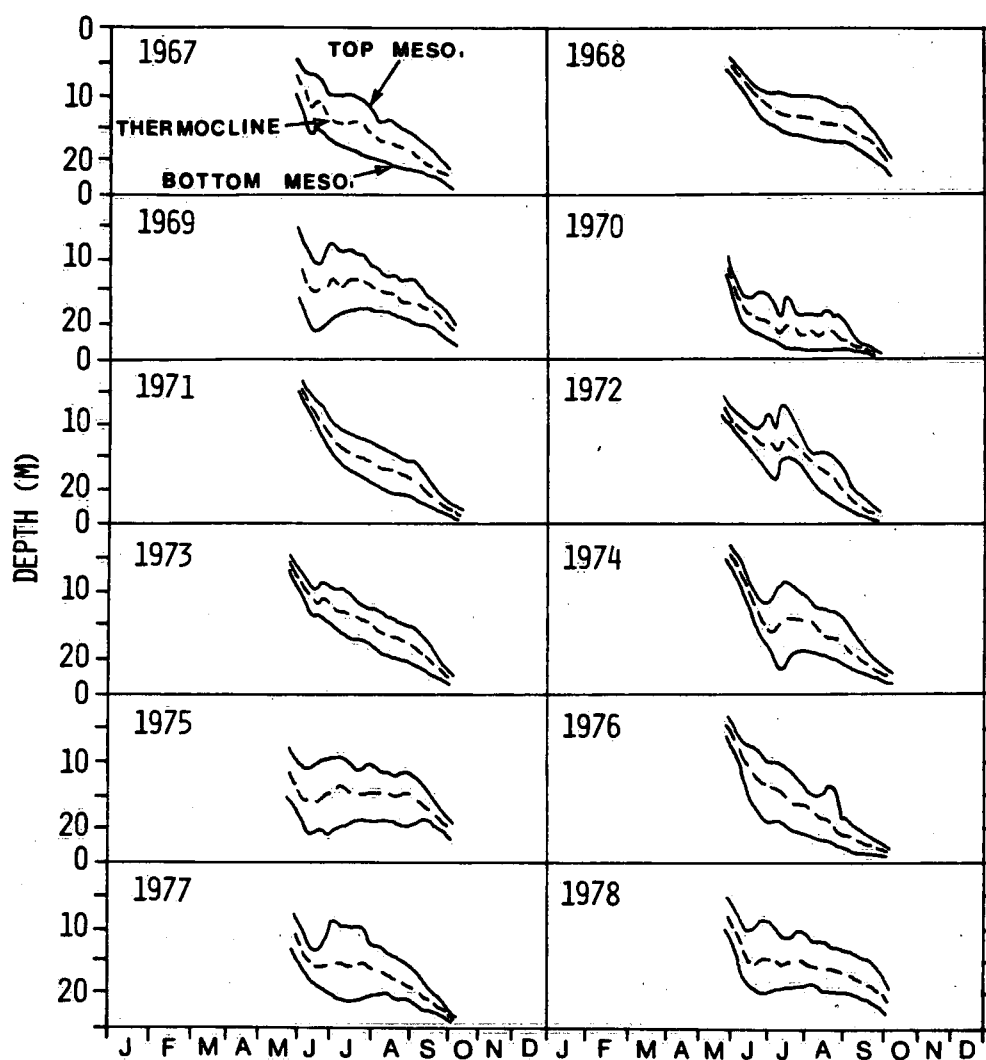


Figure 7.10. Computed positions of the thermocline (dashed lines), and the upper and lower mesolimnion boundaries (solid lines) of the Central Basin for 1967 to 1978. (This figure is the same as Figure 6.3.)

7.4.2 Verification: averaged temperatures for box models, 1967 to 1978

Figure 7.10 shows the computed positions of the thermocline as well as the upper and lower boundaries of the Central Basin for 1967 to 1978. Their importance as an integral part of the lake response to different meteorological forcing has been discussed in Section 6.2. A direct application of the computed layer positions is in the derivation of averaged temperatures which can be used in the six-box and nine-box mass balance models (Chapters 5 and 6). The results for these averaged temperatures in 1978 have been demonstrated in Figures 6.2 and 6.8. As part of the verification of the one-dimensional thermocline model, the long-term results for 1967 to 1978 are presented in Figures 7.11a to e for the six-box model and Figures 7.12a to g for nine-box model. (Strictly speaking, results for 1970 are calibration results.) The computed averaged temperature for the upper layers (Figures 7.11a, b, d) and the epilimnion (Figures 7.12a, b, e) shows excellent agreement with the observation. The lower layers, e.g. 1978 (Figures 7.11c and e), and the hypolimnia, e.g. 1968 (Figures 7.12d and g), however, sometimes show some underprediction, partly due to the addition of water level adjustment at the surface. Since the one-dimensional thermocline model uses a constant depth for each of the basins based on the 1955 water level (Subsection 4.2.6), the computed temperature profiles are then adjusted with the computed surface temperature with the top of the actual water level (Fig. 4.8). The imbalance due to the shifting of the whole computed profile is at the lower layer or hypolimnion, the bottom portion of which is assumed to have the same temperature as the bottom value computed in the profile. The fact that these imbalances do not always show up in the lower layers indicates that the method of adjustment is reasonable (see also Subsection 5.7.3).

The statistical errors and sensitivity analysis of the one-dimensional thermocline model will be discussed in Chapter 9.

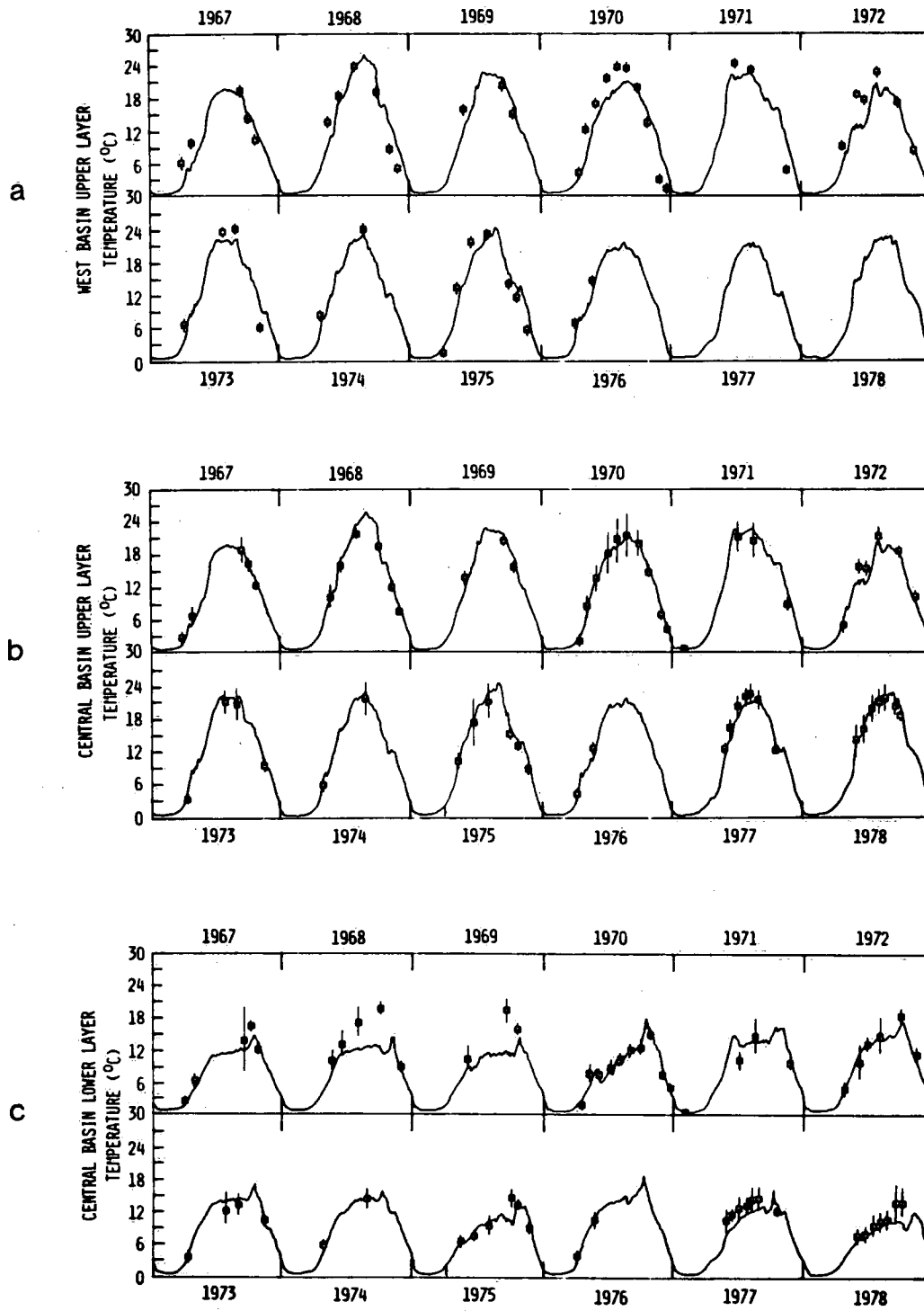


Figure 7.11. Computed (—) and observed (—■—) upper and lower layer temperatures for Lake Erie basins.

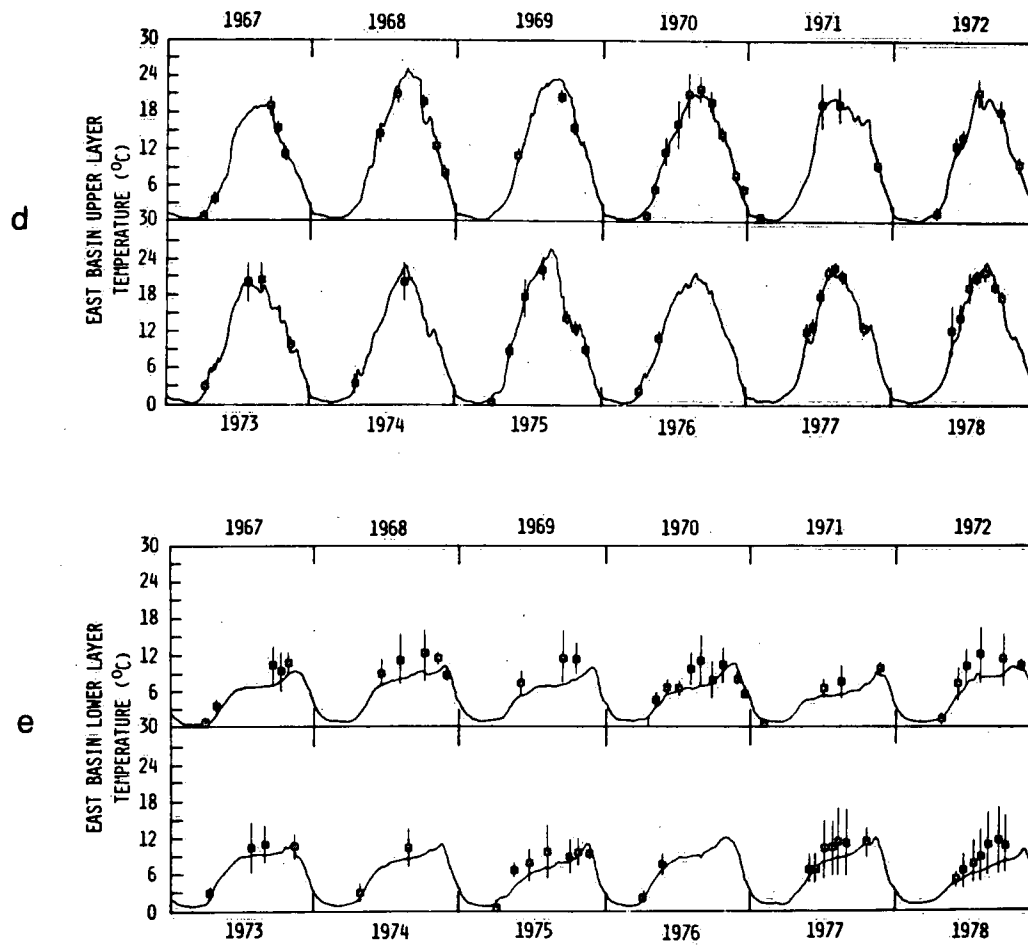


Figure 7.11. Continued.

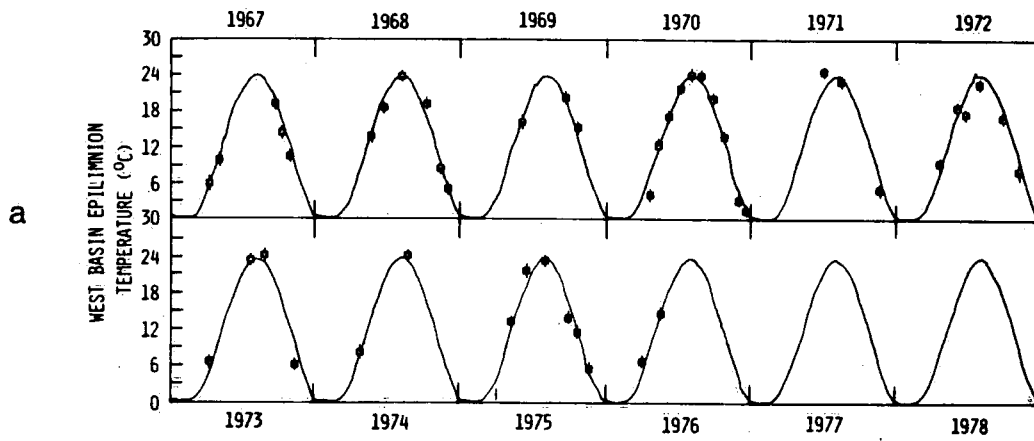


Figure 7.12. Computed (—) and observed (—■—) epilimnion, mesolimnion and hypolimnion temperatures for Lake Erie basins.

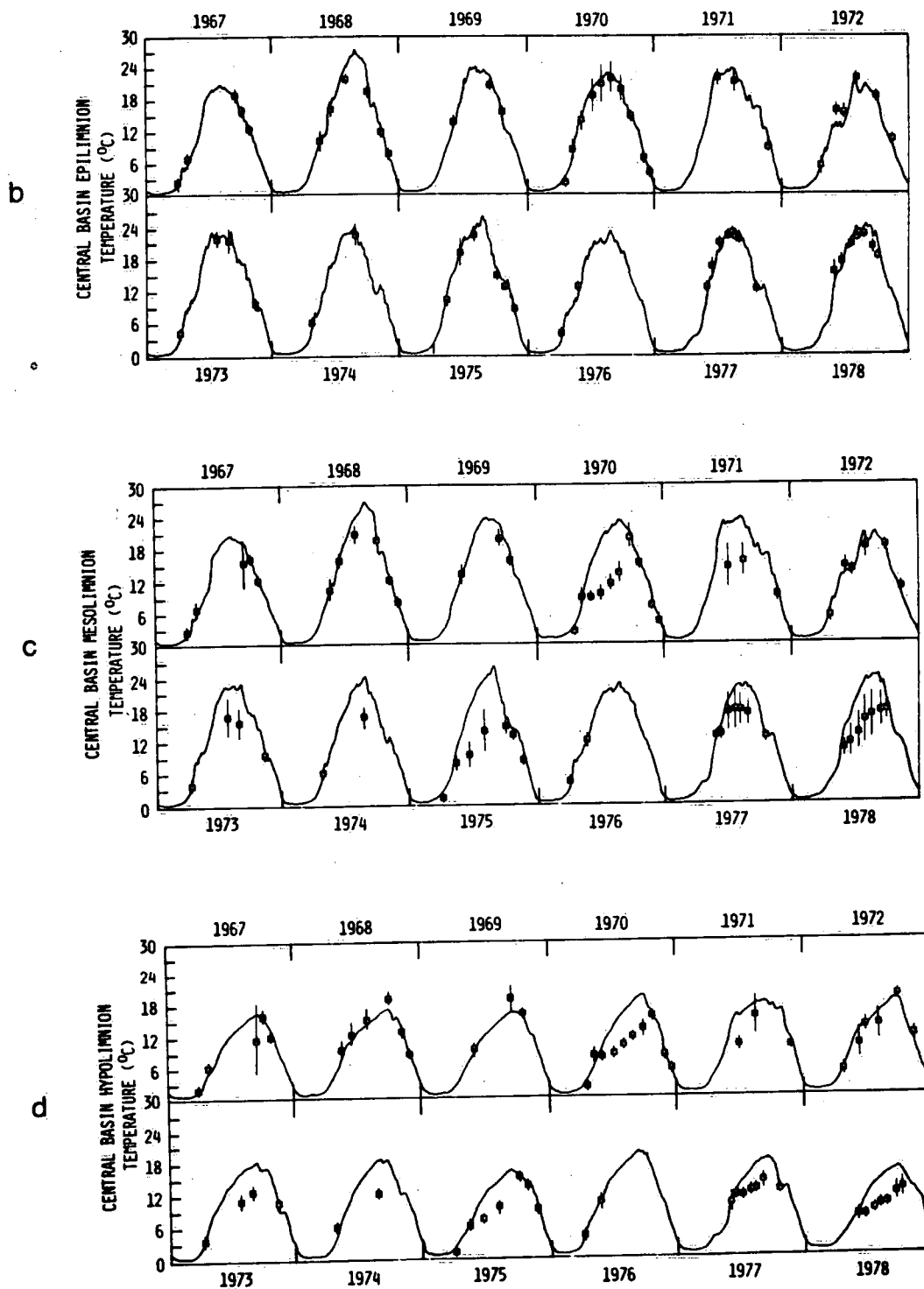


Figure 7.12. Continued.

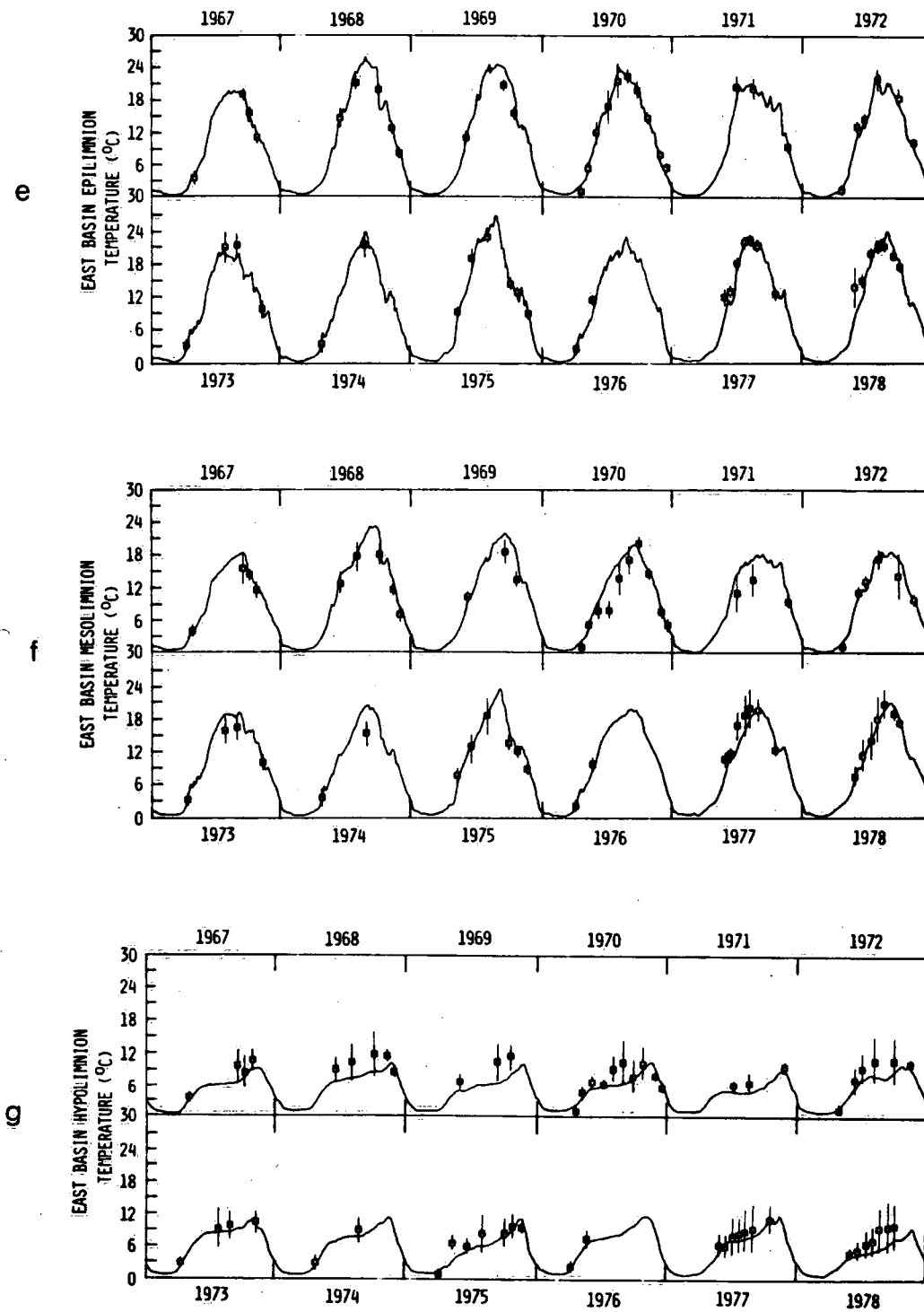


Figure 7.12. Continued.

7.5 Feedback of Heat Flux and Thermocline Models

An important consequence of surface energy exchange is the modification of the surface water temperature as well as the vertical gradients of meteorological components such as air temperature. However, the major limitation in investigating this energy exchange in large lakes is the paucity of over-lake data. This necessitates the use of observed land-based meteorological data to extrapolate to over-lake values, and the interpolation of surface water temperature from limited cruise data. This basic procedure was adopted in the one-dimensional thermocline model computations (Section 7.3). A more elaborate approach is to estimate water surface temperature and overlying air temperature by a feedback procedure in order to achieve consistency in the vertical gradients at the air-water interface.

Figure 7.13 is a schematic depicting the computational procedure for the feedback process. In general, either annually interpolated/observed or long-term mean water surface temperatures are used in combination with estimated air temperatures as first estimates for inputs to the heat balance model. Computed surface heat fluxes, either unmodified or modified by the SIT method as discussed in Section 5.3, are used as input into the thermocline model which is capable of providing, as well as new surface temperatures, estimates of water temperature with depth (Figures 7.6 and 7.7). These revised estimates of daily water surface temperatures are then fed back to the heat flux model.

Table 7.2 shows the result of one feedback cycle of the coupled heat flux - thermocline model approach. Model estimates of water surface temperature were averaged over individual cruise periods for comparison with all the data from 1967 to 1978. The best estimate is given by using the annually observed/interpolated water surface

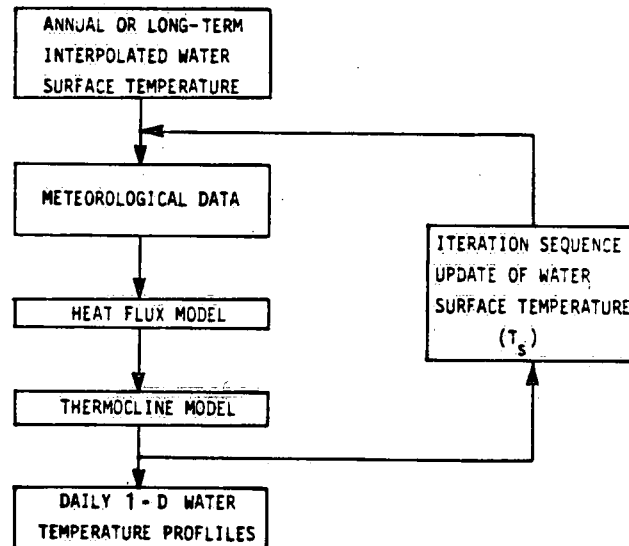


Figure 7.13. Feedback scheme for coupling the heat flux model and the thermocline model.

Table 7.2. Accuracy (σ = standard error) of Surface Water Temperature (T_s in $^{\circ}\text{C}$) Calculations by Coupled Heat Flux - Thermocline Model Approach

	Annually observed/interpolated T_s	Long-term (1967-78) mean/interpolated T_s
Heat flux modified by SIT	$\sigma = \pm 1.15^{\circ}\text{C}$	$\sigma = \pm 1.27^{\circ}\text{C}$
Heat flux with no modification	$\sigma = \pm 1.92^{\circ}\text{C}$	$\sigma = \pm 2.53^{\circ}\text{C}$

SIT = Scaling and Interpolation Technique

temperature in combination with the surface heat flux modified by SIT. The mean standard error of $\pm 1.15^{\circ}\text{C}$ is a significant achievement, considering that the number of cruises in any particular year ranged from only two to eight. The worst estimate (standard error of $\pm 2.53^{\circ}\text{C}$) is given using long-term mean water surface temperature data with no modification on the estimated heat flux. In the latter case, although the water surface temperature and air temperature have been forced to some consistency, errors remain in the estimation of the vertical heat flux and in the omission of lateral heat transports. The merit of the feedback approach is therefore not too clear, particularly in the absence of observed water temperature data.

Synthesis Models of Finer Spatial Resolutions

8.1 Introduction

Limnological phenomena can be studied at different time and spatial scales, depending on the objective of the scientific investigation. This is particularly true in the development of water quality models. On the one hand, long-term water management problems require reasonable predictive capability for simulating the overall ecosystem response of the whole lake to control strategies. On the other hand, scientific experiments are often conducted in confined areas, but with high sampling frequencies and for a short duration. Modellers are often faced with the rather difficult task of either extrapolating scientific findings from a specific site to the whole lake, or grouping data over selected homogeneous zones. A major decision is therefore required concerning the model complexity and the methodology thought to be capable of achieving the desired details. There is also concern about the degree of complexity in the compartmentalization of water quality variables, but the present discussion is limited to the dynamic and spatial complexity from the perspective of integrating physical and biochemical processes.

The simulation of the dynamic and spatial details of the distribution of water quality parameters requires models of finer grid resolution. For example, to obtain the thermal layer thicknesses for the six-box or nine-box mass balance model, it is necessary to develop a one-dimensional model for simulating the physical processes involved. Even then, the one-dimensional thermocline model (see Chapter 7) assumes knowledge of the flow field and spatial homogeneity in the other two dimensions. Thus, one can, in principle, develop models of higher dimensions. The more complex models, however, are

limited by the available knowledge and by the practicality of using them for long-term prediction (Simons, 1976a). The alternative is to keep the spatial complexity as low as possible for some variables (e.g. the six-box three variable model) and to depend on results of models of higher complexity (e.g. one-dimensional thermocline model) for those variables which need higher spatial resolutions. Thus, instead of simulating all variables with the same grid resolution, some (e.g. oxygen and phosphorus) are simulated with a coarse grid and, others (e.g. temperature), with a fine grid.

This concept of using a hierarchy of models of varying complexity, as opposed to using only one model with fixed spatial complexity, is the main discussion of this chapter. Specifically, let x , y , z be longitudinal distance, transverse distance and depth of the lake. In Section 8.2, the one-dimensional (z) dissolved oxygen model is discussed. Section 8.3 contains the discussion on the two-dimensional (x - z) model for temperature and flow field. Another kind of a two-dimensional (x - y) model, for total phosphorus, is discussed in Section 8.4. Finally, an example of a three-dimensional model is given for chloride in Section 8.5. For each of these examples, emphasis is placed on the additional spatial details, which the increase in dimensionality of the model can produce. Thus, in the one-dimensional (z) model, the effects of the turbulent eddy diffusion on the vertical dissolved oxygen profile are discussed. In the two-dimensional (x - z) model, the interbasin transports, the thermocline oscillations, and the phosphate and ammonia distributions are highlighted; in the two-dimensional (x - y) model, the relationship between the horizontal distribution of wind-wave generated turbulence energy on the physical resuspension of sediment particles is explored. In the three-dimensional model, the effects of upwelling and downwelling transports and the anticlockwise and clockwise circulations associated with rotational basin dynamics on the distribution of chloride are discussed.

All these effects have been simplified somewhat in the six-box or nine-box mass balance models but are now elaborated further in this chapter. A summary of the interrelationships among the different models is also included.

8.2 One-Dimensional (z) Dissolved Oxygen Model

The two main results of the one-dimensional (z) thermocline model discussed in Chapter 7 are the computed temperatures (e.g. Figures 7.6 and 7.7) and the computed vertical eddy diffusivities (e.g. Figures 7.4b and 7.10). Both of these results have been condensed and used in the mass balance box models (Chapters 5 and 6). If the spatial details in these computed results are to be investigated, the one-dimensional (z) framework can be used directly to simulate the water quality variables. The details can be enhanced, if we include the interbasin transport at each grid point of the one-dimensional model, such as in the case of the one-dimensional total phosphorus model proposed by Lam *et al.* (1982). For simplicity, a one-dimensional dissolved oxygen model is presented here, in which the interbasin transports are omitted, as in the case of the one-dimensional temperature computations.

The one-dimensional mass conservation equation for oxygen can be written as

$$\frac{\partial DO}{\partial t} = \frac{1}{A} \frac{\partial}{\partial z} A K_z \frac{\partial DO}{\partial z} + (P-R) - S \quad (8.1)$$

where DO is the oxygen concentration; P is the oxygen production rate during photosynthesis by algae and R is the oxygen consumption rate during algal respiration; S is a general source and sink term; z, A, and K_z are the depth, cross-sectional area and the vertical eddy diffusivity as defined in Equations 7.1 to 7.4. The photosynthesis and respiration terms may be obtained from a nutrient-plankton

submodel (e.g. Simons and Lam, 1980). For the present discussion, to eliminate the dependency on a submodel, suppose that the net oxygen produced by reaeration and photosynthesis in the epilimnion, i.e. as defined by Equations 7.2 to 7.4, is always so much that the layer is saturated with oxygen. In other words, the oxygen in this layer can be simulated by the relationship of saturated oxygen concentration with water temperature (see Table 6.1)

$$DO_s = 14.48 - 0.36 T + 0.0043 T^2 \quad (8.2)$$

where DO_s is the saturated oxygen concentration and T is the water temperature. For the mesolimnion, it is assumed that for the Central Basin, the production of oxygen by photosynthesis balances the loss of oxygen by respiration. Furthermore, it is assumed that the interbasin transport of oxygen can be omitted, so that only the vertical eddy diffusion regulates the oxygen concentration in this layer. Of course, these assumptions are rather incorrect, in view of the findings of Chapter 6. However, for demonstration purposes, it is interesting to know how different spatial scale assumptions can affect the calculated oxygen concentration. For the hypolimnion, it is simply assumed that the sediment and water oxygen demand, expressed as a constant, in $\text{mg O}_2/\text{m}^2 \text{ day}$, dominates the oxygen processes. With these assumptions, it is possible, then, to solve Eq. 8.1 by itself.

Figure 8.1 shows the computed oxygen concentration for the Lake Erie Central Basin for 1970. It is found that a combined sediment and water oxygen demand of about $0.5 \text{ mg O}_2/\text{m}^2 \text{ day}$ is required to fit the observed concentration at the bottom one metre. The sediment portion in this combined rate should therefore be within the range of the sediment oxygen demand rates (0.15 to $0.5 \text{ mg O}_2/\text{m}^2 \text{ day}$) used in the box models (Sections 6.2 and 6.3). The major deviation of the computed concentration from the observed occurs near the mesolimnion for the September 25 profile. As expected, this error is due to the

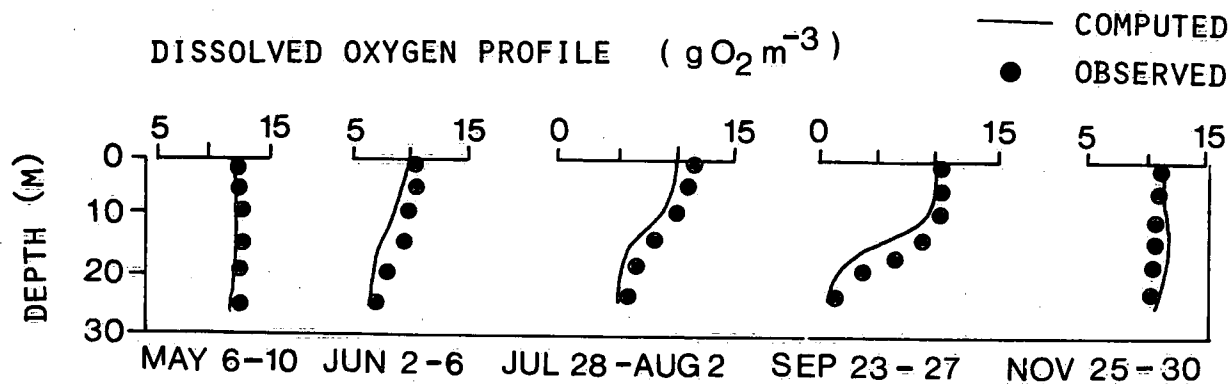


Figure 8.1. One-dimensional (z) vertical profiles of dissolved oxygen for the Central Basin, 1970.

(—) computed values, (●) observed values

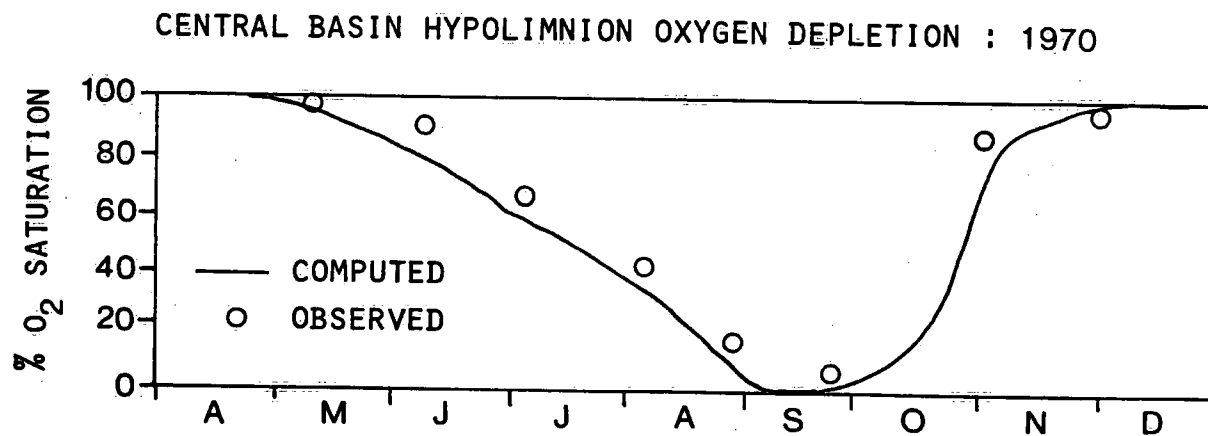


Figure 8.2. Comparison of computed and observed dissolved oxygen concentrations at 1 m above the sediment for the Central Basin, 1970.

incorrect assumption at this layer. On the other hand, the computed and observed oxygen concentrations agree well in the epilimnion, showing that the assumption of oxygen saturation is valid. As for the hypolimnion concentration, the inaccurate assumption of the mesolimnion tends to affect this layer too, except for values at the bottom one metre. Figure 8.2 shows the computed and observed oxygen concentration for the bottom one metre in the Central Basin, as achieved in the calibration of the combined sediment and water oxygen demand. The oxygen depletion rate for this volume is a constant, showing a linear decline of oxygen concentration from June to September. The anoxic condition, i.e. less than $0.5 \text{ mg O}_2/\text{L}$, extends for about three to four weeks in September and October. Note that the use of $0.5 \text{ mg O}_2/\text{L}$ for defining anoxia (cf. $1.5 \text{ mg O}_2/\text{L}$ in box models, Sections 6.2 and 6.3) is possible with the spatial details of the one-dimensional (z) model. The recovery to saturated condition for this volume occurs very quickly afterwards, as the fall overturn induces large vertical mixing (see also Fig. 7.5 for the computed thermocline position, and Fig. 7.4 for the temperature and eddy diffusivities).

The simple, one-dimensional (z) dissolved oxygen model demonstrates the strong dependence of the vertical dissolved oxygen profile on the thermal characteristics. Using a simple approach to the nutrient-plankton relationship, the computed oxygen concentration can be brought quite close to the observational data. However, the significance of the constant sediment and water oxygen demand used in the simple model must not be overemphasized, since it is more of a lumped model coefficient, specific to the one-dimensional model, than a meaningful biochemical kinetic constant with universal applicability to other lakes.

8.3 Two-Dimensional (x-z) Temperature and Flow Model

One of the limitations of the box models discussed in Chapters 5 and 6 is the assumption of flat horizontal thermal layer interfaces. While this simple assumption is shown to be adequate for the simulation of the seasonal, basin-wide distribution of water quality variables, the box models cannot explain in detail the effects of oscillatory and curved interfaces. The spatial oscillation and deformation of the thermal layers are direct results of the energy and momentum balances in the thermal and flow regimes. In the one-dimensional (z) thermocline model, a simple logarithmic velocity profile (Eq. 7.12) is assumed in order to achieve closure in the description of the turbulent eddy diffusion (Equations 7.2 to 7.4). Again, while this assumption proves to be adequate for the seasonal simulation of the basin-averaged, vertical temperature profiles, the lateral transports of heat have been omitted in the model and the logarithmic velocity profiles may not necessarily be valid for all times. Consistency in both the temperature and the velocity distributions requires an accurate description of the turbulent interactions between these two physical regimes in the three-dimensional space. An example of three-dimensional flow field computed from observed thermocline depths will be given later in Section 8.5.

To explore the main connection between the flow and thermal regimes, however, a two-dimensional (x-z) analysis can adequately reveal the major spatial variations of the thermal layers and the interbasin transports. In particular, the oxygen replenishment of the Central Basin from the Eastern Basin can be more precisely examined. In the (x-z) models, the variations in the lateral (y) directions are assumed to be uniform. For example, in Hollan and Simons (1978), the two-dimensional continuity, momentum and energy conservation equations are solved, under the assumption of rigid lid and hydrostatic flow.

The effects of the earth's rotation are simulated through the Coriolis parameter, but are confined to the x-z planes at the centre line and the two shorelines of an oblong lake. An alternative, however, is to ignore the rotational effects by fully assuming no variations in the y direction, for which the governing equations become for the centre plane

$$\frac{\partial u}{\partial x} + \frac{\partial w}{\partial z} = 0 \quad (8.3)$$

$$\frac{\partial u}{\partial t} = \frac{\partial}{\partial x} A_h \frac{\partial u}{\partial x} + \frac{\partial}{\partial z} A_v \frac{\partial u}{\partial z} - \frac{\partial}{\partial x} (P + Q) \quad (8.4)$$

$$\frac{\partial T}{\partial t} = - \frac{\partial u T}{\partial x} + \frac{\partial}{\partial x} K_h \frac{\partial T}{\partial x} - \frac{\partial w T}{\partial z} + \frac{\partial}{\partial z} K_v \frac{\partial T}{\partial z} \quad (8.5)$$

where u, v and w are the velocities along the three coordinates x, y, z, respectively; A_v and A_h are the horizontal and vertical eddy viscosities, K_h and K_v are the horizontal and vertical thermal eddy diffusivities; T is temperature; P and Q represent the barotropic and baroclinic pressure components as defined below

$$P = g\eta + P_s/\rho; \quad Q = \int_{-z}^{\eta} \frac{\Delta\rho}{\rho} dz; \quad \frac{\Delta\rho}{\rho} = \alpha_T(T-4)^2 \quad (8.6)$$

where η denotes the free surface elevation; g is the gravitational acceleration; P_s is atmospheric pressure; α_T is a thermal expansion coefficient.

The boundary conditions at surface (s) and bottom (b) are

$$\rho A_v \frac{\partial u}{\partial z} \Big|_s = \tau_{sx} \quad \text{and} \quad \rho C_p K_v \frac{\partial T}{\partial z} \Big|_s = q \quad (8.7)$$

$$\rho A_v \frac{\partial u}{\partial z}|_b = \tau_{bx} \text{ and } \frac{\partial T}{\partial z}|_b = 0 \quad (8.8)$$

where τ_s is the wind stress and τ_b is the bottom stress formulated as a quadratic function of the bottom velocities. For the horizontal turbulent eddy parameters, A_h and K_h , the constant values of $10^7 \text{ cm}^2/\text{s}$ (Simons, 1976a) and $5 \times 10^5 \text{ cm}^2/\text{s}$ (Lam and Simons, 1976), respectively, are used. The vertical thermal eddy diffusivity, K_v , is given by Equations 7.2 to 7.4 for which the computed velocities are used to define the Richardson number instead of using a logarithmic profile. The vertical eddy viscosity, A_v , is generally considered to be greater than its thermal counterpart. For simplicity, they are assumed to be equal for Richardson numbers less than 1, but $A_v = 5K_v$, otherwise.

To approximate the irregular topographical variations better, the finite-element method with triangular elements is used. Figure 8.3 shows the finite-element grid used; note that the boxes are triangular, varied in size, and aligned in vertical sections. Because of the matching required in the definition of Equations 7.2 to 7.4, an iterative procedure is used to solve Equations 8.3 to 8.8, as discussed in Lam (1982).

Briefly, two types of basis functions are used: the quadratic basis function $[\phi]$ is used for u and w , and the linear basis function $[\psi]$ is used for T . This mixed interpolation function approach is quite analogous to the staggered grid approach used in finite-difference methods (e.g. Hollan and Simons, 1978). A predictor-corrector time integration method (Lam, 1981) is used to advance the solution from the one time level to the next, at time steps of 1.5 hours. Compared with time steps of one day used in the one-dimensional thermocline model, this shorter time step corresponds to the smaller spatial scales used in the two-dimensional model.

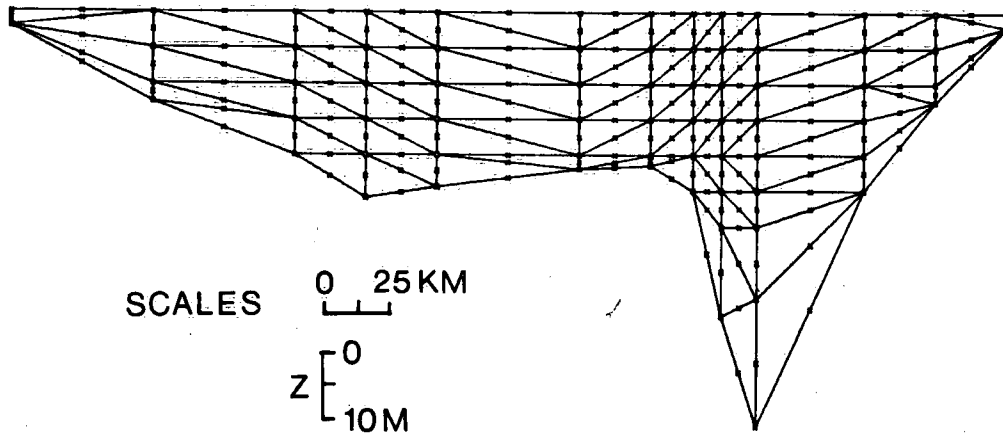


Figure 8.3. Finite-element mesh of the Lake Erie x-z model.

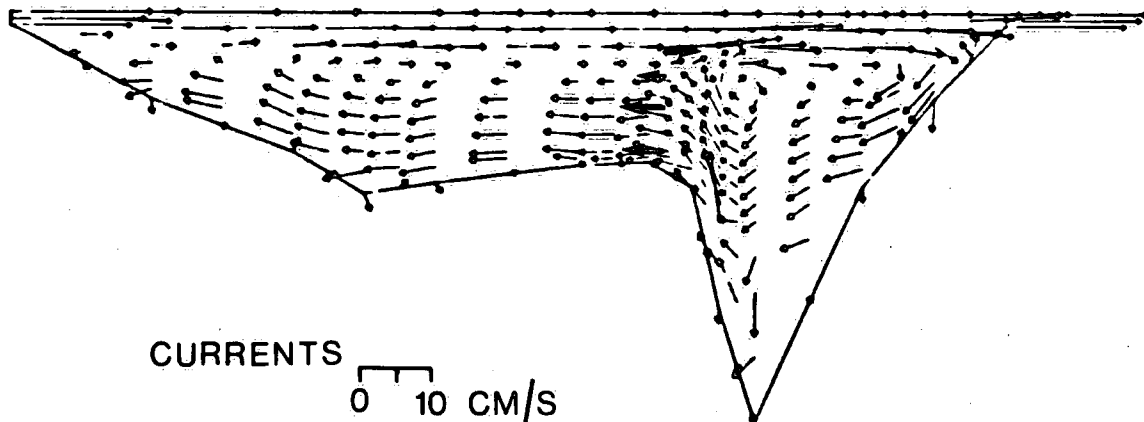


Figure 8.4. Computed (\longrightarrow) and observed (\Longrightarrow) currents for September 30, 1978.

Notice that whereas the baroclinic pressure component, Q , can be evaluated in the predictor-corrector scheme, the barotropic component P is evaluated as a correction term based on the kinematic boundary condition

$$\frac{\partial \eta}{\partial t} + \frac{\partial}{\partial x} \left\{ \int_{-D}^{\eta} u dz \right\} = 0 \quad (8.9)$$

where D is the mean depth. Because of the rigid lid approximation, Eq. 8.9 indicates that the total lateral (x) transports across any vertical (z) section (e.g. Fig. 8.3) should be equal to the hydraulic inflow and hence the outflow. Since the pressure should distribute evenly along this vertical section, the evaluation of the pressure term P consists of simply correcting each of the velocities along the section by a uniform amount such that the total lateral transport obeys Eq. 8.9.

Figure 8.4 shows the computed and observed velocities (averaged values of stations 5, 6, 8 and 9, Fig. 7.8), and Figures 8.5a and b show the observed and computed temperature distribution. The main finding is that the internal gyre, as discussed in its simplest form in Section 5.8, is much more complex, and the effects on the temperature distribution vary in space. For example, whereas the isotherms near the thermocline follow fairly straight lines parallel to the lake bottom in the Central Basin, they are distorted by the internal gyre flow near the Eastern Basin. The 14°C-isotherm shows a break or gap at the basin boundary. Some downwelling feature can be seen with the 16°C-isotherm at the eastern end of the Eastern Basin. On the other hand, the upwelling activities in the Central Basin are also discernible, e.g., in the 18°C-isotherm. These physical regime computations are also consistent with the two-dimensional contours of soluble reactive phosphorus, dissolved oxygen, and ammonia shown in Figures 3.2 and 3.4. Indeed, Eq. 8.5 can

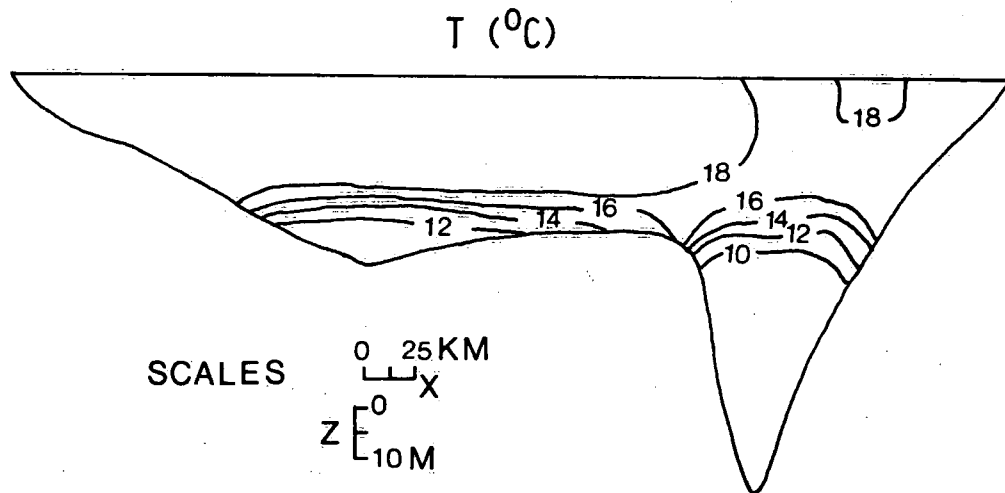


Figure 8.5a. Observed temperature in the x-z plane for Lake Erie (September 30, 1978).

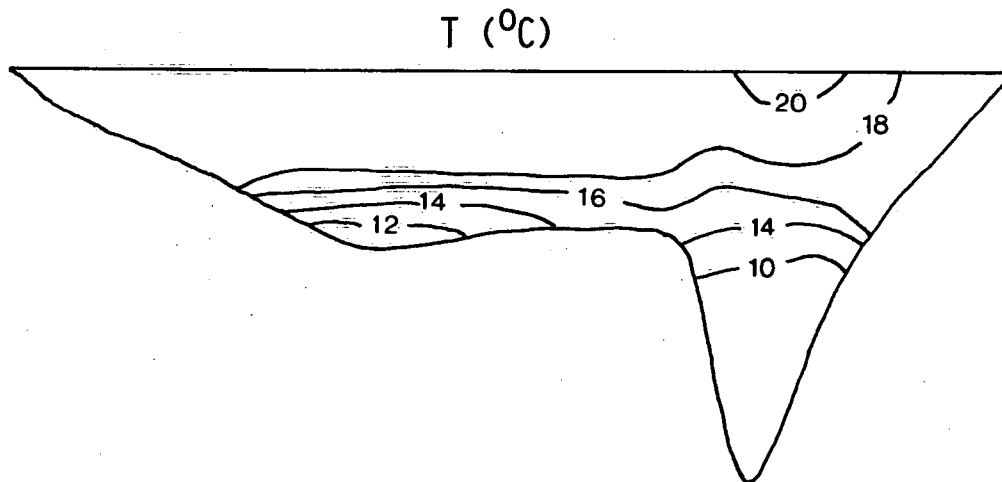


Figure 8.5b. Computed temperature in the x-z plane for Lake Erie (September 30, 1978).

be modified to simulate the two-dimensional distribution of these water quality parameters. Preliminary test results of combining the dissolved oxygen model (Eq. 8.1) and the transport model (Eq. 8.5) are quite encouraging.

Another finding is that the earth's rotational effects appear to be not too important in the x-z model, in which the length along the x-direction is much longer than the breadth in the y-direction. This may be due to the larger velocity component, u , in the x-direction than, v , in the y direction. Therefore, it is expected that in y-z models (e.g. Heinrich et al., 1981), in which the longitudinal length (x) is again longer than the lateral distance y , the Coriolis rotational effects will become more prominent. Observational data in 1977-1978 (Boyce et al., 1980) often show a shallower thermocline near the northshore than near the southshore along the Pennsylvania Ridge (Fig. 7.9).

8.4 Two-Dimensional (x-y) Model

The most commonly used two-dimensional models are the x-y models, which assume homogeneity in the vertical direction and are valid for full mixing periods such as in the winter. Of particular interest is the transport and dispersion of pollutants from the outfall to the nearshore zones and then to the offshore regions (e.g. Lam et al., 1981; Lam and Simons, 1976). The physical mechanisms for these different stages of pollutant transports are complex and very much different in terms of the horizontal dispersion characteristics (Murthy, 1976). For simplicity, an example using constant horizontal eddy diffusivity for the lake-wide transport of phosphorus is given below, although it is well known that a variable eddy diffusivity is more appropriate for the nearshore zones (Lam and Simpson, 1978).

In 1970, there were high wind periods in November and December, which caused substantial resuspension of phosphorus from the

PHYSICAL REGENERATION SUBMODEL

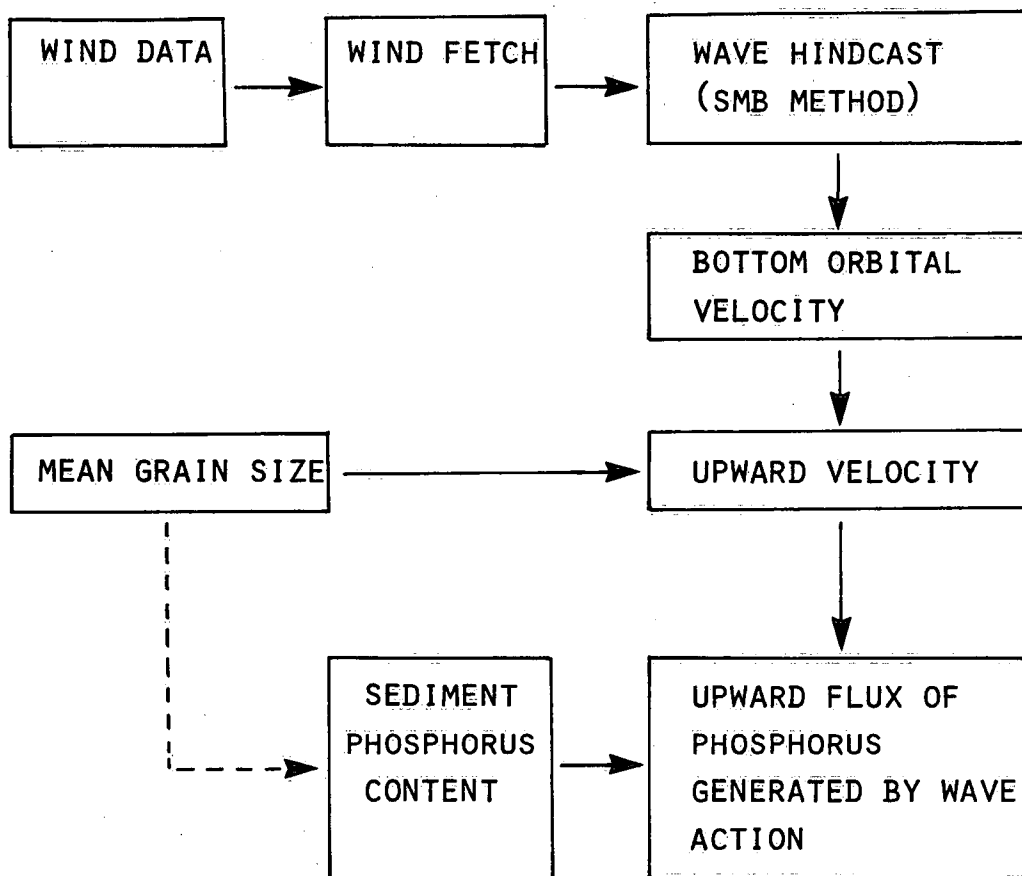


Figure 8.6. Schematic of the wind-wave sediment resuspension model.

sediments. The wind forcing has two main effects on the water movements: one effect is associated with the mean circulation and the other with wave and oscillatory motions. Whereas the mean circulation is responsible for the transport of the pollutant, the horizontal fluctuations can be parameterized by an eddy turbulent diffusivity and the wave orbital velocity. Of these three processes, the wave orbital motions are considered to be the main component of lifting forces for the resuspension of sediment particles. Based on these assumptions, Lam and Jaquet (1976) simulated the physical resuspension episodes in 1970. Briefly, the wave characteristics were hindcast with the Sverdrup-Munk-Betschneider (SMB) method. The bottom orbital velocity was derived from the wave characteristics and the excess velocity over a threshold value for a given particle size was computed. The shear stress due to the excess velocity was then formulated with the oscillatory boundary layer assumption. The upward flux of phosphorus resuspended from the sediment was simulated with the following empirical formula

$$J = K_r \rho \frac{\rho_s}{\rho_s - \rho} \frac{u_a}{u_{cr}} (u_m - u_{cr}) \cdot \hat{P}_s \quad (8.10)$$

where J is the upward flux of resuspended phosphorus (nonapatite inorganic phosphorus and organic phosphorus, in $\mu\text{g/s cm}^2$); ρ_s is the dry sediment density (about 2.6 g/cm^3); K_r is a dimensionless proportionality constant equal to 6.4×10^{-14} ; u_a is 1 cm/s as reference velocity; u_{cr} is critical shear velocity (cm/s); u_m is bottom orbital velocity (cm/s); and \hat{P}_s is the resuspension-prone phosphorus portion of the sediment (ppm). For mass balance models, Eq. 8.10 can be reformulated into a lumped and much simpler form, relating the upward flow directly to the wind speed (Somlyódy, 1979), as given by r_w in Tables 6.1 and 6.2. Figure 8.6 shows the structure of the wind-wave sediment resuspension submodel.

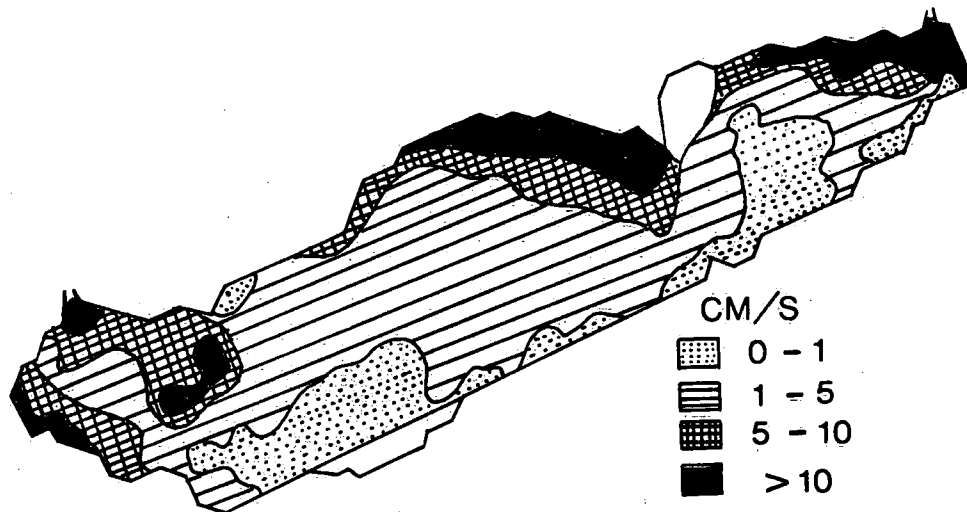


Figure 8.7. Computed mean wave bottom orbital velocities for November 1970.

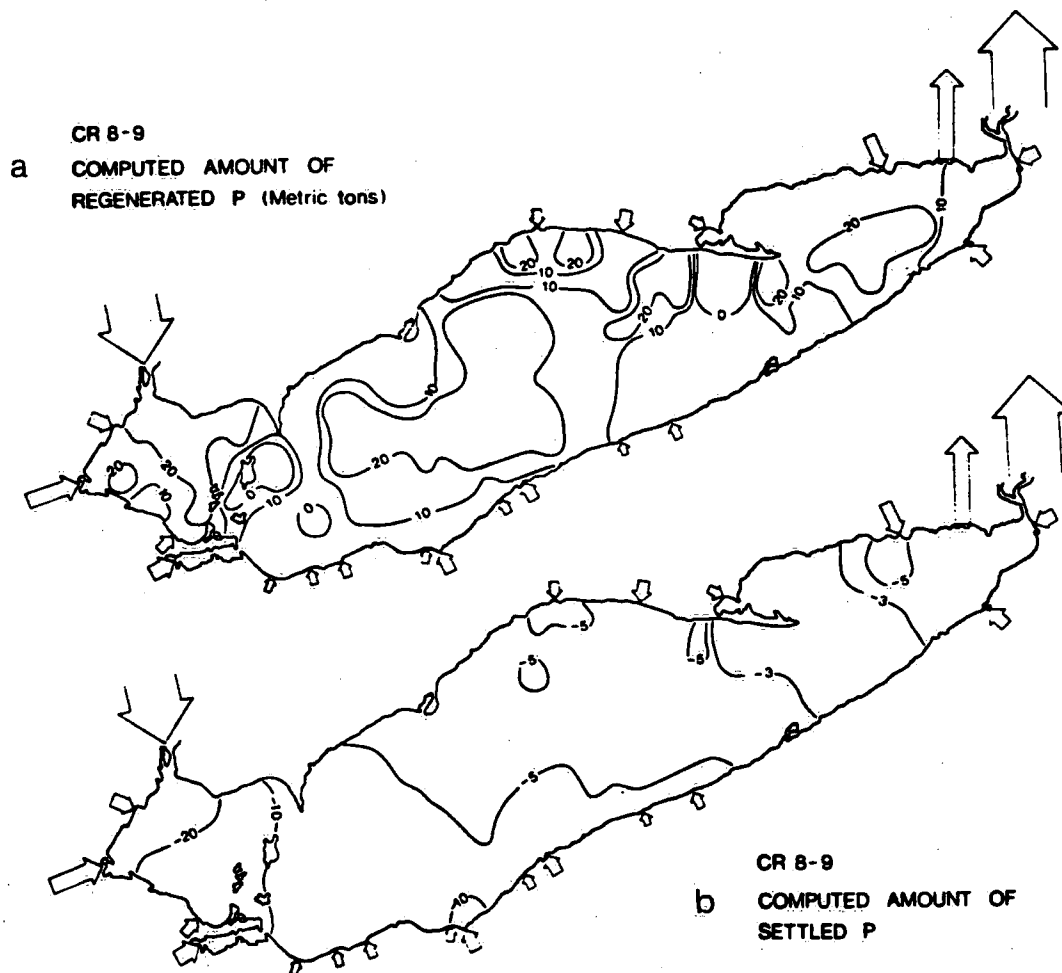


Figure 8.8. Computed amounts of (a) resuspended total phosphorus and (b) settled total phosphorus for the period October 21 to November 28, 1970.

The formula (8.10) defined the source term, $G = 10^{-6}J$, of phosphorus in the two-dimensional mass conservation equation

$$\begin{aligned} \partial h[TP]/\partial t = & - \partial(u[TP])/ \partial x - \partial(v[TP])/ \partial y \\ & + \partial(K_H h \partial[TP]/ \partial x)/ \partial x + \partial(K_H h \partial[TP]/ \partial y)/ \partial y \\ & - \sigma[PP] + G + S[TP] \end{aligned} \quad (8.11)$$

where x, y = spatial variables (cm)

t = time (s)

h = depth (cm)

$[TP]$ = concentration of total phosphorus (g/cm^3)

$[PP]$ = concentration of particulate phosphorus (g/cm^3)

u, v = vertically integrated velocities over the entire depth (cm^2/s)

K_H = horizontal diffusion coefficient ($5 \times 10^5 \text{ cm}^2/s$)

σ = settling rate (cm/s)

G = regeneration flux ($g/s \text{ cm}^2$)

$S[TP]$ = TP source term from rivers, etc. ($g/s \text{ cm}^2$).

The depth-averaged water circulations computed by the Simon's model (Simons, 1976a) were used to define the transports u and v in Eq. 8.11. Figure 8.7 shows the mean computed wave bottom orbital velocity distribution for November 1970. Note that the wave turbulence is shown to be the highest to the northwest shores, i.e., areas which have longer wind fetch. By assuming that 60% of the total phosphorus concentration is particulate, the resuspended and settled amounts of phosphorus were computed and are shown in Figures 8.8a and b. Since the resuspended portion is much larger than the settled portion during this period, the lake concentration of total phosphorus increases from about 0.6 to 1.0 $\mu\text{moles/L}$. Comparison of the computed and observed total phosphorus distribution shows close agreement (see Lam and Jaquet, 1976).

Whereas detailed calculations reveal the basic differences in mean currents and wave motions and their roles in the sediment-water cycling of phosphorus, the physically resuspended phosphorus in the winter is not all completely available for biological uptake and settles quickly. Therefore, it is possible to lump the wind-wave processes into a simpler formula for box models achieving satisfactory results (see Subsections 6.2.6 and 6.3.5). The contrast of using such different modelling complexities to attain different objectives for the same limnological phenomenon is a good example of the difference between short-term and long-term studies. These studies are complementary and could indeed be closely interrelated, particularly if the long-term emphasis shifts to site-specific problems. This point on the relationship between models of different time and spatial scales will be elaborated further in the following section.

8.5 Three-Dimensional (x-y-z) Models

Three-dimensional models are capable of providing information in great spatial detail. By simulating the horizontal and vertical variations of water quality variables, the computed results and kinetics can be tied in with the observational data more directly from station to station, instead of grouping the data in a specific direction. The obvious advantage of the three-dimensional models is to test the applicability of model coefficients, e.g. turbulent eddy diffusivity, in different locations. The disadvantage is that they are time-consuming to run and usually provide too much information for management problems (Simons, 1976b; Simons and Lam, 1978). From the point of view of multidisciplinary research, however, the influences of the physical and biochemical processes upon each other can be examined very closely with the three-dimensional model. For example, in Lam and Simons (1976), the horizontal and vertical transports of the water quality variable chloride ion concentration were simulated

LAKE ERIE COMPUTED CURRENTS
JULY 16 - AUGUST 16 , 1970

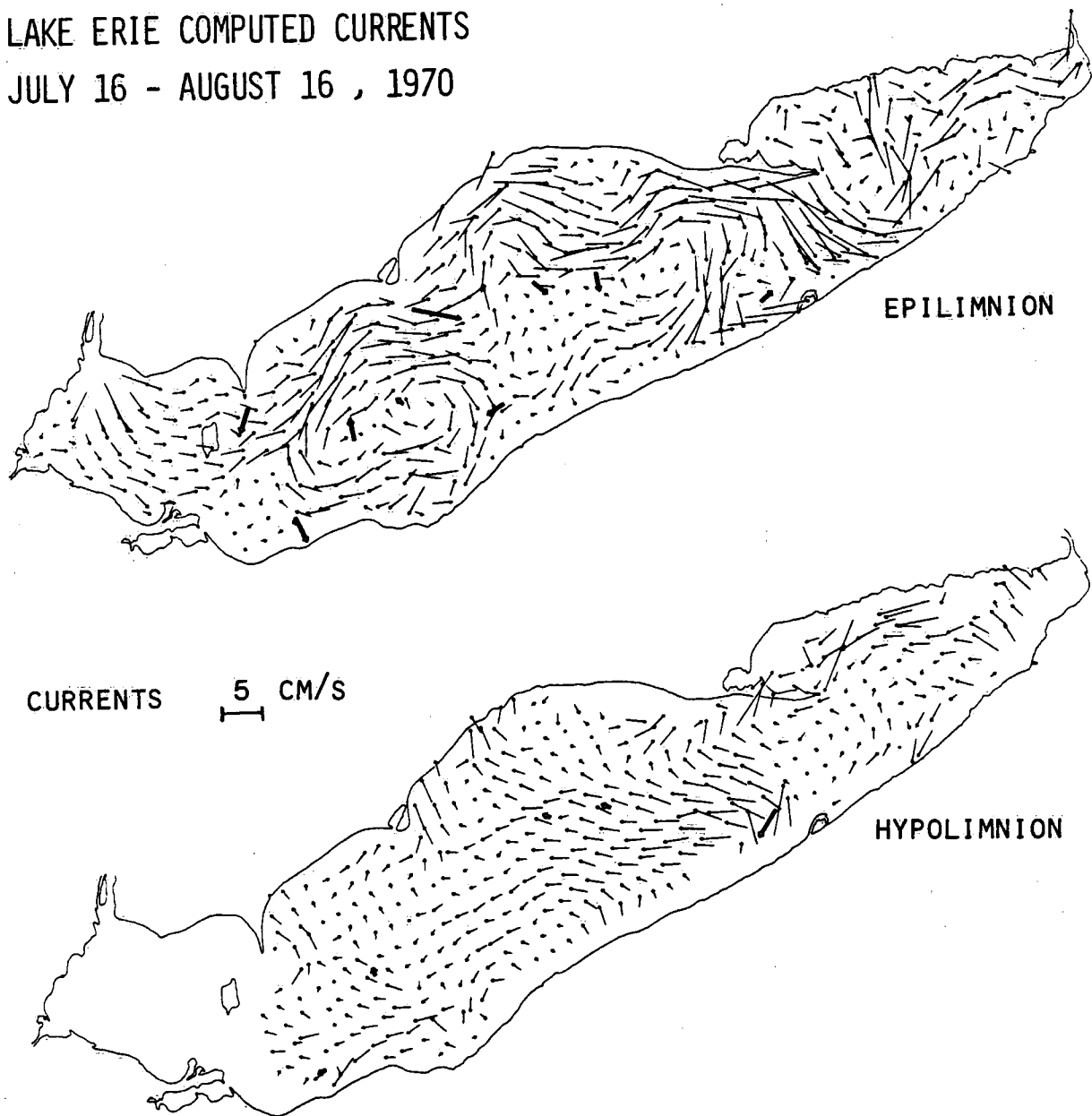


Figure 8.9. Computed (—→) and observed (▬→) currents for July 16 to August 16, 1970, for epilimnion and hypolimnion layers (from Simons, 1976a).

for Lake Erie, for the stratified period in 1970. The resulting spatial distribution revealed patterns which were related to the loading site and local circulation. The following is a brief summary of the three-dimensional results.

In contrast with the two-dimensional x-z model in which the flow field and the temperature are both computed, the approach used by Lam and Simons (1976) is based on computed currents and observed temperature data (Simons, 1976a). The observed temperature is used mainly to define the two vertical layers. Figure 8.9 shows the computed and observed currents for the epilimnion and hypolimnion for the period July 16 to August 16, 1970. The main feature is the two distinct clockwise gyres in the epilimnion of the Central Basin, which are a direct result of the spatial variation in the epilimnetic depths which are deeper in the interior than in the nearshore zones (Simons, 1976a). In the hypolimnion, the flow is clearly northwesterly, indicating an active downwelling area in the southeastern corner and an upwelling area in the northwestern corner of the Central Basin. Figure 8.10 shows the computed and observed chloride distribution for the two layers for the period July 28 to August 2, 1970. It can be seen that the contour of 650 $\mu\text{moles/L}$ conforms to the epilimnetic gyre in the Central Basin and the contours of 700 $\mu\text{moles/L}$ in both layers conform to the locations of the loading tributaries and downwelling activities in the southern shores.

Such three-dimensional details are certainly beyond what the box models (Sections 6.2 and 6.3) can simulate. In principle, one could extend the three-dimensional models to solve the flow field and temperature field simultaneously, to link up nearshore and lake-wide models, and to interface surface water models with climatic models and groundwater models. In practice, however, the complexity of water quality models is influenced by the objectives of the study. It is, therefore, important to pause here and re-examine what has been

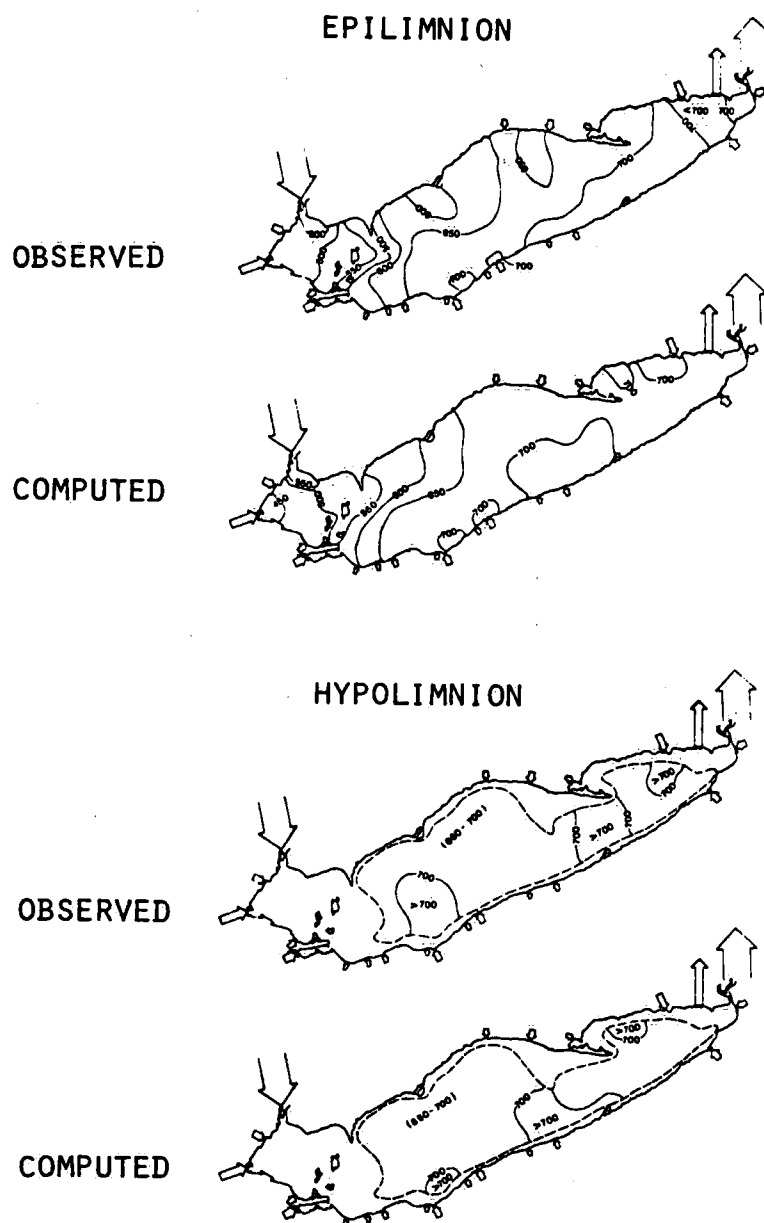
CHLORIDE CONCENTRATION ($\mu\text{MOLES/L}$) : JULY 28 - AUG. 2, 1970

Figure 8.10. Computed and observed chloride distributions for epilimnion and hypolimnion, July 28 to August 2, 1970.

achieved in terms of understanding the spatial complexity of the Lake Erie water quality problems.

In terms of scientific investigation, the inclusion of some spatial details, such as the separation of the water column into epilimnion and hypolimnion and the lake into horizontal segments by basins, offers a more realistic framework for simulating the limnological processes. For example, the three-box model discussed in Chapter 3 is capable of diagnosing the net settling and return amount of total phosphorus between the sediment and the water column. The six-box model, on the other hand, has the simplest model structure which addresses both vertical and horizontal variations. Crucial to the design of the six-box model structure is the incorporation of dynamically changing layer thicknesses. This dynamical feature allows for both entrainment and diffusive transports across the layer interface. Had the thicknesses been held constant, the diffusive transport could be used as the only turbulent mechanism, which would lead to excessive vertical mixing, when used in a coarse grid. Indeed, accurate simulation of the diffusive process calls for even finer spatial resolution than the six-box model. For example, the addition of a middle layer in the six-box model reduces the excessive intrusion of oxygen in the hypolimnion of Central Basin and prompts the use of a sediment oxygen demand rate which is more consistent with observations. In the one-dimensional (z) thermocline and oxygen models, the grid resolution is fine enough to allow the use of the diffusion transport as the only vertical turbulent mechanism. The resulting temperature profiles then supply the dynamic information of the thermal layer thicknesses. It is also found that the sediment and water oxygen demands create a gradient in the vertical oxygen profile in the hypolimnion, so that the anoxic condition is rather confined to the waters adjacent to the sediment. Hence, a realistic definition of anoxia ($0.5 \text{ mg O}_2/\text{L}$) applied at this confined region. The effects of the lateral transports can be incorporated in the two-dimensional

(x-z) model, e.g., the interaction of flow and thermal regimes. Chemically regenerated phosphorus under anoxic conditions is further shown to have been confined to the western part of the Central Basin hypolimnion because of interbasin transport. Similarly, the two-dimensional (x-y) model shows the preferred zones of physically resuspended phosphorus at the more intense wave-turbulent areas during winter storms. Finally, in the three-dimensional models, the effects of the circulation patterns and upwelling and downwelling episodes on the nearshore and offshore distributions of water quality variable in relation to the loading sites are simulated. Undoubtedly, the more spatially complex the model is, the more details of the interactions of the physical and biochemical regimes can be disclosed.

In terms of water management objectives, however, the spatial details of the water quality variables are often considered as transient effects, particularly in the nearshore zone. While these are concerns of local contaminant problems, the emphasis has been on the long-term trend of the lake-wide water quality variables. Thus, models of intermediate spatial resolution, e.g. the six-box or nine-box models, are often adequate to address such problems as the long-term lake response to nutrient loading control strategies. Our normal tendency is to think in the form of extremes; we consider a spatially simple one-box model, or else a spatially complex, three-dimensional model consisting of hundreds of boxes. However, when we come to describe models of intermediate spatial complexity, we must accustom ourselves to the description of a collection of models with progressively complex spatial resolution. In other words, models of intermediate complexity must depend, directly and indirectly, on inputs from models of finer, and sometimes coarser resolution. For example, the six-box and the nine-box models require the input of dynamic positions of the thermal layer interfaces and thicknesses as computed by the one-dimensional (z) thermocline model. The assumption of the vertical velocity profile in the one-dimensional model must be

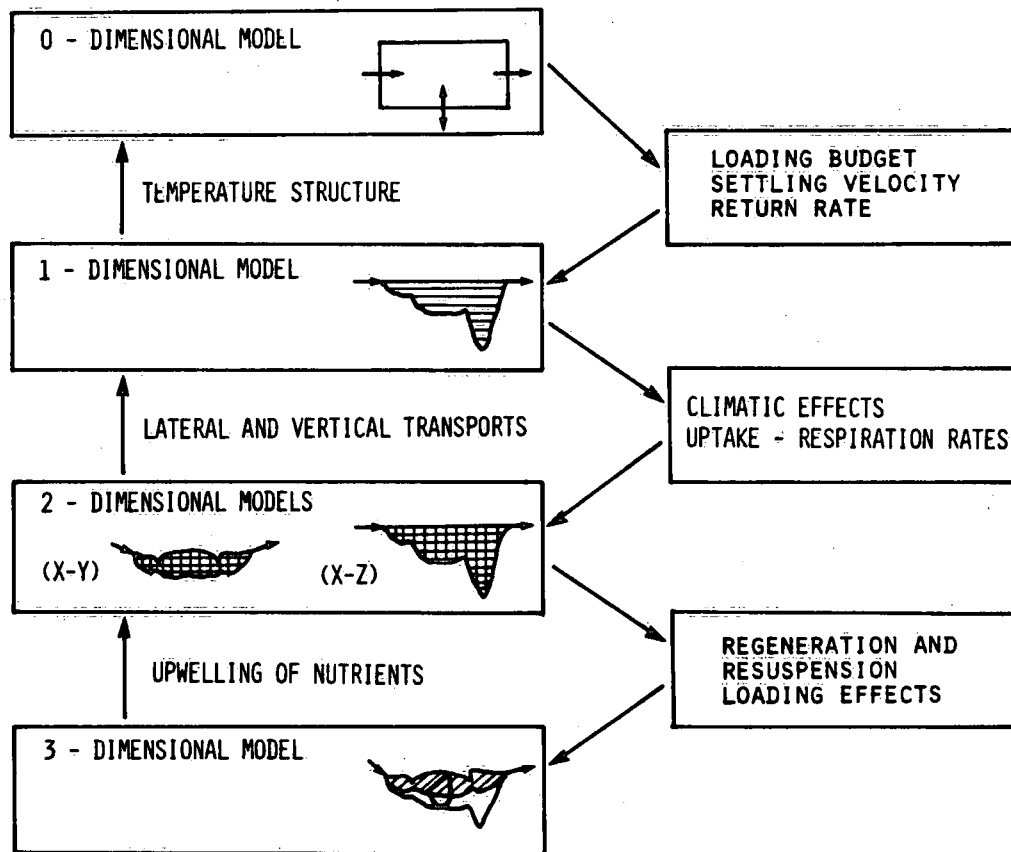


Figure 8.11. Interrelationships of models of varying spatial complexity.

ascertained and can be replaced by the computation of the flow and temperature field in the two-dimensional (x-z) models. Similarly, the internal flow gyres (Eqs. 5.31, 5.59 and 5.60) used in the six-box and nine-box must be confirmed and be integrated with the two-dimensional (x-z) results. Likewise, the upward flux formula (Eq. 8.10) used in the two-dimensional (x-y) model for wind-wave resuspension of sediments has been modified for use in the box models. The upwelling and downwelling episodes from the three-dimensional computations also support the patterns of internal flow gyre shown in the six-box, nine-box and in the two-dimensional (x-z) model results. However, the external forcing factors, such as wind or nutrient loading, remain unmodified. Indeed, because of this consistency of external input data, the computed lake concentrations from a three-dimensional model, when compressed into a lake-wide mean value, should give the same results as the box-models within the statistical variances of the observed data (see Simons, 1976b). Consequently, the outputs from models of intermediate complexity, which may have been enriched with computed results of models of higher spatial complexity, are still functions of the same external forcing factors. The lake responses to water management strategies can then be simulated according to these functions from the intermediate complex models. The extent and number of models involved depend on the management objectives, e.g. nearshore vs. lake-wide problems, and the scientific rigor associated with the objectives, for example, the dynamic changes of anoxic volumes vs. the long-term trend of lake-wide concentration of total phosphorus. Figure 8.11 shows some of the interrelationships among the models of different spatial complexity. Note that the box-models have been classified as "0-dimensional models" to indicate that they are less spatially complex than the 1-dimensional models.

Model Application: Estimated Lake Responses to Meteorological and Loading Effects

9.1 Potentials and Pitfalls

The modeller's dilemma is obvious. On the one hand, the scientific knowledge is incomplete, and even if it is complete, the model will become too complex and demand very accurate inputs. On the other hand, the model may appear to "simulate" some processes and be capable of predicting them within a given tolerance. Thus, while the immediate model application may be considered as simplistic by some modellers, its partial success in simulation could be deemed good enough by others to allow the making of predictions. When speaking of model applications, therefore, one must introduce some words of caution.

There are many models discussed in this report: their complexities and assumptions have been explored in Chapters 6, 7 and 8. It is not possible to discuss the model applications of each case, but the nine-box three-variable model proposed in Section 6.3 can be used as an example. Being a model of intermediate spatial complexity, the nine-box model depends on the more complex one-dimensional (z) thermocline model for the computed thermal layer thicknesses and water temperature as inputs. While these computed inputs could be one potential source of uncertainty as a result of the model formulation, the thermocline model in turn uses meteorological data as inputs which can introduce an additional source of errors on predictions. Similarly, the biochemical formulation of the nutrient-plankton relationships introduces errors in the computed lake concentrations, and the loading estimate is probably one of the major uncertainties.

In addition, there is the problem of interactions of processes of different time scales. The calibration of the kinetic coefficients formulated for these processes is often based on short-term (e.g. one-year) data, which are adequate for fast processes such as nutrient uptake and plankton respiration. However, accurate calibration of such kinetic coefficients as sedimentation rate and sediment oxygen demand rate requires long-term data (Vollenweider and Janus, 1981) because the response of these coefficients to nutrient loading and lake concentration changes is rather slow. The pitfalls of extrapolating short-term calibrations to long-term predictions have been discussed in Simons and Lam (1980). The same pitfalls apply to the verification of the Lake Erie nine-box model which is performed over a 12-year period. Since the coefficients used are the same as set by the calibration with the 1978 data (see Section 6.3), recalibration based on the twelve-year data of the coefficients, e.g. the sediment oxygen demand rate, is necessary.

With these limitations in mind, we can now proceed to discuss the potential applicability of the nine-box model to the Lake Erie water management problems. In this chapter, Section 9.2 summarizes the error analysis of the six-box and nine-box models and the adjusted nine-box model results of applying a linear approximation of the sediment oxygen demand rate in response to phosphorus loading reduction. Section 9.3 shows the sensitivity analysis of the adjusted nine-box model results to changes in meteorological and phosphorus loading inputs. Section 9.4 describes the simulated long-term responses of dissolved oxygen and total phosphorus concentrations to phosphorus loading reduction. Section 9.5 describes the simulated long-term water quality responses to lake water level changes. Section 9.6 outlines the strength and weakness of the nine-box model and a proposal for conducting further water quality modelling research.

9.2 Error Analysis

There are many statistical methods of estimating the errors in the computed results as compared with the observed data. A straightforward method is to define the mean relative error, E , as

$$E = \frac{1}{N} \sum_{i=1}^N \left| \frac{\hat{c}_i - c_i}{\hat{c}_i} \right| \quad (9.1)$$

where c_i and \hat{c}_i are the i th computed and observed concentrations, and N is the number of observations. The difficulties of using Eq. 9.1 have been the poor behaviour of E at low values of \hat{c}_i and the fact that the variability in the data would not be recognized. It is also poor if \hat{c}_i is much greater than c_i . A more commonly adopted error statistic (Thomann and Segna, 1980) is the median relative error, for which N is only half (i.e. 50% percentage frequency) of the total error samples which have been sorted and arranged in increasing order, according to the magnitudes of the individual relative errors. Of course, it is also possible to use the extreme values such as 10% or 90% frequency of error, but the median relative error is conventionally regarded as useful in comparisons between models (Thomann and Segna, 1980).

Figure 9.1a shows plots of the mean relative errors, E , in relation to error frequencies for total phosphorus (TP) and soluble reactive phosphorus (SRP), based on the verification (1967 to 1978) results from the six-box model of Section 6.2. Results for the Western Basin hypolimnion are not shown, because it exists only for a short time in any year. The observed concentrations are the available data as discussed in Chapter 3. The computed results of SRP are generally poorer than those of TP in terms of accuracy, particularly in the Western Basin. This is due to the fact that the uncertainties of soluble reactive phosphorus loading are the greatest in the Western

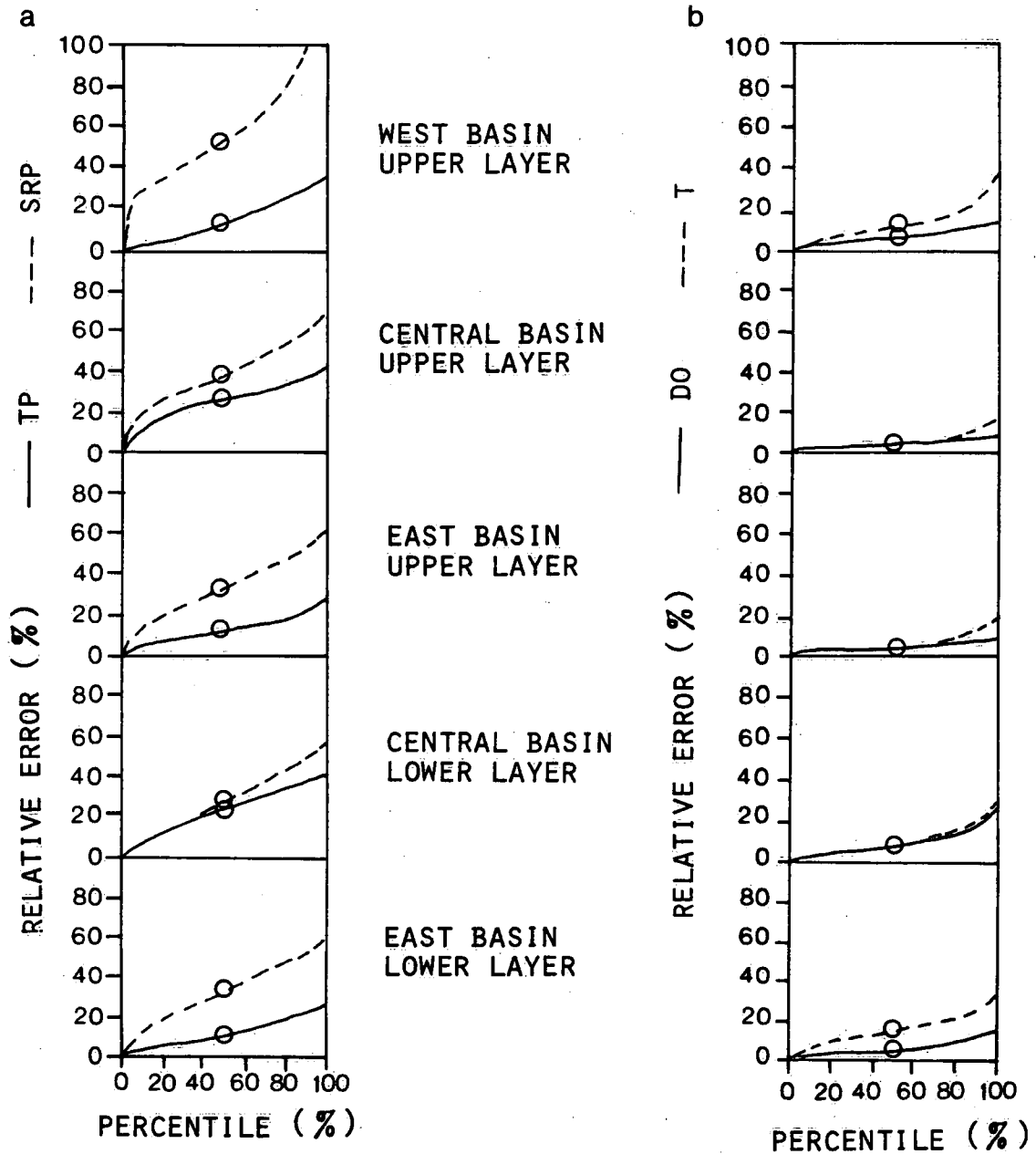


Figure 9.1. Relative errors vs. sample percentile for (a) total phosphorus (TP) and soluble reactive phosphorus (SRP), and (b) dissolved oxygen (DO) and temperature (T), as computed for the six-box model.

Basin, and the observed SRP concentrations are small (0.5 to 2.5 $\mu\text{g/L}$). Specifically, the overall median relative error for total phosphorus for all basins and layers is 14.9% and is 29.8% for the entire sampling distribution (i.e. 100% frequency). On the other hand, the overall median relative error for soluble reactive phosphorus is 35.6% and the hundred percentile frequency error is 66.5%. The large errors in SRP results are systematic in that the model consistently overpredicts the SRP concentration by about 50%, indicating that the inorganic and organic portions of the soluble phosphorus have not been accurately simulated. The use of the formula $\text{PP}=\text{OP}-5$ (see Table 6.1) could be in question. Nevertheless, if total phosphorus is used as a general indicator of the water quality, then this overprediction becomes slight in terms of the total concentrations and is therefore not a serious problem.

By contrast, the results of dissolved oxygen from the six-box model and the results of temperature from the one-dimensional thermocline model as used in the six-box model are much more accurate than the phosphorus results. As shown in Fig. 9.1b, the error distributions of dissolved oxygen and temperature are very similar, particularly in the upper layer. This is because most of the time the dissolved oxygen in the upper layer reaches saturation, as there is always an ample supply from reaeration and photosynthesis. Since oxygen saturation is a strong function of water temperature, the errors in the dissolved oxygen computation reflect those in the temperature. Furthermore, the computed dissolved oxygen in the lower layer is also largely affected by the computed layer thickness, which is strictly a result of the balance between wind mixing and thermal buoyancy. Thus, the accuracy of both the computed dissolved oxygen and temperature depends mainly on the accuracy of the meteorological inputs.

Table 9.1. Median Relative Errors in % (hundred percentile, relative errors in brackets) of the Variables in the Six-Box Model Based on Computed and Observed Results for 1967 to 1978

	Total phosphorus	Soluble reactive phosphorus	Dissolved oxygen	Temperature
Western Basin	11.2	53.1	5.7	9.2
Upper Layer	(32.7)	(132.8)	(10.4)	(37.7)
Central Basin	24.3	36.7	1.9	2.5
Upper Layer	(36.1)	(65.3)	(4.7)	(14.2)
Eastern Basin	9.8	32.1	1.9	2.4
Upper Layer	(24.1)	(56.2)	(5.1)	(14.8)
Central Basin	22.3	24.8	3.7	4.9
Lower Layer	(37.1)	(53.6)	(25.5)	(23.5)
Eastern Basin	7.0	31.2	3.8	11.4
Lower Layer	(19.1)	(54.6)	(10.5)	(35.9)
Lakewide	14.9	35.6	3.4	6.1
Mean	(29.8)	(66.5)	(11.3)	(25.2)

The meteorological inputs are more frequently and accurately measured than the loading inputs. In particular, the estimated heat flux has been modified by a scaling and interpolation technique with the available heat content measurements (see Section 5.3). Compared with the errors of total and soluble reactive phosphorus, the errors of dissolved oxygen are rather small, for example, the overall median relative error of dissolved oxygen is 3.4% and the hundred percentile error is 11.3%, and those of temperature are 6.1% and 25.2%, respectively. It is therefore very important to differentiate the loading effects from the meteorological effects in the error analysis of the model. Table 9.1 shows the median relative errors.

The same conclusions apply to the nine-box three-variable model results (see Fig. 9.2 and Table 9.2), which again show the distinctively different effects of loading and meteorological inputs. The overall mean median relative errors for total phosphorus, soluble reactive phosphorus and dissolved oxygen are 11.4%, 38.1% and 4.2%, respectively (cf. 14.9%, 35.6% and 3.4% for the corresponding six-box model results). Thus, in spite of the different layer thicknesses, the results of the two models are quite similar. The temperature results offer more interesting comparison, because they originate from the same one-dimensional model. In the nine-box case, the mean median relative error for temperature is 4.6%, whereas it is 6.1% in the six-box model, showing a slight improvement in favour of the nine-box model.

The other factor in favour of the nine-box model is the use of a sediment oxygen demand rate, $0.15 \text{ g/m}^2\text{day}$, which is in line with experimental results (e.g. Mathias and Barica, 1980). The value of $0.5 \text{ g/m}^2\text{day}$ for the six-box model has been used in the calibration but is actually considered to be too high, because of the extra oxygen inputs due to excessive diffusion in a two-layered model structure (see Section 6.2). On the other hand, although the nine-box model

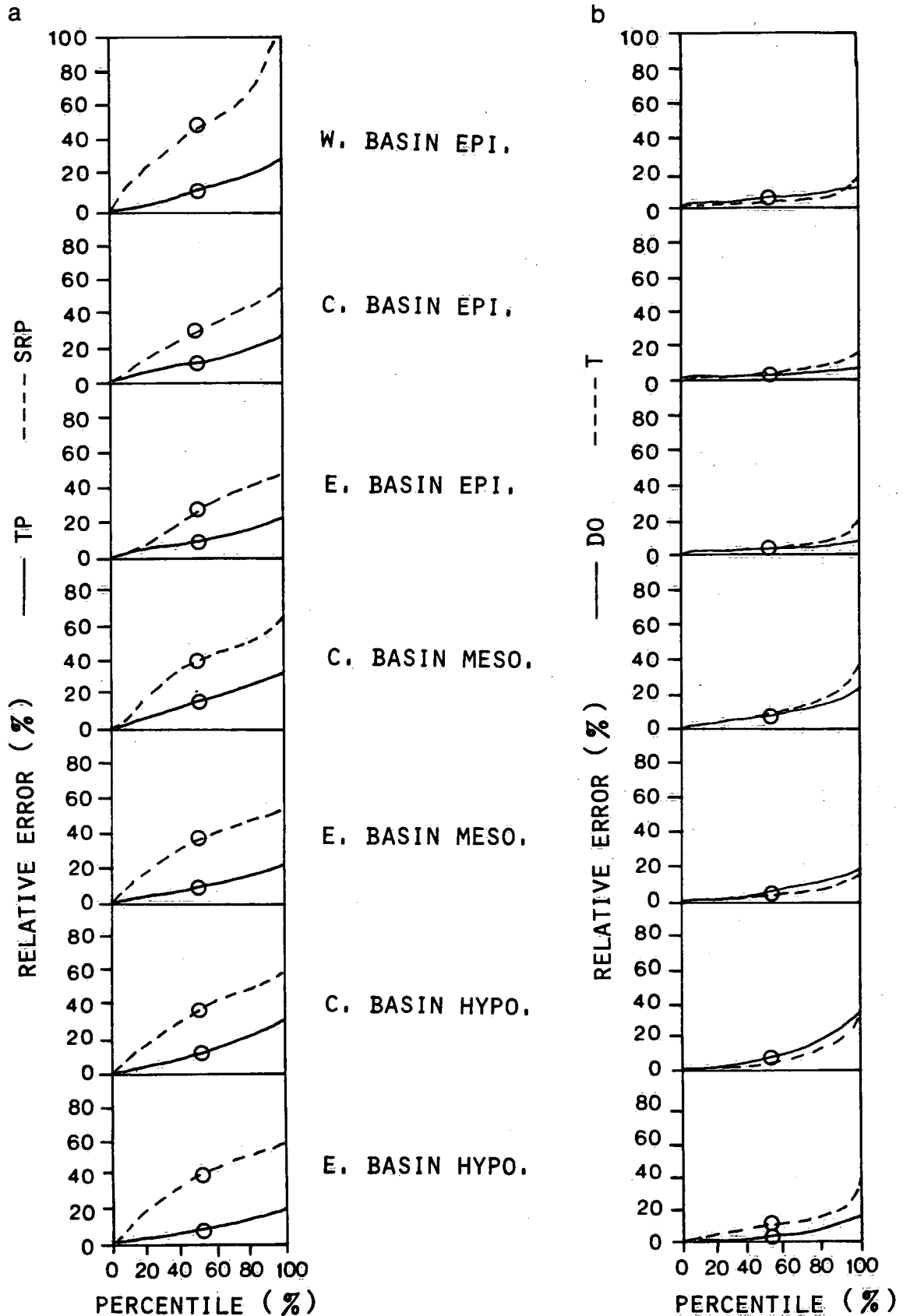


Figure 9.2. Relative error vs. sample percentile for (a) total phosphorus (TP) and soluble reactive phosphorus (SRP), and (b) dissolved oxygen (DO) and temperature (T), as computed for the nine-box model.

Table 9.2. Median Relative Errors in % (hundred percentile, relative errors in brackets) of the Variables in the Nine-Box Model Based on Computed and Observed Results for 1967 to 1978

	Total phosphorus	Soluble reactive phosphorus	Dissolved oxygen	Temperature
Western Basin	13.2	48.2	4.8	2.2
Epilimnion	(32.6)	(130.4)	(9.6)	(15.5)
Central Basin	11.7	32.1	1.2	2.7
Epilimnion	(25.9)	(65.4)	(4.0)	(14.6)
Eastern Basin	9.6	28.0	1.9	2.9
Epilimnion	(21.6)	(48.4)	(4.7)	(15.8)
Central Basin	16.4	41.1	5.8	5.7
Mesolimnion	(31.9)	(70.5)	(2.0)	(30.8)
Eastern Basin	9.8	37.0	4.6	3.1
Mesolimnion	(22.9)	(53.2)	(16.7)	(18.9)
Central Basin	12.2	37.4	7.5	5.3
Hypolimnion	(32.7)	(66.5)	(35.6)	(32.4)
Eastern Basin	7.1	42.8	3.8	10.1
Hypolimnion	(18.4)	(59.6)	(12.8)	(34.7)
Lakewide	11.4	38.1	4.2	4.6
Mean	(26.6)	(70.6)	(12.2)	(23.2)

produces very accurate results for dissolved oxygen over the twelve-year period, it is not possible to pinpoint the sediment oxygen demand rate for long-term simulation purposes. Indeed, the good accuracy is associated more with the prediction of seasonal cycles than with the long-term trend. The long-term changes due to phosphorus loading variation could only be confirmed over a much longer time span, e.g. 30 or 50 years. As such, the constant rate of $0.15 \text{ g/m}^2\text{day}$ is a very crude approximation and is not able to provide a simulation which is responsive to long-term loading changes and feedback. Ideally, accurate simulation of the feedback and transport mechanisms across the sediment-water interface should involve a mass balance submodel in order to ensure a consistent budget of dissolved oxygen and other chemical constituents in both sediment and water. In practice, like the air-water interface submodel for temperature, the available long-term data appropriate for calibrating the sediment-water submodel are limited. Therefore, a modification on the sediment oxygen demand rate discussed below is proposed as a simpler alternative.

While the nine-box model accurately simulated the strong anoxic conditions in the Central Basin in 1970 and 1977, it missed those in 1969 (see Figures 6.10d and 6.11d), for a sediment oxygen rate of $0.15 \text{ g/m}^2 \text{ day}$. From a meteorological point of view, the computed thermal layer boundaries for 1969 have been classified as the "reversal entrainment" type (see Fig. 6.3 and Section 6.2), i.e. the one which is supposed to be the most resistant to the formation of anoxia. If the anoxic events in 1970 and 1977 could be attributable to meteorological forcing, then the event in 1969 must have been the result of a larger oxygen demand from the sediment. This leads to the suspicion, then, that the sediment oxygen demand rate, calibrated as $0.15 \text{ g/m}^2\text{day}$ by using the 1978 data, is underestimated for 1969. By rerunning the model with higher rates, it is found that, to let the anoxic condition occur in that year, a value of $0.23 \text{ g/m}^2\text{day}$ at least must be used. If we assume a rate of $0.25 \text{ g/m}^2\text{day}$ and a lake-wide

total phosphorus load of 25 000 MT for 1967, and a rate of 0.15 g/m²day and a load of 15 000 MT for 1978 (see Chapter 2), then it is possible that the sediment oxygen demand rate follows a linear drop from 0.25 to 0.15 g/m²day over the twelve-year period. Assuming further that the loading of total phosphorus also drops linearly from 25 000 MT to 15 000 MT over the same period, then the sediment oxygen demand would indeed be a linear function of the total phosphorus load during this period:

$$K_s = L(TP) \times 10^{-5} \quad (9.2)$$

where K_s is the sediment oxygen demand rate in g/m²day and $L(TP)$ is the lake-wide total phosphorus load in MT. Of course, these assumptions are based on very crude information from the verification phase of the nine-box model. At best, Eq. 9.2 is only a first-order approximation over the twelve-year period. For example, application of Eq. 9.2 to the nine-box model slightly enhances the accuracy of the dissolved oxygen simulation (the mean hundred percentile relative error drops from 35.6% to 33.6%), whereas the error statistics of the other variables remain practically the same as those in the case of constant sediment oxygen demand rate. In the following sensitivity analysis and model response calculations, whenever Eq. 9.2 is assumed to hold, it is meant to be within, not outside the twelve-year period.

9.3 Sensitivity Analysis

The error analysis of the nine-box model clearly identifies two main possible error sources in the inputs: the meteorological and the loading inputs. In terms of management control strategies, it is important not only to establish the ecosystem response to man-made loading changes but also to know the sensitivity of the aquatic ecosystem to extreme meteorological conditions. Furthermore, the lake

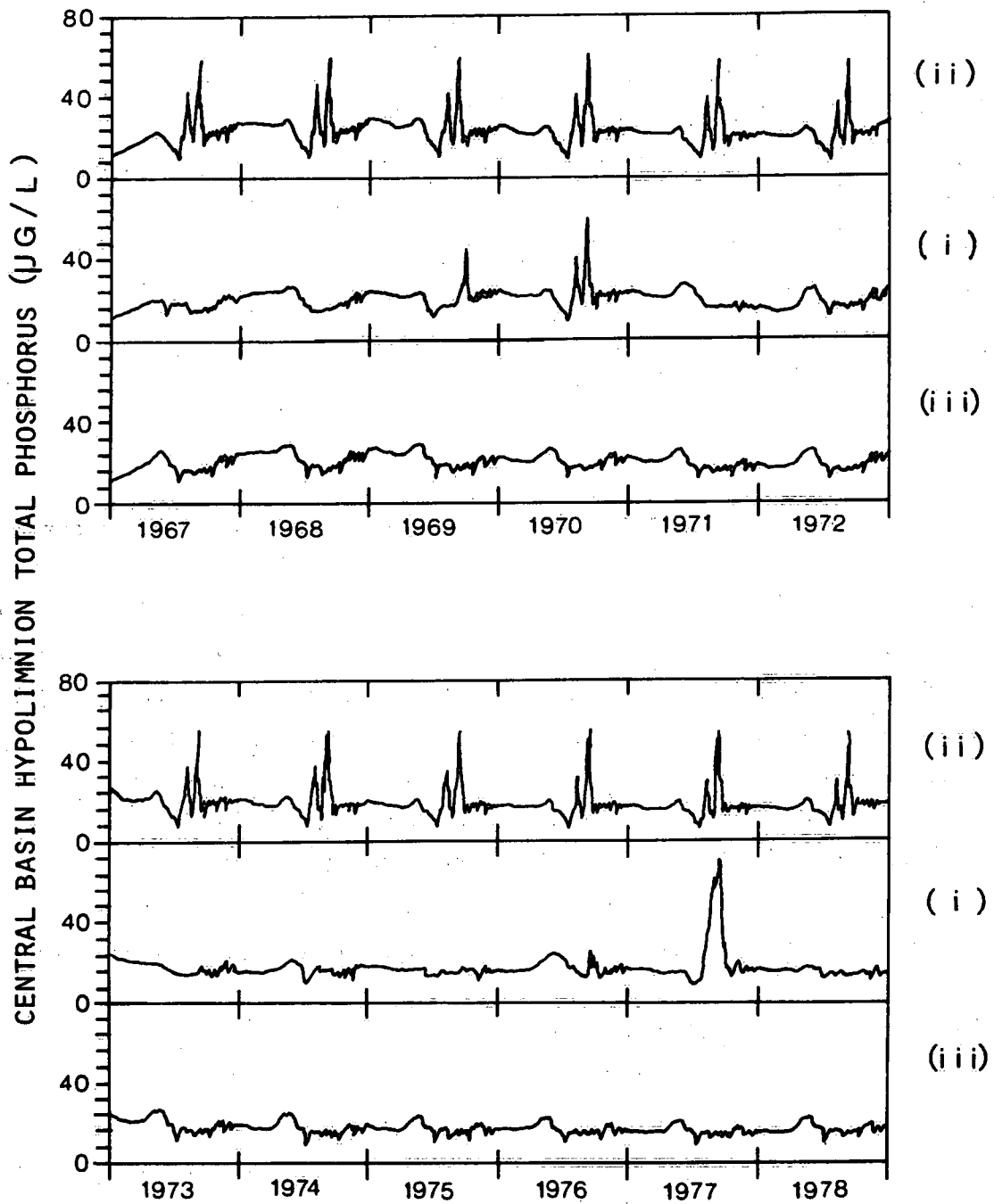


Figure 9.3. Simulated results of total phosphorus concentration in the Central Basin hypolimnion using meteorological data of (i) the actual observations 1967-78, (ii) 1970 and (iii) 1972.

response to another possible management alternative, namely water level control, should also be examined. The nine-box model offers the basis for quantifying the water quality response to these man-made and natural changes.

From the meteorological point of view, the conditions of 1970 and 1972 offer two extremes, the "shallow hypolimnion" case and the "reversal entrainment" case, respectively. The former strongly favours, and the latter strongly resists, the formation of anoxia in the Central Basin hypolimnion. If we let one of these conditions repeat each year for the twelve-year period and then let the other one repeat likewise, the resulting two curves would probably constitute the meteorological upper and lower bounds of the anoxic condition for each year over the same period. Figures 9.3 and 9.4 show the simulated results for total phosphorus and dissolved oxygen, respectively, in the Central Basin hypolimnion using, for each year, the meteorological data of (i) the actual observations, (ii) 1970 and (iii) 1972. The other inputs, such as phosphorus loadings, are the same as those used in Section 6.3 for cases (i), (ii) and (iii), except that Eq. 9.2 is used for the sediment oxygen demand rate. Note that as discussed in Section 9.2, the chemical regeneration of phosphorus in 1969 is now simulated (see Fig. 9.3i; cf. Fig. 6.11d). On the other hand, case (ii) in Fig. 9.3 shows that the anoxic phosphorus release occurs each year, whereas case (iii) shows no such condition at all. This means that weather extremes alone could have caused or discouraged the onset of anoxia for any year during 1967 to 1978. Furthermore, the wind-wave resuspension of phosphorus which occurs during stormy conditions also differs in the three cases, for example, the lake concentration of total phosphorus is about 23, 29 and 26 $\mu\text{g/L}$ at the beginning (i.e. fully mixed) part of 1969 and about 16, 17 and 16 $\mu\text{g/L}$ at the start of 1978 for cases (i), (ii) and (iii), respectively. Thus, while there is a decrease in lake concentration between 1969 and 1978 owing to the loading reduction, the weather

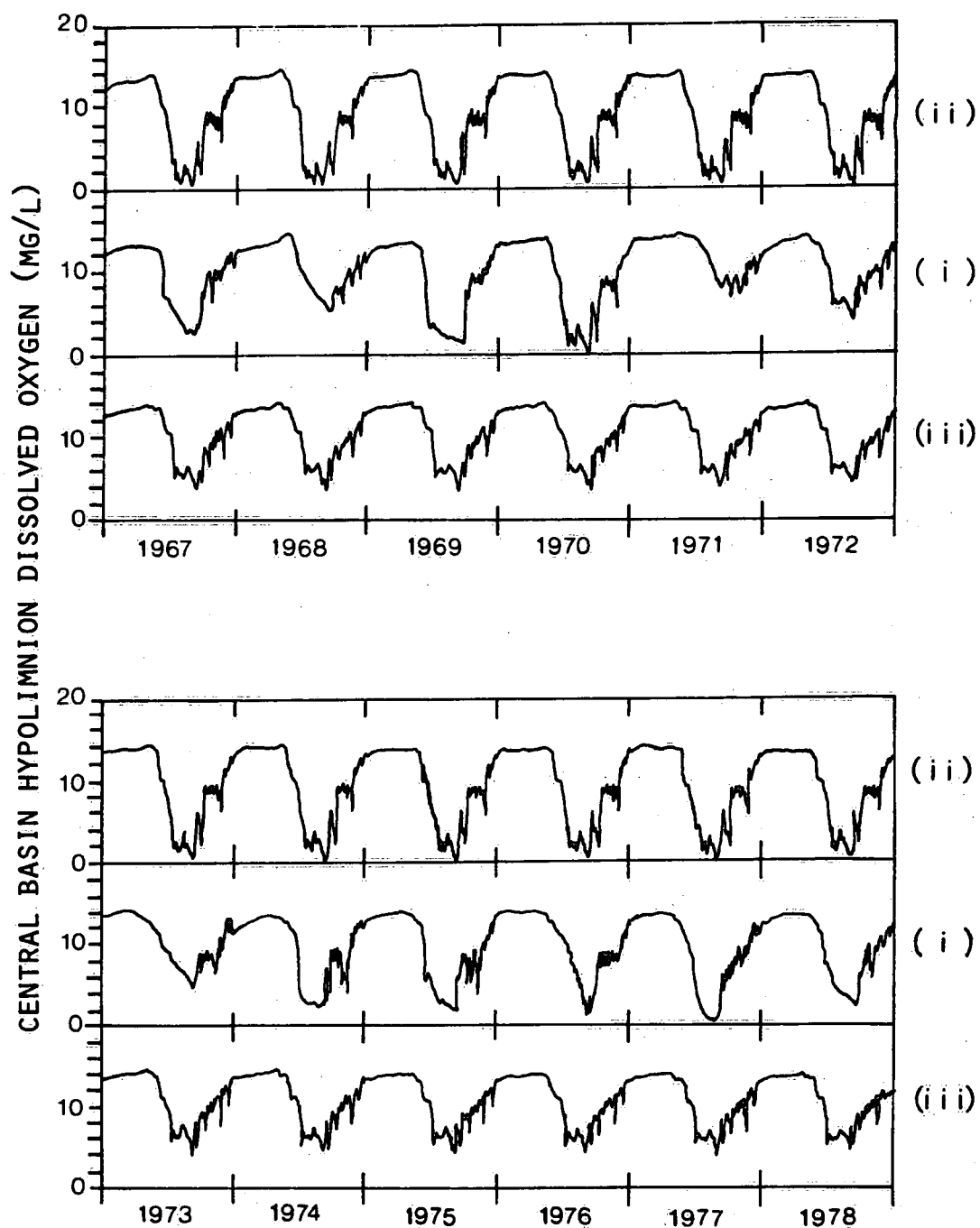


Figure 9.4. Simulated results of dissolved oxygen concentration in the Central Basin hypolimnion using meteorological data of (i) the actual observations 1967-78, (ii) 1970 and (iii) 1972.

could have introduced substantial seasonal variations on the decreasing trend. In general, the effects on the epilimnetic concentrations are much smaller. Figure 9.4 further confirms the persistent occurrence of anoxia in the Central Basin hypolimnion each year for the 1970 meteorology and its absence for the 1972 meteorology. The actual case is of course somewhere (namely case (i)) between the two weather extremes.

Of the factors influencing Lake Erie water quality, weather is uncontrollable. However, there are two other important input factors which have been frequently regulated to some extent during 1967 to 1978, namely phosphorus loading and water level. Thus, a sensitivity analysis of these two factors can be conducted with the nine-box model. The model can be recalibrated with better loading estimates which would reduce the present high degree of uncertainty. In the meantime, the model sensitivity to changes in the current loading estimates can be investigated. A straightforward test is to assume, say, a 30% increase in the total phosphorus loading data for the entire period, since the error analysis shows there is about 30% error in the lake concentration. Simons and Lam (1980) have shown that different proportions of particulate and soluble reactive components in the assumed change in the total phosphorus load can lead to different responses of the lake concentrations. To simplify the proportionality problem, then, it has been further assumed that the 30% increase applies simultaneously to the existing portions of the particulate and soluble components in the load estimates in each of the three basins. Again, the sediment oxygen demand formula, Eq. 9.2, is used, and the meteorological and other conditions remain the same as observed.

Figure 9.5 shows the computed total phosphorus concentration in the Central Basin hypolimnion, before and after the hypothetical 30% load increase (curves (i) and (ii), respectively). The load increase appears to accentuate the chemical regeneration of phosphorus

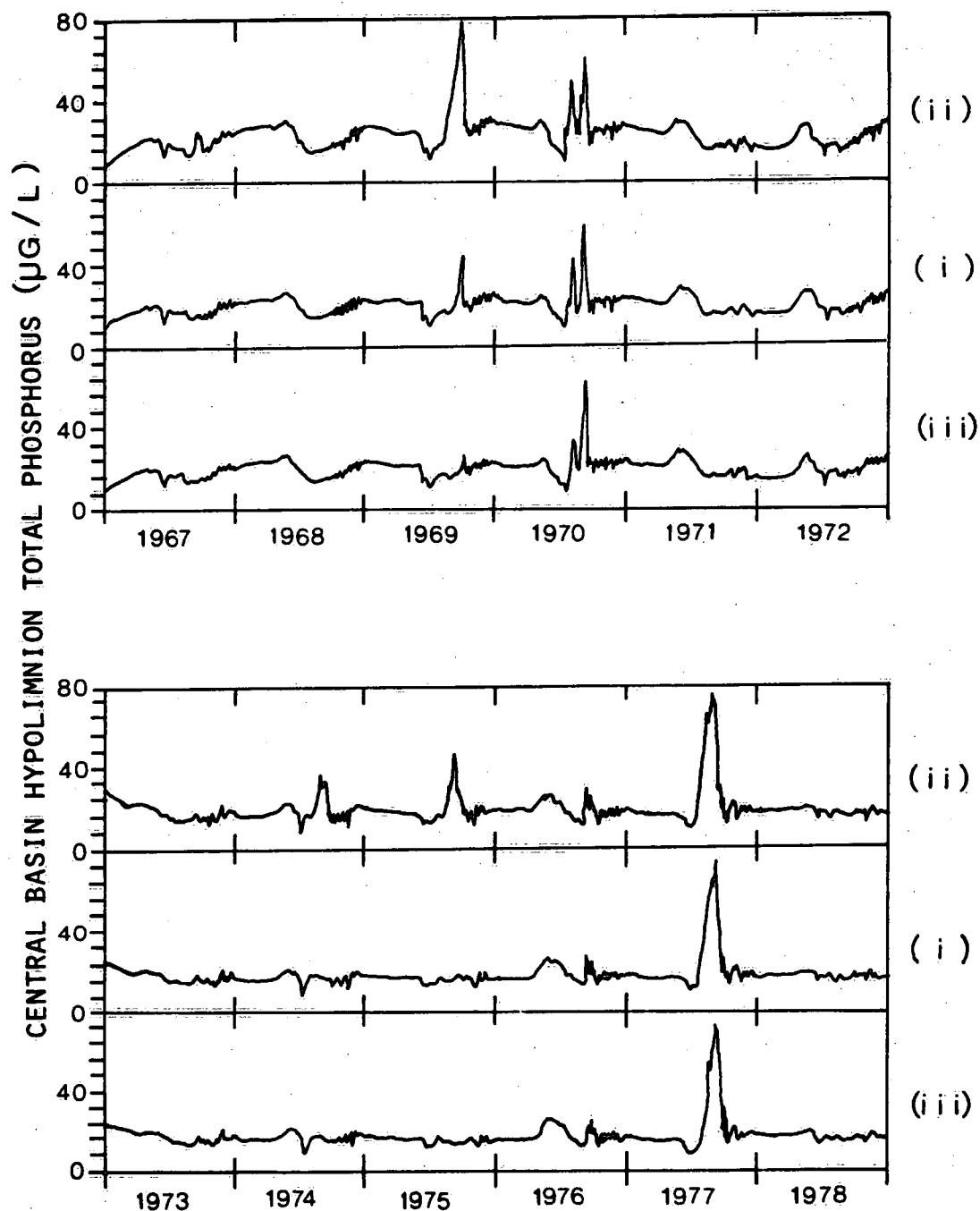


Figure 9.5. Simulated results of total phosphorus concentration in the Central Basin hypolimnion using (i) the actual observations of total phosphorus loading and water levels, 1967 to 1978; (ii) a hypothetical 30% loading increase of (i); (iii) a hypothetical increase of 0.5 m in the water levels of (i).

during the strongly anoxic years of 1969, 1970 and 1977, and to bring about moderately anoxic conditions for 1974 and 1975. The fully mixed lake concentration in early spring would become 27 $\mu\text{g/L}$ in 1969 and 17 $\mu\text{g/L}$ in 1978 for the Central Basin, up from 23 $\mu\text{g/L}$ and 16 $\mu\text{g/L}$ before the hypothetical load increase. On the other hand, the effect of the loading increase on epilimnetic dissolved oxygen, while not shown here, is very small.

Finally, the water level changes have been incorporated in the nine-box model (see Section 5.8 and Fig. 5.21). Conceptually, raising the water level allows almost an equivalent additional volume of water in the hypolimnion, provided that the water is added onto the surface before the thermal stratification, i.e., at a low enough temperature to ensure subsequent heat storage. A sensitivity test of this concept is to allow the water level to increase by 0.5 m more than its actual value (Fig. 4.8) each day during 1967 to 1978. The observed loading and meteorological inputs and Eq. 9.2 are the same as used in the results of case (1) of Fig. 9.3. The response of the hypolimnetic total phosphorus concentration to this hypothetical water level increase is shown in Fig. 9.5, curve (iii). The main result is that while the anoxic condition in 1969 almost vanishes, those in 1970 and 1977 remain.

9.4 Estimated Water Quality Response to Phosphorus Loading Reduction

The results under discussion so far pertain to dynamic changes of lake concentrations, which may or may not be at equilibrium with the loadings. It is obviously not possible to use dynamic results to infer the lake equilibrium response to loading changes. For a given set of initial lake concentrations, constant loading inputs and a fixed annual weather cycle, the lake concentrations computed by the nine-box model require five or six years to reach 90%

steady state for Lake Erie. It would probably take an even longer time if variability in the annual weather cycle was included. For simplicity, if the twelve-year period, 1967 to 1978, was chosen as a long weather pattern in itself and if the loadings were made constant, then the estimated lake concentrations at the twelfth year could indeed be regarded as "weathered" steady state results. Such a steady state approach is adopted here as the basis for estimating the water quality response to loading reduction.

Again, the linear loading feedback formula, Eq. 9.2, will be used. Thus, by varying the loading, different weathered steady state concentrations can be obtained, and response curves can be constructed. For each of these curves, e.g., springtime total phosphorus concentration in Western Basin versus loading, it is also pertinent to indicate the upper and lower bounds of the meteorological influences. Based on the twelve-year results, we can then choose the fourth year (i.e. 1970) result as one extreme case and the sixth year (i.e. 1972) result as the other extreme case. In other words, we shall construct three response curves from each twelve-year simulation: curve (1) is the "weathered" steady state result of the twelfth year; curve (2) is the "shallow hypolimnion" result of the fourth year, and curve (3) is the "entrainment reversal" result of the sixth year. In broad terms, the "shallow hypolimnion" year often consists of a calm and warm summer to be followed by a stormy winter, whereas the "entrainment reversal" year is for a stormy and cool summer to be followed by a calm winter. Figure 9.6 shows these different meteorological effects on the summer epilimnetic total phosphorus concentration, averaged over Julian days 150 to 260 and responding to changes in lake-wide total loads. While the curves (2) and (3) envelope the steady state curve (1) for the Western Basin, they become very close to curve (1) for the Central Basin and fall on the same side of curve (1) for the

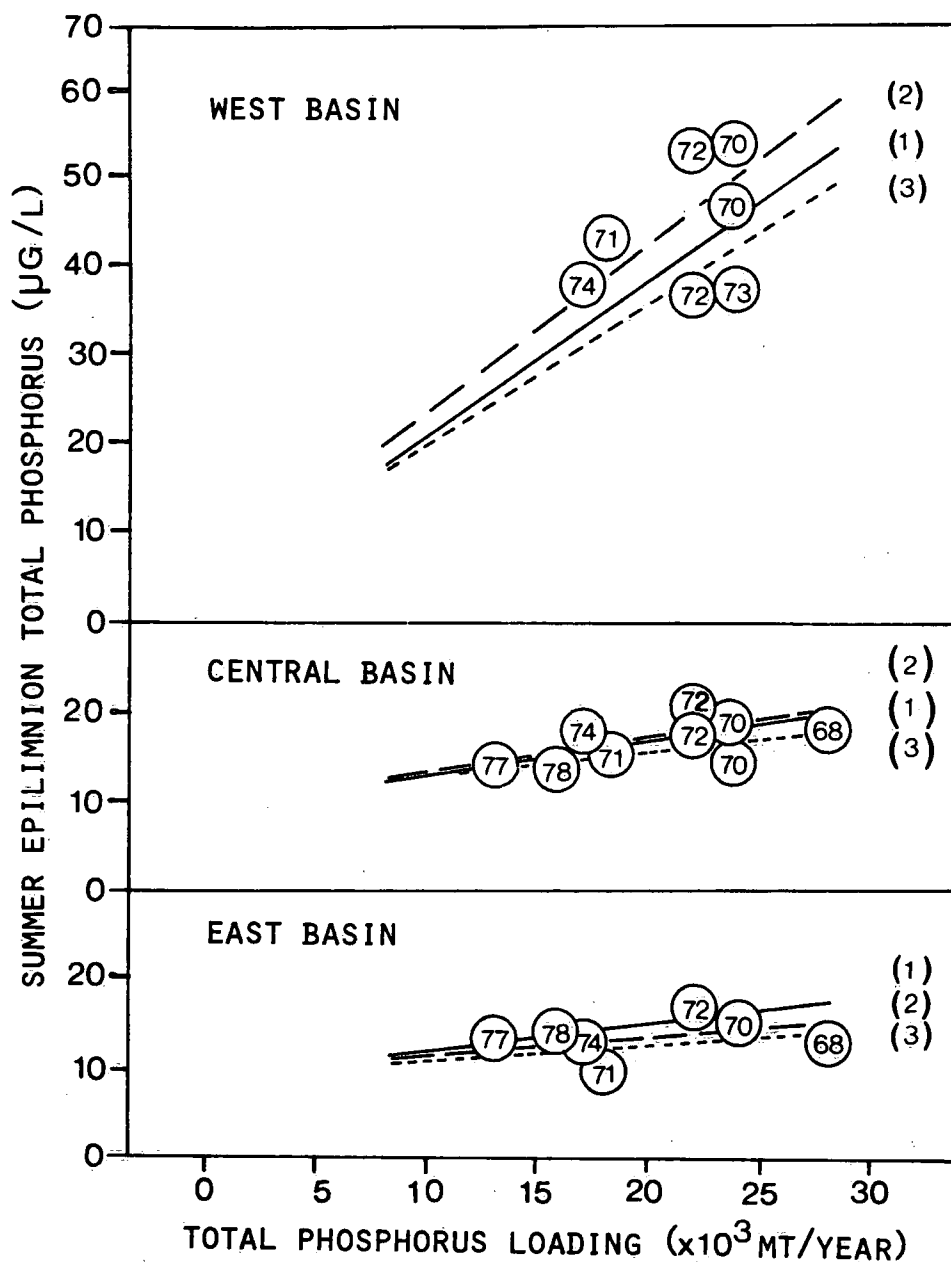


Figure 9.6. Estimated equilibrium summer epilimnetic total phosphorus concentration based on the nine-box model in response to lake-wide loading for (1) a twelve-year simulation; (2) a "shallow hypolimnion" type of thermal structure and (3) an "entrainment reversal" type of thermal structure. The circles indicate dynamic data observed in the years shown by the numbers.

Eastern Basin. This indicates lesser meteorological influence on the summer epilimnetic concentration in the latter two basins. Of course, the loading effects on the hypolimnetic total phosphorus concentration are more sensitive for different weather conditions, cf. Figures 9.3 and 9.5. In general, reduction of total phosphorus loading leads to decreases in the lake epilimnetic total phosphorus concentrations, with a faster decreasing rate for the Western Basin than for the other two basins. It is rather difficult to substantiate these steady state curves with observed concentrations, which, as remarked earlier, may or may not be at equilibrium with the loading. Nevertheless, if the observed total phosphorus concentrations are chosen for the period of Julian days 150 through 260 from selected years for which there are no major transient effects of large loading pulses, then they may lend some support to the estimated response curves. Indeed, as shown in Figure 9.6, the scatter of such selected data, while slightly wider than that provided by the estimated meteorological margins, conforms to the generally linear trend of the response curves.

The epilimnetic dissolved oxygen concentration is less sensitive to phosphorus loading changes. For Lake Erie, the most sensitive area is the hypolimnion of the Central Basin and can be demonstrated with the mean dissolved oxygen concentration averaged over Julian days 150 through 260 (Fig. 9.7a), and with the dissolved oxygen concentration just before the fall overturn (Fig. 9.7b). As shown in Fig. 9.7a, reduction in total phosphorus load tends to reduce the degree of oxygen depletion. However, two important points must be emphasized here. The estimated results are mainly due to the application of Eq. 9.2, a first-order approximation to the interaction between phosphorus loading and sediment chemistry. The approximation is derived from trend observations (Section 9.2) and applicable only for the twelve-year period. Beyond this period, extrapolation of curves such as those given in Fig. 9.7a is subjected to much larger uncertainties. Within the period, the meteorological uncertainties

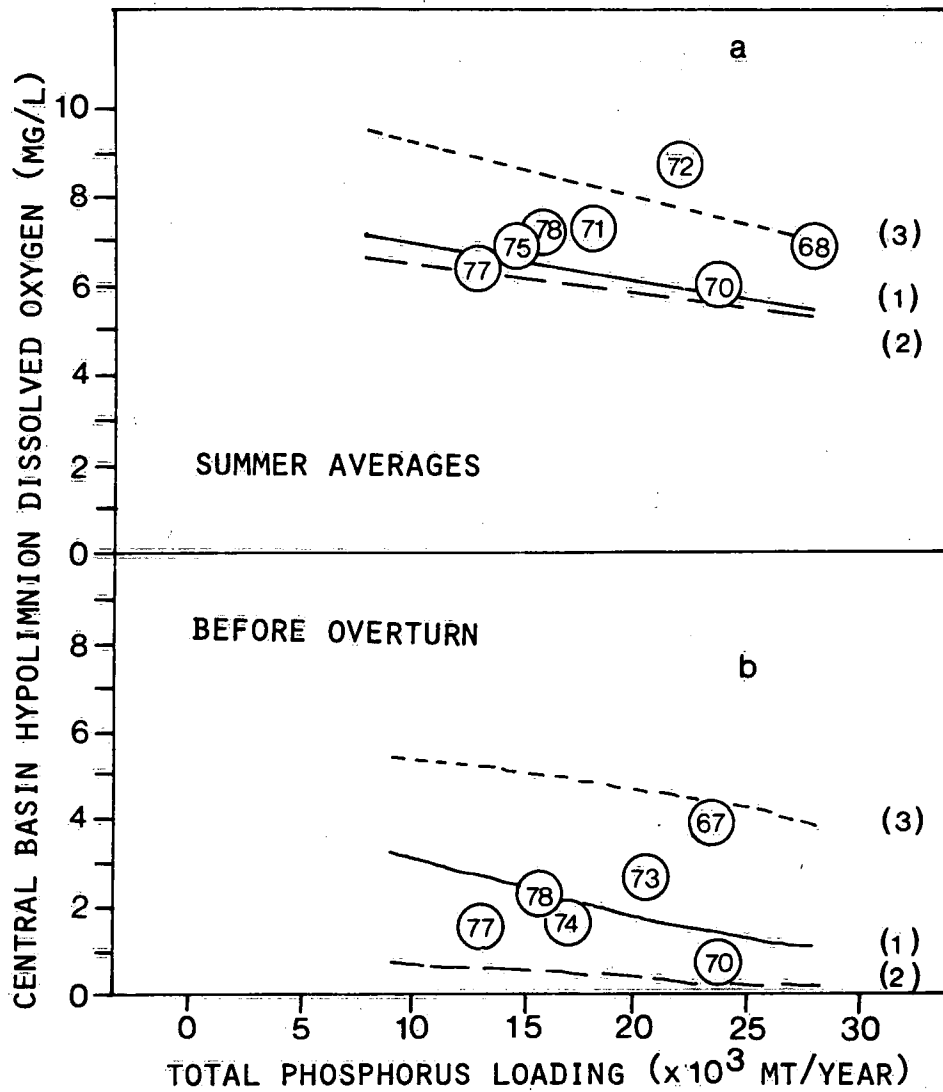


Figure 9.7. Estimated Central Basin hypolimnetic dissolved oxygen concentration (a) for summer averaged values and (b) for overturn values, based on the nine-box model in response to lake-wide loading for (1) a twelve-year simulation; (2) a "shallow hypolimnion" type of thermal structure, and (3) an "entrainment reversal" type of thermal structure. The circles indicate dynamic data observed in the years shown by the numbers.

are equal to or surpass those associated with Eq. 9.2. For example, the estimated steady state hypolimnetic oxygen concentration increases from 5.3 mg/L to 6.9 mg/L, should the total phosphorus loading be reduced from 28 000 MT to 10 000 MT, whereas the difference between the estimated concentrations of the two weather extremes is at least 1.6 mg/L for any given loading. This difference becomes even greater, about 4 mg/L (see Fig. 9.7b), if the hypolimnetic oxygen concentrations just before the fall overturn are compared. This implies that for a given loading, the basin may or may not become anoxic, depending on the meteorological conditions as the primary deciding factor. That is, the lake oxygen concentrations respond in a much less definitive manner than the lake total phosphorus concentrations to loading reduction. This is supported again by the somewhat incompatible (i.e. dynamic) observed data as plotted in Fig. 9.7a, which are volume-weighted means of the cruise data for the selected years. Similar observational support is also given in Fig. 9.7b by the oxygen concentrations measured closest to the fall overturn. It is obvious that for the range of phosphorus loading for the twelve-year period, anoxia could always occur for the weather patterns of 1970 and 1977, but would not occur for that of 1972.

The effect of phosphorus loading on the oxygen depletion problem therefore exists, but could become more understandable if long-term data were available. The case of anoxia in 1969 is an example (see Section 9.2).

9.5 Estimated Water Quality Response to Water Level Changes

The main meteorological effect on Lake Erie water quality relates to the thermal layer thicknesses and positions. The question to be considered is whether the thermal layer thicknesses and positions can be regulated by water management technologies. For small reservoirs, one "destratification" method (e.g. Henderson-Sellers,

1979) is to use high-velocity jets to force the stratified layers to mix. For a basin as large as the Central Basin, this mechanical method is obviously impractical. The other possible way is to regulate the water level. As demonstrated in Section 9.3, an increase of water level with clever timing leads to a larger hypolimnetic volume. However, an increase of water level may not be favourable in terms of ecological considerations and other aspects, e.g. the benthic organisms in the Western Basin (Burns, personal communication), shoreline erosion and wetland habitats. The following analysis therefore pertains to hypothetical cases of water level settings and the estimated water quality response to these settings in Lake Erie.

As demonstrated in Figure 9.5, the anoxia in 1969 could have been averted if the water level had been 0.5 m higher during that year. To investigate the water level effects further, we construct dissolved oxygen response curves for the Central Basin hypolimnion similar to those of Fig. 9.7 for the twelve-year period, but at different water levels. Thus, for each twelve-year computation, the observed phosphorus loading and meteorological data are used as inputs, but a constant water level is used throughout the period. Again, the results of the fourth year (1970) and the sixth year (1972) are plotted as meteorologically extreme cases, while the twelfth year (1978) result represents the steady state result for the chosen water level.

Figure 9.8a shows the mean hypolimnetic dissolved oxygen concentration in the Central Basin for Julian days 150 through 260, in response to water level variations from the 1955 water level datum, i.e. the zero level. In general, the estimated results support the plausibility of using the water level to regulate the dissolved oxygen condition in the Lake Erie Central Basin. When water level rises, the oxygen concentration rises. Some nonlinear variation is exhibited in the water level response curve because of the more complex changes in

interbasin transports, vertical entrainment and hydraulic and internal flows. By contrast, the linear variation of the phosphorus loading response curve is a direct result of Eq. 9.2. However, like the loading response, the water level response could be drastically altered by meteorological conditions. For example, there would be a very slight variation in the oxygen concentration with respect to water level changes, should a strong "reversal entrainment" weather pattern like the one in 1972 prevail (curve (3), Fig. 9.8a). This dependence on weather pattern can be further demonstrated by the estimated dissolved oxygen concentration just before the fall overturn. As shown in Fig. 9.8b, e.g., for 1 m above the 1955 water level, the oxygen concentration before the overturn could vary from 0.8 mg/L to 4.5 mg/L depending on the weather condition. It is rather difficult to confirm these estimated response curves with observed results because each point on the curve represents the "steady state" oxygen concentration with respect to a constant water level. However, if we plot some typical observed concentrations, but bear in mind that the observations are not necessarily at equilibrium with the water levels, then the scatter shown in the observed data still conforms to the margins defined by the weather extremes. In Fig. 9.8a, the observed water levels have been averaged and the observed oxygen concentrations are volume-weighted means for selected years in which there were two or more survey cruises during Julian days 150 through 260. In Fig. 9.8b, each of the observed oxygen concentrations shown is the one which is closest to the overturn point estimated by the one-dimensional thermocline model.

9.6 Further Research Needs for Lake Erie Water Quality Modelling

Both the estimated and the observed results presented in this chapter show that the dissolved oxygen and total phosphorus concentrations, particularly in the Central Basin hypolimnion, of Lake

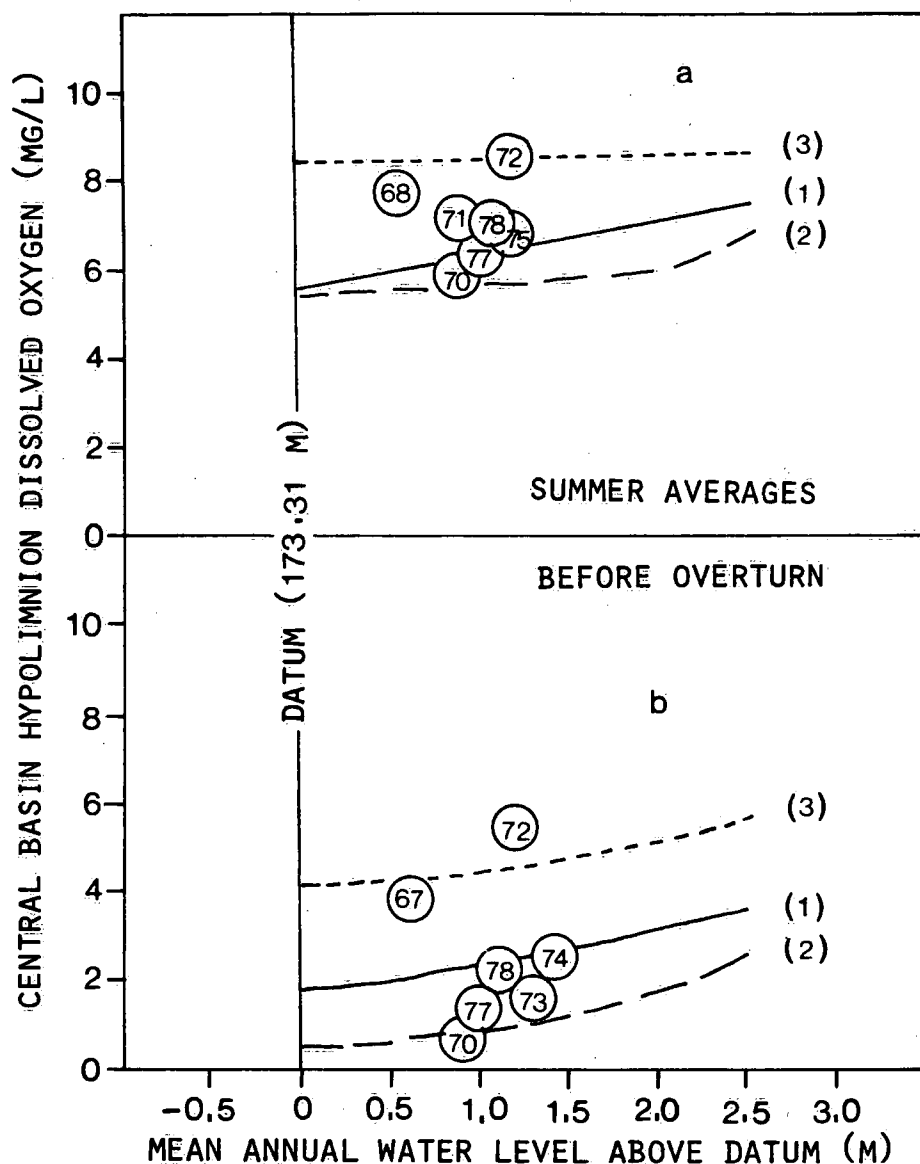


Figure 9.8. Estimated Central Basin hypolimnetic dissolved oxygen concentration (a) for summer averaged values and (b) for overturn values, based on the nine-box model in response to water level changes, with respect to the 1955 IGLD datum for (1) a twelve-year simulation; (2) a "shallow hypolimnion" type of thermal structure; and (3) an "entrainment reversal" type of thermal structure. The circles indicate dynamic data observed in the years shown by the numbers.

Erie are strongly influenced by meteorological effects. The segmentation of the lake into homogeneous layers must be based dynamically on the well-defined boundaries in the thermal regimes. Wind and solar heating have been identified as two of the more conspicuous meteorological factors which can drastically alter these thermal boundaries. Since wind, solar radiation and many other meteorological data are observed on a much more frequent basis than, for example, phosphorus loading, it is not surprising that the water temperature can be better simulated than the phosphorus components (cf. Figures 9.1 and 9.2). Indeed, simulation of water quality variables, such as the epilimnetic dissolved oxygen, which are strong functions of temperature, can also be improved. In such cases, we feel that the advancement of water quality modelling certainly relies on better inputs and models for simulating the thermal regimes in Lake Erie.

By contrast, the phosphorus dynamic simulation suffers mainly from the uncertainties of loading estimates, particularly those on the available and nonavailable forms of phosphorus for the Western Basin. The long-term trend of phosphorus concentration which is expected from the loading reduction, during 1967 to 1978, is strongly obscured by the large seasonal variability. Only until the seasonal variability is reasonably simulated, and thus isolated, would the trend be uncovered. The seasonal variability, itself, ties in closely with the meteorological effects, such as the chemical regeneration and physical resuspension of phosphorus from the sediment. Therefore, accurate phosphorus dynamics simulation requires both reliable physical models and long-term loading and lake concentration data. Of course, the model formulation of the nutrient-plankton relationship itself is an important step, which has not been advanced further than a previous attempt (Simons and Lam, 1980), but it certainly still requires further development and good measurements. The effect of phosphorus loading on the sediment oxygen demand is also poorly understood. The formula Eq. 9.2 is only a first-order

approximation of a phenomenon, which is of a time scale much longer than the twelve years under consideration.

On the whole, therefore, there are three main areas of future research for modelling Lake Erie water quality:

- (1) climatic influences on water quality,
- (2) interrelationships of long-term nutrient loading, lake concentrations and sediment chemistry, and
- (3) implementation of models of intermediate complexity following the hierarchy concept of spatial scales.

In terms of the weather influences on the water quality variables, there are actually more input factors than just wind and solar radiation which have been used in the Lake Erie models. Figure 9.9 shows how these meteorological inputs have been used in the models and connected to future linkages with other models, leading to more accurately estimated ecological responses. Since there are excellent meteorological input data available, their usage should sharpen the predictions of seasonal variability in the water quality variables. This seasonal variability and its influence on the estimated ecological response have been amply discussed in Sections 9.4 and 9.5. For example, the crucial question of whether or not a strong anoxia in any one year would occur in the Central Basin hypolimnion could only be answered if the weather pattern for that year was known first. For long-term predictions, therefore, the knowledge of the future weather patterns is a major problem. Perhaps by using the one-dimensional thermocline model, a statistical study on the frequency of occurrence of the three types of patterns, classified as "normal", "shallow-hypolimnion" and "entrainment reversal" in Section 6.2, over a sufficiently long period from past records may assist in gaining some hindcasting knowledge. An alternative is to make use of long-term climatic trend predictions as well as short-term weather

forecasts from climatic models. In both hindcasting and forecasting cases, the feedback from the thermocline and other models to the climatic models and data can be incorporated iteratively, as proposed in Section 7.5.

Of course, there are water quality variables such as the total phosphorus concentrations in the epilimnion of the Central and Eastern basins that are not so drastically affected by the thermal regimes (see Figures 6.11b and 6.11e). For these variables, the long-term response resulting from loading reduction is more apparent, albeit such a response is relatively weak (see Fig. 9.6). For other variables, this response can only be seen when the strong seasonal noises have been removed. In either case, techniques must be derived to provide better loading estimates designed for long-term mass balance calibration of sedimentation and sediment oxygen demand rates, in conjunction with the long-term surveillance of lake concentrations. As pointed out in Simons and Lam (1980), the formulation of the phosphorus dynamics, particularly the primary production, is surrounded with a high degree of uncertainty. The phosphorus and other nutrient dynamics must therefore be further investigated to pinpoint the nutrient-plankton relationship, so that more appropriate formulations can be incorporated in the models. Furthermore, the effects of toxic contaminants on the plankton primary production rates should also be included, if significant. Another major gap of knowledge lies with the transfer of chemical ions at the sediment-water interface, which may affect, for example, the sediment oxygen demand rate, and the chemical equilibria in both sediment and water. A multi-layer diffusion model structure for the sediment analogous to that of the one-dimensional (z) model for the water column must be used to assess the effects of the deeper sediment in terms of storing nutrients and depleting oxygen.

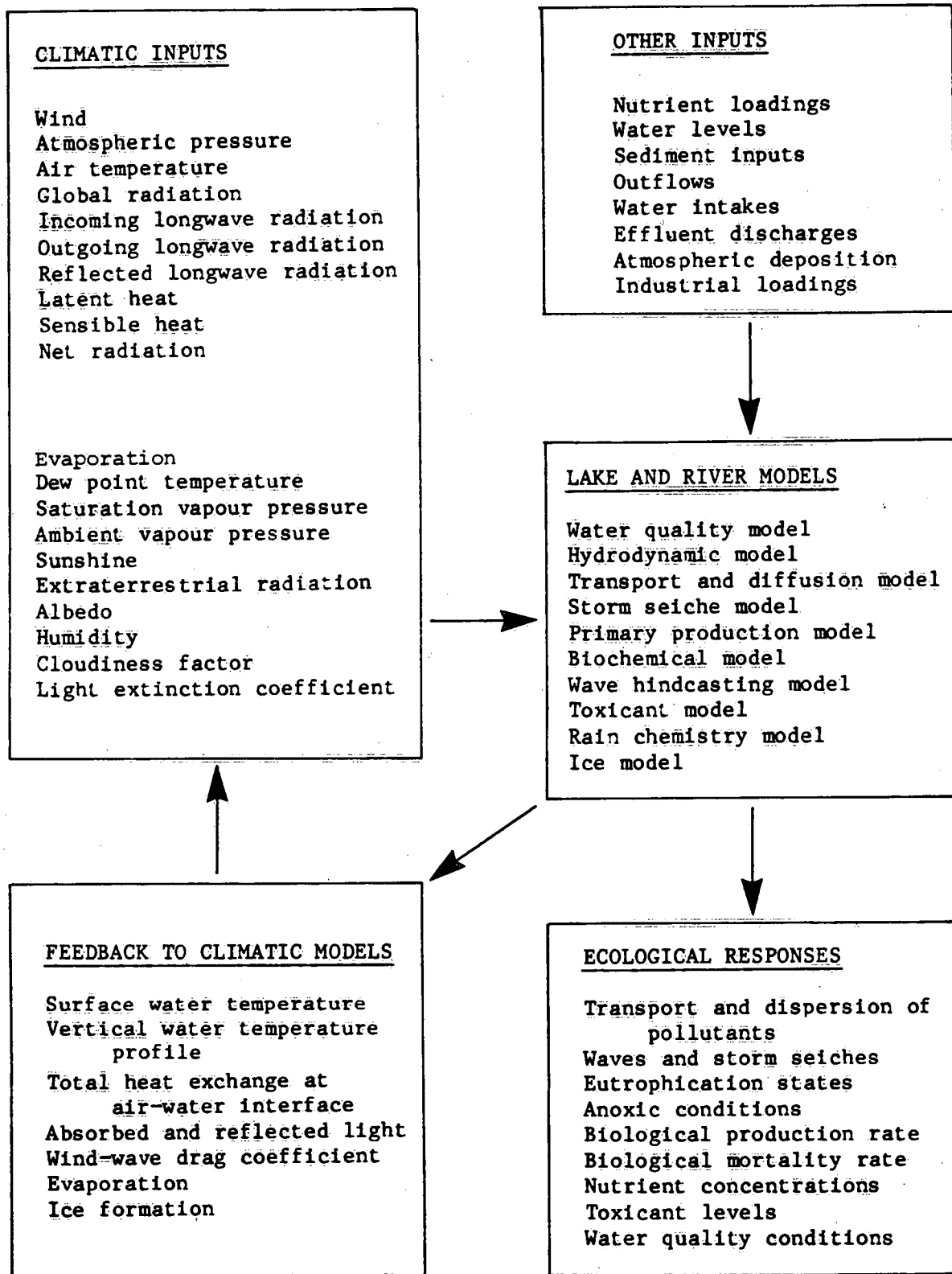


Figure 9.9. Proposed plan for the future water quality modelling research for Lake Erie.

Finally, as indicated in Figure 9.9, there are different types of models which utilize the climatic and other inputs to arrive at different ecological responses. Essentially, this multi-model methodology is necessary for developing the so-called models of intermediate complexity (see Chapter 8). Recognizing that it is not possible to simulate the entire lake ecosystem, we have resorted to the use of models with appropriate spatial complexity for individual limnological processes. For example, the proposed sediment chemistry submodel should involve a multi-layer structure in order to discern the diffusive processes between deep sediments and the overlying water. However, for the simulation of seasonal basin-wide transports of water quality variables, the nine-box model suffices. Thus, the modeller can choose the complexity of the model for different scientific or water management objectives. The more complex model may not only ascertain the limnological processes but also may provide essential information such as the estimates of thermal layer thicknesses and dynamic sediment oxygen demand rates to less complex models. Conversely, the less complex models can serve as diagnostic procedures for checking the consistency of models and data, before the more complex ones are developed. However, the exact algorithms and the criteria to switch from one model to another have not been clearly established. Perhaps the solution to the problem of an efficient design of intermediate complex models is also the key to unlock the modeller's dilemma mentioned in the introduction to this Chapter.

References

- AES. 1967 to 1978. Surface water temperatures for Lake Erie by infra-red thermometer technique. Hydrometeorology and Applications Division, Atmospheric Environment Service, Downsview, Ontario.
- Anderson, E.A. and D.R. Baker. 1967. Estimating incident terrestrial radiation under all atmospheric conditions. Water Resour. Res. 3:975-988.
- Appelby, D.J. 1977. The impact of phosphorus control activities, the experience in Ontario. Erco Industries Ltd., Toronto, Ontario, Canada, 37 pp.
- Beale, E.M.L. 1962. Some uses of computers in operational research. Industrielle Organisation, 31:51-52.
- Bennett, E.B. 1976. Effect of flowthrough on the chloride content of Lake Erie, 1964 to 1974. Canada Centre for Inland Waters, Burlington, Ontario, Canada. Unpublished Report.
- Boyce, F.M., F. Chiocchio, B. Eid, F. Rosa and F. Penicka. 1980. Hypolimnion flow between the Central and East basins of Lake Erie 1977. J. Great Lakes Res. 6:290-306.
- Burns, N.M. 1976a. Nutrient budgets for Lake Erie, 1970. J. Fish. Res. Board Can. 33:520-536.
- Burns, N.M. 1976b. Oxygen depletion in the Central and Eastern basins of Lake Erie, 1970. J. Fish. Res. Board Can. 33:512-519.
- Burns, N.M. and C. Ross. 1972. "Project Hypo". Canada Centre for Inland Waters, Burlington, Ontario, Canada, Paper No. 6, 180 pp.
- Canada Centre for Inland Waters (CCIW). 1977. Atmospheric loading of the lower Great Lakes. Acres Consulting Ltd. for Environment Canada. DSS-02SS KL347-6-0146, 88 pp.
- Charlton, M.N. 1980. Oxygen depletion in Lake Erie: Has there been any change? Can. J. Fish. Aquat. Sci. 37:72-81.
- Chiocchio, F. 1981. Lake Erie hypolimnion and mesolimnion flow exchange between Central and Eastern Basin during 1978. NWRI Manuscript APSD-81-009, CCIW, Burlington, Ontario, Canada, 94 pp.
- Coordinating Committee on Great Lakes Basic Hydraulic and Hydrologic Data. Lake Erie Outflow 1860-1964 with addendum 1965-1975, Chicago, Illinois and Cornwall, Ontario, June 1976, 20 pp.

Davies, J.A. and W.M. Schertzer. 1975. Estimating global solar radiation. Boundary-Layer Meteorology, 9:33-52.

Derecki, J.A. 1975. Evaporation from Lake Erie NOAA Technical Report ERL342-GLERL3, Ann Arbor, Mich., 84 pp.

Derecki, J.A. 1976. Heat storage and advection in Lake Erie. Water Resour. Res. 12:1144-1150.

Dilley, A.C. 1968. On the computer calculation of vapour pressure and specific humidity gradients from psychrometric data. J. Appl. Meteorol. 7:717-719.

Di Toro, D.M. and J.P. Connolly. 1980. Mathematical Models of Water Quality in Large Lakes, Part 2: Lake Erie, EPA-600/3-80-065 Report, Duluth, Minn., 231 pp.

Dobson, H.H. and M. Gilbertson. 1971. Oxygen depletion in the hypolimnion of the Central Basin of Lake Erie, 1929-1970. Proc. 12th Conf. Great Lakes Res. 14:743-748.

Dolan, D.M., A.K. Yui and R.D. Feist. 1981. Evaluation of river load estimation methods for total phosphorus. J. Great Lakes Res. 7:207-214.

Edinger, J.E., D.K. Brady and J.C. Geyer. 1974. Heat exchange and transport in the environment. Electric Power Research Institute, Cooling Water Discharge Research Project (RP-49) Report No. 14, 118 pp.

Elder, F.C., A. Andren, S.J. Eisenrich, T.J. Murphy, M. Sanderson, and R.J. Vet. 1977. Atmospheric loadings to the Great Lakes. Unpublished Manuscript. Univ. of Windsor, Ontario, Canada, 17 pp.

Fraser, A.S. 1981. Evaluation of salt in the Great Lakes. Canada Centre for Inland Waters, Environment Canada, Burlington, Ontario, 23 pp.

Fraser, A.S. and K.E. Willson. 1981. Loading estimates to Lake Erie, 1967-1976. Environment Canada, Inland Waters Directorate, Sci. Ser. No. 120, Ottawa, Ontario, 23 pp.

Hamblin, P.F. 1979. Note, Great Lakes storm surge of April 6, 1979. J. Great Lakes Res. 5:312-315.

Hanson, B., F. Rosa and N.M. Burns. 1977. Survey "8", a budget calculation program for Lake Erie. Unpublished manuscript. CCIW, Burlington, Ontario, Canada, 56 pp.

Heinrich, J., W. Lick and J. Paul. 1981. Temperatures and currents in a stratified lake: A two-dimensional analysis. J. Great Lakes Res. 7:264-275.

Henderson-Sellers, B. 1979. Reservoirs. MacMillan Press, London, 128 pp.

Henderson-Sellers, B. and D.C.L. Lam. 1982. Reformulation of eddy diffusion thermocline models. Unpublished Manuscript. Univ. of Salford, England, 15 pp.

Herdendorf, C.E. 1980. Lake Erie Nutrient Control Program - An assessment of its effectiveness in controlling lake eutrophication. EPA-600/3-80-062. Duluth, Minn., 354 pp.

Hollan, E. and T.J. Simons. 1978. Wind induced changes of temperature and currents in Lake Constance. Arch. Meteorol. Geophys. Bioclimat. Series A, 27:333-373.

International Joint Commission. 1969. Report to the International Joint Commission on the pollution of Lake Erie, Lake Ontario and the international section of the St. Lawrence River, Vol. 2., 316 pp.

International Joint Commission. 1978. Great Lakes water quality agreement between the United States of America and Canada, IJC, Windsor, Ontario, 56 pp.

International Joint Commission. 1973, 1974, 1975, 1976. Great Lakes water quality annual report, Appendix "C". Remedial Programs Subcommittee report to the Great Lakes Water Quality Board. 194/250/142 pp.

International Joint Commission. 1977. Great Lakes water quality 1977, Appendix "B". Surveillance Subcommittee report, IJC, Windsor, Ontario, 110 pp.

Ivey, G.N. and F.M. Boyce. 1982. Entrainment by bottom currents in Lake Erie. Limnol. and Oceanogr. 15 pp. (In press).

Kendall, M.G. and A. Stuart. 1968. The Advanced Theory of Statistics. Hafner Pub., New York, Vol. 3, 557 pp.

Kraus, E.B. and J.S. Turner. 1967. A one-dimensional model of the seasonal thermocline: II. The general theory and its consequences. Tellus, 19:98-105.

Kuntz, K.W. 1978. Atmospheric bulk precipitation in the Lake Erie basin. Environment Canada, Inland Waters Directorate, Rep. Ser. No. 56, Ottawa, Ontario, 10 pp.

Lam, D.C.L. 1980. Finite element simulation of anisotropic turbulent diffusion in lakes. Invited Paper. Proc. 3rd Int. Conf. on Finite Elements in Water Resources, Wang et al. (eds.), University of Mississippi, pp. 3.20-3.35.

Lam, D.C.L. 1981. Temporal and spatial constraints in data estimation problems. Applied Maths. Notes 6:20-32.

Lam, D.C.L. 1982. Finite element analysis of water quality in Lake Erie, NWRI unpublished manuscript, Burlington, Ontario, Canada, 10 pp.

Lam, D.C.L. and J.-M. Jaquet. 1976. Computations of physical transport and regeneration of phosphorus in Lake Erie, fall 1970. J. Fish. Res. Board Can. 33:550-563.

Lam, D.C.L. and W.M. Schertzer. 1980. Modelling the interaction of climate and aquatic regimes of large lakes. Invited Paper. Proc. Canadian Climate/Water Workshop, University of Alberta, Feb. 28-29, 1980. AES, Downsview, Ontario, Canada, pp. 157-160.

Lam, D.C.L. and T.J. Simons. 1976. Numerical computations of advective and diffusive transports of chloride in Lake Erie, 1970. J. Fish. Res. Board Can. 33:537-549.

Lam, D.C.L. and R.B. Simpson. 1978. Modelling coastal effluent transport using a variable finite difference grid. Advances in Computer Methods for P.D.E. II:294-300.

Lam, D.C.L., C.R. Murthy and K.C. Miners. 1981. An inverse problem approach to modelling coastal effluent plumes. Adv. Water Resources, 4:185-190.

Lam, D.C.L., W.M. Schertzer and A.S. Fraser. 1982. Mass balance models of phosphorus in sediments and water. Hydrobiologia, 91:217-225.

Lamire, F. 1961. Winds on the Great Lakes C1R-3560, TEC-380, Canada Department of Transport, Metropolitan Branch, 16 pp.

Mathias, J.A. and J. Barica. 1980. Factors controlling oxygen depletion in ice-covered lakes. Can. J. Fish. Aquat. Sci. 37:185-194.

Mellor, G.L. and P.A. Durbin. 1975. The structure and dynamics of the ocean surface mixed layer. J. Phys. Oceanogr. 5:718-728.

Millar, F.G. 1952. Surface temperatures on the Great Lakes. J. Fish. Res. Board Canada, 9:329-376.

Munawar, M. and I.F. Munawar. 1976. A lakewide study of phytoplankton biomass and its species composition in Lake Erie, April to December 1970. J. Fish. Res. Board Can. 33:581-600.

Murthy, C.R. 1976. Horizontal diffusion characteristics in Lake Ontario. J. Phys. Oceanogr. 6:76-84.

Nriagu, J.O. and C. Dale. 1974. Diagenetic formation of iron phosphates in recent lake sediments. Am. Mineral. 59:934-946.

Papadakis, J.E. 1981. Determination of the oceanic wind mixed layer depth by an extension of Newton's method. Pacific Marine Science Report, 81-9. I.O.S. Sidney, B.C., 32 pp.

Phillips, D.W. and J.G. Irbe. 1978. Lake to land comparison of wind, temperature, and humidity on Lake Ontario during the International Field Year for the Great Lakes, Environment Canada, Report Number CL1-2-77, 51 pp.

Phillips, D.W. and J.A.W. McCulloch. 1972. The climate of the Great Lakes Basin. Environment Canada, Climatological Studies, Number 20, AES, Downsview, Ontario, 40 pp.

Platt, T., K.L. Denman and A.D. Jassby. 1975. The mathematical representation and prediction of phytoplankton productivity. Environment Canada, Fish. Mar. Serv., Tech. Rep. 523, 121 pp.

Powers, C.F., D.L. Jones, P.C. Munding and J.C. Ayers. 1959. Exploration of colateral data potentially applicable to the Great Lakes hydrography and fisheries, Phase II, Special Report 7, University of Michigan, Great Lakes Research Institute, 163 pp.

Richards, T.L. and J.P. Fortin. 1962. An evaluation of the land-lake vapour pressure relationships for the Great Lakes, Pub. No. 9, University of Michigan, Great Lakes Research Division, Ann Arbor, Mich., pp. 103-110.

Robertson, D.G. and D.E. Jordan. 1978. Digital bathymetry of Lakes Ontario, Erie, Huron, Superior and Georgian Bay. Canada Centre for Inland Waters, Basin Investigation and Modelling Section, Burlington, Ontario, Canada, 10 pp.

Rodgers, G.K. 1965. The Thermal Bar in the Laurentian Great Lakes. Univ. Mich., Great Lakes Research Division, Ann Arbor, Mich., Pub. No. 13:358-363.

Rodgers, G.K. and D.V. Anderson. 1961. A preliminary study of the energy budget of Lake Ontario. J. Fish. Res. Board Canada, 18(4):617-636.

Rosa, F. and N.M. Burns. 1981. Oxygen depletion rates in the hypolimnion of Central and Eastern Lake Erie - a new approach indicates changes. NWRI unpublished manuscripts, Burlington, Ontario, Canada, 32 pp.

Sanderson, M.E. 1980. The Climate of the Essex Region of Canada's Southland. Department of Geography, University of Windsor, 105 pp.

Schertzer, W.M., F.C. Elder and J. Jerome. 1978. Water transparency of Lake Superior in 1973. J. Great Lakes Res. 4:350-358.

Simons, T.J. 1976a. Continuous dynamical computations of water transports in Lake Erie for 1970. J. Fish. Res. Board Can. 33:371-384.

Simons, T.J. 1976b. Analysis and simulation of spatial variations of physical and biochemical processes in Lake Ontario. J. Great Lakes Res. 2:215-233.

Simons, T.J. 1980. Verification of Seasonal Stratification Models. Departmental Report, Institute for Meteorology and Oceanography, University of Utrecht, the Netherlands, 12 pp.

Simons, T.J. and D.C.L. Lam. 1978. Nutrient exchange between volume elements of large lakes. Proc. Symp. Modelling the Water Quality of the Hydrological Cycle, Baden, Austria, September 1978. IAHS-AISH Pub. No. 125, pp. 185-191. Washington, D.C.

Simons, T.J. and D.C.L. Lam. 1980. Some limitations of water quality models for large lakes: a case study of Lake Ontario. Water Resour. Res. 16:105-116.

Simons, T.J., F.M. Boyce, A.S. Fraser, E. Halfon, D. Hyde, D.C.L. Lam, W.M. Schertzer, A.H. El-Shaarawi, K. Willson and D. Warry. 1979. Assessment of water quality simulation capability for Lake Ontario. Environment Canada, Inland Waters Directorate, Sci. Ser. No. 111, Ottawa, Ontario, 220 pp.

Snodgrass, W.J. 1982. Mathematical model for dissolved oxygen in three southern Ontario reservoirs. Can. Water Resour. J., Vol. 7 (In press).

Somlyody, L. 1979. Preliminary study on wind induced interaction between water and sediment for Lake Balaton/Szemes Basin/Proc. 2nd Joint NIA/IIASA Task Force Meeting on Lake Balaton Modeling, MTA, Veszprem, Hungary, 26-49.

Stadelmann, P. and M. Munawar. 1974. Biomass parameters and primary production at a nearshore and a midlake station of Lake Ontario during IFYGL. Proc. 17th Conf. Great Lakes Res., Internat. Assoc. Great Lakes Res., pp. 109-119.

Stadelmann, P., J. Moore and E. Pickett. 1974. Primary production in relation to temperature structure, biomass concentration and light conditions at an inshore and offshore station in Lake Ontario. J. Fish. Res. Board Can. 31:1215-1232.

Steele, J.H. 1965. Notes on some theoretical problems in production ecology. Mem. Ist. Ital. Idrobiol. Dott Marco de Marchi Pallanza Italy, 18 (Suppl.):383-398.

Sundaram, T.R. and R.G. Rehm. 1973. The seasonal thermal structure of deep temperature lakes. Tellus, 25:157-167.

Thomann, R.V. and J.S. Segna. 1980. Dynamic phytoplankton-phosphorus model of Lake Ontario: ten-year verification and simulations. Proc. Conf. Phosphorus Management Strategies for Lakes, Ann Arbor Sci., Mich., pp. 153-205.

Tin, M. 1965. Comparison of some ratio estimators. J. Am. Stat. Assoc. 60:294-307.

U.S. Army Corps of Engineers. 1975. Lake Erie wastewater management study, feasibility report, Dep. of U.S. Army, Buffalo Dist., N.Y., 172 pp.

U.S. Geological Survey. 1954. Water-loss investigation: Vol. 1 - Lake Hefner Studies, U.S. Geological Survey Prof. Pap. 269.

U.S. Geological Survey. 1966 to 1978. Water resources data for New York. U.S. Dep. of Interior, Water Data Reports.

Vollenweider, R.A. 1955. A nomogram for the determination of the transmission coefficient and some remarks on the method of its calculation. Swiss J. Hydrol. 17:205-216.

Vollenweider, R.A. 1968. Scientific fundamentals of the eutrophication of lakes and flowing waters, with particular reference to nitrogen and phosphorus as factors in eutrophication. OECD PAS/CSI/68.27, 194 pp.

Vollenweider, R.A. 1969. Possibilities and limits of elementary budget models for lakes (in German). Arch. Hydrobiol. 66:1-36.

Vollenweider, R.A. 1970. Models for calculating integral photosynthesis and some implications regarding structural properties of the community metabolism of aquatic systems. In Proc. IBP/PP Technical Meeting, Trebon, 14-21 September, 1969, 455-472.

Vollenweider, R.A. 1975. Input-output models with special references to the phosphorus loading concept in limnology. Swiss J. Hydrol., 37:53-84.

Vollenweider, R.A. 1976. Advances in defining critical loading levels for phosphorus in lake eutrophication. Mem. Ist. Ital. Idrobiol. Dott Marco de Marchi Pallanza Italy, 33:53-83.

Vollenweider, R.A. and L.L. Janus. 1981. Statistical models for predicting hypolimnetic oxygen depletion rates. NWRI Report, Burlington, Ontario, Canada, 38 pp.

Vollenweider, R.A., W. Rast and J. Kerekes. 1980. The phosphorus loading concept and Great Lakes eutrophication. Proc. Conf. Phosphorus Management Strategies for Lakes, Ann Arbor Sci., Mich., 207-234.

Walters, R.Z., G.F. Carey and D.F. Winter. 1978. Temperature computation for temperate lakes. Appl. Math. Modelling, 2:41-48.

Williams, J.D.H., J.-M. Jaquet and R.L. Thomas. 1976. Forms of phosphorus in the surficial sediments of Lake Erie. J. Fish. Res. Board Can. 33: 413-429.

Bibliography

- Barica, J. and J.A. Mathias. 1979. Oxygen depletion and winterkill risk in small prairie lakes under extended ice cover. J. Fish. Res. Board Can. 36:980-986.
- Beck, M.B. 1981. Operational Water Quality Management: beyond planning and design. IIASA Exec. Rep. 7, Laxenburg, Austria, 74 pp.
- Bierman, V.J. 1980. A comparison of models developed for phosphorus management with the Great Lakes. Proc. Conf. Phosphorus Management Strategies for Lakes, Loehr et al. (eds.), Ann Arbor Sci., Mich., pp. 235-255.
- Boyce, F.M. and D.C.L. Lam. 1981. The physical limnology of the North American Great Lakes. Verh. Int. Verein. Limnol. 21:1650-1665.
- Bruce, J.P. and P.M. Higgins. 1977. Great Lakes Water Quality Agreement. Prog. Water Technol. 9:13-31.
- Bull, J., O. Lilly and K. Miners. 1980. Interbasin Transport Study Lake Erie 1978: Time Series Limnological Data Summaries, May to November, 1978. NWRI unpublished report, Burlington, Ontario, 7 pp.
- Burns, N.M., J.D.H. Williams, J.-M. Jaquet, A.L.W. Kemp and D.C.L. Lam. 1976. A phosphorus budget for Lake Erie. J. Fish. Res. Board Can. 33:564-573.
- Chapra, S.C. 1980. Application of the phosphorus loading concept to the Great Lakes. Proc. Conf. Phosphorus Management Strategies for Lakes, Loehr et al. (eds.), Ann Arbor Sci., Mich., pp. 191-206.
- Chen, C.W. and G.T. Orlob. 1972. "Ecological Simulation for Aquatic Environments", Report to Office of Water Resources Research. OWRR C-2044, Water Resources Engineers, Inc., Walnut Creek, Calif.
- Davies, J.A., P.J. Robinson and M. Nunez. 1971. Field determination of surface emissivity and temperature for Lake Ontario. J. Appl. Meteorol. 10:811-819.
- Di Toro, D.M. 1980. The effect of phosphorus loadings on dissolved oxygen in Lake Erie. Proc. Conf. Phosphorus Management Strategies for Lakes, Loehr et al. (eds.), Ann Arbor Sci., Mich., pp. 191-206.
- Elder, F.C. and B. Brady. 1972. A meteorological Buoy system for Great Lakes studies. Environment Canada, Inland Waters Branch, Tech. Bull. No. 71, Ottawa, Ontario, 11 pp.

Heathcote, I.W., R.W. Weiler and J.W. Tanner. 1981. Lake Erie nearshore water chemistry at Nanticoke, Ontario, 1969-1978. J. Great Lakes Res. 7:130-135.

Lucas, A.M. and N.A. Thomas. 1972. Sediment oxygen demand in Lake Erie's Central Basin, 1970. In Project Hypo, Burns and Ross (eds.), CCIW Paper No. 6, Burlington, Ontario, pp. 45-48.

Murphy, T.P. 1980. Ammonia and nitrate uptake in the Lower Great Lakes. Can. J. Fish. Aquat. Sci. 37:1365-1372.

Murthy, C.R. 1972. An investigation of diffusion characteristics of the hypolimnion of Lake Erie. In Project Hypo, Burns and Ross (eds.), CCIW, Paper No. 6, Burlington, Ontario, Canada, 39-44.

Nriagu, J.O. 1972. Stability of vivianite and ion-pair formation in the system $\text{Fe}_3(\text{PO}_4)_2 - \text{H}_3\text{PO}_4 - \text{H}_2\text{O}$. Geochim. Cosmochim. Acta, 36:459.

Prince, A.T. and J.P. Bruce. 1972. Development of nutrient control policies in Canada. Nutrients in Natural Waters, H.E. Allen and J.R. Kramer (eds.), J. Wiley & Sons, N.Y., pp. 433-446.

Redfield, A.C., B.H. Ketchum and R.A. Richards. 1963. The influence of organisms on the composition of seawater. The Sea, N.M. Hill (ed.), Wiley, New York, 2:26-77.

Schertzer, W.M. 1978. Energy budget and monthly evaporation estimates for Lake Superior, 1973. J. Great Lakes Res. 4:320-330.

Steele, J.H. 1974. The Structure of Marine Ecosystems. Cambridge, Mass., Harvard University Press, 128 pp.

Strickland, J.D.H. 1958. Solar radiation penetrating the ocean. A review of requirements and methods of measurement with particular reference to photosynthetic productivity. J. Fish. Res. Board Can. 15:453-493.

Thomas, R.L., J.-M. Jaquet, A.L.W. Kemp and C.F.M. Lewis. 1976. Surficial sediments of Lake Erie. J. Fish. Res. Board Can. 33:385-403.

Vollenweider, R.A. and P.J. Dillon. 1974. The application of the phosphorus loading concept to eutrophication research. Nat. Res. Council Canada Rep. NRCC 13690, 42 pp.

Appendix
Interpolation Scheme for Lake Erie
Water Quality Data

Interpolation Scheme for Lake Erie Water Quality Data

A.1 Interpolation Scheme

Noting the importance of spatial considerations in the analysis of Lake Erie chemistry, we have developed a package of computer programs capable of interpolating lake data three-dimensionally and incorporating the influence of thermal stratification. The main interpolation routine is called "TWIST", a Three-dimensionally Weighted Interpolation using the Structure of Temperature. This program is a derivation of an earlier program named "SURVEY 8" (Hanson et al., 1977).

The interpolation scheme is extended over the three basins of Lake Erie. The bathymetry of Lake Erie has been digitized to a 2-km grid density by Robertson and Jordan (1978). Initial trials in computation using a 2-km grid required excessive amounts of computer time and storage. To alleviate these difficulties a 6-km grid was used with each (I,J) grid cell assigned the mean bathymetric depth of the nine 2-km grid cells within the new cell. This grid realignment produces a (70,19) matrix which satisfies both vertical and horizontal requirements for interpolation of the chemistry data.

In recognition of nearshore effects upon water quality due to many factors such as wind-wave action on shorelines and loading discharges from tributaries and municipalities, a nearshore boundary of two grid cells (12 km from the shore) was established. This boundary has the effect of lessening the impact of highly variant nearshore data upon the interpolation routine. To apply the interpolation procedure, each station is assigned to a grid cell determined by its latitude and longitude. The interpolation then proceeds with the vertical component followed by the horizontal component.

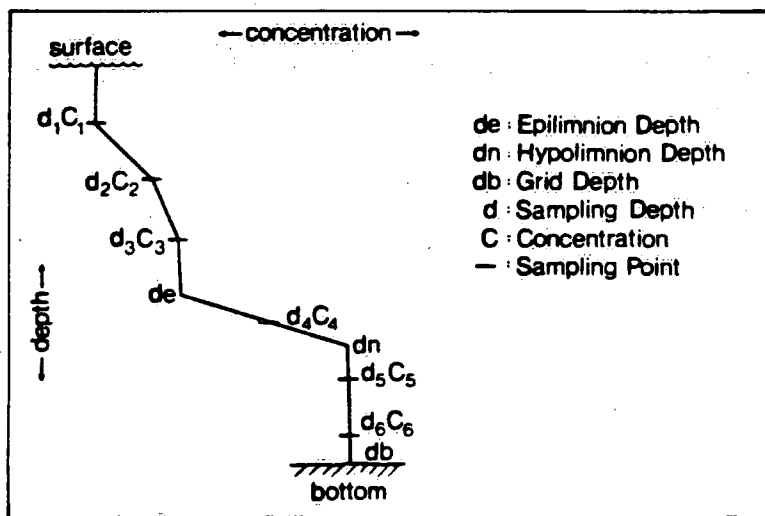


Figure A-1. Idealized station structure.

A.1.1 Vertical interpolation

The thermal structure is of significance due to the restrictive nature of the density gradient established between the epilimnetic and hypolimnetic water masses. During strongly stratified periods in the Central Basin of the lake, hypolimnetic oxygen is depleted due to aerobic decay processes at the sediment-water interface. The thermocline (mesolimnion) inhibits significant transfer of oxygen from the saturated epilimnion waters. Under anoxic conditions redox potentials become very low and become negative with the onset of reduction. This process in the Central Basin of the lake causes a release of sediment material including nutrients into the hypolimnion. Under conditions of reduction, significant quantities of ammonia are also observed. Thus, significantly different concentrations of various parameters become quasi-isolated based on the thermal structure of the water column. Typically, the Central Basin hypolimnion may be two to four metres in thickness. Clearly, an accurate method must be used to estimate concentrations within individual thermal layers.

For all stations occupied on all cruises studied between 1967 and 1978, an examination of the electronic bathythermograph (EBT) or mechanical bathythermograph profiles was made to delineate the thermal structure. From each trace (e.g. Fig. A-1) a determination was made of the depth (m) of the top (d_e) and bottom (d_n) of the mesolimnion and the lake depth, d_b . Vertical interpolation proceeds a priori from the surface to the lake bottom at station locations only. To achieve fine-scale interpolation, the water column was segmented into 20 sub-layers (10-epilimnion, 5-mesolimnion and 5-hypolimnion). Note that the total thicknesses of the epilimnion, mesolimnion and hypolimnion are $ET = d_e$, $MT = d_n - d_e$ and $HT = d_b - d_n$, respectively. Thus, the thicknesses of sublayers in the epilimnion, mesolimnion and hypolimnion are $ELT = ET/10$, $MLT = MT/5$ and $HLT = HT/5$, respectively. Furthermore, the midpoints (EM, MM and HM, respectively) of these sublayers are:

for epilimnion, $EM_1 = ELT/2$; $EM_m = EM_{m-1} + ELT$, $m=2,3...10$;

for mesolimnion, $MM_1 = d_e + MLT/2$; $MM_m = MM_{m-1} + MLT$, $m=2,3...5$;

for hypolimnion, $HM_1 = d_n + HLT/2$; $HM_m = HM_{m-1} + HLT$, $m=2,3...5$

The vertical interpolation scheme can be illustrated with an example of an idealized station structure given in Fig. A-1, in which there are six observed concentrations ($c_1, c_2...c_6$) at sampling depths of $d_1, d_2...d_6$, respectively. Suppose d_1, d_2, d_3 are found to belong to the epilimnion; d_4 belongs to the mesolimnion; and d_5, d_6 , belong to

the hypolimnion. Then, the concentration CE_m at the midpoint (EM_m) of the mth epilimnion sublayer is given by, for $m = 1, 2, \dots, 10$,

$$\begin{aligned} CE_m &= c_1, & \text{if } EM_m \leq d_1 \\ CE_m &= c_1 + \frac{c_2 - c_1}{d_2 - d_1} (EM_m - d_1), & \text{if } d_1 < EM_m \leq d_2 \\ CE_m &= c_2 + \frac{c_3 - c_2}{d_3 - d_2} (EM_m - d_2), & \text{if } d_2 < EM_m \leq d_3 \\ CE_m &= c_3, & \text{if } d_3 < EM_m \leq d_e \end{aligned}$$

By assigning concentrations of c_3 and c_5 at d_e and d_n , respectively, the concentration CM_m at the midpoint MM_m of the mth mesolimnetic sublayer is given by, for $m=1, 2, \dots, 5$,

$$\begin{aligned} CM_m &= c_3 + \frac{c_4 - c_3}{d_4 - d_e} (MM_m - d_e) & \text{if } d_e < MM_m \leq d_4 \\ CM_m &= c_4 + \frac{c_5 - c_4}{d_n - d_4} (MM_m - d_4) & \text{if } d_4 < MM_m \leq d_n \end{aligned}$$

The concentration CH_m at the midpoint HM_m of the mth hypolimnetic sublayer is given by, for $m=1, 2, \dots, 5$,

$$\begin{aligned} CH_m &= c_5, & \text{if } d_n < HM_m \leq d_5 \\ CH_m &= c_5 + \frac{c_6 - c_5}{d_6 - d_5} (HM_m - d_5), & \text{if } d_5 < HM_m \leq d_6 \\ CH_m &= c_6, & \text{if } d_6 < HM_m \leq d_b \end{aligned}$$

A.1.2 Horizontal interpolation

After the vertical interpolation at each sampling station, the concentrations at the midpoints of the 20 sublayers are all known. The next step is to interpolate horizontally, using the values. Considering only grid cells located in each of the three basins independently, horizontal interpolation proceeds using a volume-weighted polynomial procedure accessing each of the vertical layers throughout each basin. The procedure interpolates only layers that are defined as being of the same classification, i.e., epilimnion, mesolimnion, or hypolimnion and of the same vertical position with respect to the 20 layers identified previously.

At conclusion, volume-weighted estimates which are fully interpolated for every grid cell both horizontally and vertically along thermal surfaces are produced for all cruises and parameters under study.

A.1.3 Dimensional resolution

Although it would be possible to use the "TWIST" results in the form available at the conclusion of their run, it is preferable for modelling purposes to reference lake concentrations by depth rather than layer, as the layer thicknesses vary for every (I,J) grid cell. To this end a program named "TWISTER" was developed. Essentially, the function of "TWISTER" is to replace in the matrix the depth scale based upon the bathymetric depth for each (I,J) grid cell. In the first instance for the whole lake a three-dimensional (70, 19, 66) matrix of parameter concentrations with depth as the z coordinate is produced which maintains the characteristics inherent in "TWIST". This three-dimensional information is suitable for detailed resolution modelling.

A two-dimensional scheme is achieved by compressing one of the axes of the three-dimensional lake matrix. Any direction could be chosen. However, since horizontal gradients are significant in the longitudinal axis of the lake and delineation by depth is required, the transverse axis was compressed by computing the arithmetic mean for each depth interval of 1 m across the lake. The resulting matrix presents a two-dimensional array of fully interpolated concentrations. Similarly, the two-dimensional matrix can produce one-dimensional vertical concentration profiles. At this stage of reduction significant depth-related effects occurring within thermal layers may still be identified, although the averaging process lessens the distinction. Finally, the one-dimensional vector can be reduced to yield a single volume-weighted concentration for each of the three basins for a given parameter. If desired, a two-layered or three-layered structure can be retained for each basin.



3 9055 1017 2949 8

DATE DUE REMINDER

FEB 24 2000

Please do not remove
this date due slip.